Velocity Profiles and Suspended Sediment Transport in Wave-Current Flows

by

PALITHA NALIN WIKRAMANAYAKE

B.Sc. (Hons.), Civil Engineering
University of Peradeniya, Sri Lanka
(1985)

S.M., Civil Engineering
Massachusetts Institute of Technology
(1989)

SUBMITTED TO THE DEPARTMENT OF
CIVIL AND ENVIRONMENTAL ENGINEERING
IN PARTIAL FULFILLMENT
OF THE REQUIREMENTS
FOR THE DEGREE OF

DOCTOR OF PHILOSOPHY

at the

MASSACHUSETTS INSTITUTE OF TECHNOLOGY

February 1993

Signature of Author _____
Department of Civil and Environmental Engineering
January 14, 1993

Certified by _____
Ole Secher Madsen
Professor, Civil and Environmental Engineering
Thesis Supervisor

Accepted by _____
Ole Secher Madsen
Chairman, Department Graduate Committee
Department of Civil and Environmental Engineering

Dedicated with love and gratitude

to

my parents

who taught me by example

the value and rewards of education

VELOCITY PROFILES AND SUSPENDED SEDIMENT TRANSPORT IN WAVE-CURRENT FLOWS

by

PALITHA NALIN WIKRAMANAYAKE

Submitted to the Department of Civil and Environmental Engineering
on January 14, 1993, in partial fulfillment of the
requirements for the Degree of Doctor of Philosophy

ABSTRACT

This thesis investigates the transport of suspended sediment by a combined wave-current motion outside the surf zone. The objective was to calculate the velocity, suspended sediment concentration, and the resultant transport using a single consistent model. As recent field measurements indicate that the time-varying components of the velocity and concentration make a significant contribution to the net sediment flux, the solution for these components is included in the development of the model. It was decided to use a simple eddy viscosity model to solve the velocity and concentration problems.

The eddy viscosity model developed by Wikramanayake (1989) for wave-current interaction was reviewed. The inability of this model to reproduce some features of higher-order numerical turbulence models was found to be a consequence of the assumption of a time-invariant eddy viscosity. Therefore a time-varying eddy viscosity model was developed and solved for the case of a weak current relative to the waves. While this time-varying eddy viscosity model did show the features of the higher order models, it was found that the shear stresses and velocities predicted by the two eddy viscosity models were very similar.

Since the solution using the time-invariant model of Wikramanayake (1989) was much simpler and valid for the full range of wave-current interaction, this model was selected for the sediment transport model. The wave-current model was extended to include the case of a wave motion specified by several sinusoidal components. Available laboratory and field data on ripple geometry and energy dissipation were used to derive predictive relations for the equivalent roughness of movable sediment bed.

Analytic solutions were obtained for both the mean and periodic components of the suspended sediment concentration. The bottom boundary condition for the suspended sediment concentration was obtained by using a simple, yet realistic, reference concentration formulation that assumes the instantaneous near-bed concentration to be proportional to the instantaneous excess skin friction shear stress. The constant of proportionality in this equation, known as the resuspension coefficient, was the only undetermined parameter of the sediment transport model. Available field measurements of the near-bed concentration were used to determine this parameter. Different values of the resuspension coefficient were found for rippled and flat beds. These calculations highlighted several additional measurements that could be incorporated into field experiments in order to make the data more reliable.

The mean suspended sediment concentration predicted by the model was found to be in good agreement with the measured profiles. The effect of non-uniformity of

the bottom sediment on these profiles was examined using a simple extension of the model. The predicted profiles of the net sediment flux due to the mean and time-varying components were in agreement with the profiles estimated from the field measurements. The model was extended to calculate the instantaneous suspended sediment concentration under the observed irregular wave motion in the field. The time-variation of the calculated time series of the concentration was found to show some agreement with that of the observed time series. The variation of the net sediment flux with the frequency of the components was also calculated.

Finally, it was concluded that the model developed in this thesis could be used predict sediment transport under wave-current flows, to design and interpret the results of field experiments, and to investigate details of the transport process such as the variation of transport with frequency.

Thesis Advisor: Prof. Ole. S. Madsen
Title: Professor of Civil and Environmental Engineering

ACKNOWLEDGMENTS

The research in this thesis was supported by the Dredging Research Program of the Coastal Engineering Research Center, U.S. Army Corps of Engineers, Waterways Experimental Station, under Contract No. DACW-39-88-K-0047.

I would like to acknowledge here the contributions of all the people who made this thesis possible, both by direct help in my work and by making my life bearable while I completed it. I apologize for the fact that space limitations do not allow me to mention everyone by name.

First, I would like to thank my thesis and academic advisor, Prof. Ole Madsen, for all his advice, encouragement, and support over the last five and a half years. His direct approach to the physical basis of problems has often set me straight when I embarked on my many wild goose chases. In addition to being an enthusiastic and patient advisor he is also one of the best teachers I have had.

I would also like to thank the other members of my thesis committee, Profs. Chiang Mei and Ken Melville for all their helpful comments and criticism. I am probably the last Parsons Lab student to have all the "three Ms" on a thesis committee and to have taken nearly all their courses so I would like to thank them for a very thorough education in many aspects of coastal hydrodynamics.

I am very grateful to those researchers who let me have access to all the data analyzed in this thesis—sometimes even before they had looked at it themselves! I would like to acknowledge Dr. C. Vincent, Dr. P. Osborne, Prof. K. Bedford, Prof. D. Hanes and Prof. L. D. Wright and his student Jing-ping Xu for all their generosity.

After over five years, the Parsons Lab seems like a second home and that is due not to the comfortable furniture but to all the warm and wonderful people here who made me feel at home from day one. At the top of everyone's list is Pat Dixon—I always think of her as the den mother of the lab. Pat—thanks for everything. Thanks too to all the other lab staff who help to make life run on smoothly. In particular I am very thankful to Read Schusky for his incredible word processing skills and his patience with all the chopping and changing that goes on when something is written, to say nothing of the "last minute" nature of much of it! This thesis would probably be dated 1994 if he had not been around.

Then I have to thank all my "brothers- and sisters-in-arms"—the other students who have worked, played, and had fun (or at least tried to!) at the lab during my stay here, particularly those on the second floor and in the hydrodynamics section. During my first year the "old guard" consisting of people like Ying-keung Poon, Jim Bowen, Garry Willgoose, Don Polmann, and Mike Jasinski were very helpful. In the hydrodynamics section there were Andy Jessup, Gunnar Tomasson, and Mark Loewen who gave me invaluable help with all my problems. There were many others but I don't have the space to thank them all individually.

I feel very close to the group that came in with me—we have seen it all together—courses, generals, orals, proposals, defenses, and also parties, ski trips, concerts, etc. People like Paul Mathisen, Francis Felizardo, Hari Rajaram, Cheo Lee, Mike Ernst, John Durant, Nadia Dimou, Andy Dasinger, and all the rest have helped make the "long strange trip" worthwhile. Next there are all those who have come in after me—and there are many! The list includes Eric Lamarre, Lynn Reid, Ede Ijjasz-Vasquez, Rich Lewis, Elfatih El-Tahir, Glenn Moglen, Kevin Johnson, Kaye Brubaker, Roseanna Neupauer, Jenny Lee, Tom Chisholm, Shu-guang Li, Jeng-jong Lee, Roland Springer, Xue-yong Zhang, Kelly Hawk, Mindy Roberts,

Gavin Gong, Brian Cohen . . . . Thanks a lot for sharing some fun times with me—from Hydros softball to bird watching to skiing to the Grand Canyon.

Sustaining me for over five years is a major job and I am grateful to several people outside the lab. Thanks to my roommates Todd Holmes, Susan Mittman, Michael McIntosh, Sanjay Manandhar, and the rest. Also to Nanthi and the rest of the Sri Lankan community at MIT, Gaurav Shah, and Vishak Sankaran, and my many other friends in the Boston area.

I am grateful to my parents, family, and friends who sent me much needed love and support (including the edible kind) from various corners of the globe. Last but by no means least I want to thank my wife Sharmini for all her love and patience from the beginning to the end of my studies here.

Table of Contents

List of Figures

List of Tables

CHAPTER 1

INTRODUCTION AND MOTIVATION

1.1 Introduction

When undertaking engineering projects in the coastal zone it is necessary to consider the effect of the waves and currents that are nearly always present in coastal waters. Waves and currents affect structures directly by the action of fluid forces and indirectly by their ability to transport the loose bottom sediment found in most coastal regions. A knowledge of the sediment transport is needed to make predictions of such processes as shoreline erosion and beach profile change. Prediction of the sediment transport requires the estimation of the fluid velocity as well as the concentration of the sediment. As the sediment is entrained into the flow from the bottom, a knowledge of the near-bottom processes under combined wave and current flow will be of particular importance.

In deep water, the near-bottom velocity associated with the surface gravity waves is of a negligible magnitude. At these depths, the velocity field is well described by potential flow theory, which assumes that the fluid is inviscid and allows a finite slip velocity to exist at the bottom. However, as the waves move into shallower regions, the near-bottom velocity will increase and there will be a discrepancy between the finite slip velocity predicted by the potential flow solution and the no-slip boundary condition that must be satisfied by a real (viscous) fluid. Therefore it will be necessary to include the no-slip condition to obtain the velocity field very near the bottom.

Imposition of the no-slip condition introduces vorticity into the flow. Due to the oscillatory nature of the wave motion, however, this vorticity will have a limited

time to diffuse into the flow. The result is that the effects of viscosity will be limited to a thin bottom boundary layer, while the potential flow solution will be valid in the bulk of the flow. For wave periods of 6 to 12 seconds, which is the range usually observed in coastal waters, the thickness of this boundary layer will be between 1 and 10 cm.

The no-slip boundary condition also applies in the case of coastal currents, which are fluid motions with time scales of a few hours or greater. In this case the much larger time scale associated with the flow means that the viscous effects will usually have time to diffuse over the whole depth, i.e., the boundary layer thickness is comparable to the flow depth. The magnitudes of the wave and current motions in coastal regions is such that the boundary layers are usually turbulent.

The small scale of the wave boundary layer results in a large velocity shear, and therefore large rates of energy dissipation, within the layer. Furthermore, since the current boundary layer is much larger in thickness it is apparent that the shear stress due to a wave motion will be much larger than the shear stress due to a current of comparable magnitude. As the velocities due to the waves and the currents are usually of the same order of magnitude the near-bottom shear stress in coastal regions are nearly always dominated by the wave motion.

The presence of this thin wave boundary layer affects the flow in several ways. One of these is the increased flow resistance felt by a current when waves are present. The increased resistance is due to the additional mixing caused by the turbulent wave boundary layer. This mixing will reduce the velocity shear near the bottom and retard the current velocity near the bottom. The overall effect of this wave-current interaction will be to increase the effective roughness felt by the current motion.

A further effect of the wave boundary layer on the flow occurs when the bottom consists of movable sediment, usually quartz sand in coastal regions. The sediment grains on the bottom will move when the shear stress exerted on the bottom by the flow exceeds a critical value. Due to the different scales in the boundary layers it is usually the wave shear stress that dominates the mobilization of sediment. Soon after the critical shear stress for initiation of motion is exceeded, ripples will be formed on the bed. These ripples will increase the effective roughness felt by the fluid motion from a value scaled by the grain diameter to a value scaled by the ripple height. An increase in the roughness results in increased shear stress and energy dissipation in the boundary layer. Further increase in the wave motion will lead to the disappearance of the ripples and to sheet flow where a layer of grains moves to and fro on the bed. Therefore, the bottom roughness due to a movable bed is itself a function of the intensity of the wave motion.

The transport of sediment is usually divided into two modes—bedload and suspended load transport. Bed load transport is defined as taking place in the region of high concentration near the bed where transport is due primarily to grains rolling and jumping along the bottom. Suspended load transport is defined as taking place in the main body of the flow where grain-grain collision is negligible and the grains are carried in suspension by the fluid turbulence.

The bed load flux can be thought of as being a function of the bottom shear stress, while the suspended load flux is a function of both the bottom shear stress, which controls the quantity of entrained sediment, and the fluid velocity. The shear stress and velocity are in turn a function of the fluid forcing and the bedforms. This demonstrates the complicated nature of the interaction between the fluid motion and the movable bed. A further complication is that stable stratification associated with the gradient of suspended sediment concentration could dampen the turbulence

in the wave boundary layer. All these possible interactions should be kept in mind when modeling the sediment transport by waves and currents.

Despite the fact that sediment is usually mobilized by the wave motion it is apparent that a purely linear symmetric wave motion would not result in a net flux of sediment. However, the sediment thus mobilized could be transported by any factor—such as wave non-linearity, a superimposed current, or wave-induced mass transport—that causes an asymmetry in the wave motion. For example consider the case of a weak current acting together with a strong wave motion. While the net bed load flux due to the asymmetric bed shear stress may be small, the current may be able to transport significant quantities of the sediment that is brought into suspension by the wave motion.

This mechanism of sediment mobilization by the wave motion and transportation by the mean current velocity was commonly accepted in previous treatments of the transport of suspended sediment by waves and currents. Nearly all the proposed models for sediment transport under waves and currents compute the transport as the product of the mean concentration by the mean velocity. The time variation of the suspended sediment concentration and the net flux due to the product of the time-varying concentration and the time-varying fluid velocity were not considered. A possible reason for the neglect of these components may have been that sufficiently detailed data were not available to validate this concept.

However, recent field experiments, such as those reported by Vincent and Green (1990) and Hanes and Huntley (1986), have shown that the flux due to the time-varying components of velocity and concentration potentially can be of the same order of magnitude as, and in some cases dominates, the flux due to the product of the mean velocity and the mean concentration. Some measurements of the

instantaneous suspended sediment concentration under waves will be discussed in the next section to show the importance of the time-varying components.

1.2 Evidence for the Importance of the Time-varying Components

The neglect of the time-varying concentration would imply that the mean concentration is the more important component. However, laboratory experiments have shown that the instantaneous sediment concentration under a wave motion is strongly time dependent. Entrainment and suspension from rippled beds have been observed by Homma, Horikawa, and Kajima (1965), Nakato et al. (1977), and Sleath (1982). Measurement of the instantaneous concentration shows from two to five peaks for each wave cycle. Visual observation indicates that these peaks correspond to the passage of vortices shed from the ripple crest carrying entrained sand past the measurement point. The variation from the mean has been observed to be as much as 100 percent of the mean value.

Sleath (1982) has observed that the lee vortices entrain sand by trapping sediment carried over the ripple crest and by active erosion from the lee slope of the ripple. The quantity of sand entrained in a vortex is proportional to the strength of the flow over the ripple. The vortex is then thrown outwards in a direction opposite to the flow that created it. In the case of a wave and current flow the vortex formed when the wave velocity is in the current direction will contain more sand and be thrown back against the current. Nielsen (1988) suggested that this mechanism could explain the observation by Inman and Bowen (1963) that the transport caused by waves and a current over a rippled bed was against the current.

For example, some of the measurements of Nakato et al. (1977) are shown in Figure 1. The figure shows the instantaneous sediment concentrations measured

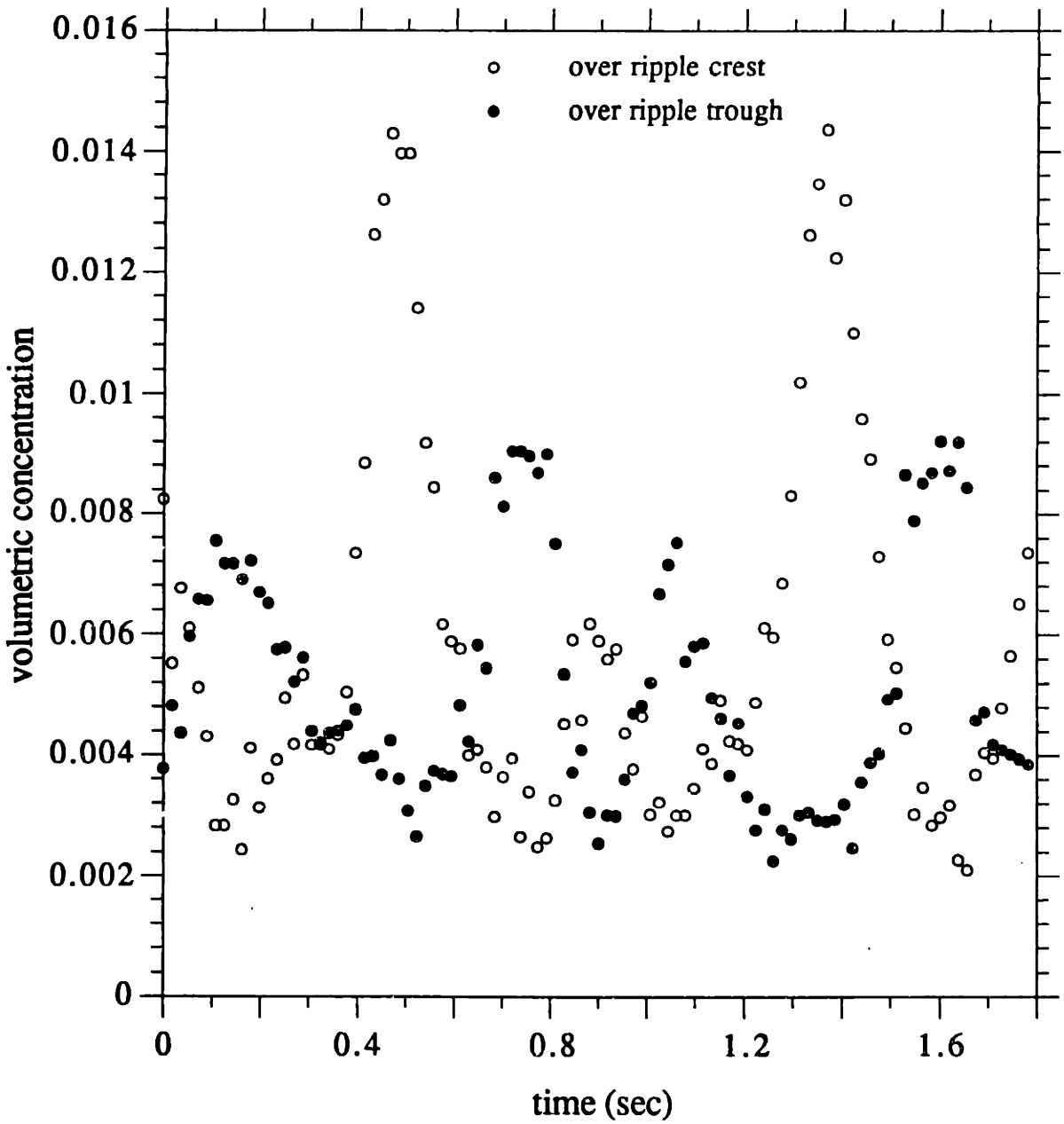

Figure 1. Measured instantaneous suspended sediment concentration over a wave period above a rippled bed from Test 2 of Nakato et al. (1977)

over a ripple crest and a ripple trough under a pure wave motion. The level of measurement is 3 mm above the level of the ripple crest. The grain diameter is 0.14 mm, the wave period, T, is 1.8 sec, and the near-bottom excursion amplitude is 76 mm. The origin of the time axis corresponds to the maximum horizontal velocity in the shoreward direction.

The figure shows that there are four peaks in each record for a wave period. Nakato et al. explain these peaks using the vortex shedding mechanisms described above. In the record over the ripple crest, the large peaks at around T/4 and 3T/4 correspond to the shedding of the vortex after the flow reverses direction. Since the ripple wavelength, which was 85 mm, is less than the magnitude of the near-bottom excursion, which is 152 mm, the vortex shed by a certain ripple will be carried beyond the adjacent ripple. It is the arrival of the vortex from the adjacent ripple that causes the peak at around T/2 and T over the ripple crest.

Similarly for the record over the trough, the peaks at around 3T/8 and 7T/8 are caused by the vortices shed at times T/4 and 3T/4 from the shoreward and seaward crest, respectively. The peaks at T/8 and 5T/8 were caused by the sediment-entraining vortex prior to being shed at T/4 and 3T/4. For the record over the crest the peak volumetric concentration is 1.4×10^{-2} while the mean value is 5.7×10^{-3}. For the record over the trough the corresponding values are 9.2×10^{-3} and 5.1×10^{-3}, respectively. These comparisons demonstrate the strongly time-varying nature of the suspended sediment concentration.

The instantaneous concentration over a flat bed, i.e., sheet flow conditions, has been measured by Horikawa, Watanabe, and Katori (1982) and Staub, Jonsson, and Svendsen (1984). The data show two peaks in the concentration for each wave cycle. The measurements very close to the bottom indicate that the concentration

peaks there correspond to the maximum flow velocity. The variation from the mean is as much as 60 percent of the mean concentration.

Therefore laboratory data indicate that the time-varying component of the concentration under waves is of the same order of magnitude as the mean concentration. The concentrations must be multiplied by the velocities in order to calculate the fluxes. The common situation in coastal sediment transport is for waves to be accompanied by a weak current motion, i.e., the wave or time-varying velocity is stronger than the current or mean velocity. Under these conditions the only way in which the time-averaged product of the periodic components could be much smaller than the product of the mean values is if the phase difference between velocity and concentration is close to 90 degrees.

However, as observed in the laboratory experiments the peaks in the concentration are caused by, and therefore correlated with, the times of high wave velocity. This correlation would lead us to expect that the time-averaged product of the periodic components of the concentration and velocity is at least of the same order of magnitude as the product of the mean concentration and the mean velocity. Such a possibility has been ignored by nearly all models proposed for the transport of suspended sediment by waves and currents.

As mentioned above, a probable reason for the very few models that have considered the time-varying component of the concentration is the paucity of data against which such a model can be compared. All the measurements described above were from small scale laboratory experiments using a pure wave motion. The extrapolation of these laboratory measurements to field conditions is a dubious proceeding under the best of circumstances.

Recent developments in instrumentation, however, have permitted detailed measurements of the instantaneous velocity and suspended sediment concentration under waves and currents. Such measurements have been reported by Hanes and Huntley (1986), Huntley and Hanes (1987), Doering and Bowen (1988), Vincent and Green (1990), Kim (1990), Hanes (1991), and Greenwood, Osborne, and Bowen (1991), among others.

In these experiments the instantaneous sediment concentration was measured at frequencies from 1 to 4 Hertz—either by using optical backscatter sensors at several points near the bottom or by using an acoustic concentration meter to obtain the profile of suspended sediment in the bottom region. Simultaneous measurements of the horizontal velocities were made at one or more points on the same vertical line. Using these measurements estimates of the instantaneous and time-averaged fluxes could be made over the near-bottom region.

A portion of the measurements reported by Hanes (1991) is shown in Figure 2. The figure shows the instantaneous suspended sediment concentration averaged over the region 0.5–4.5 cm above the bed, along with the instantaneous velocity in the wave direction measured at a point 15 cm above the bed. The concentration was measured by an acoustic concentration meter and the velocity by an electromagnetic current meter. The instruments were sampled simultaneously at a rate of 4 Hz.

The figure shows the strongly time-varying nature of the near-bottom concentration. There is a definite correlation between the peaks in the velocity record and the peaks in the concentration record. Another feature of the data is the effect of a few large waves in suspending large amounts of sediment. It is obvious that a model that considers only the mean velocity and concentration would not be able to represent the field observations.

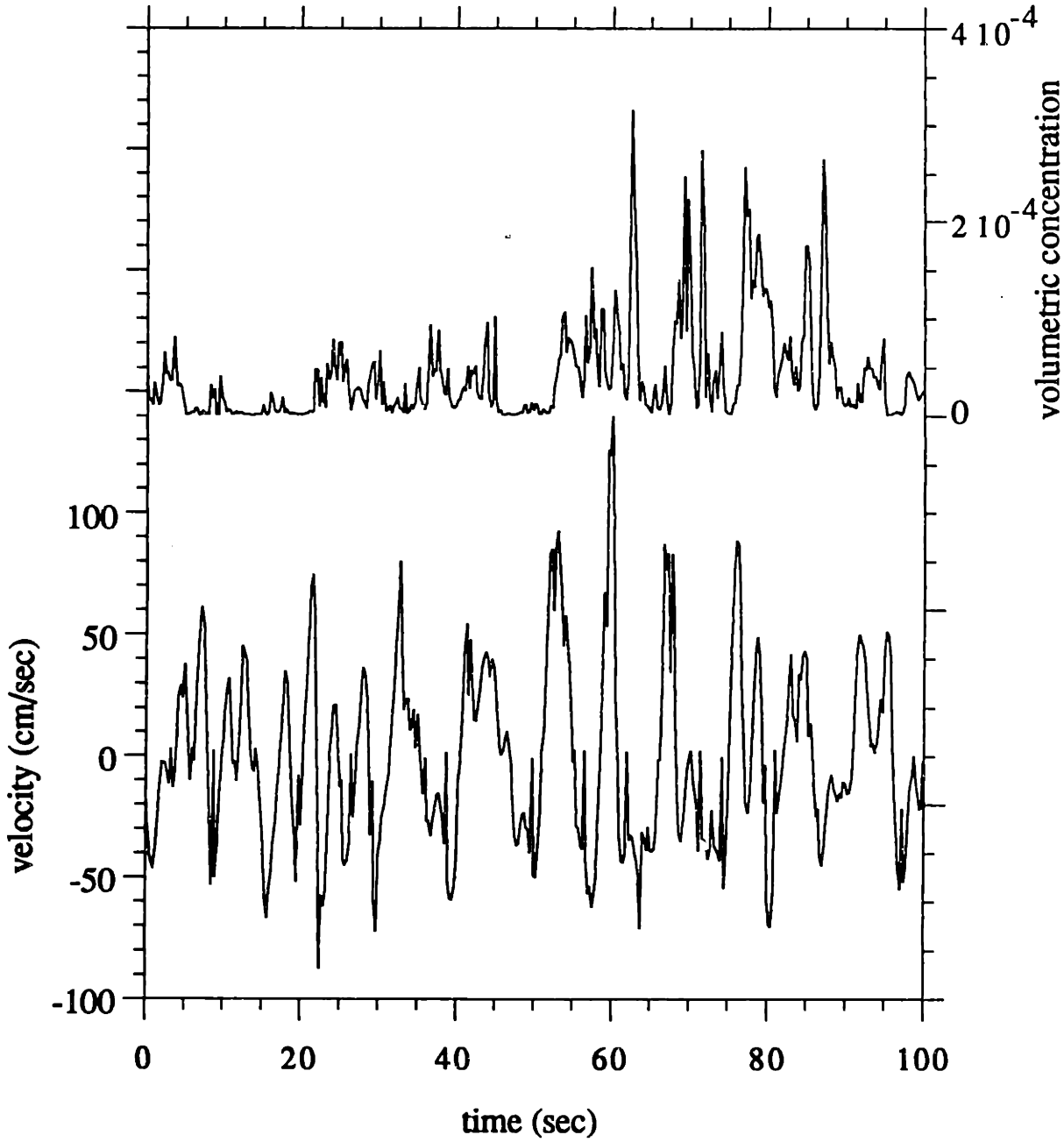

Figure 2. 100-second time series of near-bottom suspended sediment concentration and velocity in the wave direction from Hanes (1991)

Vincent and Green (1990) measured the instantaneous concentration over a rippled bed and observed variations in the instantaneous concentration that were consistent with the vortex shedding mechanism described above. They found that the transport very close to the bed was dominated by the periodic components and not by the mean values. Huntley and Hanes (1987) estimated that while the transport due to the mean components was offshore, the transport due to the time-varying components was about twice as large in the opposite direction, so that the net transport was onshore. Similar results have been reported by other researchers.

The effect of wave groups on the suspension and transport of sediment in the field was analyzed by Osborne and Greenwood (1992). They investigated the frequency dependence of the suspended sediment flux by calculating the co-spectrum of the velocity and the concentration. The co-spectrum showed that while flux at frequencies close to the incident short wave frequency of around 0.2 Hz was onshore, flux at frequencies around 0.04 Hz was offshore. Osborne and Greenwood (1992) showed that this offshore flux was caused by the increased concentration due to the passage of the wave group coinciding with the offshore phase (trough) of the forced long wave associated with the wave group. A similar effect of wave groupiness is shown by the laboratory data of Sato (1992).

The preceding discussion shows that the strongly time-varying nature of the near-bottom suspended sediment concentration has been observed in both laboratory and field experiments. The field data are consistent with the mechanisms of suspension observed in the laboratory. These mechanisms suggest that there is a strong correlation between the time-varying velocity and concentration components. Therefore any model for the transport of suspended sediment by waves and currents should include the time-varying components of the concentration and calculate the flux as the time-averaged product of instantaneous velocity and concentration. If

only the mean components are considered it is possible that the result obtained for the transport will be incorrect in direction as well as in magnitude.

1.3 Objective

The objective of the present work is to develop a simple but realistic model to calculate the sediment transport under flows consisting of non-breaking waves combined with a current. Such a model would consist of three main parts. First, a hydrodynamic model is needed to calculate the velocities and associated shear stresses. Next, a sediment model must be developed that calculates the distribution of suspended sediment in the water column. Finally, these two solutions must be combined to calculate the bed load and the suspended load transports. As described above, recent field experiments show the importance of including the time-varying components in this calculation.

The model to be developed should be as simple as possible, preferably analytical in nature, without neglecting any important physical principles. The various sections of the model should also be consistent with each other. This requirement means that it is not necessary to solve any particular aspect of the solution with greater accuracy than the least accurate section of the model. In the case of sediment transport the calculation of the suspended sediment concentrations will be the least well defined aspect of the problem, so that deriving an exact solution for the velocity would not improve the overall accuracy of the model.

Wikramanayake (1989) discussed various methods of solving the hydrodynamic problem and selected eddy viscosity models as the appropriate method based on the criteria of simplicity and consistency mentioned above. He compared the results of some of the more recent models proposed in the literature with data from laboratory

experiments and with numerical solutions of the governing equations using more complex models. None of these models was found to give an adequate fit to the data. Wikramanayake (1989) then developed an improved eddy viscosity model, without the use of additional fitting parameters, that gave a satisfactory agreement with the data. The model resulted in analytical solutions for the velocity and shear stress and was valid for the full range of wave-current interaction.

1.4 Review of Previous Models for the Suspended Sediment Problem

Some existing models for the problem of suspended sediment transport will be reviewed in this section in order to find out if any of the existing models can be used for the calculations proposed in this work. In contrast to the plethora of models developed for wave and wave-current boundary layer flows there are relatively few models proposed in the literature for the suspension and subsequent transport of sediment by waves and currents. One of the reasons for this situation is the difficulty of making experimental measurements of the suspended sediment concentration, particularly under field conditions, and especially near the bottom where the concentrations are the highest. As a result, approaches to this problem tend to be qualitative rather than quantitative and the models are more empirical than those used for the velocity.

One of the first models for the distribution of suspended sediment under waves was the mixing length model of Homma, Horikawa, and Kajima (1965) which used the potential wave velocity to derive the mixing length. Another mixing length model was proposed by Bakker (1974). Other models that do not use the eddy viscosity approach are the empirical model of Vongvisessomjai (1986) and the k-ϵ model of Hagatun and Eidsvik (1986).

Kennedy and Locher (1972) reviewed various formulations of the problem and attempted to fit measured profiles of the mean concentration using different eddy viscosity models. They concluded that the form of the profiles was well described by all three models considered. Nielsen (1979) used an eddy viscosity that was constant over the depth to analyze the mean concentration profiles measured in the laboratory. He derived an eddy viscosity and a mean bottom concentration from these profiles and then attempted to obtain an empirical relationship for these values in terms of the wave, sediment and ripple parameters. Nielsen (1986) obtained an empirical relation for the mean bottom concentration that was valid for both a rippled and a flat bed.

Skafel and Krishnappan (1984) proposed an eddy viscosity model that had a velocity scale proportional to the shear velocity and a length scale proportional to the wave orbital amplitude at the bottom. The bottom concentration was obtained by considering the bed load transport. Fredsoe, Anderson, and Silberg (1985) presented a model that had an eddy viscosity and boundary layer thickness that varied in time. The reference concentration was obtained by extending the steady flow formulation of Engelund and Fredsoe (1976) to the case of unsteady flow.

Glenn and Grant (1987) extended the wave-current model of Grant and Madsen (1979) to include the stratification effect of sediment in suspension resulting in a combined wave-current-sediment model. This model, along with that of Fredsoe, Anderson, and Silberg (1985), are the only two models that account for both the sediment and the velocity profiles. The net transport predicted by the Glenn and Grant (1987) model was analyzed by Goud (1988). She calculated the suspended sediment transport by integrating the product of the mean velocity and the mean concentration. This method of calculating the suspended load transport ignores any correlation between the periodic components of the velocity and the concentration.

Even in the model of Fredsoe, Anderson, and Silberg (1985), which calculated the time-varying concentration, the transport was calculated considering only the mean values.

The only previous model that used both the mean and time-varying components to calculate the transport was that of Nielsen (1988). He developed three simple models of sediment transport, two of which were somewhat heuristic in nature. The third used an eddy viscosity that was constant with depth to obtain a solution for the mean and time-varying components of the concentration. The boundary condition used was a pick-up type condition with a delta function input specified at the each velocity reversal. However, the transport was calculated using a velocity component with a constant magnitude and phase throughout the depth. This approach would ignore the relationships between the velocity and the concentration components. Furthermore, no information was given on how to obtain the magnitude of the eddy viscosity from the specified velocities. Therefore this model is incomplete and ignores some aspects of the problem that may have physical relevance.

In summary it can be said that none of the previous models proposed in the literature are suitable for the purpose of calculating the suspended sediment problem in the manner described in the preceding section. Another important drawback to all the preceding models is that the calibration of the model parameters has not been done very thoroughly, probably due to the paucity of reliable field data. Thus the present "state of the art" of suspended sediment transport modeling can be improved by the inclusion of the periodic terms in a new model and by the consistent calibration of this model using the recently available field data.

1.5 Outline of the Thesis

The goal of this thesis is to extend the turbulent eddy viscosity model developed by Wikramanayake (1989), which dealt with purely hydrodynamic aspects of wave-current interaction, to the case of suspended sediment under wave and current flows. The treatment is limited to the case of non-breaking waves over a horizontal bottom. The objective is to formulate a theoretical framework for the problem that together with recent field measurements of the instantaneous suspended sediment concentration can be used to develop a predictive model for sediment transport in the coastal zone.

The hydrodynamic model developed by Wikramanayake (1989) is reviewed in Chapter 2. Wikramanayake (1989) showed that the inability of this model to represent some aspects of the wave-current interaction shown by more complicated numerical models was due to the assumption of a time-invariant eddy viscosity. The development of a time-varying eddy viscosity model to investigate these features is outlined in Appendix A. Considering the requirements of consistency in accuracy between the different aspects of the model, however, the time-invariant model was selected for use in the sediment transport model.

As the model is to be calibrated using data obtained under the irregular wave conditions seen in the field, the representation of these conditions by a few periodic waves is discussed. Since some aspects of field waves required a specification by more than one wave component, the hydrodynamic model is extended to account for a wave motion specified by an arbitrary number of wave components. The hydrodynamic model uses the equivalent bottom roughness as an input parameter. However, as described in Chapter 1.1, this value is not known for a movable sediment bed. Therefore available laboratory and field data are utilized in

Chapter 3 to derive predictive relations for the equivalent roughness applicable to field conditions.

The development of the sediment transport model is carried out in Chapter 4. A simple model is given for the bed load transport. The governing equation for the distribution of the suspended sediment concentration is solved using the selected eddy viscosity model. The solution was found to depend on the boundary condition specified near the bed. A simple but realistic equation for this reference concentration is selected and the formulation of the reference values for the mean and periodic components is described. The calculations involved in the model are outlined with the help of a flow chart. The model contains only a single undetermined parameter which is obtained after comparison of the model results using field data.

The results of the model are compared with available measurements of the mean and instantaneous suspended sediment concentration from the field in Chapter 5. Finaliy, the development and results of the model are summarized in Chapter 6. Possible extensions of the model are discussed along with the implications of the model results for the design of field experiments and the interpretation of field data.

CHAPTER 2

THE HYDRODYNAMIC MODEL

The hydrodynamic model that is used to calculate the velocities and shear stresses used in the sediment transport model of Chapter 4 is described in this chapter. The time-invariant eddy viscosity model developed by Wikramanayake (1989) is reviewed briefly together with the solution for the wave and current velocities. The relative merits of the time-invariant eddy viscosity model described here and the time-varying model developed in Appendix A are discussed and the time-invariant model selected for the solution of the suspended sediment problem. The representation of the irregular wave motion observed in the field by a few periodic components is described. Finally, the hydrodynamic model is extended to include the case of many periodic wave components.

2.1 Review of the Time-Invariant Eddy Viscosity Model

The solution of the wave-current problem using the time-invariant eddy viscosity model of Wikramanayake (1989) is given in this section. The horizontal velocity, u, is written as

$$u = u_w + u_c \tag{1}$$

where u_c is the time-invariant (current) and u_w is the periodic (wave) component of the horizontal velocity respectively.

The linearized boundary layer equation for u_w was derived by Wikramanayake (1989) as

$$\frac{\partial u_w}{\partial t} = -\frac{1}{\rho}\frac{\partial p_w}{\partial x} + \frac{\partial}{\partial z}\left[\nu_t \frac{\partial u_w}{\partial z}\right] \tag{2}$$

where

ρ = density of water

p_w = time-varying component of pressure

x = direction of wave motion

z = height above the bottom

t = time

ν_t = turbulent eddy viscosity.

The boundary conditions for Equation 2 are

$$u_w = 0 \quad \text{at} \quad z = z_0 \tag{3}$$

and

$$u_w \to u_\infty \quad \text{as} \quad z \to \infty \tag{4}$$

where u_b is the near-bottom wave velocity and z_0 is defined by

$$z_0 = \frac{k_n}{30} \tag{5}$$

where k_n is the equivalent Nikuradse roughness.

The governing equation for the current velocity, u_c, was derived, assuming a constant-stress near-bottom layer, to be

$$\nu_t \frac{du_c}{dz} = \frac{\tau_c}{\rho} = u_{*c}^2 \tag{6}$$

where

τ_c = mean (current) shear stress

u_{*c} = shear velocity based on current shear stress

The boundary condition for Equation 6 is that

$$u_c = 0 \quad \text{at} \quad z = z_0 \tag{7}$$

Equations (2) and (6) must be solved for the velocities u_w and u_c using the time-invariant eddy viscosity model proposed by Wikramanayake (1989). This model is given by

$$\nu_t = \begin{cases} \kappa u_{*cw} z & z \leq \alpha\delta \\ \kappa u_{*cw} \alpha\delta & \alpha\delta \leq z \leq \alpha\delta/\epsilon \\ \kappa u_{*c} z & \alpha\delta/\epsilon \leq z \end{cases} \tag{8}$$

where

$\kappa = 0.4$ = von Karman's constant

α = model parameter

u_{*cw} = shear velocity based on maximum combined shear stress.

In Equation 8 δ is the boundary layer length scale defined by

$$\delta = \frac{\kappa u_{*cw}}{\omega} \tag{9}$$

where ω is the radian wave frequency, while ϵ, given by

$$\epsilon = \frac{u_{*c}}{u_{*cw}} \tag{10}$$

is a parameter that expresses the relative strength of the current motion with respect to the waves.

A sketch of the variation of eddy viscosity with the vertical coordinate z is given in Figure 3. The model is based on the two-layer model put forward by Grant and Madsen (1979) with the bottom layer scaled by the shear velocity based on the maximum shear stress and the upper layer scaled by the current shear velocity. The intermediate region ensures a smooth transition between the layers. Comparison of

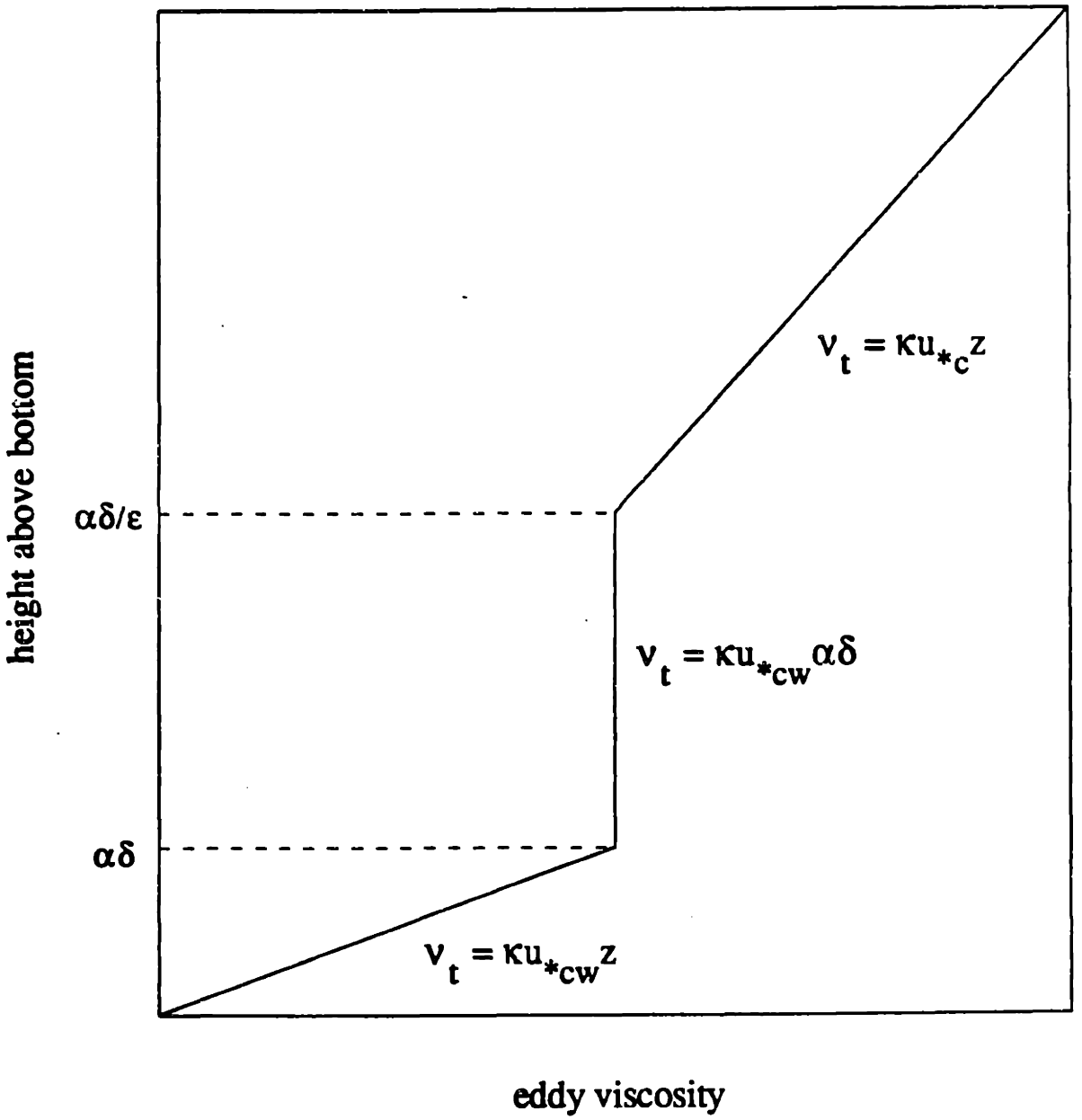

Figure 3. Variation of the eddy viscosity with height above the bottom

the results of this model with laboratory and numerical results led Wikramanayake (1989) to recommend the adoption of 0.5 as a suitable value for the parameter α.

2.1.1 Solution for the Current Velocity

The eddy viscosity distribution of Equation 8 can be substituted into Equation 6 to obtain an equation that is solved by using the boundary conditions of Equation 7 and matching the solution at the levels $z = \alpha\delta$ and $z = \alpha\delta/\epsilon$. The solution is obtained as

$$u_c = \begin{cases} \epsilon\frac{u_{*c}}{\kappa}\ln\left[\frac{\zeta}{\zeta_0}\right] & \zeta < \alpha \\ \epsilon\frac{u_{*c}}{\kappa}\left[\frac{\zeta}{\alpha} - 1 + \ln\left[\frac{\alpha}{\zeta_0}\right]\right] & \alpha < \zeta < \alpha/\epsilon \\ \frac{u_{*c}}{\kappa}\left\{\ln\left[\frac{\zeta}{\alpha/\epsilon}\right] + 1 + \epsilon\left[\ln\left[\frac{\alpha}{\zeta_0}\right] - 1\right]\right\} & \alpha/\epsilon < \zeta \end{cases} \tag{11}$$

In Equation 11 ζ is the non-dimensional vertical coordinate defined by

$$\zeta = \frac{z}{\delta} \tag{12}$$

and ζ_0 is defined by

$$\zeta_0 = \frac{z_0}{\delta} \tag{13}$$

A typical current velocity profile is shown in Figure 4a where $\epsilon = 0.4$, $u_{*c} = 2.5$ cm/s, $\delta = 3.3$ cm, and $z_0 = 0.17$ cm. The profile has three regions that correspond to the three layers in the eddy viscosity model of Equation 8. The upper and lower layers are logarithmic and the dotted line extending the upper logarithmic section to the line $u_c = 0$ shows that the effective roughness (z_{oc}) caused by the wave boundary layer is much larger than the real value of z_0.

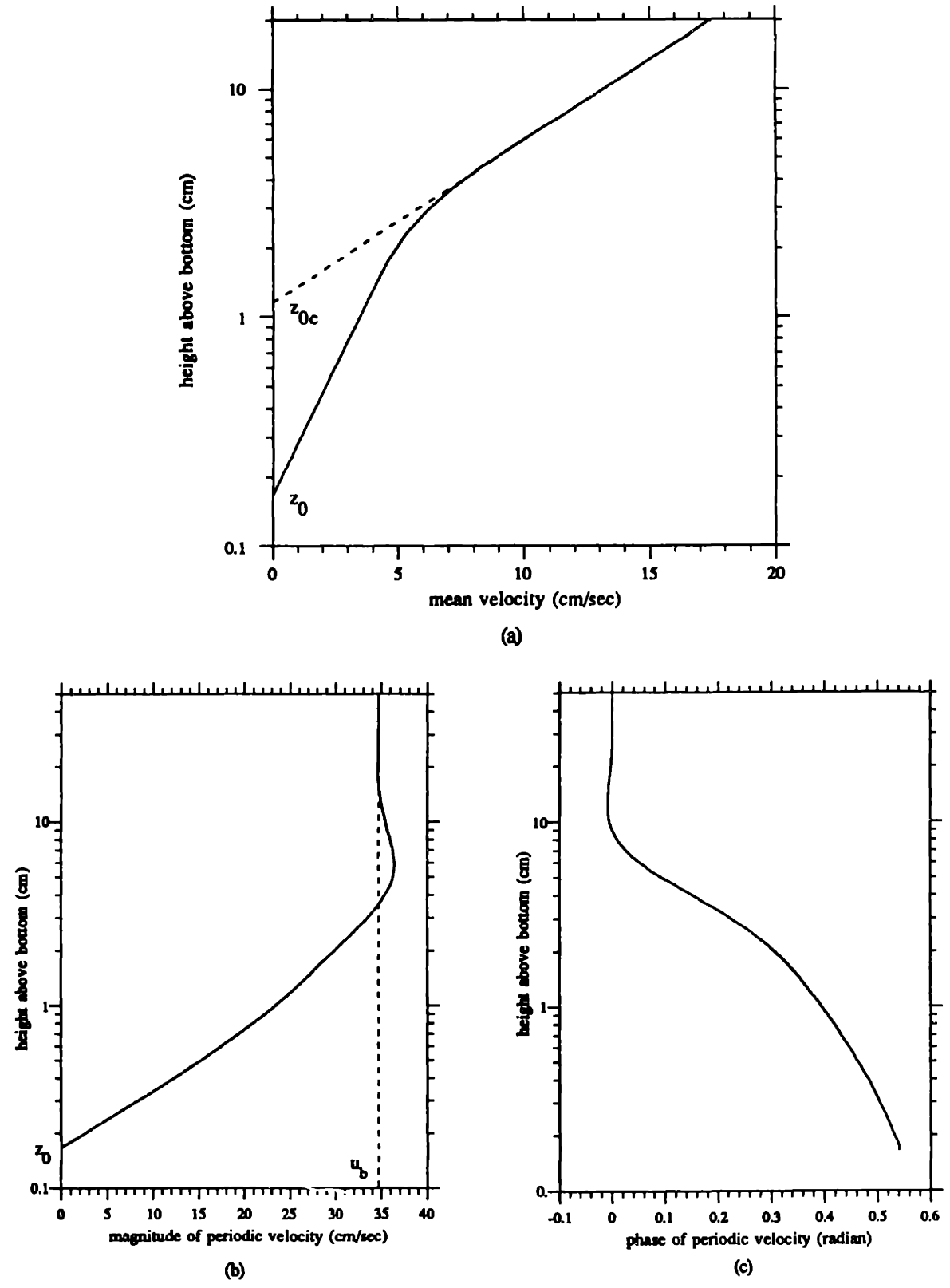

Figure 4. Profiles of a) current (mean) velocity, b) magnitude of the periodic velocity, and c) phase of the periodic velocity for an example where u_b = 34.7 cm/s, ω = 0.72 rad/s, k_n = 5.2 cm, and u_{*c} = 2.5 cm/s

2.1.2 Solution for the Wave Velocity

Equation 2, for the wave velocity, is solved by noting that

$$\frac{\partial u_\infty}{\partial t} = -\frac{1}{\rho}\frac{\partial p_w}{\partial x} \tag{14}$$

where u_∞ is the near-bottom potential wave velocity given by

$$u_\infty = u_b \cos \omega t \tag{15}$$

with ω being the wave radian frequency.

Introducing Equation 14 into Equation 2 gives

$$\frac{\partial(u_w - u_\infty)}{\partial t} = \frac{\partial}{\partial z}\left[\nu_t \frac{\partial}{\partial z}(u_w - u_\infty)\right] \tag{16}$$

The solution of Equation 16 can be simplified by writing

$$\frac{u_w - u_\infty}{u_b} = \mathrm{Re}\{u_d e^{i\omega t}\} \tag{17}$$

where Re{ } means the real part of the bracketed quantity and u_d is a complex function of z. Substitution of Equation 17 into Equation 16 leads to

$$\frac{d}{dz}\left[\nu_t \frac{du_d}{dz}\right] - i\omega u_d = 0 \tag{18}$$

From Equations 3, 4, and 17 the boundary conditions for this equation will be

$$u_d = -1 \quad \text{at} \quad z = z_0 \tag{19}$$

and

$$u_d \to 0 \quad \text{as} \quad z \to \infty \tag{20}$$

The eddy viscosity distribution of Equation 8 can be substituted in Equation 18 to obtain equations for u_d. Wikramanayake (1989) obtained the solution for u_d for the region $\zeta < \alpha$ as

$$u_d = A[\text{ker}(2\sqrt{\zeta}) + i\ \text{kei}(2\sqrt{\zeta})] + B[\text{ber}(2\sqrt{\zeta}) + i\ \text{bei}(2\sqrt{\zeta})] \tag{21}$$

where ker, kei, ber, and bei are the Kelvin functions of zeroth order and ζ is defined by Equation 12. A and B are undetermined complex constants.

For the region $\alpha < \zeta < \alpha/\epsilon$ the solution is obtained as

$$u_d = Ce^{\sqrt{i/\alpha}\zeta} + De^{-\sqrt{i/\alpha}\zeta} \tag{22}$$

with C and D being complex constants.

The solution in the region $\zeta > \alpha/\epsilon$ is obtained as

$$u_d = E[\text{ker}(2\sqrt{\zeta/\epsilon}) + i\ \text{kei}(2\sqrt{\zeta/\epsilon})] + F[\text{ber}(2\sqrt{\zeta/\epsilon}) + i\ \text{bei}(2\sqrt{\zeta/\epsilon})] \tag{23}$$

where E and F are complex constants.

The complex constants A, B, C, D, E, and F must be determined using the boundary condition of Equations 19 and 20 by matching the solution at the levels $\zeta = \alpha$ and $\zeta = \alpha/\epsilon$. Equation 20 leads to

$$F = 0 \tag{24}$$

while Equation 19 results in

$$A[\text{ker}(2\sqrt{\zeta_0}) + i\ \text{kei}(2\sqrt{\zeta_0})] + B[\text{ber}(2\sqrt{\zeta_0}) + i\ \text{bei}(2\sqrt{\zeta_0})] = -1 \tag{25}$$

where

$$\zeta_0 = \frac{z_0}{\delta} = \frac{k_n}{30\delta} \tag{26}$$

Matching the values of u_d and du_d/dz at the level $\zeta = \alpha$ results in the relations

$$A[\mathrm{ker}(2\sqrt{\alpha}) + i\,\mathrm{kei}(2\sqrt{\alpha})] + B[\mathrm{ber}(2\sqrt{\alpha}) + i\,\mathrm{bei}(2\sqrt{\zeta\alpha})]$$
$$- Ce^{\sqrt{i}\alpha} - De^{-\sqrt{i}\alpha} = 0 \tag{27}$$

and

$$A[\mathrm{ker}'(2\sqrt{\alpha}) + i\,\mathrm{kei}'(2\sqrt{\alpha})] + B[\mathrm{ber}'(2\sqrt{\alpha}) + i\,\mathrm{bei}'(2\sqrt{\zeta\alpha})]$$
$$- C\sqrt{i}e^{\sqrt{i}\alpha} - D\sqrt{i}e^{-\sqrt{i}\alpha} = 0 \tag{28}$$

where the primes in Equation (28) denote differentiation with respect to the argument of the function.

Matching u_d and $du_d/d\zeta$ at the level $\zeta = \alpha/\epsilon$ leads to

$$Ce^{\sqrt{i}\alpha/\epsilon} + De^{-\sqrt{i}\alpha/\epsilon} - E[\mathrm{ker}(2\sqrt{\alpha}/\epsilon) + i\,\mathrm{kei}(2\sqrt{\alpha}/\epsilon)] = 0 \tag{29}$$

and

$$C\sqrt{i}e^{\sqrt{i}\alpha/\epsilon} + D\sqrt{i}e^{-\sqrt{i}\alpha/\epsilon} - E[\mathrm{ker}'(2\sqrt{\alpha}/\epsilon) + i\,\mathrm{kei}'(2\sqrt{\alpha}/\epsilon)] = 0 \tag{30}$$

Equation 26, 27, 28, 29, and 30 form a set of five simultaneous equations for the complex constant A, B, C, D, and E. The coefficients depend solely on the parameters ζ_0, α, and ϵ. Once these parameters are specified the set of equation can be solved and the value of u_d obtained using the appropriate equation from Equations 21, 22, and 23. Since u_d is a complex number both the magnitude and phase of the wave velocity can be obtained by using Equation 17.

A typical wave velocity profile is shown in Figure 4b where $u_b = 34.7$ cm/s, $\omega = 0.72$ rad/s, and $z_0 = 0.17$ cm. The profile is close to logarithmic in the lower region and then overshoots the near bottom value u_b before returning to that value for

larger values of z. The corresponding profile of the phase of the velocity with respect to the phase of the near bottom velocity is shown in Figure 4c.

2.1.3 Closure of the Wave Problem

The solution for u_c and u_w so far has been developed in terms of the shear velocities u_{*c} and u_{*cw}, which are also unknowns that must be determined as part of the solution. The combined wave-current shear velocity u_{*cw} is related to the wave and current shear stresses by

$$\rho u_{*cw}^2 = \tau_{cw} = \max\{(\tau_w^2 + 2\tau_w\tau_c\cos\phi_{cw} + \tau_c^2)^{1/2}\} \tag{31}$$

where

τ_{cw} = maximum combined shear stress

τ_w = wave shear stress

τ_c = current shear stress

ϕ_{cw} = angle between the waves and the current

The wave problem is closed by defining the wave shear stress, τ_w, as

$$\frac{\tau_w}{\rho} = \left[\nu_t \frac{\partial u_w}{\partial z}\right]_{z=z_0} \tag{32}$$

while the current shear stress is either specified or determined iteratively by using the specified current velocity. The details of the iterative solution can be found in Wikramanayake (1989).

The solution of the wave-current problem requires the input of the wave, current, and bottom parameters. The wave is specified by the near-bottom wave velocity u_b and the radian wave frequency ω. The bottom parameter is the bottom

roughness, specified by k_n, the equivalent Nikuradse sand roughness, which is scaled by the grain diameter for flat beds and the ripple height for rippled beds. The current is given by a specified current shear stress, or by a specified value of the mean (current) velocity at a certain height above the bottom, which may also be replaced by a specified depth-averaged mean velocity. The angle between the current and the wave direction, ϕ_{cw}, must also be specified.

Once the hydrodynamic problem is solved the wave and current velocities, u_c and u_w, are determined as a function of the height above the bottom. The representation of u_w in Equation 17 as a complex number means that once u_w is determined as a complex number both its magnitude and its phase with respect to the near-bottom wave motion will be known.

Similarly, the wave shear stress defined in Equation 32 using the complex quantity u_w, is also determined as a complex number. This allows the phase of τ_w, with respect to the near bottom velocity, to be determined as well as its magnitude. The phase of the bottom shear stress is important in determining the phase of the time-varying components of the reference concentration.

2.2 Selection of an Eddy Viscosity Model for the Sediment Transport Problem

Wikramanayake (1989) compared the results of the time-invariant eddy viscosity model outlined in the preceding section to those of laboratory experiments and the numerical model of Davies et al. (1988). The model results were in excellent agreement with the experimental and numerical results for the case of waves in the same direction as the current. However, for the case of waves at an angle to the current, the model could not reproduce the sensitivity of the current velocity to the angle between the waves and the current, ϕ_{cw}, shown by the numerical turbulence

model of Davies et al. (1988). The model also failed to predict the deflection of the mean velocity near the bottom away from direction of the mean shear stress when $0 < \phi_{cw} < 90$.

Wikramanayake (1989) showed that the inability of the model to reproduce these features was a consequence of the assumption of a time-invariant eddy viscosity. He recommended that any further sophistication of the eddy viscosity models for wave-current interaction should allow the eddy viscosity to vary with time. The development of a time-varying eddy viscosity model is given in Appendix A. An approximate solution to the wave-current problem was obtained for the case of a weak current relative to the waves.

Comparison with the data for waves and the current in the same direction, in Figures A7 and A8, resulted in agreement similar to the comparison with results of the time-invariant model. For the case of waves at an angle to the current the time-varying model showed greater sensitivity to changes in ϕ_{cw} than the time-invariant model. These results are shown in Figure A9 and A10 respectively. Furthermore, as shown by Figures A11 and A6, the time-varying model showed the deflection of the mean velocity shown by the results of Davies et al. (1988), as well as the presence of a third harmonic wave velocity, which is a feature seen in experimental measurements. However, the results of the time-varying model were not in complete agreement with those of the numerical model of Davies et al. (1988). As there is no experimental verification for the case where $0 < \phi_{cw} < 90$, which is the range in which the deflection of the mean velocity is predicted, it is not possible to conclude whether the time-varying model or the numerical turbulence model gives the better results.

Comparing the results of the two eddy viscosity models in Figures A9 and A10 shows that for the case of waves at an angle to the current, the difference in the mean velocity profiles outside the wave boundary layer is less than 10 percent, a difference that is fairly small compared to the uncertainty in the specification of parameters such as the bottom roughness. The deflection of the mean velocity from the direction of the current shear stress, for the case of waves at 45° to the current, shown in Figure A11, decreases from a value of about 15° very near the bottom to about 5° near the top of the wave boundary layer. Again this value is not very significant compared to uncertainties in specifying the wave and current directions. The two models predict nearly identical values of the maximum bottom shear stress, a factor that is important in the suspended sediment model.

As far as the application of the model to the suspended sediment problem is concerned the most important aspect is the calculation of the time-varying concentration profiles. Time variation in the suspended sediment profile can arise due to a time-varying reference concentration as well as due to a time-varying eddy viscosity. However, an inspection of the results of the laboratory experiments discussed in Chapter 1 shows that the time variation in the concentration is greatest very near the bottom. This observation implies that the time-varying reference concentration is the important mechanism in the forcing of a time variation in the suspended sediment concentration.

In summary it can be concluded that the time-varying eddy viscosity brings out aspects of the wave-current interaction that are not shown by the time-invariant model. However, in the context of suspended sediment transport computations it appears that these effects are not very significant when compared to other possible uncertainties. These uncertainties include measurement error, the specification of the wave and current conditions, the bottom roughness, the grain diameter, and the

resuspension coefficient. The time-invariant model has the advantages of a relatively simple solution and validity over the full range of wave-current interaction. Therefore it is decided to use the time-invariant eddy viscosity model to calculate the fluid velocities and sediment concentrations that are needed to obtain the suspended sediment transport.

2.3 Representation of Irregular Waves

The wave-current interaction model described in Chapter 2.1 was derived for the case of a single sinusoidal wave component. However, the wave motion observed in the field is irregular in nature with contributions from many different frequencies. Since both the calibration of the model and its application are intended for field conditions a method of representing the irregular wave motion in the field by a single wave component, given by a magnitude and a period, must be specified as part of the model development.

The simplest method of specifying u_{br}, the representative magnitude for the near-bottom wave velocity, is to relate it to the power spectrum of the observed wave record, S_{ub}, by

$$u_{br} = \sqrt{2\int S_{ub} d\omega} \tag{33}$$

a method that has the advantage of conserving the total wave energy.

The most elementary method of selecting the period of the representative wave is to specify it as the peak period of the power spectrum of the velocity record. However, this method is not suitable when the spectrum is not narrow banded. For example, Figure 5 shows the velocity spectrum for the velocity data shown in Figure 2. The peak period of this spectrum is about 8 seconds (0.125 Hz). It may

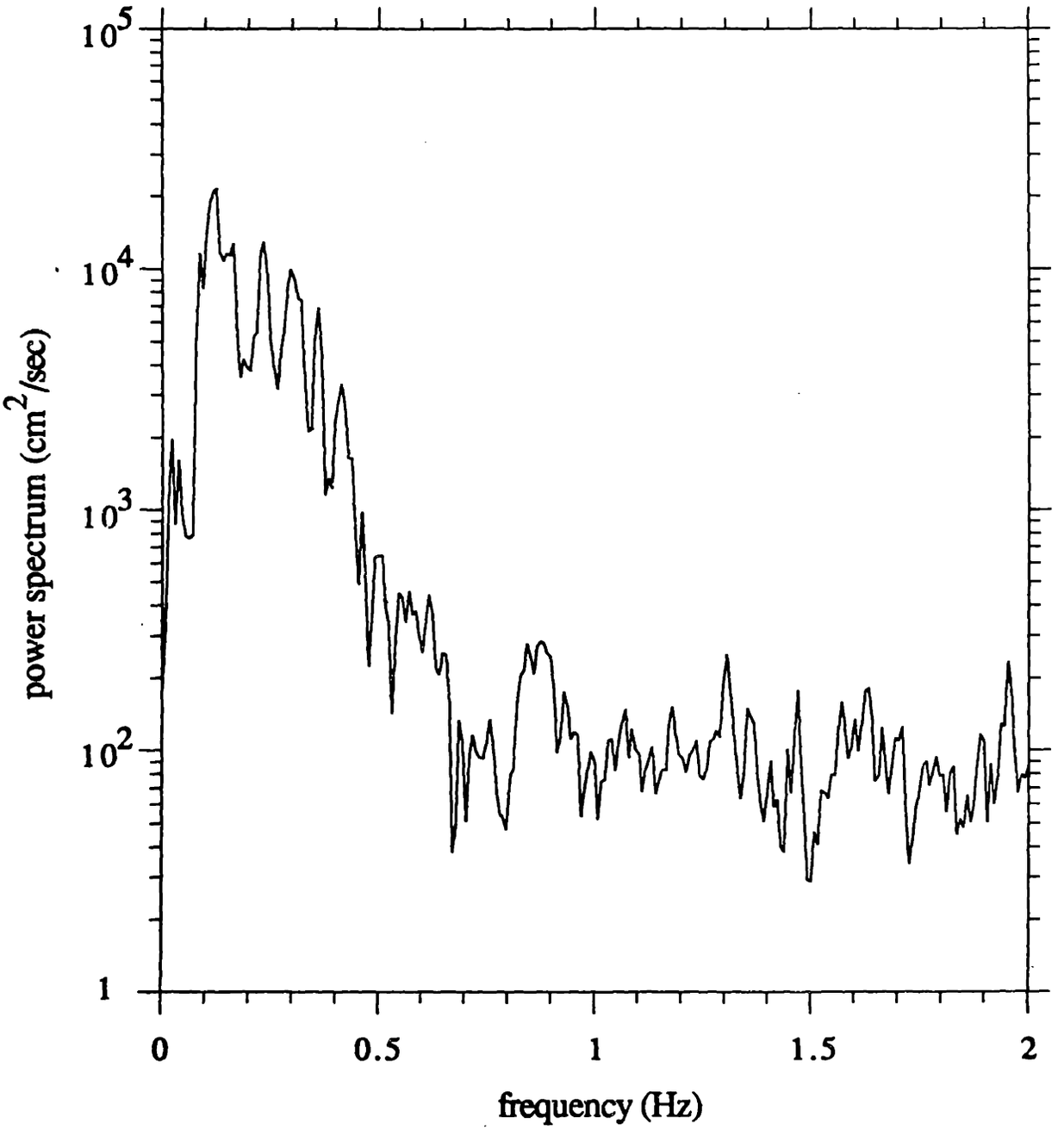

Figure 5. Power spectrum of wave velocity for run 2 of the data of Hanes (1991)

appear that the spectrum in Figure 5 indicates a wave motion consisting of an 8-second wave and its higher harmonics. However, an analysis of the velocity record shows a zero down-crossing period of 3.5 seconds, a result that does not support this hypothesis. Therefore it can be concluded that the peak period is not a good representative value for this spectrum.

Madsen (1992) showed that the representative frequency, ω_r, for the interaction of a current with an irregular wave motion was given by

$$\omega_r = \frac{\int S_{ub}\omega d\omega}{\int S_{ub} d\omega} \tag{34}$$

where S_{ub} is the power spectrum of the wave velocity. Use of Equation 34 for the spectrum shown in Figure 5 results in a period of 3.8 seconds (0.26 Hz), which is regarded as a better representative value than the peak period.

Equations 33 and 34 can be used to obtain the representative single wave when the power spectrum of the near-bottom wave velocity is known. However, some features of the irregular wave motion seen in the field indicate that using a single sinusoidal component for the wave conditions will result in an incorrect assessment of the sediment transport. Two such features are wave asymmetry and wave groups.

Wave asymmetry, a feature that is present in velocity records obtained in shallow water, occurs when the wave velocity is not the same during the forward and reverse parts of the wave cycle. For example consider the velocity record shown in Figure 2 which is a portion of the cross-shore velocity time series data obtained by Hanes (1991). The record has a strong positive skewness with a coefficient of skewness of 0.52. It is probable that the asymmetry of the wave motion would be

important when considering the suspended sediment transport because of the increased transport under the wave crests relative to that under the wave troughs.

One way to represent the asymmetric wave motion is by considering two wave components, u_{b1} and u_{b2}, that are in phase with each other, with u_{b2} having twice the frequency of u_{b1}. The magnitudes of u_{b1} and u_{b2} can be obtained by analyzing the velocity record on a wave-by-wave basis as done by Vincent and Green (1990). The analysis results in a set of positive and negative peak velocities for each wave. The representative positive and negative wave velocities, u_{bp} and u_{bn}, are taken as the root-mean-square value of each set. The magnitudes of u_{b1} and u_{b2} are then found by

$$u_{b1} = \frac{u_{bp} + u_{bn}}{2} \tag{35}$$

and

$$u_{b2} = \frac{u_{bp} - u_{bn}}{2} \tag{36}$$

For the data sets used in Chapter 4 for which the full velocity time series was available it is found that u_{b1} obtained from Equation 35 was quite similar to u_{br} obtained from Equation 33. The total wave energy for the single wave and the two wave representations was also nearly the same. These results show that the representation of the wave motion by u_{b1} and u_{b2} calculated from Equations 35 and 36 preserves the observed wave energy while accounting for some of the observed wave asymmetry.

When representing the observed wave motion by u_{b1} and u_{b2} as defined in Equations 35 and 36 it seems reasonable to use the zero down-crossing period obtained by the wave-by-wave analysis as the period of the component with magnitude u_{b1}. Comparison of the periods obtained from Equation 34 and the

wave-by-wave analysis for the data sets used in Chapter 4 shows that the two methods give very similar results. These results show that the representation by the two wave components u_{b1} and u_{b2} obtained by the wave-by-wave analysis can simulate the observed wave asymmetry while agreeing with Equations 33 and 34. Therefore this method will be used to obtain the representative wave components for the calibration of the model using field data in Chapter 4.

The presence and effects of wave groups have been discussed by Hanes (1991) and Osborne and Greenwood (1992) among others. One way to account for wave groups is to represent the wave motion by two wave components of nearly equal frequency. However, inspection of data from the field, such as those shown in Figure 2, shows that such a simple approach will usually be unable to reproduce the observed wave record. Another approach, which is the method used in Chapter 5.5, is to select a portion of the velocity record and fit it by a large number of wave components that are harmonics of a principal wave that has a period equal to the length of the record.

The methods discussed above to simulate the effects of wave asymmetry and wave groups result in representations of the observed wave motion by more than one wave component, while the model described in Chapter 2.1 is derived for the case of a single wave component. Therefore it is necessary to extend the model to include more than one sinusoidal wave component. This development will be done in the next section.

2.4 Extension of the Wave-Current Model to Include Many Wave Components

As discussed in the preceding section, simulation of such features as wave asymmetry and wave groups involves the specification of the wave motion by more

than one sinusoidal component. The wave-current model will be extended to include an arbitrary number of wave components in this section. It should be noted that even though some of the irregular motion observed in the field may be due to the effects of non-linearity, the representation here is taken to be a linear superposition of sinusoidal components such that the required feature in the observed wave record is reproduced.

In the general case where many wave components are considered the near-bottom wave motion can be written as

$$u_b(t) = u_{b1}\cos(\omega_1 t + \phi_1) + u_{b2}\cos(\omega_2 t + \phi_2) + \cdots \tag{37}$$

where u_{b1}, ω_1, and ϕ_1 are the magnitude, frequency, and phase of the first component, respectively. Similarly, the wave velocity u_w can be written as

$$u_w = u_{w1} + u_{w2} + \cdots \tag{38}$$

where u_{w1} has a frequency ω_1, and u_{w2} has a frequency ω_2.

Since the equation governing u_w, Equation 2, is linear, Equation 38 can be substituted into Equation 2 and components of the same frequency grouped to obtain different equations for each component of the wave motion. For example, the equation for the first component would be

$$\frac{\partial u_{w1}}{\partial t} = -\frac{1}{\rho}\frac{\partial p_{w1}}{\partial x} + \frac{\partial}{\partial z}\left[\nu_t \frac{\partial u_{w1}}{\partial z}\right] \tag{39}$$

As before the pressure gradient term is related to the external wave motion by

$$\frac{\partial u_{\infty 1}}{\partial t} = -\frac{1}{\rho}\frac{\partial p_{w1}}{\partial x} \tag{40}$$

where in this case

$$u_{\infty 1} = u_{b1}\cos(\omega_1 t + \phi_1) \tag{41}$$

Defining

$$\frac{u_{w1} - u_{\infty 1}}{u_{b1}} = \mathrm{Re}\left\{u_{d1}e^{i(\omega_1 t+\phi_1)}\right\} \tag{42}$$

and using Equations 40, 41, and 42 in Equation 39 the governing equation for u_{w1} is obtained as

$$\frac{d}{dz}\left[\nu_t\frac{du_{d1}}{dz}\right] - i\omega_1 u_{d1} = 0 \tag{43}$$

with boundary conditions

$$u_{d1} = -1 \quad \text{at} \quad z = z_0 \tag{44}$$

and

$$u_{d1} \to 0 \quad \text{as} \quad z \to \infty \tag{45}$$

The wave shear stress due to each component is defined, just as in the case of a single wave component, by

$$\tau_{w1} = \left[\nu_t\frac{\partial u_{w1}}{\partial z}\right]_{z=z_0} \tag{46}$$

where τ_{w1} is the wave shear stress corresponding to the first wave component.

Equations 43 and 46 are very similar to Equations 18 and 32, which were obtained for the case of a single wave component. However, before the eddy viscosity distribution of Equation 8 is used to solve Equation 43 the parameters u_{*cw} and δ that appear in Equation 8 must be defined for the case of many wave components. For the case of a simple wave component u_{*cw} was based on the maximum combined shear stress, τ_{cw}, defined by Equation 31.

The above definition of u_{*cw} can also be used for the case when wave asymmetry is simulated by two wave components that are in phase, one with twice the frequency of the other. In this situation the combined shear stress will have a regular maximum that occurs with the frequency of the first wave component. Therefore u_{*cw} can be defined by

$$\rho u_{*cw}^2 = \tau_{cw} = (\tau_{wm}^2 + 2\tau_{wm}\tau_c \cos\phi_{cw} + \tau_c^2)^2 \tag{47}$$

where τ_{wm} is the maximum wave shear stress defined by

$$\tau_{wm} = \max(\tau_{w1} + \tau_{w2}) \tag{48}$$

with τ_{w1} and τ_{w2} being the shear stresses due to the two wave components obtained using Equation 46.

The definition of the boundary layer scale, δ, given by Equation 9 for the case of a single wave, requires the use of an appropriate wave frequency. For the simulation of wave asymmetry the appropriate frequency would be that of the first component, leading to

$$\delta = \frac{\kappa u_{*cw}}{\omega_1} \tag{49}$$

The definitions of u_{*cw} and δ in Equation 47 and 49 are for the special case of simulation of wave asymmetry. However, for the general case of several wave components with an arbitrary phase relationship the definition of u_{*cw} based on the maximum shear stress will no longer be appropriate. In this situation u_{*cw} can be defined by Equation 31 but with τ_w defined to be the shear stress due to an equivalent periodic wave that is representative of the sum of the many individual components.

In other words the general method for many wave components is to calculate u_{*cw} based on a single representative wave using the model as described in Chapter 2.1. Following the work of Madsen (1992) the amplitude of this representative wave, u_{br}, should be taken as

$$u_{br} = \sqrt{\Sigma u_{bi}^2} \tag{50}$$

where u_{bi} are the amplitudes of the individual components. The representative frequency, ω_r, is defined similar to Equation 34 by

$$\omega_r = \frac{\Sigma \omega_i u_{bi}^2}{\Sigma u_{bi}^2} \tag{51}$$

where ω_i are the frequencies of the individual components.

The boundary layer length scale, δ, is then defined by

$$\delta = \frac{\kappa u_{*cw}}{\omega_r} \tag{52}$$

Once u_{*cw} and δ are defined as above the eddy viscosity distribution of Equation 8 can be used to solve the wave velocity problem for each individual wave component. For example, the solution for u_{w1}, the component of frequency ω_1, can be written as

$$u_{d1} = A[\mathrm{ker}(2\sqrt{\sigma_1\zeta}) + i\ \mathrm{kei}(2\sqrt{\sigma_1\zeta})] + B[\mathrm{ber}(2\sqrt{\sigma_1\zeta}) + i\ \mathrm{bei}(2\sqrt{\sigma_1\zeta})] \tag{53}$$

for the region $\zeta < \alpha$,

$$u_{d1} = Ce^{\sqrt{i\sigma_1/\alpha}\zeta} + De^{-\sqrt{i\sigma_1/\alpha}\zeta} \tag{54}$$

for the region $\alpha < \zeta < \alpha/\epsilon$, and

$$u_{d1} = E[\mathrm{ker}(2\sqrt{\sigma_1\zeta/\epsilon}) + i\ \mathrm{kei}(2\sqrt{\sigma_1\zeta/\epsilon})] + F[\mathrm{ber}(2\sqrt{\sigma_1\zeta/\epsilon}) + i\ \mathrm{bei}(2\sqrt{\sigma_1\zeta/\epsilon})] \quad (55)$$

for the region $\zeta > \alpha/\epsilon$.

In Equations 53, 54, and 55 ζ is the non-dimensional coordinate defined by Equation 12 using the appropriate definition of δ. The parameter σ_1 represents the relative frequency of the component, and in this case is given by

$$\sigma_1 = \frac{\omega_1}{\omega_r} \quad (56)$$

Equations 53, 54, and 55 are very similar to Equations 21, 22, and 23 with the only difference being the presence of the term σ_1. The six unknown coefficients A, B, C, D, E, and F in Equations 53, 54, and 55 can be found as before by using the boundary conditions of Equations 44 and 45 and matching the values of u_{d1} and $du_{d1}/d\zeta$ at the levels $\zeta = \alpha$ and $\zeta = \alpha/\epsilon$. The analysis in Chapter 4.3.4 will show that the solution for the periodic velocity is a special case of the solution for the periodic concentration. The solution for the current is the same as for the single wave case except for the new definitions of u_{*cw} and δ. The entire wave-current problem is solved iteratively as before by first assuming a value of u_{*cw}, solving the wave and the current equations, and obtaining an updated value of u_{*cw} from Equations 31 or 47. This process is repeated until the results converge.

Thus the wave-current model is now capable of handling an arbitrary number of wave components together with a current. Combining the solutions for the wave component and the current makes it possible to calculate the velocity as a function of depth at any time within the period considered. However, these solutions require a knowledge of the bottom roughness parameter z_0, which is not usually known for the movable sediment beds found in the field. Therefore the problem of estimating

the bottom roughness from a knowledge of the wave, current, and sediment conditions will be considered in the next chapter. In terms of the solution of the hydrodynamic problem determination of the bed roughness will add another level of iteration to the solution, i.e., a value of the roughness must be assumed a priori and then updated after the shear stresses are known.

CHAPTER 3

CALCULATION OF THE EQUIVALENT ROUGHNESS FOR MOVABLE SAND BEDS

The calculation of the wave and current velocities by the hydrodynamic model outlined in Chapter 2 requires a knowledge of the equivalent Nikuradse roughness of the bed. The equivalent roughness is related to the size of the bedforms. However, as explained in Chapter 1, when the bed consists of movable sand grains the bedforms themselves are dependent on the intensity of the flow. Therefore it is necessary to calculate the dimensions of the bedforms as part of the solution to the hydrodynamic problem. Simple relations for the calculation of the equivalent roughness will be derived in this chapter. As the process of bedform formation is far too complex for theoretical treatment the approach here is to use experimental data to obtain empirical relations for the size of the bedforms and the equivalent roughness.

3.1 Concept of Equivalent Roughness

The concept of equivalent roughness was introduced in the study of steady rough turbulent flow over plane beds. In such flows the individual roughness elements are not shielded by the viscous sub-layer and experience the full effects of the external flow. On a microscopic scale the bed shear stress is due to the form drag and skin friction on the individual elements. However at distances from the bed that are large compared to the size of these elements the effects of each element cannot be resolved and what is seen is the turbulent motion caused by many elements. At these distances therefore it is possible to define an "average" bottom shear stress.

Measurements of the mean velocity profile in steady flows, as described by Schlichting (1968), showed that at these distances the flow velocity u can be represented by an equation of the form

$$\frac{u}{u_*} = \frac{1}{\kappa}\ln\left[\frac{z}{z_0}\right] \tag{57}$$

where

$u_* = \sqrt{\tau/\rho}$ = shear velocity

κ = von Karman's constant

z_0 = a measure of the boundary roughness

τ = average bottom shear stress

Thus values of u_* and z_0 can be obtained from the measured velocity profile. However, the relationship between the value of z_0 thus obtained and the actual size of the roughness elements depends on the shape of the elements. Nikuradse (1932) introduced the concept of equivalent roughness to account for roughness elements of various geometries. The equivalent roughness, k_n, in fully rough turbulent flow, is defined as the diameter of uniform sand grains that, when closely packed together, produce the same boundary resistance as the surface under consideration. This definition of the bottom roughness can be extended to any geometry that has sufficient regularity to allow the definition of an average shear stress. The exact value of this representative roughness must either be established by experiment or by extrapolation from experimental results for similar geometries.

Measurements of velocity profiles in the region where the logarithmic relation of Equation 57 holds showed that z_0 was related to k_n by

$$z_0 = \frac{k_n}{30} \tag{58}$$

The parameter z_0 has been used widely in theoretical models as a boundary condition for the level at which the velocity u vanishes. It should be noted that this is a purely conceptual extrapolation as Equation 57 does not hold very near the bed, i.e., at levels where u actually vanishes. However, this method has been used quite successfully to relate the bottom roughness and the velocity profile in steady flows, while having the advantage that it is a simple formulation.

For these reasons the roughness concepts developed for steady turbulent flows have been used virtually unchanged in the analysis of oscillatory boundary layers. The eddy viscosity model described in Chapter 2 applied the no-slip boundary condition for the velocity problem, i.e., Equations 3 and 7, at the level z_0. Furthermore the bottom shear stress was evaluated by calculating the velocity gradient at the level z_0 in Equations 32 and 46. A useful parameter that relates the maximum bottom wave shear stress, τ_{bm}, to the near-bottom wave velocity, u_b, is the wave friction factor, f_w, which is defined by

$$\tau_{bm} = \frac{1}{2}\rho f_w u_b^2 \tag{59}$$

For rough turbulent flow the solution for the velocity in Chapter 2 can be combined with the definition of the bottom shear stress in Equation 32 and the definitions of Equations 58 and 59 to obtain an expression for the friction factor. Wikramanayake (1989) shows that the friction factor is a function of the parameter A_b/k_n, where A_b is the near-bottom excursion amplitude, defined by

$$A_b = \frac{u_b}{\omega} \tag{60}$$

and k_n is the equivalent roughness which is related to z_0 by Equation 58. The quantity Ab/k_n is referred to as the relative roughness.

The resulting relation is shown in Figure 6a, which shows that for a given value of k_n the value of f_w decreases rather slowly with an increase in A_b. It should be noted that the concept of equivalent bed roughness is valid only when the wave boundary layer is much larger than the physical height of the roughness elements, a condition that is satisfied when A_b/k_n is large.

For laminar flow the friction factor can be obtained by solving the linearized equations for the wave boundary layer. The resulting equation is

$$f_w = \frac{2}{\sqrt{Re}} \tag{61}$$

where Re is the flow Reynolds number defined by

$$Re = \frac{u_b A_b}{\nu} \tag{62}$$

with

ω = radian frequency of the wave motion

ν = kinematic viscosity of the fluid

For smooth turbulent flow the friction factor must be found using experimental measurements. In this case too the friction factor is found to depend only on the flow Reynolds number defined by Equation 62. The variation of the friction factor with the Reynolds number for both laminar and smooth turbulent flow is shown in Figure 6b which was taken from the paper by Jonsson (1966).

3.2 Estimation of the Equivalent Roughness

Both the equivalent roughness, k_n, and the parameter z_0, which is related to k_n by Equation 58, cannot be measured directly. Therefore it is necessary to link these

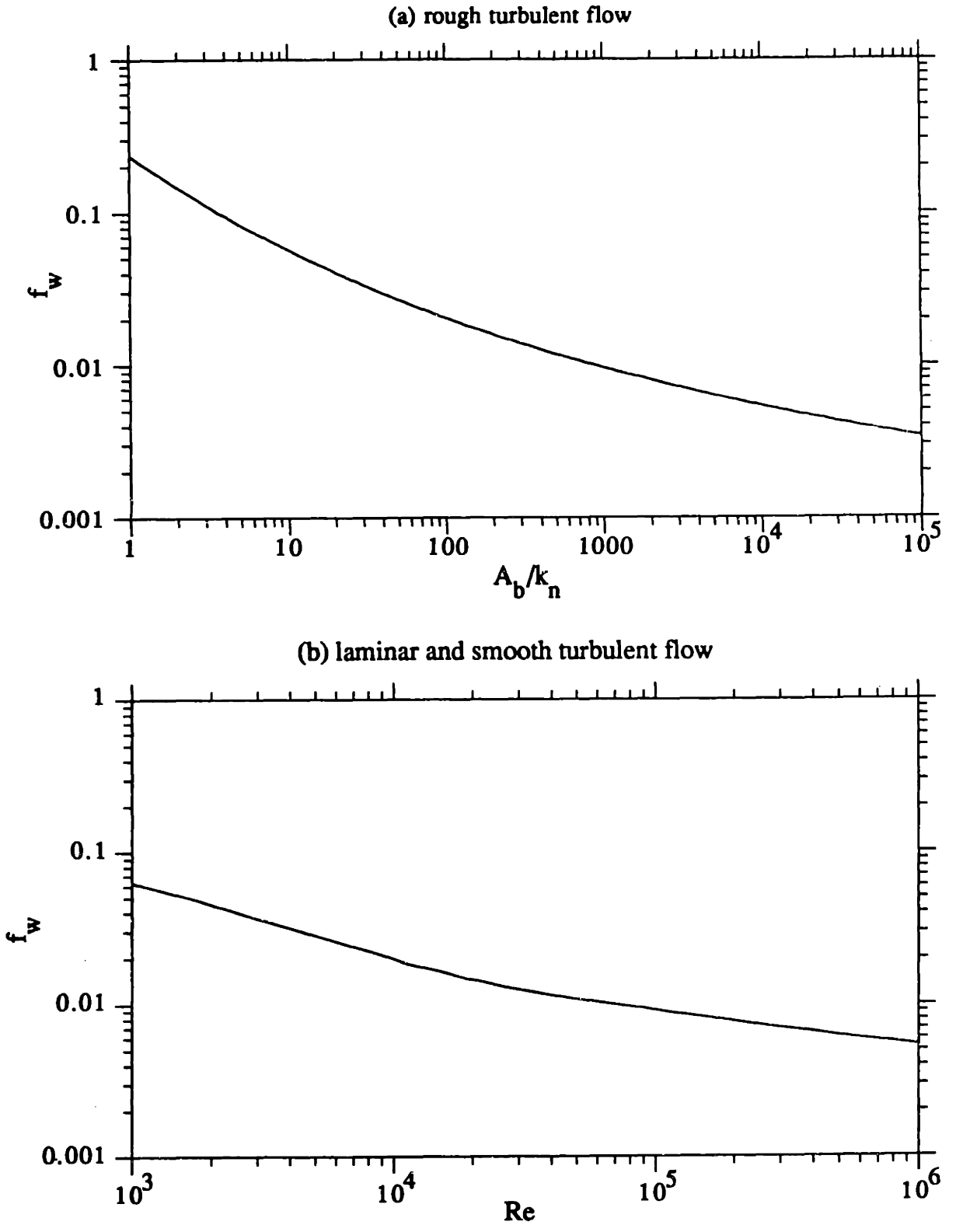

Figure 6. Friction factor curves for a) Rough turbulent flow; b) Laminar and smooth turbulent flow

parameters to quantities that can be measured. The wave friction factor defined in Equation 59 provides such a link. If the friction factor can be determined experimentally, the theoretical solution shown in Figure 6a can be used to calculate the value of A_b/k_n, and since A_b will be known from the wave parameters used, the value of k_n can be found.

As the use of different wave boundary layer theories will result in different relationships between the friction factor and the relative roughness, A_b/k_n, the calculated values of k_n will depend on the particular theoretical model used. Thus it is important to use the same theoretical model when predicting the friction factor using the empirical relations for the roughness obtained in this chapter. In other words the relations derived here should only be used in conjunction with the eddy viscosity model of Chapter 2.

The friction factor has been determined from laboratory and field measurements by three main methods, one direct and two indirect. The direct method is to measure the bed shear stress due to the wave motion using a device such as a shear plate. Then the friction factor can be calculated directly from Equation 59. This is the method used by Riedel et al. (1972) for fixed beds roughened by sand grains. However, there would be experimental difficulties involved in using this method with movable sand beds.

One of the indirect methods is to use measurements of the instantaneous velocity profile within the wave boundary layer. Such measurements were used by Jonsson and Carlsen (1976) to obtain the the shear stress in two ways. One was by the numerical integration of the equation of motion using the velocity measurements at various phases, while the other assumed that Equation 57 was applicable very near the bed so that the quantity u_*, and hence the shear stress, could be found.

Both these methods have the disadvantage that the velocity profile at various phases of the external flow must be measured very near the bottom. Additional difficulties arise when the bed is rippled as the velocities over the crest and the trough of the ripples will vary differently. The first method also requires the calculation of the rate of change of velocity with time as a function of depth, while the second method involves fixing a theoretical bed level in order to obtain a logarithmic velocity profile and a decision as to how far the logarithmic region extends.

The other indirect method of obtaining the friction factor is through measurements of the energy dissipation in the wave boundary layer. This has been done by measuring the wave attenuation in a wave flume or by measuring the energy input needed to maintain the motion when a wave tunnel or oscillating bed is used. Compared to the measurement of the instantaneous velocity these measurements are relatively easily made and can be done equally well for both fixed and movable beds. Another advantage over both the preceding methods is that the energy dissipation provides an averaged measure of the shear stress over several ripple lengths instead of a point measurement.

The average dissipation per unit area in the wave boundary layer, E_d, can be related to the near-bottom velocity, u_b, by an energy dissipation factor, f_e, defined by

$$E_d = \frac{2}{3\pi}\rho f_e u_b^3 \tag{63}$$

Once the energy dissipation is measured it is however, necessary to assume a relationship between the dissipation and the shear stress so that the friction factor can be calculated from Equation 59. In other words a relation between the factors

f_w and f_e must be developed. Kajiura (1968) derived an expression for the energy dissipation, E_d, in the form

$$E_d = \overline{\tau_b(t)u_b(t)} \tag{64}$$

where $\tau_b(t)$ and $u_b(t)$ are the instantaneous bed shear stress and near-bottom wave velocity, respectively, and the overbar denotes the average over a wave period. Equation 64 can be evaluated to obtain a relation between f_w and f_e only if the time variation of the bed shear stress is known.

Lofquist (1986) has measured both the instantaneous shear stress and the average energy dissipation over a rippled sand bed in a wave tunnel. These measurements can be used to calculate both f_w, which is defined in Equation 59 using the peak shear stress, and f_e as defined in Equation 63, using the dissipation. The results for f_w and f_e are plotted against each other in Figure 7. The figure shows that with the exception of a few points where f_w is much greater than f_e, the two values are nearly equal. Fitting a relation of the form $f_e = \alpha f_w$ results in a value of $\alpha = 1.06$ with a standard deviation of 0.057, while the relation $f_e = f_w$ has a standard deviation of 0.059.

A closer examination of the experimental conditions shows that the points that show a value of f_w much greater than f_e correspond to runs where the ripple length was the greatest and the number of ripples in the test section the least. Under these conditions the effect of end conditions can be expected to have the greatest effect. Therefore it seems reasonable to disregard these points and to interpret the results as showing that f_w as defined by Equation 59 and f_e as defined by Equation 63 are identical for rippled sand beds.

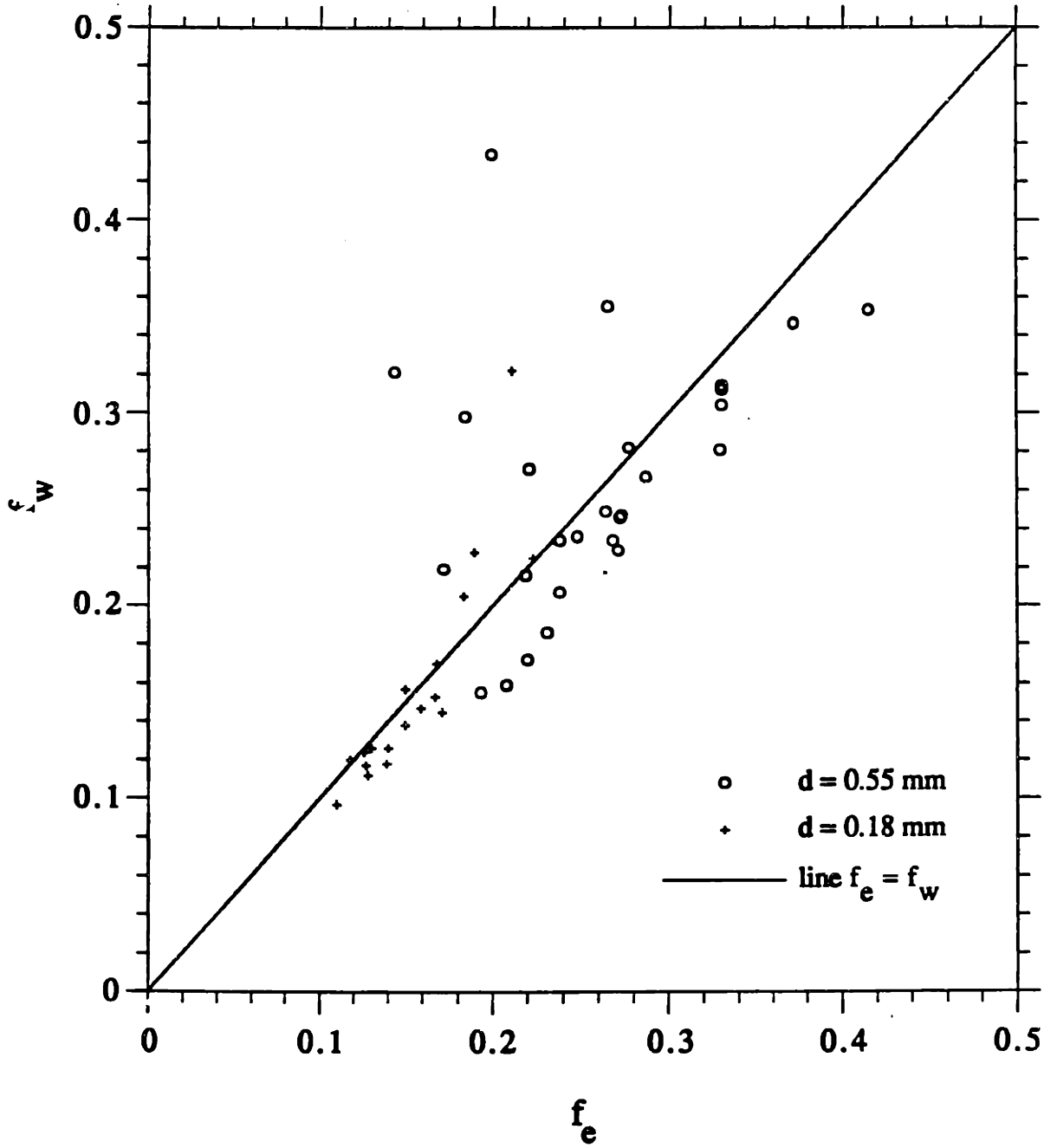

Figure 7. Comparison of the values of f_e and f_w obtained from the experimental measurements of Lofquist (1986)

Using the solution for the wave velocity in Equation 32 for the bed shear stress would result in a sinusoidal variation of the shear stress with a phase lead over the near-bottom wave velocity. The magnitude of the phase lead is a function of the relative roughness A_b/k_n ranging from 42° for $A_b/k_n = 1$, to 16° for $A_b/k_n = 100$. Evaluating the energy dissipation using this variation of the shear stress in Equation 64 results in values of the ratio f_e/f_w that range from 0.87 for $A_b/k_n = 1$ to 1.13 for $A_b/k_n = 1000$. Thus the calculation supports the conclusion from the experimental results that f_e is approximately equal to f_w.

The above discussion has shown that the simplest and most practical method of estimating the friction factor is by using measurements of the energy dissipation. The estimates of the friction factor can be transformed into estimates of the relative roughness using the friction factor curve of Figure 6a. It will then be possible to obtain values of the equivalent roughness, k_n, that correspond to known wave and sediment parameters and measured bed geometries and thus obtain empirical relationships between all these quantities.

The goal of this chapter is to develop predictive relations for the equivalent roughness of a movable bed given the wave and sediment parameters. The simplest way of accomplishing this goal would be to use experimental data that measure these quantities to derive a direct relationship between the roughness and the wave and sediment parameters. Formulae of this type have been proposed by Vonvisessomjai (1987, 1988) and Madsen et al. (1990).

However, these formulae are based entirely on data from laboratory experiments. The analysis of ripple geometry in the next section will show that the ripple geometry observed under field conditions is quite different from the geometry seen under regular waves in the laboratory. These differences are due to both the

irregularity and the much larger periods of waves in the field compared to the waves used in the laboratory experiments. Wikramanayake and Madsen (1990) show that the extrapolation of the laboratory relations to the field can result in significant errors. The field measurements of energy dissipation are too few and subject to too many errors to make a direct prediction reliable.

A more reasonable approach is to make the prediction of the equivalent roughness in two stages. The bed geometry can be predicted using the available field measurements. The equivalent roughness corresponding to the predicted geometry can be predicted using the laboratory experiments that measured energy dissipation and ripple geometry. This method accounts for the differences in ripple geometry while allowing the use of the large quantity of laboratory measurements of the energy dissipation under waves.

3.3 Estimation of the Bedform Geometry

The geometry of wave-generated bedforms will be examined in this section with the purpose of deriving predictive relations for use under field conditions. Experimental data on ripple geometry are available from both laboratory and field conditions. The data from the laboratory have been obtained under both monochromatic (regular) and spectral (irregular) wave motions while the field data is necessarily obtained under irregular wave conditions. The elements of ripple geometry most often measured in the experiments are the ripple length, λ, and the ripple height, η.

The sources, grain diameters, and wave periods of the data from laboratory experiments using regular and irregular waves and from field experiments are summarized in Tables 1, 2, and 3 respectively. Tables 1 and 2 show that the a large

Table 1

Summary of Available Data on Ripple Geometries from Laboratory Experiments with Regular Waves

Source of data	Diameter of sand (mm)	Range of periods (s)	Type of apparatus	Number of data points
Mathisen (1989)	0.12	2.6	WF	6
Sato (1988)	0.18	1-7	WT	12
	0.56	1.5-5	WT	10
Rosengaus (1987)	0.20	2.2-3	WF	9
Lambie (1984)	0.09	2.3-7.5	WT	20
	0.15	2.7-7.2	WT	27
Miller & Komar (1980)	0.178	3-5	WF	4
Nielsen (1979)	0.082	1.0-1.7	WF	24
	0.17	1.7	WF	10
	0.36	1.7	WF	10
Lofquist (1978)	0.18	3-8	WT	6
	0.55	2.5-12	WT	23
Mogridge & Kamphuis (1972)	0.36	1-2.5	WF	50
	0.36	2.5-14	WT	21
Carstens et al. (1969)	0.19	~3.53	WT	6
	0.297	~3.53	WT	17
	0.585	~3.53	WT	19
Kennedy & Falcon (1965)	0.095	1.07-2.34	WF	4
	0.32	1.39-1.57	WF	6
Inman & Bowen (1963)	0.2	1.4-2	WF	2

WT: wave tunnel WF: wave flume

Table 2

Summary of Available Data on Ripple Geometries from Laboratory Experiments Using Irregular Waves

Source of data	Diameter of sand (mm)	Range of significant period (s)	Type of apparatus	Number of data points
Mathisen (1989)	0.12	~2.5	WF	9
	0.2	~2.5	WF	3
Sato (1988)	0.18	3-5	WT	21
	0.56	1.5-3	WT	13
Rosengaus (1987)	0.2	~2.5	WF	8

WT: wave tunnel WF: wave flume

Table 3

Summary of Available Data on Ripple Geometries from Field Measurements

Source of data	Range of grain diameters (mm)	Range of significant period (s)	Number of data points
Boyd et al. (1988)*	0.1	4.9-11.4	20
Nielsen (1984)	0.11-0.62	5.7-12.9	39
Miller and Komar (1980)*	0.165-0.287	6-18.1	33
Dingler (1974)	0.128-0.616	6.9-13.9	24
Inman (1957)	0.081-0.635	5-16	53

*Ripple wavelength only

majority of the laboratory experiments have been performed using regular waves. The tables also show that the majority of the laboratory experiments have used a wave period of between 1 and 3 seconds while the wave periods observed in the field range from 5 to 18 seconds. The relative merits of different laboratory apparatus and laboratory and field conditions is discussed in detail by Wikramanayake and Madsen (1990).

The problem of ripple formation on a sand bed under a wave motion involves at least seven parameters. These are the characteristic frequency, ω, and the characteristic velocity, u_b, of the wave motion, the sediment grain diameter, d, and density, ρ_s, the fluid density, ρ, and kinematic viscosity, ν, and the acceleration due to gravity, g. Since these parameters have three dimensions it follows that the ripple geometry can in principle be described as a function of four independent non-dimensional variables based on these seven parameters.

However, as the analysis of ripple data by Stefanick (1979) and Nielsen (1979) among others show, the scatter of the data and the variation in the results from different experimental facilities is such that the determination of such a function is not a realistic expectation. The approach of past investigators has been to try and use one or two of the most important non-dimensional variables to correlate the data and obtain an empirical predictive relation.

One of the most useful non-dimensional parameters for characterizing wave-sediment interaction is the skin friction Shields parameter ψ', defined by

$$\psi' = \frac{\tau_{wm}'}{\rho(s-1)gd} \tag{65}$$

where

τ_{wm}' = maximum wave skin friction shear stress

ρ = fluid density

$s = \rho_s/\rho$ = specific density of the sediment

d = sediment grain diameter

The parameter ψ' is proportional to the ratio between the surface shear stress on a flat sediment bed, which tends to mobilize the grains, and the submerged weight of the grains, which tends to oppose grain motion. The concept of skin friction shear stress was introduced to distinguish the shear stress acting on individual grains from the total bed shear stress, which is the sum of the skin friction and the form drag due to any ripples that may be present. The skin friction is generally calculated by using the grain diameter as the equivalent roughness. For very fine sediment, the flow very near the grains may not be rough turbulent. To allow for this possibility the friction factor is calculated using both the rough turbulent relation in Figure 6a and the smooth turbulent relation of Figure 6b with the larger value used to calculate the skin friction shear stress from Equation 59.

Madsen and Grant (1976) showed that ψ' could be used together with the Shields curve obtained from steady flow data to characterize the initiation of motion under waves provided that the maximum wave skin friction shear stress was used in the definition of ψ'. Many researchers, for example Stefanick (1979), have used ψ' to describe ripple geometry as well. For example, Figure 8 shows the ripple steepness—defined as η/λ—for the laboratory data obtained with regular waves plotted against the non-dimensional variable ψ'. The points plotted with a steepness of 10^{-2}, i.e., at the bottom of the graph, are those runs for which a flat bed was observed.

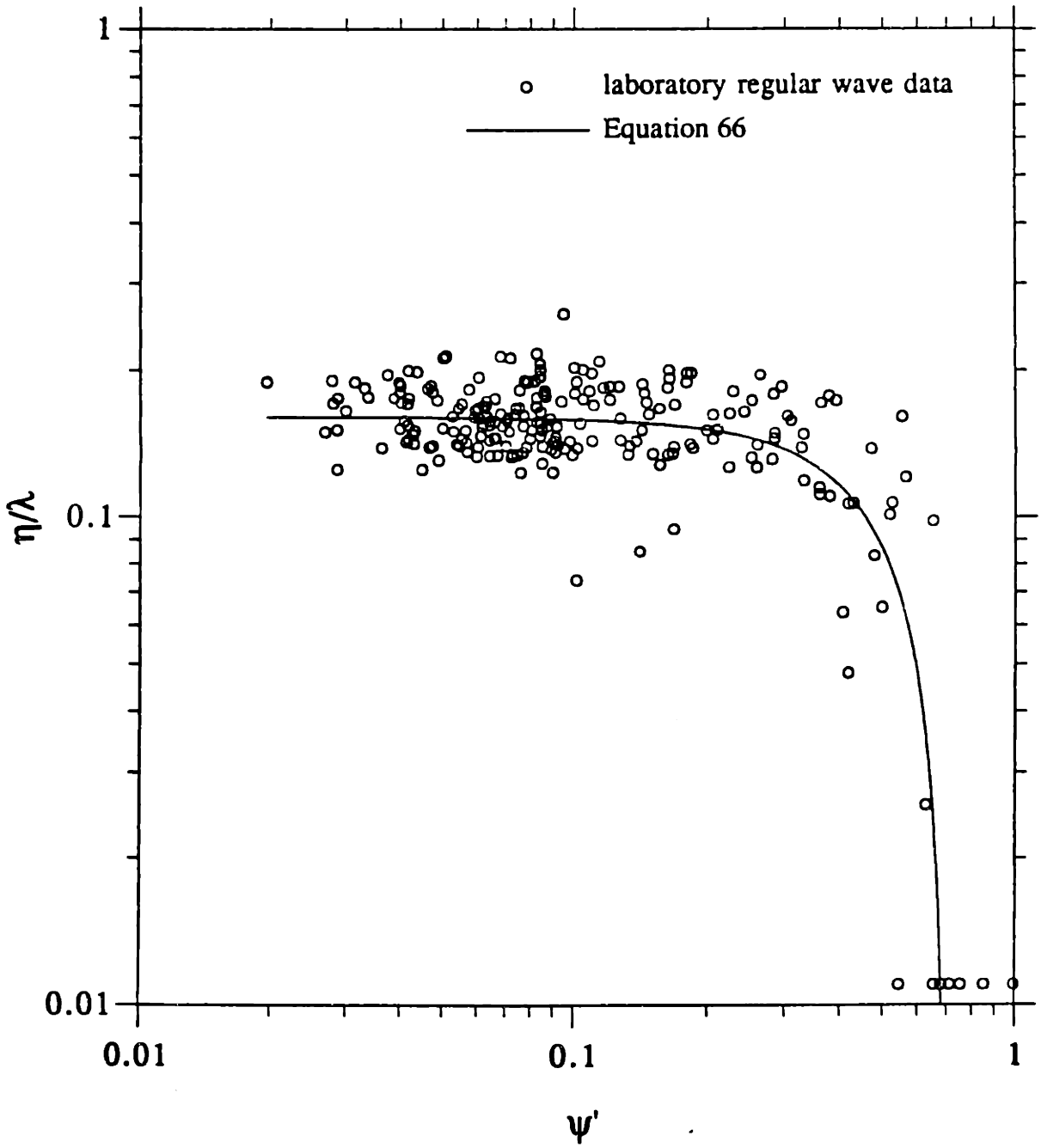

Figure 8. Variation of ripple steepness observed under regular waves in the laboratory with ψ' and the empirical relation given by Equation 66

The figure shows that the parameter ψ' is quite successful in correlating the data. The solid line in the figure is the relation

$$\frac{\eta}{\lambda} = 0.16 - 0.36\psi'^{2.28} \quad 0.02 < \psi' < 0.7 \tag{66}$$

The coefficients of Equation 66 are obtained by minimizing the relative error Δ which is defined by

$$\Delta = \exp\left\{\left[\frac{1}{n}\sum_{1}^{n}(\ln(y) - \ln(\hat{y}))^2\right]^2\right\}^{1/2} \tag{67}$$

where y is the measured value and $\hat{y}$ the predicted value. This measure of the error was selected over the more commonly used root-mean-square error because the measured values span a large range. The relative error is defined using the logarithms of the predicted and measured quantities and the value of Δ is thus a multiplicative factor that indicates the possible variation about the predicted value. For example, the value of Δ for the fit shown in Figure 8 is 1.28, which indicates an average error of 28%.

Figure 9 is a plot of the ripple height, η, normalized by the excursion amplitude A_b, against ψ' for the same data set. As in Figure 8, the points plotted at the bottom of the graph, i.e., with a value of $\eta/A_b = 0.001$, are the runs for which a flat bed was observed. The solid line is given by

$$\frac{\eta}{A_b} = 0.27 - 0.33\psi'^{0.55} \quad 0.02 < \psi' < 0.7 \tag{68}$$

with a relative error of 1.55 in this case.

All the data in Figures 8 and 9 were obtained using regular waves. The next step is to compare the relations of Equations 66 and 68 with the results obtained using irregular waves. However, before this is done a single wave velocity and

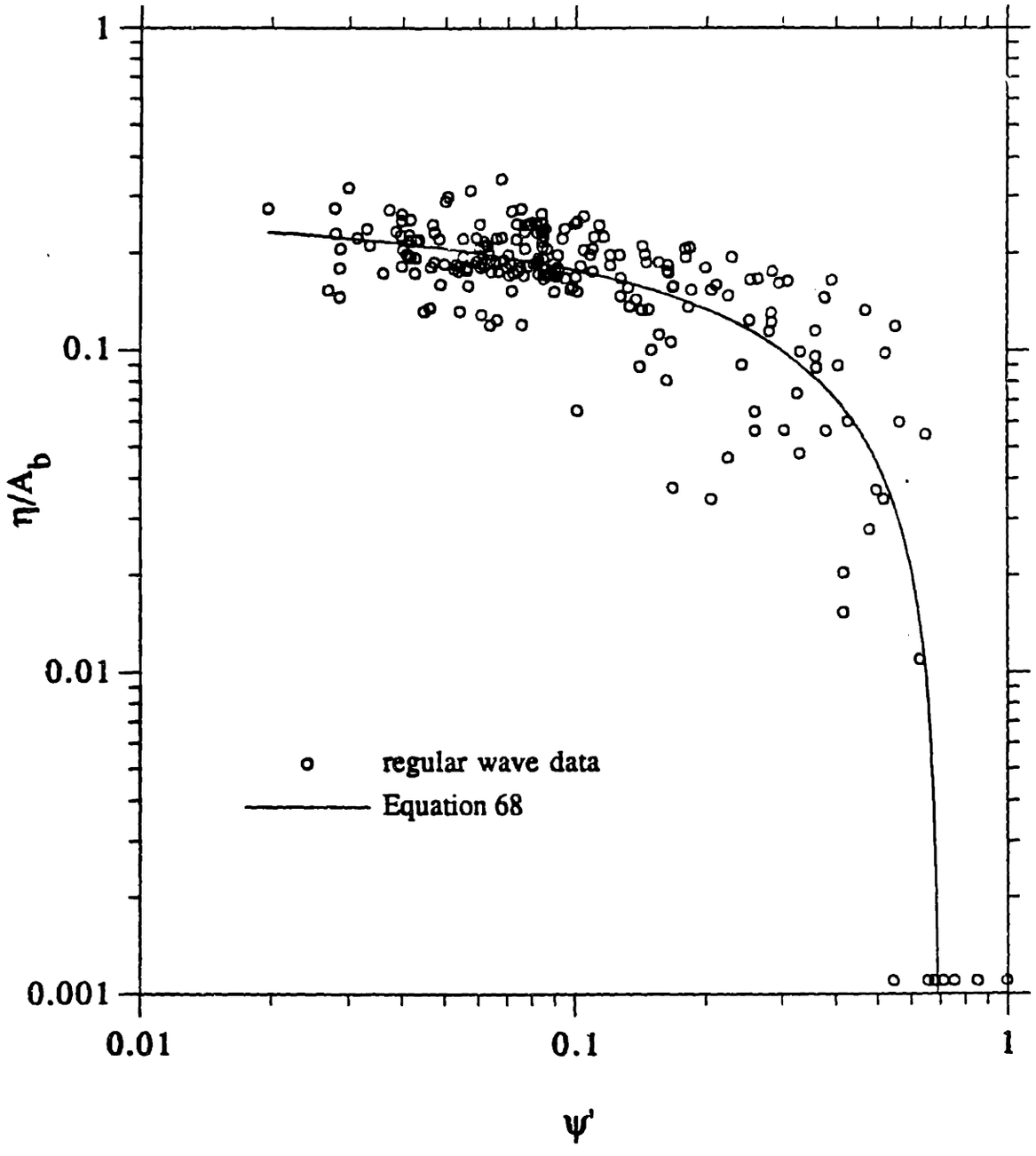

Figure 9. Variation of normalized ripple height observed under regular waves in the laboratory with ψ' and the empirical relation given by Equation 68

frequency must be selected to represent the irregular wave motion in these experiments. As in Chapter 2, the root-mean-square wave velocity defined in Equation 33 is selected as the representative velocity. When the waves were characterized by the significant wave velocity the reported value was divided by a factor of $\sqrt{2}$ to obtain the root-mean-square velocity. While the representative frequency was defined by Equation 34 in Chapter 2, all the field experiments only report the significant period. However, for a narrow-banded wave spectrum the significant period will be quite similar to the definition in Chapter 2, so that using the reported wave period will not cause much error.

The ripple steepness observed under irregular waves in the laboratory and the field are plotted against the parameter ψ' in Figure 10. The solid line shows the relationship given by Equation 66. The figure shows that for values of ψ' less than 0.04 the irregular wave data agrees with the relation for the regular wave data. However, after that point the steepness observed in the field decreases with an increase in ψ' while the regular wave data of Figure 8 do not show this decrease until about the point $\psi' = 0.3$. The flat bed points for the field data are in the range $\psi' = 0.15$–0.55 while the corresponding range for the regular wave data is $\psi' = 0.55$–1.0. No ripples are observed in the field for values of ψ' greater than 0.3. Another feature of the field data is that the scatter of the data is much greater, reflecting the greater uncertainties in the measured wave conditions and ripple geometry in the field.

The data measured under irregular waves in the laboratory show similar differences when compared to the regular wave data as the field data. However, the differences are smaller, with the deviation from Equation 66 occurring after about $\psi' = 0.09$ and the flat bed points being in the range $\psi' = 0.25$–0.45. No ripples are observed for values of ψ' greater than 0.4. Thus it appears that the data from

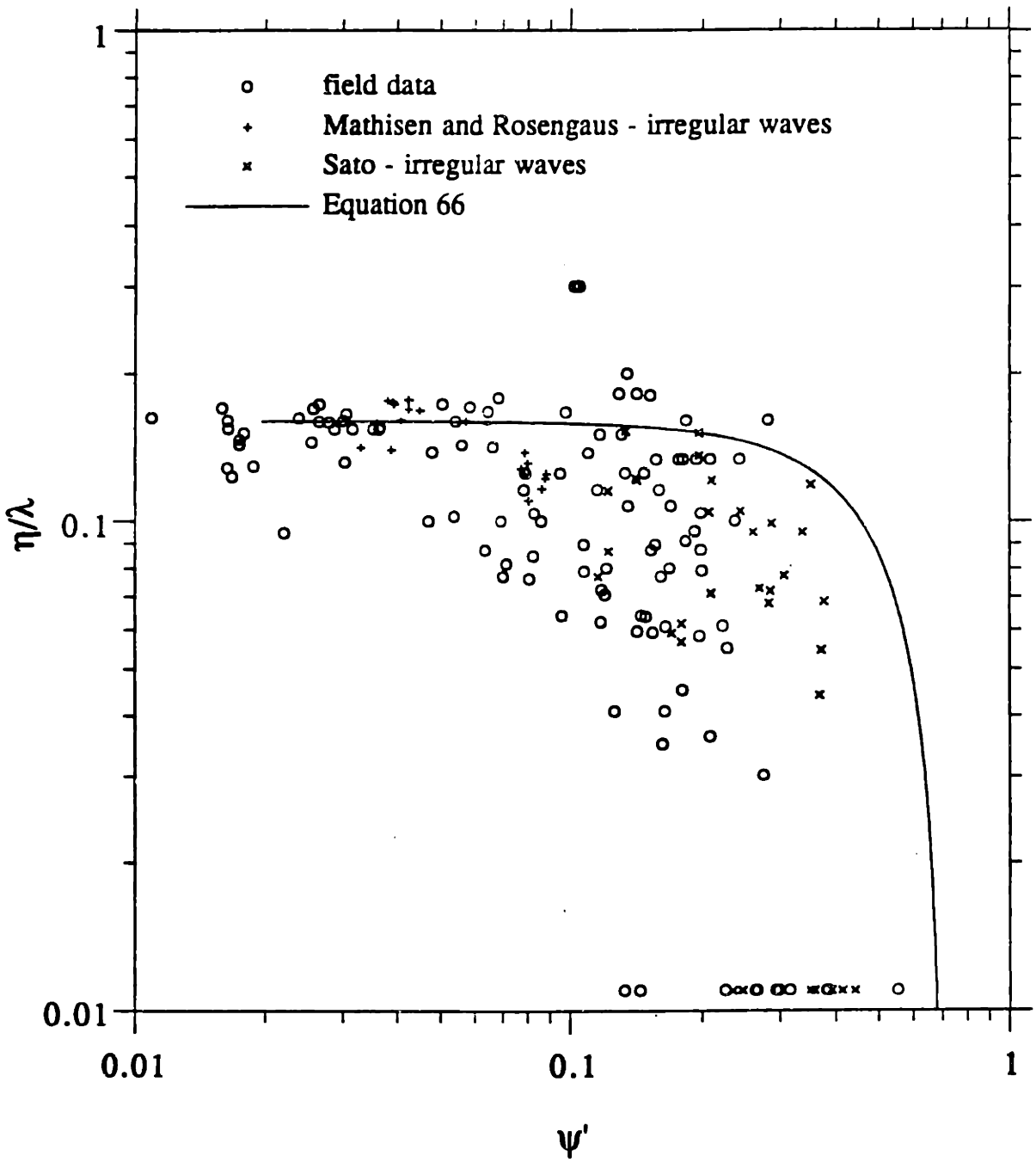

Figure 10. Comparison of the ripple steepness observed in the field and under irregular waves in the laboratory with Equation 66

irregular waves in the laboratory fall between the regular wave data and the field data.

A possible alternative explanation for the differences between the irregular wave laboratory data and the regular wave data is that they are due to variations in the apparatus and not to the irregularity of the waves. The ripple steepnesses under regular and irregular waves observed by Mathisen (1989), Rosengaus (1987), and Sato (1988) are compared in Figure 11. The figure clearly shows the effect of wave irregularity. In particular the data of Sato (1988), obtained using wave periods of up to 5 seconds at values of ψ' up to 0.75, show that while ripples exist at $\psi' = 0.7$ for regular waves, a flat bed is achieved for ψ' greater than 0.45 for irregular waves.

The ripple heights observed in the field and under irregular laboratory waves are shown in Figure 12 along with the regular wave relation of Equation 68. The ripple heights are non-dimensionalized by the representative excursion amplitude, A_{br}, which is defined by

$$A_{br} = \frac{u_{br}}{\omega_r} \tag{69}$$

where u_{br} and ω_r are the representative wave velocity and frequency respectively.

Figure 12 also shows the same general features as Figure 10, with the field data falling below the regular wave curve for values of ψ' greater than 0.04. The data from irregular wave laboratory experiments fall in between the field and the regular wave data. Therefore it can be concluded that there are definite differences between the geometry observed under regular and irregular waves. One of the most important differences are that the ripple steepness under irregular waves deviates from a nearly constant value of about 0.16 at values of ψ' much lower than the

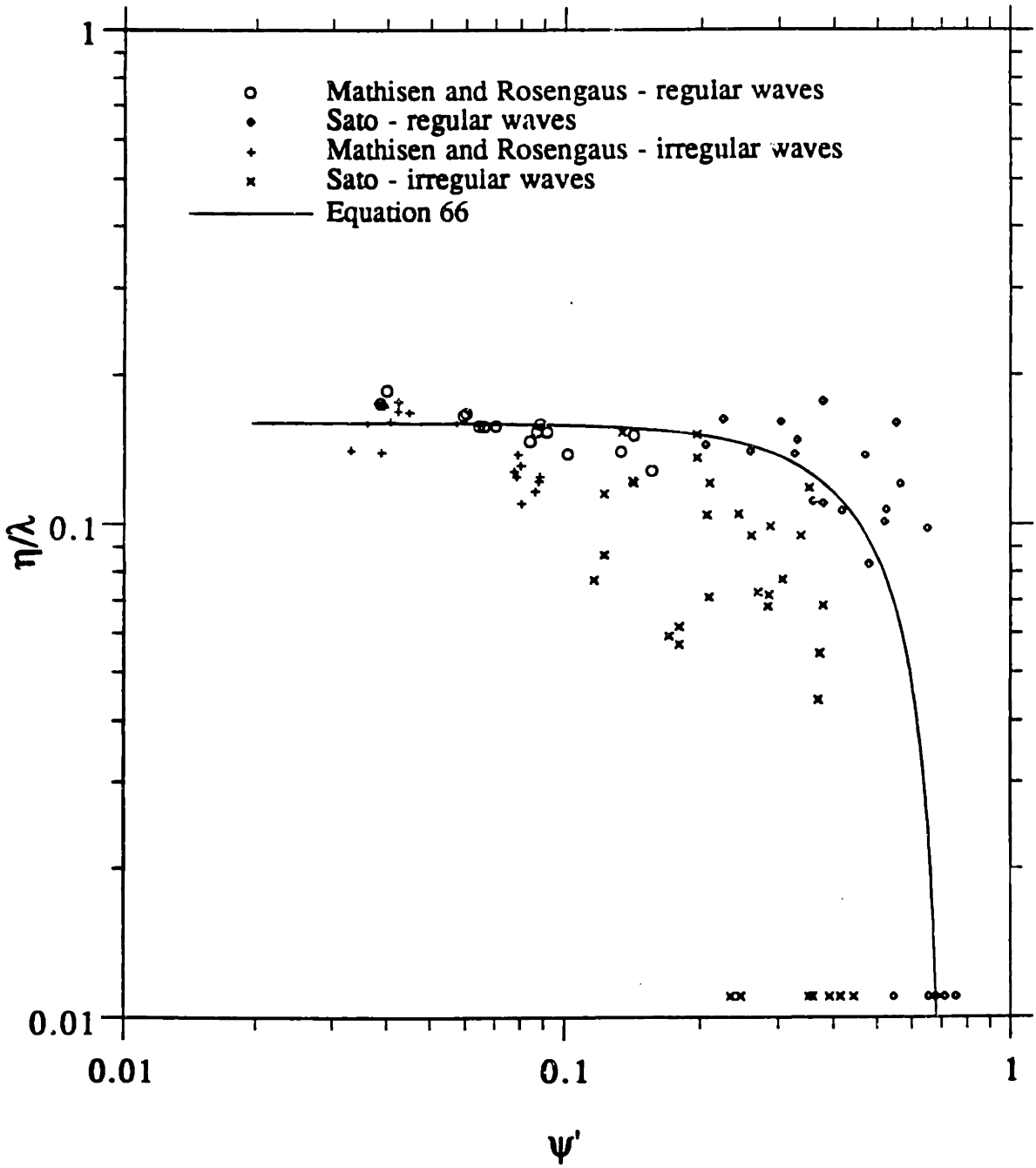

Figure 11. Comparison of the ripple steepness observed under irregular waves in the laboratory by Sato (1988), Rosengaus (1987) and Mathisen (1989) with the data obtained using regular waves by the same researchers and Equation 66

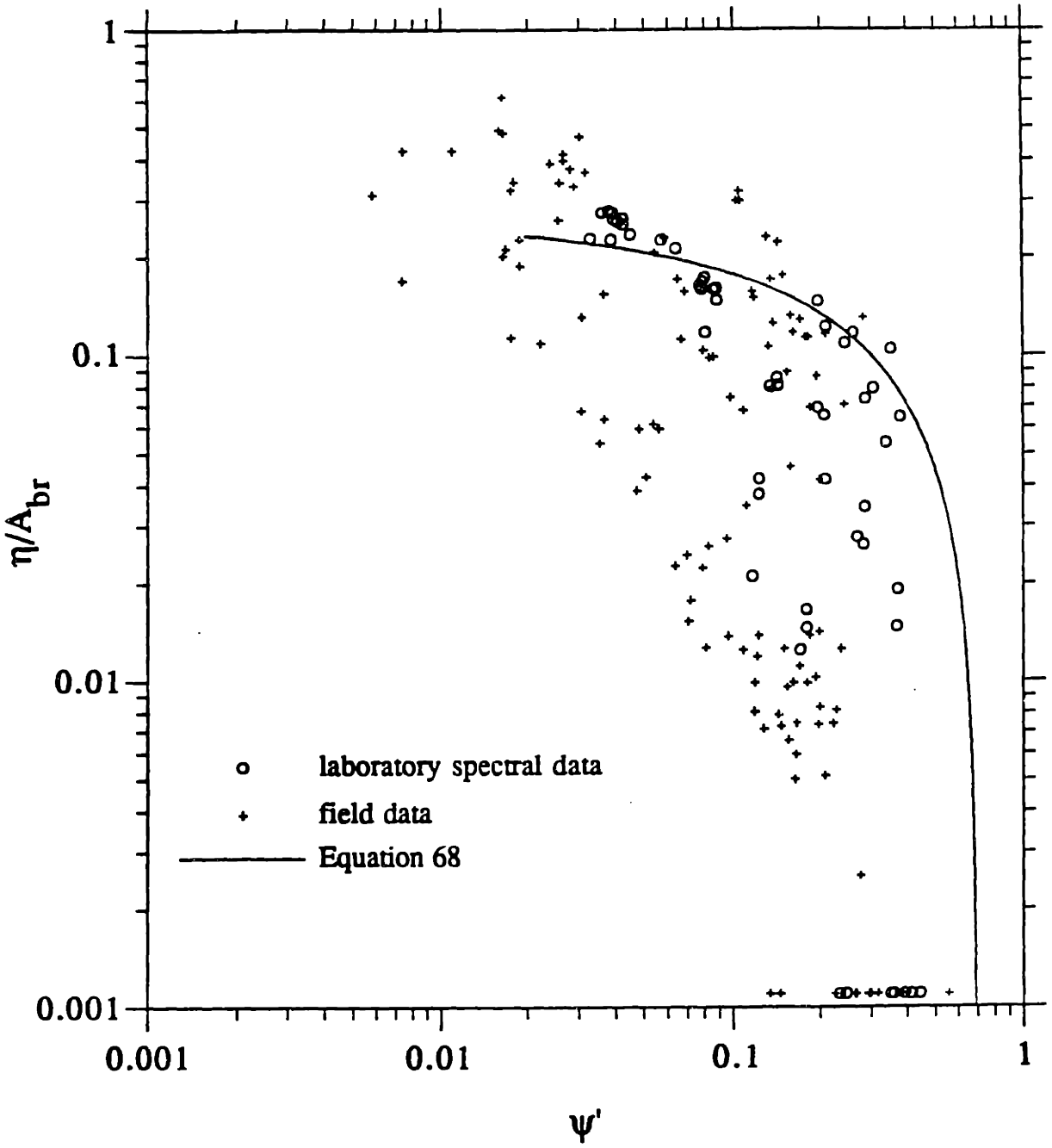

Figure 12. Comparison of the normalized ripple heights observed in the field and under irregular waves in the laboratory with Equation 68

regular wave data. The point of departure has been referred to as the break-off point by Grant and Madsen (1982).

Experimental observations show that the break-off point is a transition between sharp crested "equilibrium" ripples of steepness about 0.16 and the more rounded ripples observed at higher values of ψ'. The early break-off point under irregular waves with the same total energy as the regular waves can be explained by the occurrence of larger individual waves, that act to decrease the steepness, under irregular wave conditions. Mathisen (1989) analyzed the geometry of ripples in more detail and showed that ripples under an irregular wave motion were more rounded than those under equivalent regular waves. Another important difference is that the disappearance of ripples, resulting in sheet flow conditions, occurs at lower values of ψ' for the irregular wave data. This difference can also be explained by the presence of larger than average waves under irregular wave conditions.

The data obtained under irregular waves in the laboratory is found to fall between the regular wave data and the field data. Wikramanayake and Madsen (1990) analyzed the ripple lengths under regular and irregular wave data and showed that the deviations from the regular wave data were greatest when the representative period of the irregular wave was the largest. Table 2 shows that the data of Mathisen (1989) and Rosengaus (1987) were obtained with relatively small periods of about 2.5 seconds while Sato (1988) used periods of between 1.5 and 5 seconds. This difference in the periods is reflected in the data shown in Figure 11 where the data of Sato (1988) shows a greater deviation from the regular wave data than the data of Mathisen (1989) and Rosengaus (1987).

Some researchers, for example Dingler and Inman (1976), noted the difference between the regular wave and the field data and suggested that the difference could

be resolved if the significant wave was used as the representative wave. Use of the significant wave would have the effect of translating the data shown in Figures 10, 11, and 12 by increasing the value of ψ' by approximately a factor of 2, while the data in Figure 12 would also have the values of η/A_b reduced by a factor of $\sqrt{2}$. Examination of the figures shows that such a translation would not resolve the differences between the data and the curve representing the regular wave data.

Therefore it can be concluded that due to the significant differences between ripple geometry under regular and irregular waves the use of empirical relations derived using regular wave data are not appropriate for use in predicting field ripple geometry. Since the limited number of laboratory experiments using irregular waves are done using wave periods that are smaller than those seen in the field, the only way to predict ripple geometry in the field is by using relations based entirely on field data.

The non-dimensional variable ψ' was used as the independent variable in Figures 8 to 12 because it was found to be the best single parameter to correlate the laboratory regular wave ripple data. However, Figures 10 and 12 show that when the field data is plotted against ψ' the data shows considerable scatter. The ripple geometry observed in the field is found to give a better correlation with the parameter Z, defined by

$$Z = \frac{\psi'}{S_*} \tag{70}$$

where S_* is defined by

$$S_* = \frac{d}{4\nu}\sqrt{(s-1)gd} \tag{71}$$

with ν being the kinematic viscosity of the fluid.

The analysis of the link between the ripple geometry and the equivalent roughness, k_n in the next section shows that k_n is scaled by the ripple height. The ripple heights observed in the field, normalized by the representative excursion amplitude, A_{br}, are plotted against Z in Figure 13. The solid line represents the predictive relation

$$\frac{\eta}{A_{br}} = \begin{cases} 0.018\ Z^{-0.5} & 0.0016 < Z < 0.012 \\ 0.0007Z^{-1.23} & 0.012 < Z < 0.18 \end{cases} \tag{72}$$

for the normalized ripple height and is obtained with a relative error of 2.5. The data in Figure 13 show that ripples are only observed for values of Z less than 0.18. Therefore the value Z = 0.18 will be used as the level above which sheet flow conditions are expected to exist.

The data on ripple steepness observed in the field are plotted against Z in Figure 13a for the sake of completeness. The solid line represents the predictive relation

$$\frac{\eta}{\lambda} = \begin{cases} 0.15\ \ Z^{-0.009} & 0.0016 < Z < 0.016 \\ 0.0105Z^{-0.65} & 0.016 < Z < 0.18 \end{cases} \tag{72a}$$

3.4 Relation between the equivalent roughness and the ripple geometry

The ripple height under field conditions can be calculated using the predictive relation given by Equation 72. There still is the question of how to relate the ripple geometry to the equivalent roughness, k_n. As explained in section 3.2, available laboratory measurements of energy dissipation over fixed and movable beds will be used in this section to derive these relationships for rippled beds and for conditions of sheet flow.

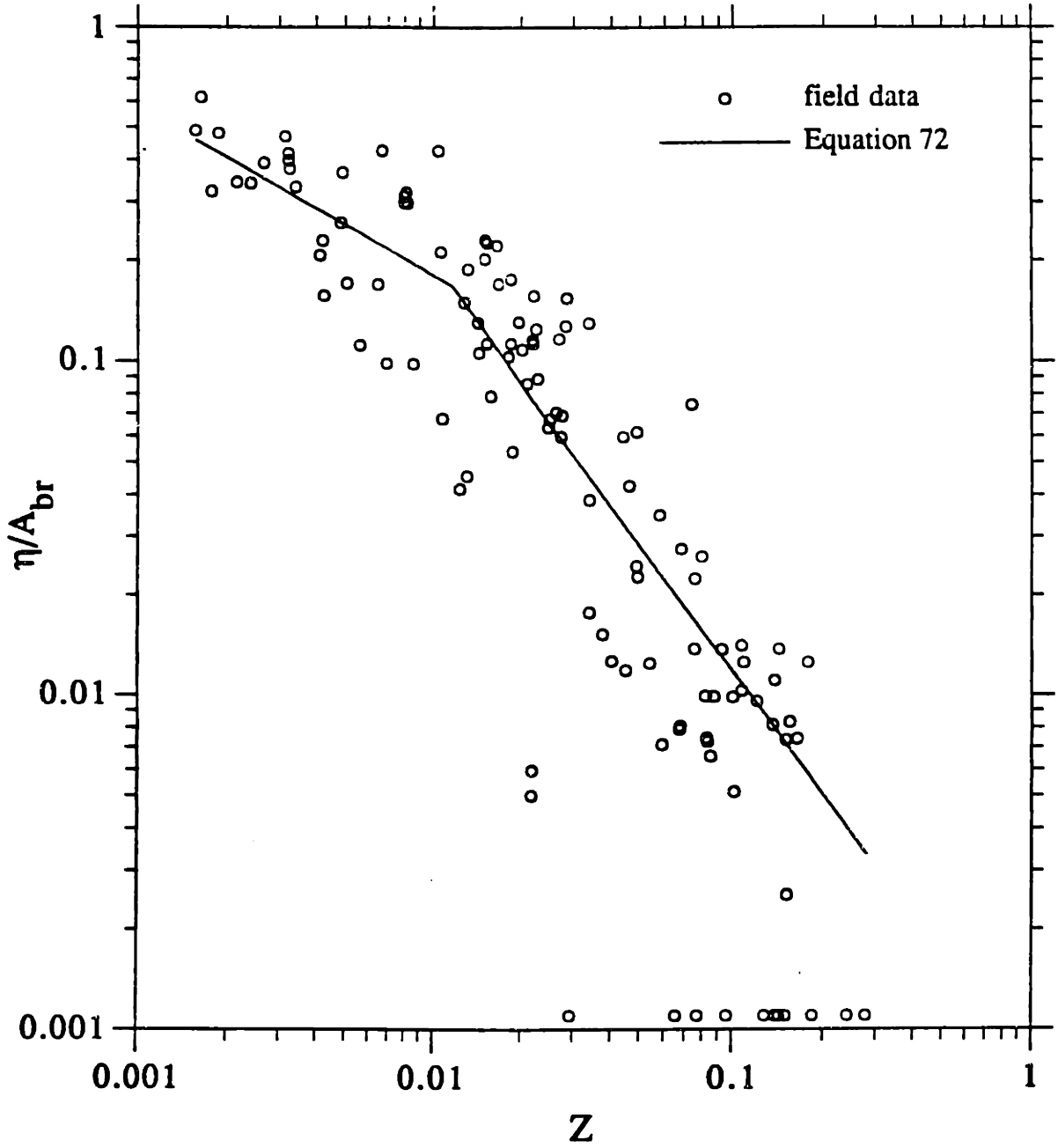

Figure 13. Variation of the normalized ripple height observed in the field with the parameter Z and the empirical relation of Equation 72

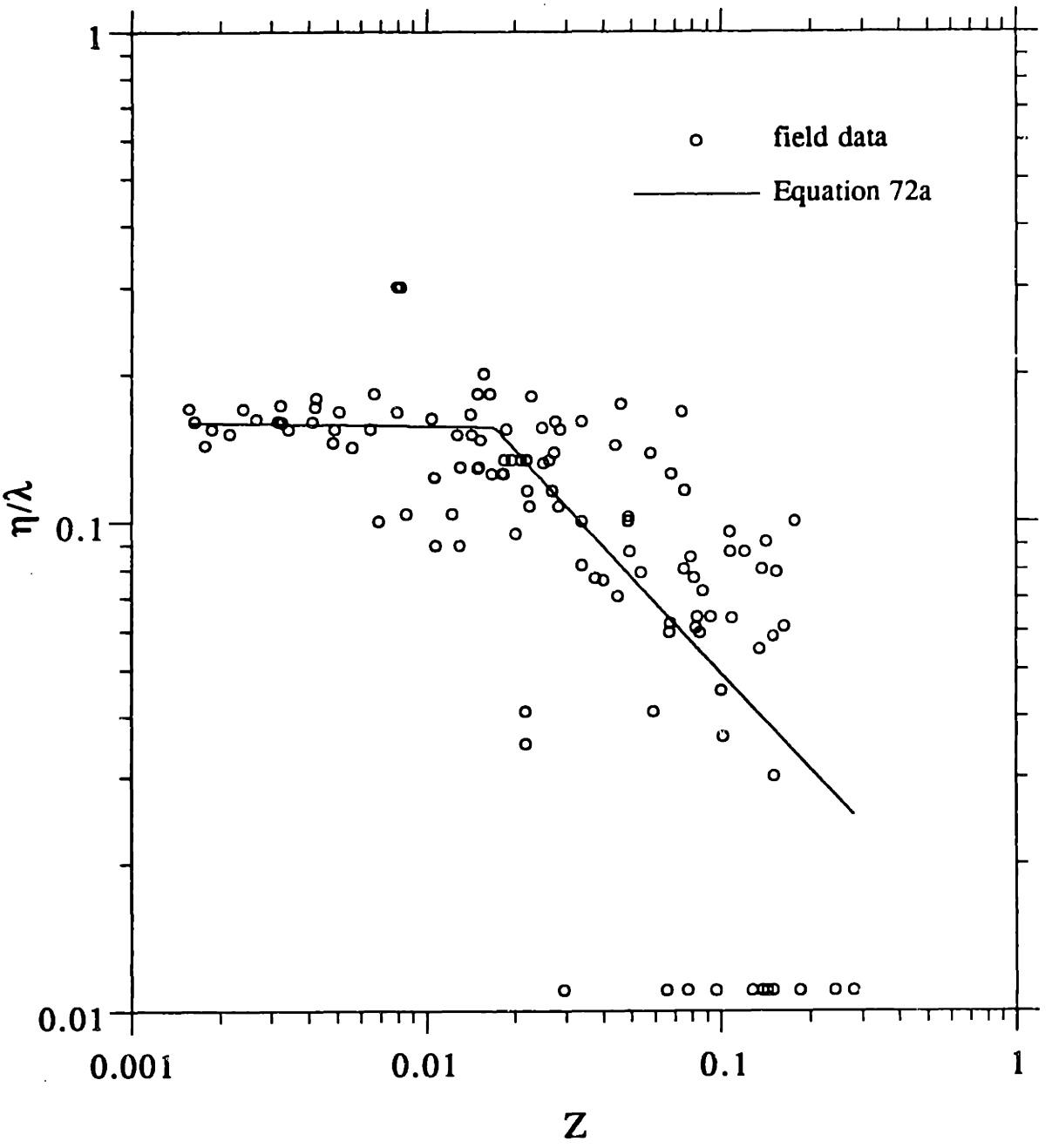

Figure 13A. Variation of the ripple steepness observed in the field with the parameter Z and the empirical relation of Equation 72a

3.4.1 Rippled Beds

The equivalent roughness, k_n, due to bedforms can be expected to be scaled by the size of the bedforms. The simplest relation is to set k_n to be proportional to the height of the bedforms, i.e.,

$$k_n \sim \eta \tag{73}$$

Grant and Madsen (1982) argued that k_n should depend on the spacing of the ripples as well as their height and suggested a relation of the form

$$k_n \sim \frac{\eta^2}{\lambda} \tag{74}$$

Some details of the available data on energy dissipation over a rippled bed are given in Table 4. The table shows that nearly all these experiments have been performed using a regular wave motion. While it may be overly optimistic to expect the results of regular wave experiments on energy dissipation to apply to irregular field waves, the use of these results is the only way to link the field ripple geometry relations developed above to the equivalent roughness.

The results of the fixed bed experiments will be discussed first. For a fixed bed, where there are no moving grains of sediment, the parameters ρ_s, d, and g are not present in the problem, leaving only the flow Reynolds number Re, defined by

$$Re = \frac{u_b^2}{\omega\nu} \tag{75}$$

The measured values of the friction factor can be converted into values of the relative roughness, A_b/k_n, using the rough turbulent friction factor curve of Figure 6a. The value of k_n can be found using the relative roughness and the known value of A_b. The ratio k_n/η derived from the data of Bagnold (1946) and Sleath

Table 4

Summary of Available Laboratory Data on Energy Dissipation under Waves

Sources of data	Type of apparatus and wave condition	Diameter of sand (mm)	Range of periods (s)	Number of data points
Mathisen (1989)	WF, R	0.12	2.6	6
	WF, IR	0.12	2.6	11
		0.2	2.6	5
Rosengaus (1987)	WF, R	0.2	2.2-3	17
	WF, IR	0.2	2.6	10
Lofquist (1986)	WT, R	0.18	3.9-14.2	20
		0.55	2.7-9.4	62
Sleath (1985)	OB, R	fixed bed	0.6-18.1	61
Carstens et al. (1969)	WT, R	0.19	3.5	5
		0.297	3.5	15
		0.585	3.5	20
Bagnold (1946)	OB, R	fixed bed	0.3-5.6	59

WF: wave flume; WT: wave tunnel; OB: oscillating bed
R: regular waves; IR: irregular waves

(1985) is plotted against Re in Figure 14. The figure shows that while some points in each data set show a trend of increasing k_n/η with an increase in Re, most of the points are clustered around a constant value of k_n/η. This constant value, which would be the constant of proportionality in Equation 73, is around 5 for the data of Bagnold (1946) and about 3 for the data of Sleath (1985).

Sleath (1985) used a sinusoidal profile with a steepness of 0.23 for his artificial ripples while Bagnold (1946) used a profile composed of circular arcs which formed sharp-crested ripples with a steepness of 0.15. Sleath (1985) found that the low values of the friction factor, and therefore of k_n/η, were observed during the transition from laminar flow when flow separation and vortex formation were just beginning. Since the flow over sand ripples in the field is most often rough turbulent these points are not important for the present analysis. Sleath (1985) argued that the effect of transition was less apparent in the data of Bagnold (1946) because the sharp crest of the ripples in those experiments would have caused flow separation at the crest even at low flow velocities.

As both Sleath and Bagnold used the same value of the ripple steepness for all their experiments it is not possible to determine which of Equations 73 and 74 provides a better representation of the equivalent roughness. If the ratio $k_n/(\eta^2/\lambda)$ is plotted against Re the constant of proportionality in Equation 74 is found to be 33 and 12.5 for the data of Bagnold and Sleath, respectively.

Equilibrium ripples formed under regular waves are sharp crested and have slopes of about 30 degrees. In these respects they resemble the profile used by Bagnold (1946) which had a crest angle of 120 degrees. However, these artificial ripples had a very sharp edge, a feature that sand ripples cannot have. Mathisen (1989) observed that ripples under irregular waves have crests that are more

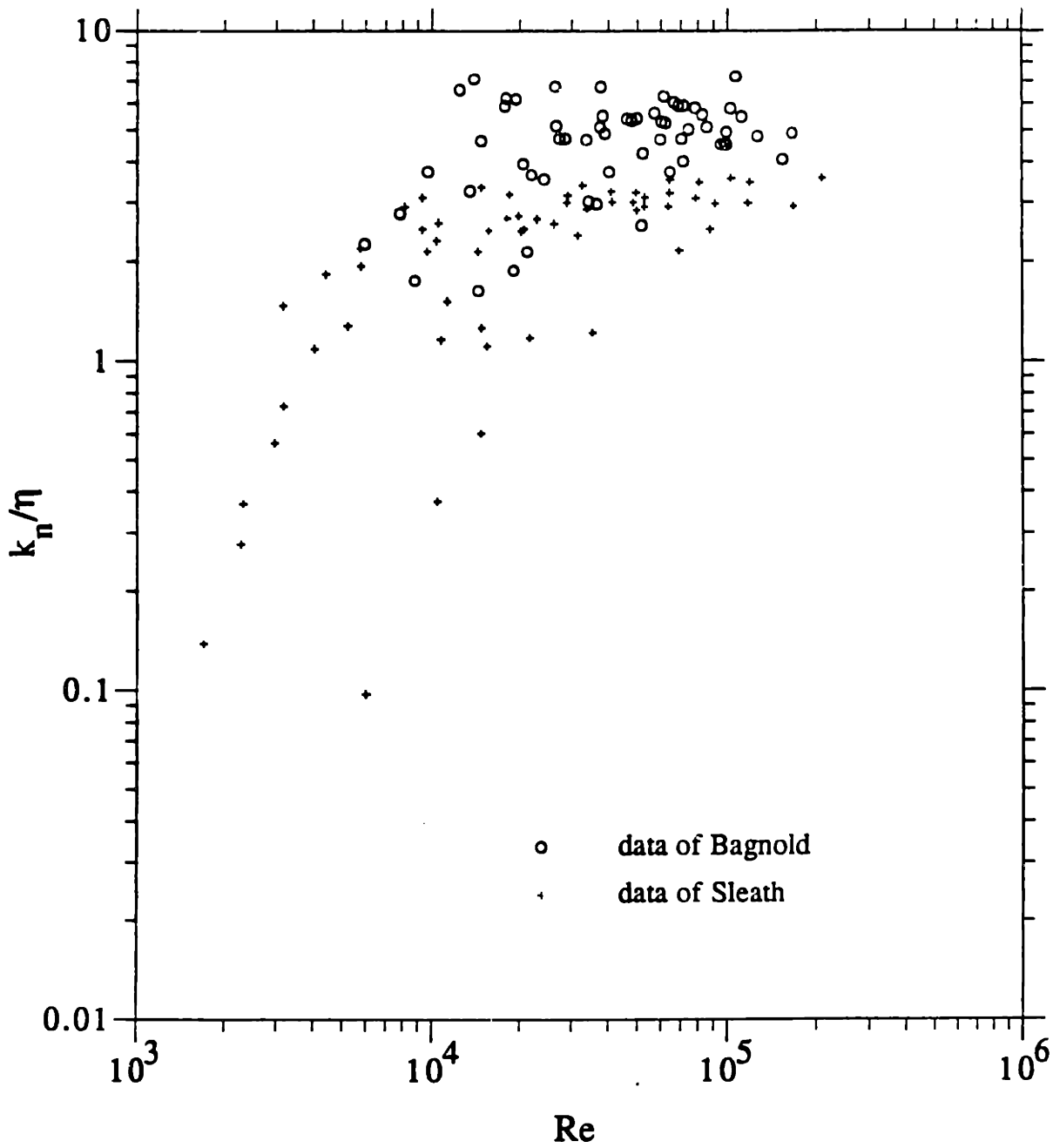

Figure 14. Variation of the ratio k_n/η with the flow Reynolds number Re for the fixed bed data of Bagnold (1946) and Sleath (1985)

rounded than those under regular waves. Thus the geometry of field ripples is probably somewhere in between the two extremes represented by the artificial beds used by Bagnold and Sleath. Another difference between their artificial ripples and sand ripples is the smooth surface used for the artificial ripples. However, as the form drag over the ripples is expected to dominate when the ripple height is much greater than the grain size, this difference is probably negligible.

The analysis of the fixed bed measurements showed that both Equations 73 and 74 were plausible representations of the equivalent roughness but could not discriminate between them. The next step is to examine the data on energy dissipation over a rippled sand bed. These are the data of Carstens et al. (1969), Lofquist (1986), Rosengaus (1987), and Mathisen (1989). As both Rosengaus (1987) and Mathisen (1989) used the same apparatus their data will be considered together in the analysis that follows. Lofquist (1986) also measured the dissipation and ripple dimensions during the growth of the ripple to the equilibrium dimensions. While these data were not obtained under equilibrium conditions, the results showed that the growth rate was small relative to the time needed to measure the dissipation, implying that the disequilibrium is not important. Therefore these data will be used in the present analysis to extend the range of ripple heights and steepness over which the dissipation has been measured. They are plotted separately in the figures and not used to obtain the empirical relations.

The ratio k_n/η is plotted against the parameter ψ' in Figure 15 for the data of Carstens et al. (1969), Lofquist (1986), Rosengaus (1987), and Mathisen (1989). Although the scatter of the data is quite high, the figure shows that the ratio k_n/η is well represented by a constant value. The best fit coefficient for Equation 73 is 4.0 with a value of 1.27 for the relative error, Δ, defined in Equation 67. It should be noted here that this is obtained by minimizing the error in the resultant friction

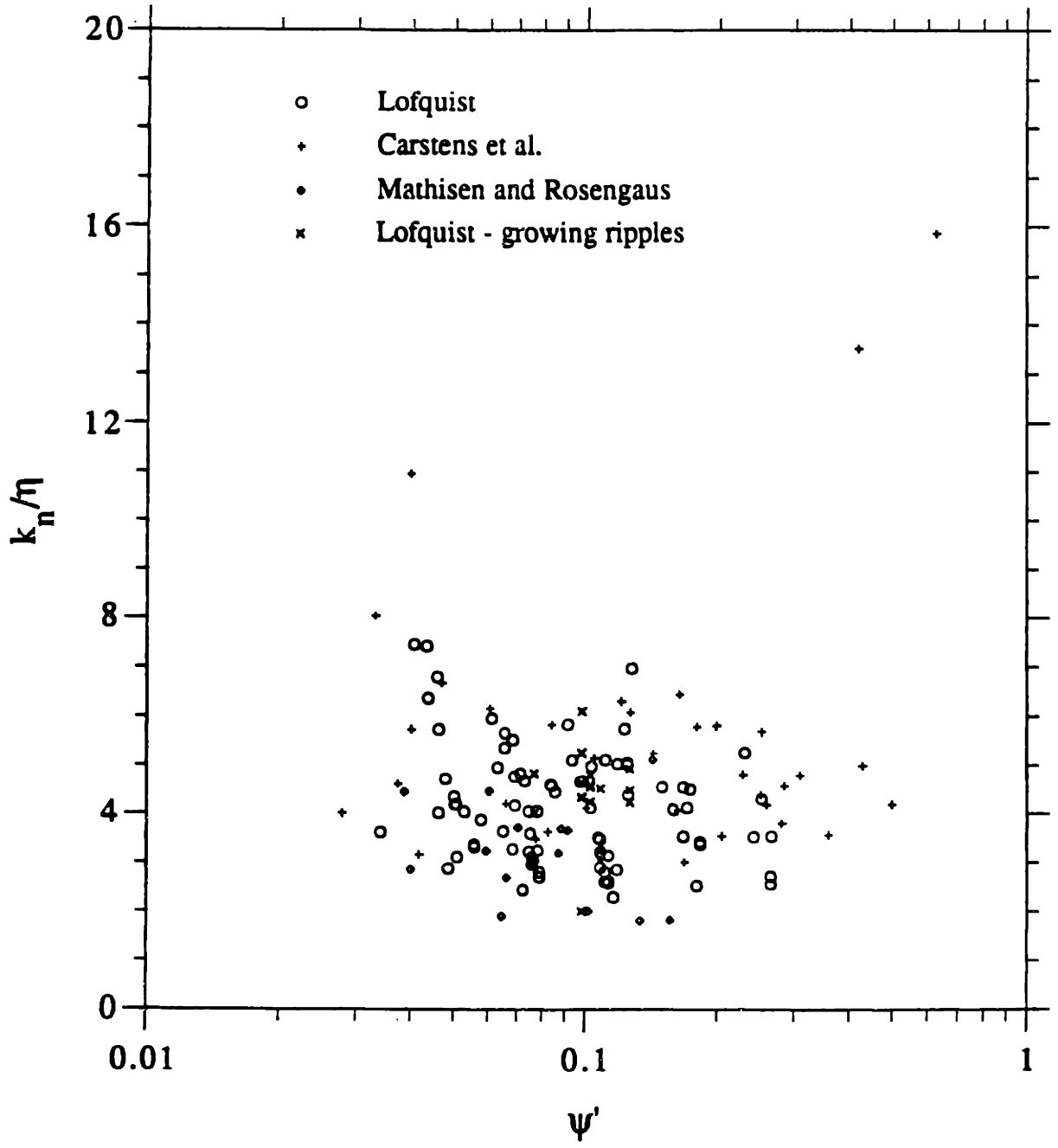

Figure 15. Variation of the ratio k_n/η with ψ' for the movable bed data of Carstens et al. (1969), Lofquist (1986), Rosengaus (1987), and Mathisen (1989)

factor. This method is employed because it is the friction factor that has been measured. The figure shows that two points from the data set of Carstens et al. (1969), obtained at relatively high values of shear stress, indicate values of k_n/η that are much larger than the values shown by the rest of the data.

The corresponding best fit coefficient for Equation 74 was 26 with a relative error of 1.35. The two relations are compared in Figure 16 which is a plot of the ratio k_n/η against the ripple steepness. The figure shows that while both Equations 73 and 74, with coefficients of 4 and 26 respectively, seem to be equally valid when the steepness is between 0.1 and 0.2, Equation 73 does better for the data with a lower steepness. The two points from the data of Carstens et al. (1969) commented on in the preceding paragraph appear in this figure as points with high values of k_n/η but with low values of ripple steepness.

Therefore it is proposed that the equivalent roughness for a rippled bed under regular waves is given by

$$k_n = 4\eta \tag{76}$$

with the resulting relative error in the predicted friction factor being 1.27.

Relating k_n to the multiple of the ripple height and some power of the ripple steepness did not improve upon the fit given by Equation 76. Various other forms for the equivalent roughness were examined, including the suggestion of Jonsson (1980) that k_n was proportional to the grain diameter, and none of them were found to perform as well as the proposed relation.

The measured values of the friction factor are plotted against the relative roughness, A_b/k_n, calculated using Equation 76, in Figure 17 along with the friction factor curve of Figure 6a. If Equation 76 is a perfect correlation all the points

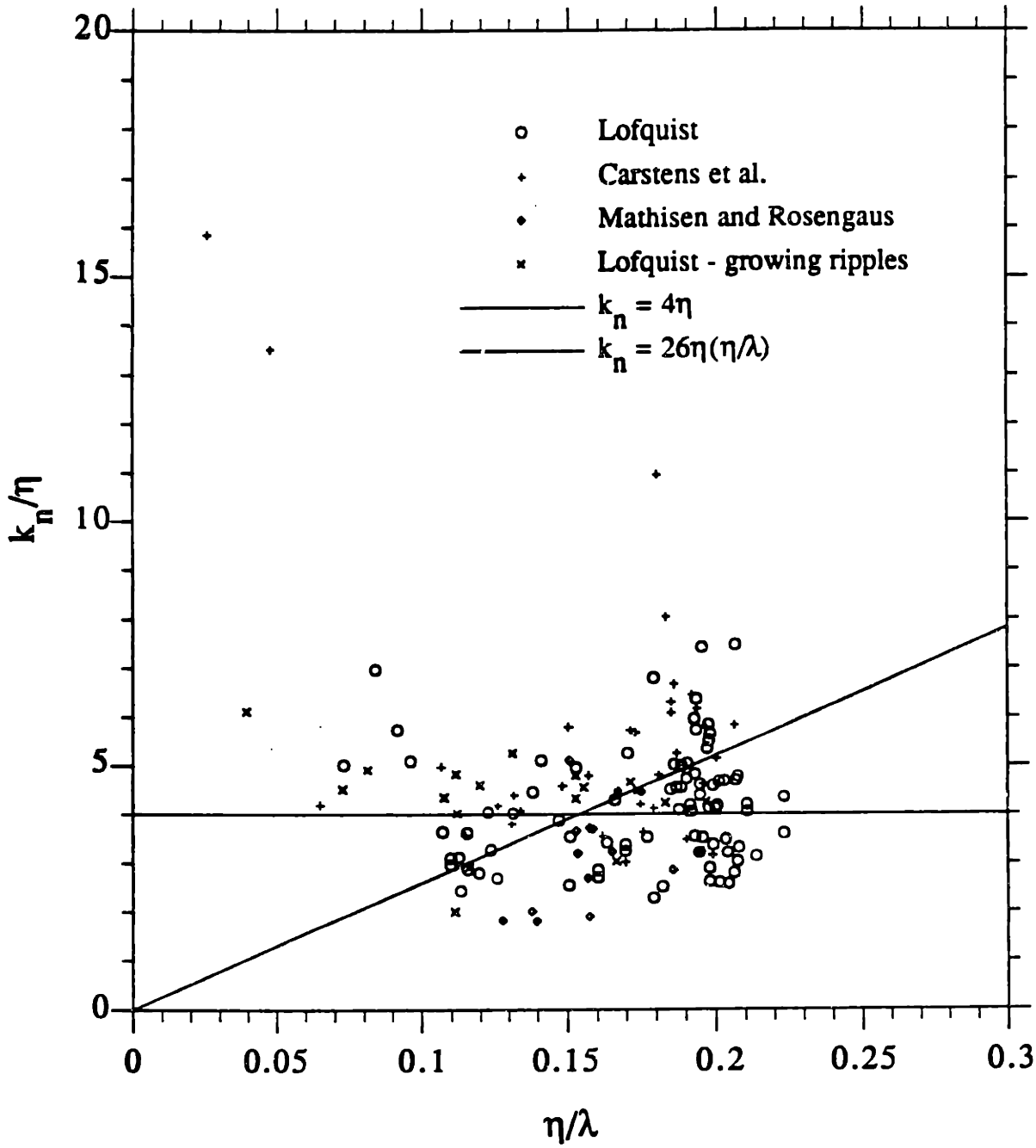

Figure 16. Variation of the ratio k_n/η with the ripple steepness for the regular wave movable bed data of Carstens et al. (1969), Lofquist (1986), Rosengaus (1987), and Mathisen (1989)

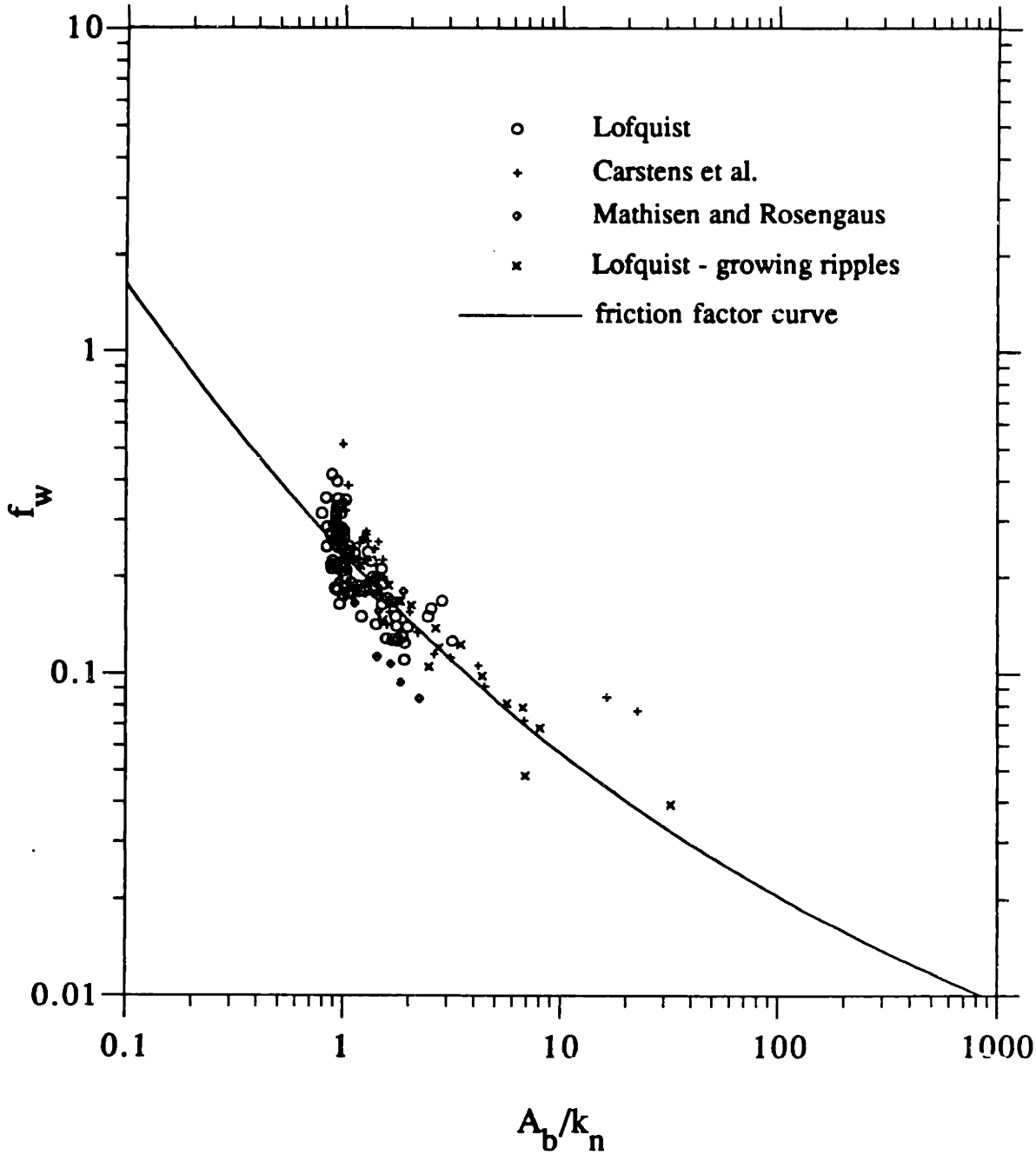

Figure 17. Variation of the observed friction factor, f_w, with the ratio A_b/k_n compared to the friction factor curve of Figure 6a

should fall on this curve. It is encouraging that the data from the growing ripples obtained by Lofquist (1986) are also well represented by the curve, even though they were not used to obtain the best fit coefficient in Equation 73.

It should be recalled that the fixed bed experiments of Sleath (1985) and Bagnold (1946) gave values of 3 and 5, respectively, for the constant in Equation 73. Since the value obtained from the sand beds lies in this range it can be concluded that the bulk of the energy dissipation over a rippled sand bed is due to the form drag created by the ripples and not to the skin friction caused by the sand grains.

Grant and Madsen (1982), and later Nielsen (1983), suggested that the increased sediment motion occuring at high values of the shear stress would cause additional flow resistance and derived an expression for the corresponding increase in the equivalent roughness. Grant and Madsen (1982) based their expression on three points in the data set of Carstens et al. (1969) where a rather large value of f_e was measured even though the ripple steepness was low. These three points are the points from the data of Carstens et al. (1969) in Figure 16 which have a steepness less than 0.1. While one of the points lies close to the curve $k_n = 4\eta$ the other two show k_n/η to be about 15. These two points also lie above the friction factor curve in Figure 17.

However, Figure 16 also shows several data points, obtained by Lofquist (1986) for both equilibrium and growing ripples, with a steepness less than 0.1, that are in general agreement with Equation 73. Furthermore, Figure 15 shows that while the two aberrant points of the data set of Carstens et al. (1969) indicate an increase in roughness at high shear stress, i.e., large ψ', there are two other points from the same data set with values of ψ' greater than 0.4 which agree with Equation 73.

The expression for the additional roughness due to the sediment transport derived by Nielsen (1983) was based on some measurements obtained by Carstens et al. (1969) over an initially flat bed. However, the value of ψ' in these experiments was such that this flat bed would eventually have become rippled. Thus it is possible that the unexpectedly high values of f_e, and therefore the equivalent roughness, obtained from these experiments was due to the presence of ripples on the bed. While these ripples may have been much smaller than the final equilibrium ripples they would still have been significantly larger than the grain size, which is the expected scale for the equivalent roughness over a flat bed.

The question of the validity of these expressions for the roughness caused by increased sediment transport could be resolved by making energy dissipation measurements over beds that are in a condition of sheet flow. Unfortunately, no such measurements are available at present. Experiments conducted by Wilson (1989) on the flow resistance due to a moving layer of sediment under steady flow conditions indicate that the expressions of Grant and Madsen (1982) and Nielsen (1983) would result in estimates of the equivalent roughness that are significantly greater than the measured values. Therefore it is concluded that the available data do not justify the inclusion of a term to represent the possible additional roughness caused by the sediment transport.

The analysis so far has been of energy dissipation measurements over rippled beds with a regular wave motion. The only data for irregular waves are those of Mathisen (1989) and Rosengaus (1987) who measured energy dissipation under irregular waves over a rippled sand bed in a wave flume. Using the representative wave velocity, U_{br}, and frequency ω_r, defined by Equations 50 and 51, these measurements can be used to calculate a representative value of f_e and therefore a value of the equivalent roughness. The ratio k_n/η for both the regular and irregular

wave data of Mathisen (1989) and Rosengaus (1987) are shown in Figure 18 plotted against the representative value of ψ'.

The figure shows a wide scatter in the data, indicating the experimental difficulty in obtaining values of f_e at low values of ψ'. A similar scatter of the data at low values of ψ' can be seen in Figure 15. The data in Figure 18 show that the irregular wave data indicate a slightly lower value for the ratio k_n/η than the do the regular wave data. However, when considering the wide scatter of the data, the limited range of ψ' and the errors involved in predicting field ripple geometry, it seems reasonable to ignore this difference at present and consider that the equivalent roughness for a rippled bed under irregular waves is also given by Equation 73.

It should be noted here that if the significant wave had been used as the representative wave the bottom velocity used to calculate f_e would have been greater than the equivalent near-bottom velocity, U_{br}, by a factor of $\sqrt{2}$. This difference would have resulted in the calculated values of f_e being reduced by a factor of $2\sqrt{2}$ leading to equivalent roughnesses much lower than those obtained here. Therefore it can be concluded that the use of the equivalent wave defined by Equations 50 and 51 leads to a scaling of the equivalent roughness that is much closer to that obtained using regular waves than if the significant wave were used.

3.4.2 Sheet Flow Conditions

The analysis of ripple geometry data from the field in section 3.3 suggested that the ripples would disappear and give way to conditions of sheet flow for values of the parameter Z, defined by Equation 70, greater than 0.18. As noted above there have been no measurements made of energy dissipation under sheet flow conditions

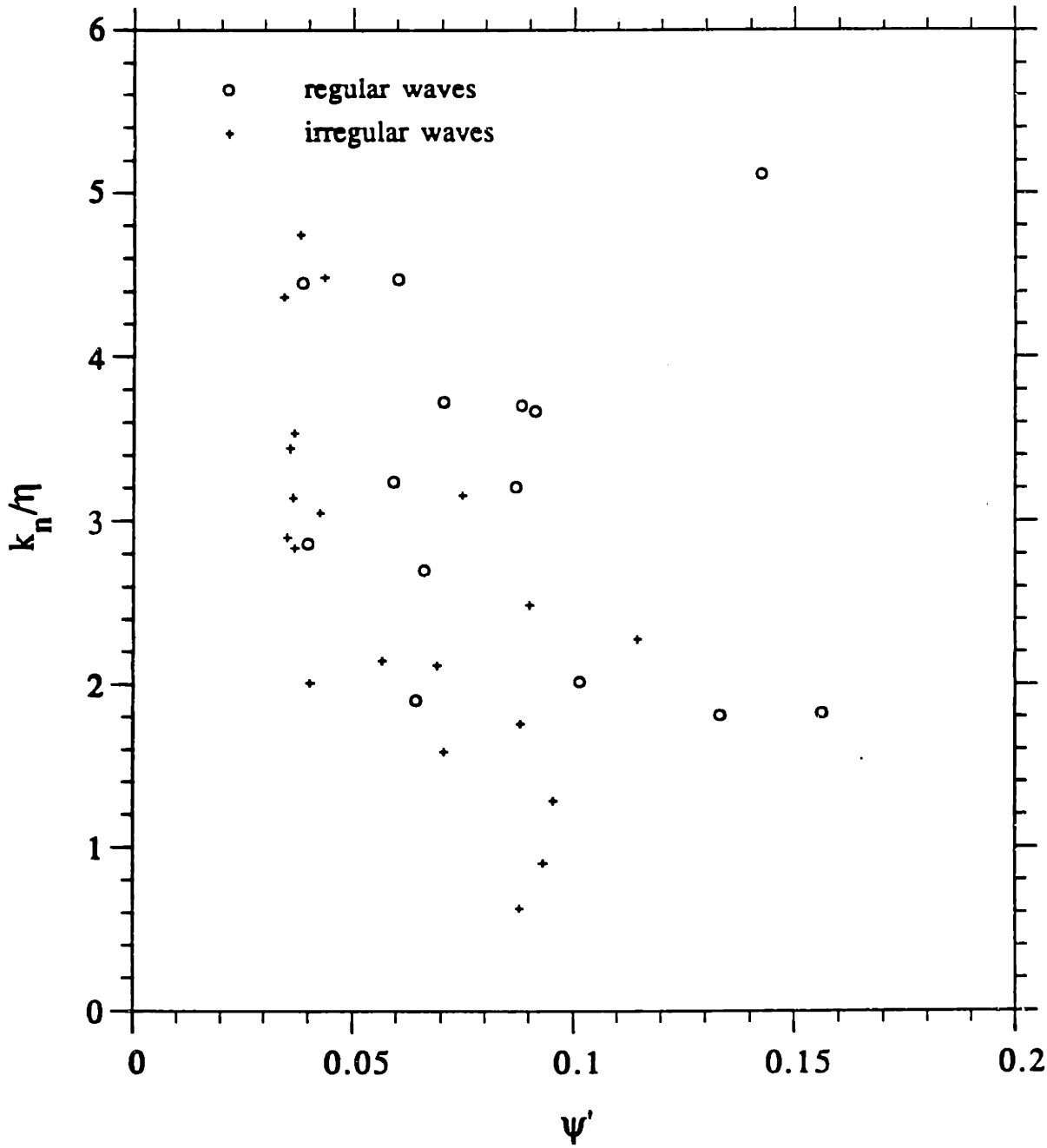

Figure 18. Variation of the ratio k_n/η with ψ' for the irregular wave movable bed data of Rosengaus (1987) and Mathisen (1989)

under a wave motion. The only available data for steady flow conditions are those of Wilson (1989) who measured the flow resistance caused by sheet flow. He proposed an expression of the form

$$k_n = 5d\psi \tag{77}$$

where d is the grain diameter.

Although it was not clear what shear stress is to be used to calculate the Shields parameter, ψ, in Equation 77, the fact that it corresponds to sheet flow conditions indicated that the total bed shear stress should be used in this case. The ripple data under irregular waves in the laboratory and field indicate that sheet flow occurs for when ψ' is greater than about 0.4. As Equation 77 indicates, the equivalent roughness for sheet flow is scaled by the grain diameter, so that the total shear stress obtained using this roughness is expected to be about 1–10 times the skin friction shear stress, which is calculated using $k_n = d$. Assuming a value of $\psi = 2$ in Equation 77 results in the simple relation

$$k_n = 10d \tag{78}$$

Some recent measurements of the current velocity profile in the field under sheet flow conditions (Madsen et al. (1992)) indicate a roughness of $k_n = 12$ d. This result shows that Equation 78 is a reasonable assumption. However, it must be emphasized that the equivalent roughness for sheet flow conditions is an area where much research is required.

3.5 Summary and Discussion

The objective of this chapter was to derive predictive relations for the equivalent roughness, necessary to perform the wave-current interaction computations

described in Chapter 2. A survey of the available data on ripple geometry showed that relations developed using laboratory data on regular waves were not applicable to field conditions and that there were very few measurements of energy dissipation in the field. Therefore the only available method was to derive predictive relations for the ripple geometry using the field data and obtain relations linking the ripple geometry and the equivalent roughness using laboratory data.

The resulting predictive relations for the equivalent roughness, k_n, are

$$k_n = \begin{cases} 4\eta & Z < 0.18 \\ 10d & Z > 0.18 \end{cases} \tag{79}$$

where the parameter Z is defined by Equation 70, d is the grain diameter, and η the ripple height. The ripple height is calculated using the relation

$$\frac{\eta}{A_{br}} = \begin{cases} 0.0181Z^{-0.5} & Z < 0.012 \\ 0.0007Z^{-1.23} & Z > 0.012 \end{cases} \tag{80}$$

It should be noted that the excursion amplitude, A_{br}, in Equation 80 and the skin friction Shields parameter, ψ', in Equation 70 are based on the equivalent wave defined by Equations 33 and 34.

The calculation of the friction factor proposed here is a two-step process, both of which involve uncertainties. However, what is of importance is the total uncertainty in the prediction of the friction factor. For example, consider the case of a wave motion specified by an equivalent near-bottom velocity, U_{br}, of 50 cm/sec, and a frequency of 1.0 rad/sec, over a bed consisting of sand grains of diameter 0.02 cm. The value of A_{br} will then be 50 cm. These values are chosen to obtain a rippled bed.

Using the friction factor curve and Equations 65 and 71, the value of ψ' and S_* are found to be 0.29 and 2.8 respectively, so that the parameter Z has a value of 0.1. With these values of A_{br} and Z, Equation 79 predicts a rippled bed with ripples of height 0.57 cm. Since the relative error for this equation is 2.5, a possible range for the ripple height is 0.23–1.43 cm. The equivalent roughness, k_n, is calculated from Equation 73 to have a value of 2.3 cm within a range of 0.92–5.7 cm. It should be recalled that the relative error of 1.27 involved in obtaining Equation 73 was based on the relationship between the ripple heights and the predicted friction factors. Therefore this error should be included only after the calculation of the friction factors using the curve in Figure 6a.

The relative roughness A_b/k_n is found to be 21.7 within a range of 8.8–54.3 so that a value of 3.8×10^{-2} is obtained for the friction factor while the range is 5.6×10^{-2}–2.6×10^{-2}. Including the relative error of 1.27 expands this to 7.1×10^{-2}–2.1×10^{-2}. These two extremities differ from the calculated value by factors of 1.87 and 0.55, respectively. Therefore the uncertainty for the total calculation is approximately 1.84. The total uncertainty is less than the multiple of the two individual errors involved because of the slope of the friction factor curve in Figure 6a.

The above calculation shows that there is considerable uncertainty in determining the friction factor in the field. The value of 1.84 in the uncertainty for the friction factor will result in corresponding values of 1.84 and 1.36 for the wave shear stress and wave shear velocity, respectively. The principal contribution to the uncertainty is the large error involved in the prediction of the ripple height. Therefore it is very important that the ripple geometry be measured during field experiments.

The situation is even more unclear in the case of sheet flow conditions. Equation 78 is only an assumption with limited support from field data. The equivalent roughness due to sheet flow could be investigated in two ways. One is by making energy dissipation measurements over a sand bed. The other possible method is to measure the mean velocity at more than one point in the vertical during field experiments made under sheet flow conditions which was the method used by Madsen et al. (1992).

CHAPTER 4

SEDIMENT TRANSPORT MODEL

The extended wave-current model of Chapter 2 and the movable bed roughness relations developed in Chapter 3 can be used to obtain the velocity field and the related bed shear stresses for a fluid motion specified by several linearly superposed wave components and a current. A model that calculates the sediment transport caused by this velocity field will be developed in this chapter. Sediment transport is usually subdivided into the bed load and suspended load components as they are caused by two different physical mechanisms. The calculation of the bed load transport using the conceptual bed load transport model of Madsen (1991) is outlined. As this model uses the concept of skin friction shear stress a method to derive this component of the shear stress is described.

The governing equation for the distribution of suspended sediments is stated and solved using the eddy viscosity distribution of Equation 8. As the solution requires the specification of a boundary condition near the bottom the next section is devoted to developing such a condition for wave-current flows. The hydrodynamic and sediment transport models are then summarized and the calculations involved explained using a simple flow chart. The only undetermined coefficient of the model is the resuspension coefficient, γ_0. The determination of this parameter using recent high-quality field measurements is described in the final section.

4.1 Bed Load Transport Model

Madsen (1991) considered the case of fully rough turbulent flow over a flat sand bed. By assuming that the logarithmic velocity profile was valid very close to the grains he related the fluid velocity seen by the stationary grains to the shear

velocity based on the bottom shear stress. A simple force balance between the drag force on a sediment grain and the static friction of the sand bed showed that the initiation of motion was indicated by a constant value of the Shields parameter, a result that is supported by experimental data.

Madsen (1991) then used the equation of motion for a sediment grain rolling on the bed to examine the response of such a grain to changes in the fluid motion. The analysis showed that the response time of grains with diameters in the range commonly found in coastal regions is on the order of 0.1 seconds. This time is much smaller than the wave period, which is the time scale for changes in the external flow under wave conditions. The above result means that the sediment grains can be assumed to react instantaneously to changes in the near bottom flow and that bed load formulations derived assuming steady external flow conditions can be extended to wave dominated conditions by using the shear velocity based on the instantaneous shear stress.

A simple model of bed load transport by rolling and sliding grains was derived by balancing the excess bottom shear stress, i.e., the difference between the bottom shear stress and the shear stress required to initiate motion, with the flow resistance due to the moving grains. The resulting expression for the transport was found to be similar in form and magnitude to the empirical bedload transport formula of Meyer-Peter and Muller.

Since the idea of transport solely by rolling and sliding is realistic only for shear stresses that are slightly above the critical value for the initiation of motion, Madsen (1991) next considered the case of grain motion by saltation. By simplifying the equation of motion he was able to obtain solutions for quantities such as the jump length, the jump time, and the height of the jump. A balance of

the momentum lost by the grains when they hit the bed with the excess shear stress resulted in a transport formula that was once again quite similar to the Meyer-Peter Muller formula.

The fact that very similar formulae for the bed load transport resulted from these two quite different conceptual models, coupled with the demonstration that the bed load transport reacts very quickly to changes in the mean flow, led Madsen (1991) to propose a generalized form of the Meyer-Peter and Muller formula for the calculation of the instantaneous bed load transport under wave-current conditions. This equation relates the non-dimensional bed load transport, $\vec{\Phi}_b$, to the skin friction shear stress by

$$\vec{\Phi}_b(t) = \begin{cases} \dfrac{8}{1 \pm \dfrac{\tan\beta(t)}{\tan\phi_m}} \left(|\psi'(t)| - \psi_{cr}\right)^{3/2} \dfrac{\vec{\tau}_b'(t)}{|\vec{\tau}_b'(t)|} & |\psi'(t)| > \psi_{cr} \\ 0 & |\psi'(t)| < \psi_{cr} \end{cases} \tag{81}$$

In this equation $\vec{\tau}_b'(t)$ is the instantaneous skin friction shear stress, $\psi'(t)$ is the Shields parameter based on the instantaneous skin friction shear stress given by

$$\psi'(t) = \frac{|\vec{\tau}_b'(t)|}{\rho(s-1)gd} \tag{82}$$

and ψ_{cr} is the critical Shields parameter for the initiation of motion. In Equation 82 ρ is the density of water, s the specific gravity of the sediment grains, g the acceleration due to gravity, and d the grain diameter.

The angle $\beta(t)$ in Equation 81 is the slope of the bed in the direction of $\vec{\tau}_b'(t)$, the positive sign is to be used when $\vec{\tau}_b'(t)$ is upslope and the negative sign when $\vec{\tau}_b'(t)$ is downslope. $\beta(t)$ can be calculated from the maximum bed slope angle β_0 and the angle between the direction of upward slope and the wave direction. ϕ_m is

the friction angle of the sediment which for quartz sand is taken as 36° (Madsen, 1991).

The concept of skin friction, which will be discussed in the next section, has been introduced here to account for the case of a rippled bed. The non-dimensional transport, $\vec{\Phi}_b$, is related to the dimensional value, $\vec{q}_b$, in units of volume per unit length per unit time, by

$$\vec{\Phi}_b = \frac{\vec{q}_b}{\sqrt{(s-1)gdd}} \tag{83}$$

In the calculation of the bed load, $\vec{\tau}'_b(t)$ is calculated from the wave and current skin friction shear stresses derived from the selected skin friction model. The directional instantaneous transport, $\vec{\Phi}_b(t)$, can be calculated from Equation 81. Integration of the components of $\vec{\Phi}_b(t)$ in the wave and wave-normal directions over a wave period will give the net transport in these directions.

4.2 Skin Friction Model

The calculation of the bed load transport in the previous section was based on the skin friction shear stress. The concept of skin friction was developed to extend models, such as that of Madsen (1991), that were initially developed for a flat bed, to the case of a rippled bed. For a flat bed the only scale for the bed roughness is the diameter of the sediment grains that make up the bed. In this case it is reasonable to expect that the total bottom shear stress, τ_b, will act to mobilize the grains and make them available for suspension.

The situation changes when bedforms are present. The bottom shear stress is now the sum of the two components—the form drag due to the ripple shape and the

skin friction drag on the ripple surface. The roughness due to the form drag is scaled by the bedform height while the roughness due to the skin friction is scaled by the grain diameter. Since the bedform height is generally much greater than the grain size, the roughness seen by the flow at heights that are much greater than the bedform height will be scaled by the bedform height.

However, the movement of sediment as bed load occurs in a thin layer of a thickness that is usually much less than the bedform height. Therefore it is apparent that the appropriate shear stress necessary to describe this process should be the skin friction shear stress and not the bed shear stress which is dominated by the form drag. Thus the skin friction shear stress must be estimated before using an equation, such as Equation 81, to predict the bed load transport.

The values τ_{cw}, τ_w, and τ_c, which are combined wave and current, wave, and current shear stresses, respectively, are calculated using the wave-current model outlined in Chapter 2, which uses the full bed roughness. The equivalent Nikuradse roughness for a movable bed under field conditions can be calculated using the empirical formulae given in Chapter 3. The problem is to estimate the skin friction shear stresses τ_w' and τ_c', due to the waves and the current respectively. These can then be used to calculate the instantaneous skin friction shear stress.

Glenn (1983) suggested that τ_w' and τ_c' could be estimated by running the wave-current model with the same wave and current specifications but with the roughness taken as the grain roughness. The current was specified for this model by a given value of the mean velocity at an elevation that was usually well above the wave boundary layer.

This specification implies that the current velocity calculated with the shear velocities u_{*c} and u_{*cw}, and using the full roughness, should match the specified

value. If the same specification is used to calculate u_{*cw}', and thence τ_c', using the grain roughness, the value of τ_c' thus obtained would be dependent upon the level at which the current is specified. As this level is usually specified to be well above the wave boundary layer this method of calculating τ_c' is not consistent with the expectation that the skin friction shear stresses should only affect the flow within the boundary layer.

One way of removing this inconsistency is to require the matching of the current velocities to be done at the level δ defined in Equation 33. In other words the skin friction current shear stress τ_c' is estimated by running the wave-current model with the original wave specification, the roughness taken as the grain roughness and the current specified to be the value of the mean veloicty at the level $z = \delta$ calculated from the solution to the wave-current problem that used the full roughness.

4.3 Solution of the Suspended Sediment Problem

4.3.1 The Governing Equation

Sediment is considered to be in suspension when the grains are supported entirely by fluid forces. In this case the profile of the suspended sediment concentration is governed by the diffusion equation. With the assumption of negligible horizontal concentration gradients this equation can be written as

$$\frac{\partial c}{\partial t} = w_f \frac{\partial c}{\partial z} + \frac{\partial}{\partial z}(F_d) \tag{84}$$

where

c = instantaneous sediment concentration

w_f = fall velocity of the sediment grains

F_d = diffusive sediment flux

t = time

z = height above the bottom

It should be noted that Equation 84 is valid only in the region where the concentration is small enough to make intergranular collisions negligible, i.e., it is not valid very near the bottom where the sediment moves mostly as bed load. The neglect of horizontal gradients would seem to be inapplicable in the case of a rippled bed which could have large horizontal variations caused by the entrainment of sediment by vortices. In this case c is understood to be the concentration averaged over a distance that is large compared to the ripple wavelength but small compared to the wavelength of the wave motion.

Equation 84 requires two boundary conditions, one each at the top and bottom boundaries of the flow. The upper boundary condition is generally specified as zero sediment flux through the free surface. For the case of non-breaking waves in fairly deep water this condition is equivalent to the requirement that c approach zero for large values of z. The bottom boundary condition is usually specified as a prescribed value of either the concentration or the sediment flux at some level near the bed. The relative merits of these two methods are discussed in Chapter 4.4 and the reference concentration method selected for this study.

These boundary conditions show an important difference between the suspended sediment problem and the fluid velocity problem, which is governed by an equation similar to Equation 84. The fluid velocity in the boundary layer is forced by, and

therefore scaled by, the near-bottom wave velocity while the suspended sediment concentration is forced and scaled by the prescribed reference value near the bottom. Therefore this boundary condition is a critical component of any suspended sediment model. Possible formulations of this component of the model will be discussed in Chapter 4.4.

Under conditions of turbulent flow, which is nearly always the case in coastal wave boundary layers, the diffusive flux, F_d can be written as

$$F_d = -\overline{c'w'} \tag{85}$$

where c' and w' are the turbulent fluctuations in the concentration and vertical velocity, respectively, and the overbar denotes averaging in time.

In order to solve Equation 84 and obtain c as a function of z and t it is necessary to express the diffusive flux F_d in terms of the mean flow characteristics. Since this flux arises due to turbulent mixing along a concentration gradient it is usually expressed, analogous to molecular diffusion, as

$$F_d = -\overline{c'w'} = \nu_t \frac{\partial c}{\partial z} \tag{86}$$

where ν_t is referred to as the turbulent eddy diffusivity. It will be assumed in this report that the turbulent diffusivities for mass and momentum are the same, i.e., turbulent eddy diffusivity and eddy viscosity are assumed identical and the terms are used interchangeably from here on. Another assumption made in the present model is that the suspended-sediment-induced stratification is negligible. Equation 84 must be solved using the eddy viscosity distribution of Equation 8.

The diffusive flux F_d in Equation 84 can be expressed in terms of the eddy viscosity and concentration gradient as in Equation 86. After this is done the governing equation can be written as

$$\frac{\partial c}{\partial t} = w_f \frac{\partial c}{\partial z} + \frac{\partial}{\partial z}\left[\nu_t \frac{\partial c}{\partial z}\right] \tag{87}$$

Since both the mean and time-varying components of the concentration are of interest, separate equations for each component of the suspended sediment concentration, c, can be derived by writing c as

$$c = \bar{c} + \tilde{c}_1 + \tilde{c}_2 + \cdots \tag{88}$$

where $\bar{c}$ is the mean concentration and $\tilde{c}_1$ and $\tilde{c}_2$ are periodic components with frequencies ω_1 and ω_2, respectively. As the time variation of the concentration is forced by the wave motion, it can be expected that the frequencies of the periodic components of the concentration will be first and higher harmonics of the frequencies of the wave motion defined in Equation 37.

The definition of Equation 88 can be substituted into Equation 87. Since the fall velocity w_f and the eddy viscosity ν_t are time-invariant and Equation 87 is linear in c, separate equations for each component can be obtained. The mean and the time-varying components will be considered separately in the next two sections.

4.3.2 Solution for the Mean Concentration

Substituting the definition of Equation 88 into Equation 87 and taking the time-average results in an equation for the mean concentration of the form

$$0 = w_f \frac{\partial \bar{c}}{\partial z} + \frac{\partial}{\partial z}\left[\nu_t \frac{\partial \bar{c}}{\partial z}\right] \tag{89}$$

Integrating once with respect to z and using the boundary condition of no sediment flux through the free surface we obtain

$$0 = w_f \bar{c} + \nu_t \frac{\partial \bar{c}}{\partial z} \tag{90}$$

The solution of Equation 90 using the eddy viscosity distribution in Equation 8 is facilitated by the introduction of a non-dimensional vertical coordinate ζ that is defined by

$$\zeta = \frac{z}{\delta} \tag{91}$$

where δ is defined in Equation 52.

The use of this definition in Equation 90 along with the eddy viscosity model of Equation 8 results in the equation for $\bar{c}$ being obtained as

$$0 = \begin{cases} a\frac{\partial \bar{c}}{\partial \zeta} + \frac{\partial}{\partial \zeta}\left[\zeta \frac{\partial \bar{c}}{\partial \zeta}\right] & \zeta < \alpha \\ a\frac{\partial \bar{c}}{\partial \zeta} + \alpha \frac{\partial^2 \bar{c}}{\partial \zeta^2} & \alpha < \zeta < \alpha/\epsilon \\ a\frac{\partial \bar{c}}{\partial \zeta} + \epsilon \frac{\partial}{\partial \zeta}\left[\zeta \frac{\partial \bar{c}}{\partial \zeta}\right] & \alpha/\epsilon < \zeta \end{cases} \tag{92}$$

where

$$a = \frac{w_f}{\kappa u_{*cw}} \tag{93}$$

is the non-dimensional fall velocity.

The two commonly used bottom boundary conditions for the suspended sediment concentration are discussed in Chapter 4.4 and the reference concentration formulation selected for this study. Therefore the solution for the concentration given here will be in terms of a reference concentration specified at some level near the bottom. Obtaining the solution in terms of a specified near-bottom flux instead of a specified concentration is a straightforward derivation.

The boundary condition for the mean concentration $\bar{c}$ is that

$$\bar{c} = \bar{c}_r \quad \text{at} \quad \zeta = \zeta_r = \frac{z_r}{\delta} \tag{94}$$

where

$\bar{c}_r$ = mean reference concentration

z_r = reference level

and ζ_r is usually smaller than α.

For $\zeta < \alpha$ the solution is obtained as

$$\bar{c} = \bar{c}_r \left[\frac{\zeta}{\zeta_r}\right]^{-a} \qquad \zeta < \alpha \tag{95}$$

For the region $\alpha < \zeta < \alpha/\epsilon$ the solution to Equation 92 is

$$\bar{c} = A_1 e^{-a\zeta/\alpha} \tag{96}$$

where A_1 is a constant. After matching with Equation 95 at the level of $\zeta = \alpha$ to obtain A_1, the solution is found to be

$$\bar{c} = \bar{c}_r \left[\frac{\alpha}{\zeta_r e}\right]^{-a} e^{-a\zeta/\alpha} \qquad \alpha < \zeta < \alpha/\epsilon \tag{97}$$

For $\zeta > \alpha/\epsilon$ the solution is

$$\bar{c} = A_2(\zeta)^{-a/\epsilon} \tag{98}$$

where A_2 is a constant to be determined by matching with Equation 97 at the level $\zeta = \alpha/\epsilon$. The solution is obtained as

$$\bar{c} = \bar{c}_r \left[\frac{\alpha}{\zeta_r e}\right]^{-a} \left[\frac{e\epsilon}{\alpha}\right]^{-a/\epsilon} (\zeta)^{-a/\epsilon} \qquad \alpha/\epsilon < \zeta \tag{99}$$

A typical mean concentration profile, where a = 0.63, $\delta = 2$ cm, and $\epsilon = 0.33$, is shown in Figure 19a. As with the current profile this profile has three regions. For a pure wave flow field only the two lower sections of the profiles would be seen, i.e., according to the theory presented here the second section, linear in Figure 19a, would extend from the level $z = \alpha\delta$ upward.

4.3.3 Solution for the Periodic Components of the Concentration

The solution of the governing equation for a time-varying component, $\tilde{c}_1$, with frequency ω_1, will be derived in this section. In order to keep the solution as general as possible ω_1 is allowed to be different from the representative frequency, ω_r, that was used to define the length scale δ in Equation 52.

The equation for $\tilde{c}_1$ is found to be

$$\frac{\partial \tilde{c}_1}{\partial t} = w_f \frac{\partial \tilde{c}_1}{\partial z} + \frac{\partial}{\partial z}\left[\nu_t \frac{\partial \tilde{c}_1}{\partial z}\right] \tag{100}$$

The boundary conditions for this equation are

$$\tilde{c}_1 = \tilde{c}_{1r} = \mathrm{Re}\{c_{1r} e^{i\omega_1 t}\} \quad \text{at} \quad z = z_r \tag{101}$$

and the condition of no sediment flux through the free surface. In practice this second condition is equivalent to requiring that $\tilde{c}_1$ go to zero as z becomes very large.

As $\tilde{c}_1$ is a periodic quantity the solution of Equation 100 is facilitated by defining $\tilde{c}_1$ as

$$\frac{\tilde{c}_1}{c_{1r}} = \mathrm{Re}[c_1(z) e^{i\omega_1 t}] \tag{102}$$

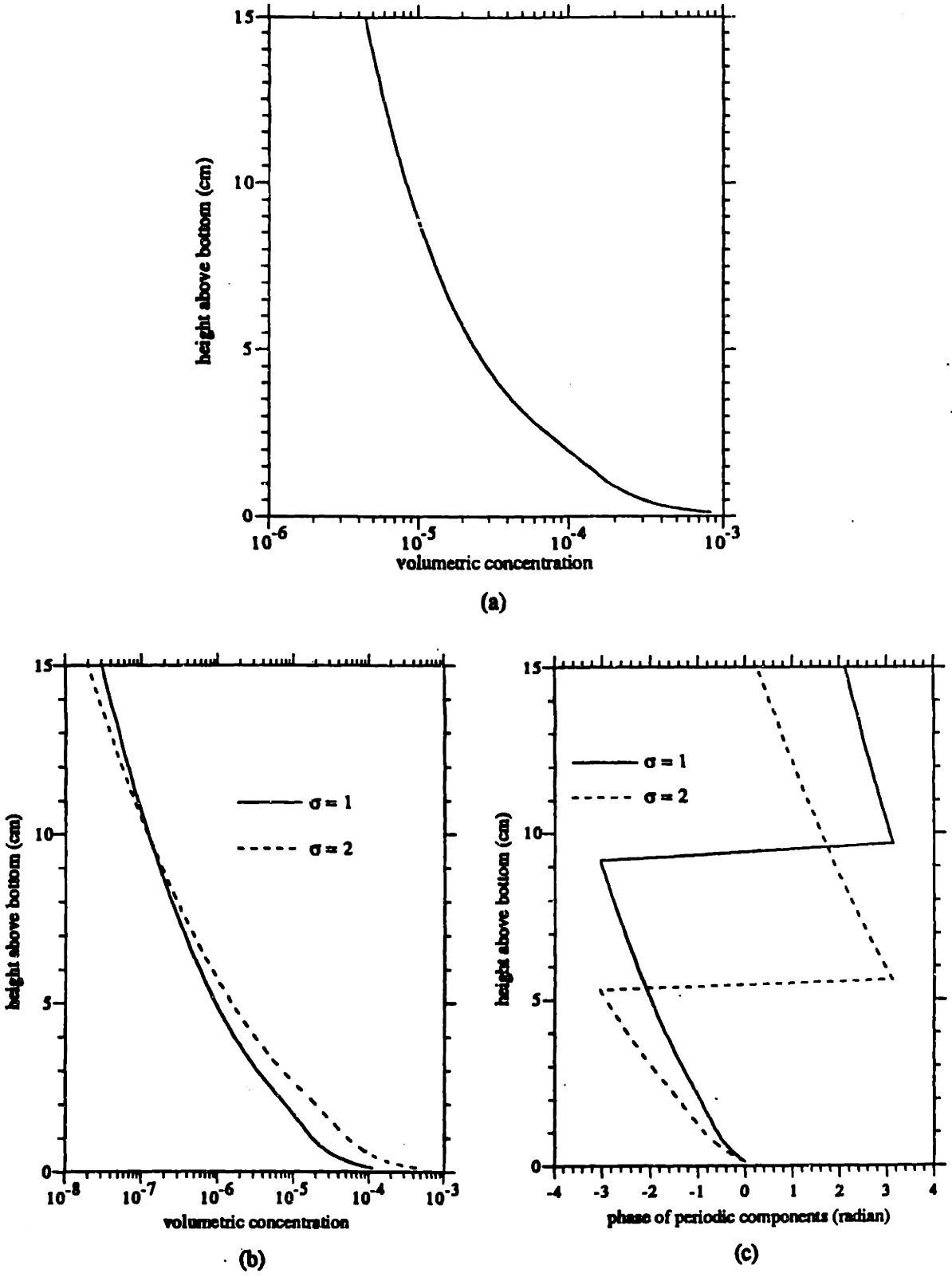

Figure 19. Profiles of a) mean concentration, b) magnitude of periodic concentration components with $\sigma = 1$ and $\sigma = 2$, and c) phase of periodic components for an example where a = 0.63, $\delta = 2$ cm, and $\epsilon = 0.33$

where c_1 is a complex function of z. Equation 101 arises from the reference concentration formulation that is selected as the bottom boundary condition in Chapter 4.4.

Using this definition in Equation 100 the governing equation for c_1 is found to be

$$i\omega_1 c_1 = w_f \frac{\partial c_1}{\partial z} + \frac{\partial}{\partial z}\left[\nu_t \frac{\partial c_1}{\partial z}\right] \tag{103}$$

with boundary conditions

$$c_1 = 1 \quad \text{at} \quad z = z_r \tag{104}$$

and

$$c_1 \to 0 \quad \text{as} \quad z \to \infty \tag{105}$$

The definition of c_1 in Equation 102 means that the phase of c_1 is the phase with respect to the phase of $\tilde{c}_{1r}$, the reference value for this component.

Using the eddy viscosity distribution of Equation 8 and the non-dimensional vertical coordinate ζ given in Equation 91 the equations governing c_1 are found to be

$$i\sigma c_1 = \begin{cases} a\frac{\partial c_1}{\partial \zeta} + \frac{\partial}{\partial \zeta}\left[\zeta \frac{\partial c_1}{\partial \zeta}\right] & \zeta < \alpha \\ a\frac{\partial c_1}{\partial \zeta} + \alpha \frac{\partial^2 c_1}{\partial \zeta^2} & \alpha < \zeta < \alpha/\epsilon \\ a\frac{\partial c_1}{\partial \zeta} + \epsilon \frac{\partial}{\partial \zeta}\left[\zeta \frac{\partial c_1}{\partial \zeta}\right] & \alpha/\epsilon < \zeta \end{cases} \tag{106}$$

where

$$\sigma = \frac{\omega_1}{\omega_r} \tag{107}$$

and the boundary conditions are

$$c_1 = 1 \quad \text{at} \quad \zeta = \zeta_r = \frac{z_r}{\delta} \tag{108}$$

and

$$c_1 \to 0 \quad \text{as} \quad \zeta \to \infty \tag{109}$$

Equation 106 must be solved in each region and the solutions matched at the levels $\zeta = \alpha$ and $\zeta = \alpha/\epsilon$. For the region $\zeta < \alpha$ the equation is

$$\zeta^2\frac{\partial^2 c_1}{\partial \zeta^2} + \zeta(1+a)\frac{\partial c_1}{\partial \zeta} - i\sigma\zeta c_1 = 0 \tag{110}$$

Comparing this equation with Equation 127 on page 152 of Hildebrand (1976) we see that the solution can be written as

$$c_1 = \zeta^{-a/2} Z_a(i^{3/2}2\sqrt{\sigma\zeta}) \tag{111}$$

where Z_a is the generalized Bessel function of order a. The solution can be expressed conveniently in terms of Kelvin functions as

$$c_1 = A\zeta^{-a/2}[\mathrm{ker}_a(2\sqrt{\sigma\zeta}) + i\mathrm{kei}_a(2\sqrt{\sigma\zeta})] + B\zeta^{-a/2}[\mathrm{ber}_a(2\sqrt{\sigma\zeta}) + i\mathrm{bei}_a(2\sqrt{\sigma\zeta})] \tag{112}$$

where A and B are constants.

For the region $\alpha < \zeta < \alpha/\epsilon$ the equation is

$$\alpha\frac{\partial^2 c_1}{\partial \zeta^2} + a\frac{\partial c_1}{\partial \zeta} - i\sigma c_1 = 0 \tag{113}$$

and the solution can be written as

$$c_1 = Ce^{r_+\zeta} + De^{r_-\zeta} \tag{114}$$

where C and D are constants and r_+ and r_- are found from

$$r_\pm = \frac{-a \pm \sqrt{a^2+4i\sigma\alpha}}{2\alpha} \tag{115}$$

For $\zeta > \alpha/\epsilon$ the equation is

$$\zeta^2\frac{\partial^2 c_1}{\partial\zeta^2} + \zeta\left[1+\frac{a}{\epsilon}\right]\frac{\partial c_1}{\partial\zeta} - \frac{i}{\epsilon}\sigma\zeta c_1 = 0 \tag{116}$$

and the solution can be written in terms of Kelvin functions as

$$\begin{aligned} c_1 = {} & E\zeta^{-a/2\epsilon}[\mathrm{ker}_{a/\epsilon}(2\sqrt{\sigma\zeta/\epsilon}) + \mathrm{ikei}_{a/\epsilon}(2\sqrt{\sigma\zeta/\epsilon})] \\ & + F\zeta^{-a/2\epsilon}[\mathrm{ber}_{a/\epsilon}(2\sqrt{\sigma\zeta/\epsilon}) + \mathrm{ibei}_{a/\epsilon}(2\sqrt{\sigma\zeta/\epsilon})] \end{aligned} \tag{117}$$

where E and F are constants.

Using the boundary condition that c_1 should vanish as z becomes very large and noting that the functions ber and bei blow up at large arguments (Abramowitz and Stegun, 1971) we obtain

$$F = 0 \tag{118}$$

The remaining constants A, B, C, D, and E must be obtained by using the boundary condition at $\zeta = \zeta_r$ and matching the concentrations and concentration gradients at the levels $\zeta = \alpha$ and $\zeta = \alpha/\epsilon$.

Using the boundary condition of Equation 108 we have

$$\begin{aligned} & A\zeta_r^{-a/2}[\mathrm{ker}_a(2\sqrt{\sigma\zeta_r}) + \mathrm{ikei}_a(2\sqrt{\sigma\zeta_r})] \\ & \quad + B\zeta_r^{-a/2}[\mathrm{ber}_a(2\sqrt{\sigma\zeta_r}) + \mathrm{ibei}_a(2\sqrt{\sigma\zeta_r})] = 1 \end{aligned} \tag{119}$$

The solution of Equation 112, valid for the region $\zeta < \alpha$, is used for the application of the boundary condition to obtain Equation 119 because it is assumed that $\zeta_r < \alpha$. If $\zeta_r > \alpha$ Equation 119 should be replaced by a similar equation obtained by applying the boundary condition of Equation 108 together with the appropriate solution for c_1.

Matching the concentrations at $\zeta = \alpha$ from Equations 112 and 114 we have

$$A(\alpha)^{-a/2}[\mathrm{ker}_a(2\sqrt{\sigma\alpha}) + \mathrm{ikei}_a(2\sqrt{\sigma\alpha})] + B(\alpha)^{-a/2}[\mathrm{ber}_a(2\sqrt{\sigma\alpha}) + \mathrm{ibei}_a(2\sqrt{\sigma\alpha})] - Ce^{r_+\alpha} - De^{r_-\alpha} = 0 \quad (120)$$

Matching the concentration gradients at $\zeta = \alpha$ from Equations 112 and 114 we have

$$A\alpha^{-a/2-1}\left\{\alpha^{1/2}\sqrt{\sigma}[\mathrm{ker}'_a(2\sqrt{\sigma\alpha}) + \mathrm{ikei}'_a(2\sqrt{\sigma\alpha})] - \frac{a}{2}[\mathrm{ker}_a(2\sqrt{\sigma\alpha}) + \mathrm{ikei}_a(2\sqrt{\sigma\alpha})]\right\} + B\alpha^{-a/2-1}\left\{\alpha^{1/2}\sqrt{\sigma}[\mathrm{ber}'_a(2\sqrt{\sigma\alpha}) + \mathrm{ibei}'_a(2\sqrt{\sigma\alpha})] - \frac{a}{2}[\mathrm{ber}_a(2\sqrt{\sigma\alpha}) + \mathrm{ibei}_a(2\sqrt{\sigma\alpha})]\right\} - r_+Ce^{r_+\alpha} - r_-De^{r_-\alpha} = 0 \quad (121)$$

where the primes, i.e., ker′, denote the derivatives of the functions with respect to their arguments.

Equating the concentrations from Equations 114 and 117 at the level $\zeta = \alpha/\epsilon$

$$Ce^{r_+\alpha/\epsilon} + De^{r_-\alpha/\epsilon} - E\left[\frac{\alpha}{\epsilon}\right]^{-a/2\epsilon}\left[\mathrm{ker}_{a/\epsilon}\left[\frac{2\sqrt{\sigma\alpha}}{\epsilon}\right] + \mathrm{ikei}_{a/\epsilon}\left[\frac{2\sqrt{\sigma\alpha}}{\epsilon}\right]\right] = 0 \quad (122)$$

Equating the concentration gradients at this level we have

$$Cr_+e^{r_+\alpha/\epsilon} + Dr_-^{r_-\alpha/\epsilon} - E\left\{\frac{\sqrt{\sigma}(\alpha/\epsilon)^{-a/2\epsilon}}{\sqrt{\alpha}}\left[\mathrm{ker}'_{a/\epsilon}\left[\frac{2\sqrt{\sigma\alpha}}{\epsilon}\right] + \mathrm{ikei}'_{a/\epsilon}\left[\frac{2\sqrt{\sigma\alpha}}{\epsilon}\right]\right] - \frac{a}{2\epsilon}\left[\frac{\alpha}{\epsilon}\right]^{-a/2\epsilon-1}\left[\mathrm{ker}_{a/\epsilon}\left[\frac{2\sqrt{\sigma\alpha}}{\epsilon}\right] + \mathrm{ikei}_{a/\epsilon}\left[\frac{2\sqrt{\sigma\alpha}}{\epsilon}\right]\right]\right\} = 0 \quad (123)$$

Equations 119 through 123 form five simultaneous equations for the five complex coefficient A, B, C, D, and E. Once these are solved the distribution of c_1 can be found in each region using Equations 112, 114, or 117. The five coefficients are functions of the parameters ζ_r, α, σ, a, and ϵ. Of these α is a fixed model parameter while ζ_r, a, and ϵ can be calculated using the results of the wave current model. σ is

the ratio of the frequency of the concentration components ω_l to the frequency ω_r that was used to define the length scale δ in Equation 52.

Figure 19b shows two profiles of the magnitude of the periodic component of concentration, where a = 0.63, $\epsilon = 0.33$, and $\delta = 2$ cm, with $\sigma = 1$ and $\sigma = 2$. The figure shows that the periodic components decrease more rapidly with increasing z than the mean concentration. The rate of decrease also increases with increase in the parameter σ (i.e., higher frequency). Figure 19c shows the phase of the two components with respect to the phase of the reference value for each component.

4.3.4 Relationship between the Solutions for the Velocity and the Concentration

As derived in Equation 43 of Chapter 2, the governing equation for a periodic velocity component, u_{wl}, with frequency ω_l is

$$\frac{d}{dz}\left[\nu_t \frac{du_{dl}}{dz}\right] - i\omega_l u_{dl} = 0 \tag{124}$$

where u_{dl} is related to u_{wl} by Equation 42.

Using the eddy viscosity distribution of Equation 7 and the non-dimensional vertical coordinate ζ defined by Equation 91 the equations for u_{dl} are found to be

$$i\sigma u_{dl} = \begin{cases} \dfrac{\partial}{\partial\zeta}\left[\zeta\dfrac{\partial u_{dl}}{\partial\zeta}\right] & \zeta < \alpha \\ \alpha\dfrac{\partial^2 u_{dl}}{\partial\zeta} & \alpha < \zeta < \alpha/\epsilon \\ \epsilon\dfrac{\partial}{\partial\zeta}\left[\zeta\dfrac{\partial u_{dl}}{\partial\zeta}\right] & \alpha/\epsilon < \zeta \end{cases} \tag{125}$$

Comparing Equations 125 and 106 shows that Equation 125 can be obtained by setting a = 0 in Equation 106. Therefore the solution for u_{dl} in the three regions can be obtained from the solution for c_l in Equations 112, 114, and 117 by setting

$a = 0$ in those three equations. The resulting equations will be the solution for u_{d1} in terms of five unknown coefficients. These coefficients must be found by using the boundary conditions and matching the solution at $\zeta = \alpha$ and $\zeta = \alpha/\epsilon$ just as for c_1.

The boundary conditions for u_{d1} are given by

$$u_{d1} = -1 \quad \text{at} \quad \zeta = \zeta_0 = \frac{z_0}{\delta} \tag{126}$$

and

$$u_{d1} \to 0 \quad \text{as} \quad \zeta \to \infty \tag{127}$$

Equations 126 and 127 are very similar to Equations 108 and 109, which are the boundary conditions for the equation governing c_1. The only difference is that u_{d1} is set to -1 at $\zeta = \zeta_0$ while c_1 is set to 1 at $\zeta = \zeta_r$. Thus the five simultaneous equations that must be solved to find the coefficients in the solution for u_{d1} will be Equations 119, 120, 121, 122, and 123 with $a = 0$ and the right-hand side of Equation 113 set to -1 instead of 1, with ζ_0 replacing ζ_r in Equation 113.

This similarity between the solutions for the velocity and concentration is useful in writing the program for the wave-current-sediment problem. If the solution for the velocity is required the only changes to the input are that $a = 0$, the reference level is given as ζ_0 instead of ζ_r, and a flag that sets the right-hand side to the correct value.

4.4 The Bottom Boundary Condition for Sediment in Suspension

The boundary conditions of Equations 94 and 108, along with the condition that the concentration should vanish at large z, mean that all the components of the concentration are scaled by the specified reference value near the bottom. This reference value reflects the complicated interaction of the fluid motion with the

movable bed—a process that is not well understood. Therefore some of the equations proposed for the reference concentration will be reviewed in this section.

Equations 94 and 108 are based on the specification of the bottom boundary condition as a given value of the concentration at some reference level near the bottom. As mentioned in Chapter 4.3, another condition that has been used is a given upward sediment flux at the reference level. The first type of condition, used throughout this study, is referred to as the reference concentration condition and is expressed as

$$c = f_1(\tau,d) \quad \text{at} \quad z = z_r \tag{128}$$

while the second type, referred to as the pickup or entrainment condition, is expressed as

$$-\nu_t \frac{\partial c}{\partial z} = f_2(\tau,d) \quad \text{at} \quad z = z_r \tag{129}$$

Equations 128 and 129 imply that either the concentration or the sediment flux at the level z_r is a function of parameters such as the bottom shear stress and the grain diameter. Such formulations of the boundary condition include the unstated assumption that the entire supply of sediment indicated by these equations is actually available from the bed. Therefore such boundary conditions are not suitable when the supply of a particular size class is limited or when suspension of sediment sizes that are not present in the local bed material are considered.

In Equations 128 and 129 the functions f_1 and f_2 indicate that the specified concentration or flux is a function of the shear stress, τ, and the grain diameter, d. The choice of a formulation for the bottom boundary condition has been the subject of discussion in the recent literature. Simple models of bed load processes, such as

that of Madsen (1991) outlined in Chapter 4.1, indicate that Equation 128 should be used.

However, Equation 128 has been criticized because it implies that the reference concentration will vanish if the function on the right-hand side vanishes. This implication is not physically realistic as there will be a continual supply of sediment falling from above, thus ensuring a non-zero value of concentration at the reference level.

Soulsby (1991) has examined the difference in the solution for the concentration when these two formulations are applied by using a simple constant-in-depth eddy viscosity model. He showed that the mean concentration profile in steady flow does not depend on which formulation is used.

For wave-current flow Soulsby (1991) assumed a simple linear relation with the shear stress for the functions f_1 and f_2 in Equation 128 and 129. He obtained solutions for the mean and time-varying concentration using each of these equations as a boundary condition, for the case of a non-reversing shear stress. By matching the solution for the mean concentration Soulsby (1991) obtained a relation between these two equations.

However, when this relation was used for the time-varying concentration it was found that the concentration obtained using the reference concentration formulation was always greater than the concentration obtained using the pick-up condition, by a constant factor. This factor was found to increase with increasing frequency and eddy viscosity and decrease with increasing sediment fall velocity.

The difference in the solution for the periodic components can be explained by considering the physical meaning of Equations 128 and 129. Equation 128 implies

that the concentration at $z = z_r$ changes as a function of the shear stress. The amount entrained into the flow depends only on the value of the eddy viscosity, i.e., the ability of the turbulence to entrain sediment. Equation 129 on the other hand implies that the entrainment itself is a function of the shear stress.

Matching the solution for the mean concentration implies that given enough time (approaching zero frequency) the quantity of sediment supplied by Equation 129 is the same as the quantity set by Equation 128. However, when considering periodic (non-zero frequency) components the flow will not have sufficient time to entrain as much sediment from the pick-up condition as from the reference concentration condition. Thus the periodic components will always be smaller when Equation 129 is used, with the difference increasing with the frequency. Increased eddy viscosity and decreased fall velocity will also tend to increase this difference because these factors allow the flow to take up greater quantities of sediment through Equation 128, while Equation 129 limits the supply of sediment.

Thus the work of Soulsby (1991) shows that while the two formulations can be matched for the mean concentration, they will then give different results for the periodic components. Equation 128 has been selected as the bottom boundary condition for the model presented in this report. This selection is based on the conceptual bed load model of Madsen (1991) which indicates that the shear stress affects the sediment concentration in the bed load layer, rather than the flux of sediment from this layer.

It is probable that this equation will show a lower reference concentration than actually exists during the interval where the shear stress decreases due to the effect of sediment settling from above. This error will definitely occur whenever the

predicted reference concentration is zero. However this error will be balanced by the error involved in expressing the exact reference concentration as the sum of a few sinusoidal components. As an example, the approximation to the reference concentration in Figure 20 does not vanish while the exact value does.

The diffusion equation used to describe the suspended sediment profile is based on the assumption that grain-grain collisions are negligible. This is clearly not valid in the region very close to the bed where the concentration is high and the transport is due primarily to rolling and small jumps rather than to the suspended grains being carried by the fluid. As a result the transport process has long been considered as taking place due to two mechanisms—bed load transport which takes place very near the bed and suspended sediment transport which takes place in the main body of the flow. The boundary condition for the diffusion equation is applied at the border between the two regions. Since the separation of the flow into these two regions is somewhat artificial this border is not well defined and therefore it must be specified and used consistently.

Since the sediment that is brought into suspension is entrained from the bed load layer it is apparent that the reference concentration must depend on processes in this layer. Most of the theoretical development and experimental verification for the reference concentration has been done for steady open channel flow. The most commonly used formulation for unsteady flows is simply an extension of a steady flow approach. Therefore the development of the reference concentration for steady flow will be discussed first.

4.4.1 Reference Concentration for Steady Flows

As mentioned above, it is natural to expect the magnitude of the reference concentration, $\bar{c}_r$, for the suspended sediment to depend on the magnitude of the bed transport. Einstein (1950) suggested that $\bar{c}_r$ for steady channel flow be defined by the average concentration in the bed load layer, i.e., by

$$\bar{c}_r = \frac{q_B}{h_T u_B} \tag{130}$$

where q_B is the bed load transport, h_T the height of the bed load layer, and u_B the velocity of the grains in the bed layer. He used his own expressions for these quantities to derive a formulation for the reference concentration.

However Equation 130 can be used with any bed load transport formulation that calculates the three quantities on the right-hand side. For example the bed load load formulation of Yalin (1963) assumes that the concentration in the bed load layer is proportional to S' where S' is a measure of the excess bottom shear stress and is given by

$$S' = \frac{\psi'}{\psi_{cr}} - 1 \tag{131}$$

where as ψ' is the Shields parameter based on the skin friction shear stress and ψ_{cr} is the critical Shields parameter for the initiation of motion.

Smith (1977) used Yalin's bed load transport equation in Equation 130 to derive

$$\bar{c}_r = \frac{c_b \gamma_0 S'}{1 + \gamma_0 S'} \tag{132}$$

where c_b is the volume concentration of a loose sand bed and γ_0 is an undetermined constant that is known as the resuspension coefficient. The value of c_b is usually taken as 0.65. The term in the denominator was included in order to insure that $\bar{c}_r$

does not exceed c_b when S′ becomes very large. However since γ_0 is found to $O(10^{-4}–10^{-3})$ and S′ is O(10) Equation 132 is effectively a linear relationship between S′ and the reference concentration.

Smith and McLean (1977) used velocity and suspended sediment measurements from the Columbia River to derive a value of 2.4×10^{-3} for γ_0. They set the reference level for the application of Equation 132 to be equal to z_0 where $z_0 = k_n/30$ with k_n being the Nikuradse roughness of the sand grains. If Equation 132 is to be used with their value of γ_0 it is important that this same reference level be used.

This formulation of the reference concentration has been widely adopted and many researchers have attempted to verify Equation 132 using data from various types of flows. These comparisons have resulted in γ_0 values ranging from $O(10^{-5}–10^{-2})$. Several attempts to verify Equation 132 using steady flow data from the laboratory and the field were reviewed by Zettler (1991). He found that some of the analyses done had been inconsistent with the Smith and McLean method in that different reference levels had been used to determine γ_0 and in one case the total bottom shear stress was used instead of the skin friction shear stress.

A consistent analysis of some steady flow data was attempted by Zettler (1991). He found that the data did not support the simple relationship of Equation 132. He then conducted a regression analysis allowing the reference concentration to be a function of both the grain size and S′. The reference level was taken as 7d where d is the grain diameter. The results of the analysis were plotted as curves of reference concentration against S′ for each grain size. It was found that for grain sizes less than about 0.1 mm the relationship between $\bar{c}_r$ and S′ was approximately linear with a constant of proportionality that was 3×10^{-4}, 4×10^{-3}, and 2×10^{-2} for grain diameters of 0.04 mm, 0.07 mm, and 0.1 mm, respectively. For grains sizes greater

than 0.1 mm the behavior is more complicated with $\bar{c}_r$ decreasing with S' for small values of S'. It should be noted that for the larger grain sizes the experimental values of S' were not very large.

The expressions for the bed load transport and the height of the saltating layer derived in the saltation model of Madsen (1991) can be substituted in Equation 132 to derive a formula for the reference concentration. The relation obtained in this fashion shows that the reference concentration is proportional to S'. The constant of proportionality in this equation is weakly dependent on S', and for moderate to large values of the ratio ψ'/ψ_{cr} the constant is found to be in the range 0.6–1.0×10^{-2}. The height of the saltating layer for these conditions is estimated to be in the range 3–10 d.

In summary, it can be said that while the data do not validate the general applicability of Equation 132, both the data and the conceptual bed load model of Madsen (1991) support the idea of a linear relationship between the non-dimensional excess shear stress, S', and the reference concentration with a constant of proportionality that may depend on the grain diameter. Therefore, it is proposed to adopt a simplified form of Equation 132 as the reference concentration, i.e.,

$$\bar{c}_r = c_b \gamma_0 S' \tag{133}$$

for the model presented in this report. The value of the resuspension coefficient γ_0 must be determined using field measurements of suspended sediment. The reference level will be taken as 7 d. This reference level is supported by the result for the height of the saltating layer in the bed load model and is also more realistic than the level z_0 used by Smith and Mclean (1977) because z_0 may be less than the grain diameter when the equivalent roughness is small.

4.4.2 Mean Reference Concentration under Waves

The discussion so far has considered only steady flows. Glenn and Grant (1987) suggested that the Smith and McLean equation could be used to calculate the mean reference concentration for wave and wave-current conditions. This was based on the demonstration by Grant and Madsen (1982) that sand grains rolling on the bottom, i.e., grains in the bed load layer, would respond to changes in the near-bottom velocity with a time scale that was much smaller than the wave period. Therefore Glenn and Grant (1987) assumed that the instantaneous reference concentration, $c_r(t)$, was given by

$$c_r(t) = \begin{cases} \dfrac{c_b \gamma_0 S'(t)}{1 + \gamma_0 S'(t)} & S'(t) > 0 \\ 0 & S'(t) < 0 \end{cases} \tag{134}$$

where $S'(t)$ was calculated from Equations 82 and 131 using the instantaneous skin friction shear stress. The mean concentration was obtained by averaging this value over a wave period. They set the reference level at z_0 and set γ_0 to be 0.002, a value that was based on experimental data from the laboratory.

There have been some attempts to verify this reference concentration using data from field experiments. Drake and Cacchione (1989) reported the results of a field experiment conducted in about 90 m depth on the California shelf. The mean sediment size ranged from 0.016 to 0.024 mm. Velocity was measured 20, 50, 70, and 100 cm above the bottom and suspended sediment concentrations were measured 190 cm above the bottom using optical methods, and the pressure was measured at a height of 200 cm. The wave-current model of Grant and Madsen (1979) and the suspended sediment model of Glenn and Grant (1987) were used to analyze the data and predict the reference concentrations and shear stresses.

The analysis resulted in γ_0 values ranging from 2×10^{-5} to 3×10^{-4}. The observed value of γ_0 was seen to decrease with increasing S'. Drake and Cacchione attributed this to armoring of the bed and to increasing substrate cohesiveness. This variation could equally well be explained by saying that $\bar{c}_r$ is proportional to $S'^{0.9}$ with a constant of about 1×10^{-4}. However the possible sources of error in these estimates, such as the effect of sediment sorting and flocculation and the fact that a single measured concentration is extrapolated to the near-bed level, make such speculation unwarranted.

Similar experiments are reported by Wiberg and Smith (1983) and Shi et al. (1985). Using the same models for the wave-current-sediment interaction results in estimates for γ_0 of 1×10^{-5} and $1.4–4.4\times10^{-4}$ from the two studies. The field experiment reported by Vincent and Green (1990), which will be discussed in greater detail later, yielded estimates of $1–1.7\times10^{-4}$ for γ_0 but with the reference level set at 2 cm above the bed instead of at z_0 as recommended by Glenn and Grant (1987).

As far as the verification of the mean reference concentration recommended by Glenn and Grant (1987) is concerned the results of these field experiments are mixed. On the one hand the trend of decreasing γ_0 with S' observed by Drake and Cacchione is evidence that it is not perfect. However, when considering the widely varying conditions of measurement and the possible sources of error involved, it is encouraging that the estimates of γ_0 fall in the range $1\times10^{-5}–4.5\times10^{-4}$.

A major weakness of the first three field experiments is that only a single measurement of the sediment concentration is made and that this is at an elevation above the bottom much larger than the wave boundary layer length scale. This results in the measured concentration being multiplied by a very large factor to

obtain the near-bottom value, a procedure which would magnify uncertainties in parameters such as the fall velocity and grain diameter. The experiment reported by Vincent and Green (1990) had concentration measurements every 1 cm above the bottom. In theory each of these measurements could be used to estimate a value of γ_0. However the values reported by them are based only on the measured concentration at a height of 2 cm.

4.4.3 Time-Varying Reference Concentration under Waves

The discussion so far has considered only the reference value for the mean component of the concentration. In order to solve the equations formulated in this chapter a reference concentration is required for the periodic components as well. When specifying the reference value for these components the ratio of the time-varying component to the mean component is of interest in addition to the absolute value of the components because it is this ratio that will determine the significance of the time-varying concentration in the calculation of the mean sediment flux.

Madsen (1991) showed that the motion of the sediment grains very near the bottom could be assumed to react instantaneously to changes in the external flow. Therefore Equation 133, which was selected for the calculation of the reference concentration in steady flows, can be extended to the case of unsteady flow in the form

$$c_r(t) = \begin{cases} c_b \gamma_0 S'(t) & S' > 0 \\ 0 & S' < 0 \end{cases} \tag{135}$$

where $c_r(t)$ is the instantaneous reference concentration and $S'(t)$ is the instantaneous value of the non-dimensional excesss shear stress given by

$$S'(t) = \frac{|\psi'(t)| - \psi_{cr}}{\psi_{cr}} \tag{136}$$

In Equation 136 ψ_{cr} is the critical Shields parameter for the initiation of motion and $\psi'(t)$ is the Shields parameter based on the instantaneous skin friction shear stress, $\tau'(t)$, defined as

$$\psi'(t) = \frac{\tau'(t)}{\rho(s-1)gd} \tag{137}$$

4.4.4 Formulation of the Reference Concentration for the Periodic Components

The skin friction shear stresses calculated using the procedure described in the preceding section can be used in Equation 135 to obtain the time-varying reference concentration. However, the solution to the governing equation derived in the first section of this part required the specification of the reference concentration as a reference value for each component of the concentration and not as an arbitrary function of time. The derivation of the reference values for each component will be done in this section. The situation considered here will be the case where wave asymmetry is simulated by two wave components in phase with each other, one having twice the frequency of the other.

Equations 135 and 136 can be combined to write the instantaneous reference concentration as

$$c_r(t) = \begin{cases} \dfrac{c_b\gamma_0(|\psi'(t)|-\psi_{cr})}{\psi_{cr}} & |\psi'(t)| > \psi_{cr} \\ 0 & |\psi'(t)| < \psi_{cr} \end{cases} \tag{138}$$

$\psi'(t)$ is the Shields parameter based on the instantaneous skin friction shear stress which can be written as

$$|\psi'(t)| = \frac{|\hat{\tau}'(t)|}{\rho(s-1)gd} \tag{139}$$

where $|\hat{\tau}'(t)|$ is the magnitude of the instantaneous skin friction shear stress vector and is given by

$$|\hat{\tau}'(t)| = [\tau_w'(t)^2 + 2\tau_w'(t)\tau_c'\cos\phi_{cw} + \tau_c'^2]^{1/2} \tag{140}$$

with $\tau_w'(t)$ being the instantaneous wave skin friction shear stress, τ_c' the current skin friction shear stress, and ϕ_{cw} the angle between the waves and the current.

The hydrodynamic model was extended to include the case of many wave components in Chapter 2. Once the parameters u_{*cw} and δ are defined it was shown that the individual wave shear stresses and phases could be obtained from Equation 46. As outlined in Chapter 4.2 the skin friction shear stresses are obtained by using the grain diameter as the equivalent roughness with the current specified as the calculated mean velocity at the level $z = \delta$. For the case of two waves in phase with each other $\tau_w'(t)$ can be written as

$$\tau_w'(t) = \tau_{w1}' \cos(\omega t+\phi_{b1}) + \tau_{w2}' \cos(2\omega t+\phi_{b2}) \tag{141}$$

where τ_{w1}' and τ_{w2}' are the wave skin friction shear stresses for each component and ω is the frequency of the principal component.

Substituting from Equations 139, 140, and 141 into Equation 132, the instantaneous reference concentration, $c_r(t)$, can be written as

$$c_r(t)=\begin{cases} c_b\frac{\gamma_0\psi_{w1}'}{\psi_{cr}}[([\cos\theta + r_\tau\cos(2\theta+\phi)]^2 \\ \quad + 2\mu'^2[\cos\theta + r_\tau\cos(2\theta+\phi)]\cos\phi_{cw} \\ \quad + \mu'^4)^{1/2} - r_\varphi] & |\psi'(t)| > \psi_{cr} \\ 0 & |\psi'(t)| < \psi_{cr} \end{cases} \tag{142}$$

where ψ_{w1}' is the Shields parameter based on τ_{w1}', μ' is given by

$$\mu'^2 = \frac{\tau_c'}{\tau_{w1}'} \tag{143}$$

and r_1, ϕ, and r_φ by

$$r_1 = \frac{\tau_{w2}'}{\tau_{w1}'} \tag{144}$$

$$\phi = \phi_{b2} - \phi_{b1} \tag{145}$$

and

$$r_\varphi = \frac{\psi_{cr}}{\psi_{w1}'} \tag{146}$$

Equation 142 gives the time-variation of the reference concentration. In the formulation presented here we consider only two wave components, with frequencies ω and 2ω. Therefore, the only components of the concentration that contribute to the time-averaged sediment flux will be those with the same frequencies. These components can be extracted by approximating the instantaneous reference concentration, $c_r(t)$, by

$$c_r(t) \approx \frac{c_b \gamma_0 \psi_{w1}'}{\psi_{cr}}(\bar{r} + r_1\cos(\theta+\phi_1) + r_2\cos(2\theta+\phi_2)) \tag{147}$$

where θ is the phase of the shear stress τ_{w1}' and is given by

$$\theta = \omega t + \phi_{b1} \tag{148}$$

The coefficients $\bar{r}$, r_1, ϕ_1, r_2, ϕ_2 can be found by expanding Equation 142 as a Fourier series. In the case considered here ϕ in Equation 145 is very small so that τ_{w1}' and τ_{w2}' in Equation 141 are nearly in phase. The result is that ϕ_1 and ϕ_2 in Equation 147 are negligible, i.e., the coefficient of $\sin\theta$ and $\sin2\theta$ from the Fourier expansion are negligible. However, if a different formulation, for example one based on the measurements shown in Figure 1, is used where the peaks of $c_r(t)$ do not

coincide with the peaks of τ_{w1}', ϕ_1, and ϕ_2 may be important. In this case r_1 and r_2 can be represented by complex numbers to include these phase differences.

The three term Fourier expansion of the instantaneous reference concentration of Equation 147 is compared to the exact value given by Equation 142 in Figure 20. The figure shows the reference concentration, normalized by the term $(c_b \gamma_0 \psi_{w1}')/\psi_{cr}$, as a function of θ, the phase of τ_{w1}'. In this example μ_1' is 0.35 and the ratios r_φ and r_t are 0.27 and 0.25 respectively, while the coefficients $\bar{r}$, r1, and r2 are found to be 0.41, 0.17, and 0.36, respectively.

The figure shows that the three term approximation of Equation 147 is quite a good approximatio⁻ of the exact form of Equation 142. The values of the Fourier coefficients show that the periodic components of the reference concentration are comparable to the mean component, with the reference value for the component of frequency 2ω found to be larger than that for the component of frequency ω. These differences are due to the assumed time variation of the reference concentration in Equation 142. Since the shear stress $|\tau'(t)|$ has two peaks for each wave cycle there will be a pronounced component of frequency 2ω. A component of frequency ω can exist only if there is some asymmetry in the shear stress. In this case, where the wave asymmetry is simulated by two waves, the component of frequency ω is caused both by the wave asymmetry and by the presence of a current. For a purely sinusoidal wave motion, with no current, there will not be a concentration component with the frequency of the wave motion.

The procedure outlined in this section forms the link between the hydrodynamic and sediment problems. The instantaneous bottom shear stress obtained from the hydrodynamic problem is converted into the instantaneous reference concentration using Equation 138. The reference concentration can then be approximated by the

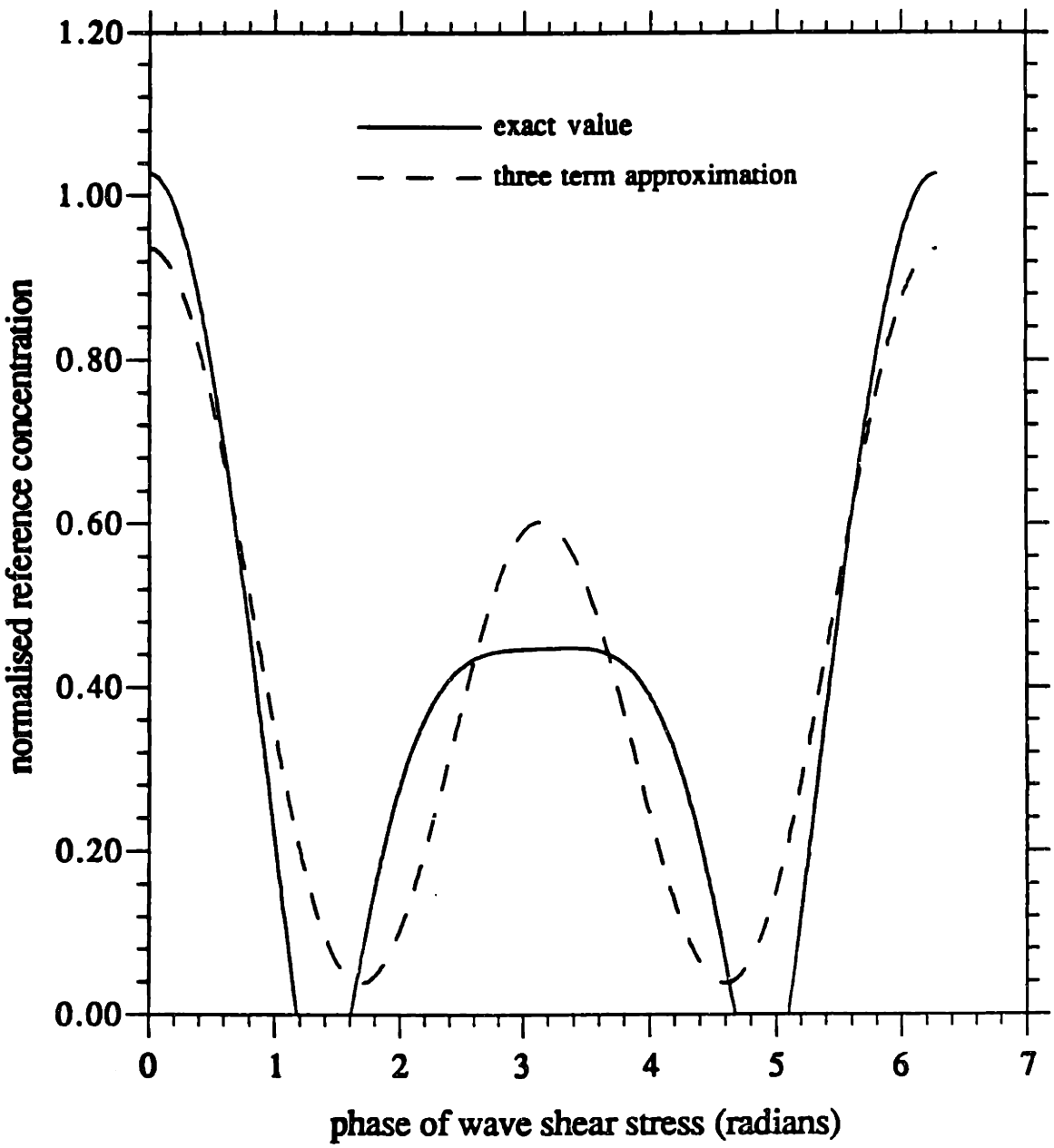

Figure 20. Comparison of the instantaneous reference concentration of Equation 142 with its three-term approximation in Equation 147

required number of sinusoidal components to obtain the reference value for each component. These values can then be used in the solution derived earlier in this chapter to obtain the concentration at any depth.

4.5 Summary of Model Development and Calculations

The development in this chapter has built on the wave-current and roughness models of the two preceding chapters to derive a complete sediment transport model. The required input parameters are the wave, current, sediment, and flow specifications. The wave motion is specified by one or more sinusoidal components with the magnitude of the near-bottom velocity, frequency, and phase as the parameters for each component. The current is usually specified by a mean velocity at a certain elevation and the angle made by this velocity with the wave direction. The sediment is specified by a grain diameter and specific gravity and if available, a fall velocity. The flow is specified by the depth and the density and kinematic viscosity of the fluid.

The principal steps involved in the calculation of the transports are given in the flow chart in Figure 21. The figure shows that the hydrodynamic problem is solved first by iteration until the variables have converged. The solution of the wave-current problem for the values of u_{*c} and u_{*cw} for a given value of the roughness, k_n, is itself an iterative process that is described by Wikramanayake (1989). Once the hydrodynamic problem is solved the velocity field and skin friction shear stresses will be known. These skin friction shear stresses can be then used in a formulation similar to that outlined in the preceding section to obtain the reference values of the various components of the concentration.

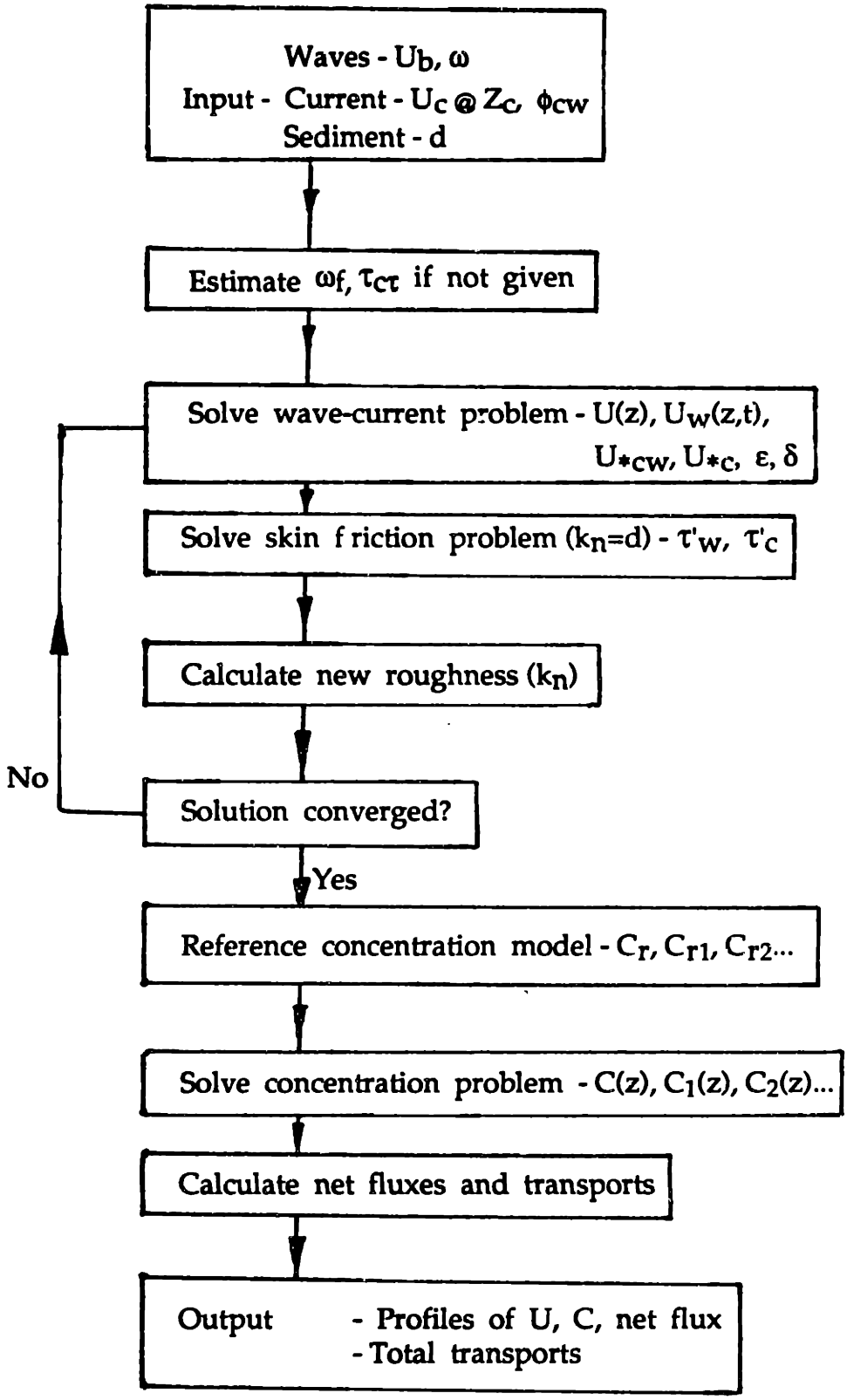

Figure 21. Flow chart of the sediment transport model

Once the concentration and velocity distribution are known the net flux of sediment, $\vec{T}$, can be found as

$$\vec{T} = \vec{T}_w + \vec{T}_c \tag{149}$$

where $\vec{T}_w$ is net the flux due to the time-varying components of velocity and concentration while $\vec{T}_c$ is the flux due to the mean components. $\vec{T}_w$ and $\vec{T}_c$ are denoted as vectors in Equation 149 because the transport caused by the wave and current motions will be in the directions of the wave and current velocity vectors, respectively.

$\vec{T}_w$ can be found from

$$\vec{T}_w = \overline{\vec{\tilde{u}}\,\tilde{c}} \tag{150}$$

where $\vec{\tilde{u}}$ is the wave velocity vector and the overbar denotes the average over the period, while $\vec{T}_c$ is given by

$$\vec{T}_c = \vec{\bar{u}}\bar{c} \tag{151}$$

where $\vec{\bar{u}}$ is the current velocity vector.

The calculation of $\vec{T}_w$ in Equation 150 requires the phase difference between the velocity and concentration component. For the example in Chapter 4.4.4 this phase difference can be found because ϕ_1 and ϕ_2 in Equation 147 link the phase of the concentration component to the phase of τ_{w1}', which in turn is linked to the phase of the near-bottom wave velocity through ϕ_{b1}.

The sediment transport model thus developed is completely deterministic except for the value of the resuspension coefficient, γ_0, of Equation 135. Once this parameter is known it is possible to calculate the suspended sediment concentration

and flux, given the wave, current, and sediment characteristics. Therefore the next section will be devoted to the determination of an appropriate value for the resuspension coefficient. It must be remembered that the value of γ_0 that is derived in the next part is valid only for the reference concentration model selected in this report, i.e., Equation 135, with the reference level of 7d and the skin friction shear stress calculated as outlined above.

4.6 Determination of the Resuspension Coefficient, γ_0

The only undetermined parameter in the suspended sediment model developed in this chapter is the resuspension coefficient, γ_0. The conceptual model of bed load transport developed by Madsen (1991) indicates that γ_0 lies in the range $6-10\times10^{-3}$. However, the conceptual model was developed for the restricted conditions of relatively low shear stress, where intergranular collisions are negligible, acting on a flat bed. Since the sediment suspension model is to be used for both rippled beds and sheet flow, where grain-grain interactions are significant, a value of γ_0 that is correct for these conditions is required. Due to the complicated nature of fluid-sediment interactions, it is not possible to derive a theoretical expression for the reference concentration under these conditions. Therefore the only way to obtain a value for γ_0 is by comparing the model predictions to experimental measurements.

Experimental measurements of the suspended sediment concentration under wave and wave-current conditions have been made in the laboratory and the field. Laboratory measurements have the advantage over field measurements in that they are made under well-controlled hydrodynamic conditions. Furthermore the sediment size and grading can be controlled and the bedforms observed during the experiments.

However, the range of wave and current conditions that can be realized in the laboratory is limited by the size of the apparatus. The geometry of sand ripples generated in the laboratory was found to differ significantly from the ripple geometry observed in the field in Chapter 2. These differences appear to be caused by the irregularity of the waves and by the longer wave periods seen in the field. Therefore calibrating the model with the data from the small-scale laboratory experiments presently available does not seem appropriate.

Most of the recent measurements of instantaneous suspended sediment concentration have been made in the field. Many of these experiments have used acoustic backscatter sensors, which can make non-intrusive measurements close to the bed. It will be shown later in this section that the errors involved in the determination of γ_0 increase as the height of the measurement increases. For these reasons, and bearing in mind that the ultimate applications of the model will be for field conditions, the determination of γ_0 in this part will be done using field data.

4.6.1 Description of the Data Sets

The data sets to be used are those of Vincent and Green (1990), Wright et al. (1991), Hanes (1991), Bedford et al. (1990), and Vincent and Osborne (personal communication). The cooperation shown by Drs. C. Vincent, P. Osborne, L. D. Wright, K. D. Bedford, and D. Hanes in giving us access to these data is acknowledged with gratitude. Some general information about each field site and the instrumentation is given in Table 5. All the measurements were made outside the surf zone above sandy beds.

The data sets will be referred to by the code letters given in the table. The code letters VG, CW, CC, DK, and MB refer to the data of Vincent and Green (1990),

Table 5

Site Location and Instrumentation for the Field Data Sets

Investigator	Location of site	Code	Velocity measurement	Concentration measurement	Frequency of sampling (Hz)	Duration of burst (min)
Vincent and Green (1990)	Holkham, UK	VG	EMCM at 20 cm	ABS every 1 cm	1.72	12.4
Vincent and Osborne (1991)	Cornwall, UK	CW	EMCM at 10 cm	ABS every 0.5 cm	4.22	4.2
Hanes (1991)	Cape Canaveral, FL	CC	EMCM at 15 cm	ABS every 0.5 cm	4	8.5
Wright et al. (1990)	Duck, NC	DK	EMCM at 20 cm	OBS at 15,35,65,105 cm	1	17.1
Bedford et al. (1989)	Mobile, AL	MB	EMCM at 114 cm	ABS every 1.16 cm	1-concentration 2-velocity	10

Vincent and Osborne (presonal communication), Hanes (1991), Wright et al. (1991), and Bedford et al. (1990), respectively.

The horizontal velocity in the experiments was measured by an electromagnetic current meter (EMCM) that measured two components of the velocity that were at right angles to each other. Wright et al. (1991) used a series of optical backscatter sensors (OBS) placed at different heights above the bottom to measure the instantaneous suspended sediment concentration, while the other investigators used acoustic backscatter sensors (ABS) to measure the instantaneous concentration.

OBS devices use a light source together with a sensor that records the backscattered light to make a point measurement of the suspended sediment concentration. The calibration of such sensors is described by Kim (1990). The ABS instrument utilizes the sound scattered by the sediment in suspension. The sound emitter and the measuring transducer are usually placed about 60-100 cm above the bed. A very short pulse of high frequency (1–5 MHz) sound is emitted and the backscattered signal recorded. By recording the scattered sound at several discrete times it is possible to estimate the concentration at several distances (range bins) from the instrument with the same pulse. The results of several closely spaced (within a few microseconds) pulses is averaged to obtain an estimate of the instantaneous concentration at each range bin. The interpretation of these measurements and the calibration of ABS instruments is discussed by Thorne et al. (1991).

Both the OBS and ABS instruments have been estimated to have an error of 10% under ideal conditions though this error may be much larger under field conditions. The advantages of the ABS over the OBS are that it does not disturb the flow and that it can measure the concentration at several points simultaneously.

For these reasons it is possible to make measurements much closer to the bed with an ABS than is possible with an OBS.

Table 6 shows the mean depth and grain diameter for each data set along with a description of the data obtained for this study. The quantities u and v in Table 6 are the horizontal velocities measured by the two-axis EMCMs in the experiments. It was possible to obtain the full time series for velocity and concentration only for the data sets CW and DK. However the method used to determine the value of γ_0 in this part requires only the mean of the measured concentration, the mean velocity, and a representative wave velocity and period. Therefore all the data sets in Table 6 could be used to calculate γ_0.

4.6.2 Procedure

The data sets described above are to be used to determine γ_0 which is the constant of proportionality in Equation 135. Averaging both sides of this equation over a time that is large compared to the wave period results in

$$\bar{C}_r = C_b \gamma_0 \overline{S'} \tag{152}$$

which relates the time-averaged concentration at the reference level of $z_r = 7d$ to the time-averaged value of S'. The time-averaged value of S' can be computed from the solution to the hydrodynamic problem that is outlined in Chapter 2. Therefore if the mean concentration at the reference level can be measured γ_0 can be determined very easily from Equation 152.

However measuring the concentration at the reference level selected in this model, which is very close to the bed, is extremely difficult. The only available alternative is to estimate the concentration at the reference level using the measured

Table 6

Description of Available Measurements from the Field Experiments

Data set code	Number of runs available	Data Available		Bed Condition	Mean depth (m)	Mean Grain diameter (cm)
		Concentration	Velocity			
VG	2	$\bar{c}$ every 1 cm	$\bar{u}$, $\bar{v}$ at 20 cm significant wave velocities at 20 cm	rippled	1.8	0.023
CW	1	c(t) at 4.22 Hz every 0.5 cm	u(t), v(t) at 10 cm	rippled (geometry measured)	1.75	0.03
CC	6	times series of c(t) averaged between 0.5 and 4.5 cm	u(t), v(t) at 15 cm	flat bed	2.0	0.018
DK	11	c(t) at 15, 35, 60, and 105 cm	u(t), v(t) at 20 cm	not observed	8.1	0.01
MB	12	$\bar{c}$ every 1.16 cm	$\bar{u}$, $\bar{v}$ at 114 cm significant near bottom wave velocity	not observed	5.7	0.023

mean concentration at a higher level. This estimation is done using the solution for the mean concentration given by Equations 95, 97, and 99 . The parameters a, ϵ, and δ that appear in these equations can be calculated using the solution to the hydrodynamic model.

It should be noted here that Figure 19a shows that the mean concentration decreases quite rapidly with height above the bottom. The estimation of the concentration at the reference level from a measured mean value will therefore be a process of magnification. Any errors in the measured mean value will be magnified by a corresponding amount. Furthermore, small changes in the parameters a, ϵ, and δ could result in large changes in the estimated value. The potential for error is particularly large in the case of the parameter a, the ratio of the sediment fall velocity to the shear velocity defined in Equation 93, because it appears as an exponent in Equations 95, 97, and 99.

The functional form of these equations, and also the curve in Figure 19a, indicate that the possible error in the estimation of the concentration at the reference level increases with the height from which the estimation is made. Therefore it is desirable to use data sets where the concentration was measured as close to the bottom as possible. It was mentioned in Chapter 4.4 that a major drawback of many previous measurements used to determine γ_0 was the relatively large height—sometimes as much as 2 meters above the bottom—at which the concentration was measured.

Some researchers, for example Hill et al. (1988), have attempted to avoid the estimation of concentrations very close to the bed by defining the reference level to be the level of the lowest concentration measurements. However, definition of the reference level in this way is quite arbitrary and has no physical relation to the level

dividing the bed load and suspended load regions, unlike the reference concentration model used in this report. Furthermore, as this definition is not related to the boundary layer length scale δ, which scales the variation of the concentration, the values of γ_0 derived in this manner will depend on the hydrodynamic conditions of each particular data set and will not be generally applicable.

The estimation of the reference concentration requires that the hydrodynamic problem be solved first. The input values needed for the hydrodynamic model are the wave and current conditions and the sediment properties. In the data sets selected here, there is only one measurement of the velocity. Thus the current is simply specified by the measured mean velocity at the level of the current meter. All the researchers have reported the mean grain diameter. Vincent and Green (1990) measured the fall velocity of the bottom sediment. The fall velocity for the other data sets can be calculated from the empirical relation given by Madsen and Grant (1976).

The complete time series of the horizontal velocity in two directions at right angles to each other was obtained for the data sets CW, CC, and DK. The wave direction was defined as the direction in which the variance of the instantaneous velocity was the greatest. The angle between this direction and the direction of the mean velocity was taken as the angle between the wave and current directions, ϕ_{cw}. For the other data sets ϕ_{cw} was taken to be the given value.

The final requirement is to represent the irregular wave motion observed in the field by one or more periodic components. The simplest method is to use a single component, with magnitude u_{br} and frequency ω_r, defined by Equations 33 and 34. However, this would ignore the wave asymmetry observed in many of the data sets considered here. The asymmetry can be included by considering two components of

magnitudes u_{b1} and u_{b2}, one with twice the frequency of the other, that are in phase. The values of u_{b1} and u_{b2} can be found from Equation 35 and 36 with u_{bp} and u_{bn} obtained by a wave-by-wave analysis. The period of the component with magnitude u_{b1} can be taken as the zero down-crossing period. It was mentioned in Chapter 2.3 that this representation gives a total wave energy and a wave period very similar to the representation by the single wave defined by Equation 33 and 34.

Of the five data sets considered here the full velocity record is available for the sets CC, CW, and DK thus allowing the calculation of u_{b1}, u_{b2}, and the period from a wave-by-wave analysis. For the data set VG, these values are given by Vincent and Green (1990). The periods given by Bedford et al. (1990) for the MB data set was the peak period. In these sets however, inspection of the velocity spectra in Bedford et al. (1990) shows that the Equation 34, which gives the period of the centroid of the spectrum, would have given wave periods similar to the peak period. Therefore the peak period can be expected to be quite similar to the zero down crossing period in this case.

The ranges of wave and current parameters for each data set to be used to solve the hydrodynamic model are given in Table 7. The table shows that the analysis of the velocity records for the data set DK resulted in very small values of u_{b2}. This result is expected as this data set was obtained in relatively deep water (8 m) where the effects of wave non-linearity—which is the cause of wave asymmetry—are negligible. The only wave information available for the MB data set was the significant wave velocities. The values in Table 7 were obtained by dividing the given velocities by a factor of $\sqrt{2}$ to obtain a representative velocity that corresponds to the definition of Equation 33. As the depth for the set MB was 5.7 m it is likely that wave asymmetry was quite small so that setting $u_{b2} = 0$ in this case will not result in much error.

Table 7

Input Parameters for the Wave-Current-Sediment Model from the Data Sets used to Determine γ_0

Data Set	u_{b1} (cm/s)	u_{b2} (cm/s)	T (s)	Specified current velocity (cm/s)	Level of current specification (cm)	Mean grain diameter (cm)	Fall Velocity Measured (cm/s)	Fall Velocity Calculated (cm/s)
VG	34.7-35.0	7.4-7.8	5.8-5.9	14.8-18.0	20	0.023	2.25	
CW	27.7	7.5	5.2	4.7	10	0.03	--	4.0
CC	47.4-62.9	7.7-15.0	3.5-5.4	19.8-37.0	15	0.018	--	1.95
DK	30.3-47.6	0.4-1.1	5.9-8.2	7.4-35	20	0.01	--	0.80
MB	19.7-31.0	--	5.6	15.8-23.9	114	0.023	--	2.78

The details of the calculations were described in Chapter 4.5. In this part the main concern is to use the calculated shear velocities to extrapolate the measured mean concentrations down to the reference level so that γ_0 can be found from Equation 152. In the case of the CC data set, where available information is the average concentration between 0.5 cm and 4.5 cm, the calculated concentration is averaged between these two levels assuming $\gamma_0 = 1$ and the true value of γ_0 obtained by dividing the measured value of the average concentration by the calculated value using $\gamma_0 = 1$. It should be noted here that even though the bottom ripple geometry was measured for data set CW, it is not used in the initial model calculations. This is because the model is developed as a fully predictive model with the ripple geometry calculated as part of the solution of the hydrodynamic problem.

4.6.3 Results of the Calculations

Some of the results of the hydrodynamic model for the various data sets are given in Table 8. Ranges have been given for the sets that included more than one run. The model predicted a rippled bed for the sets VG, CW, MB, and one run of set CC while a flat bed was predicted for the remaining five runs of CC and the set DK. However, Hanes (1991) reported a flat bed for all the runs in the set CC. The value of the parameter Z in Equation 70, which was used to calculate the ripple height, was 0.17. This value is very close to 0.18 which is the upper limit for ripples observed in the field.

The calculated ripple height for the set CW was 1.6 cm while Vincent and Osborne (personal communication) report a ripple height between 3 and 4 cm, i.e., the predicted ripple height is too low by a factor of about 2. This error is within the relative error of Equation 72, which is 2.5. These differences between the observed

Table 8

Some Important Output Parameters of the Hydrodynamic Model for the Data Sets Used to Determine γ_0

Data set	Current shear velocity u_{*c} (cm/s)	Combined shear velocity u_{*cw} (cm/s)	Boundary layer length scale δ (cm)	Shields parameter based on wave skin friction stress ψ'_w	Critical Shields parameter ψ_{cr}	Non-dimensional paramater for ripple geometry Z	Calculated ripple height η (cm)
VG	2.0-2.3	6.84-6.86	2.53-2.58	0.217	0.046	0.062	0.68-0.71
CW	1.1	6.0	2.0	0.123	0.040	0.023	1.62
CC	2.3-3.1	5.2-6.8	1.3-2.3	0.40-0.61	0.055	0.17-0.32	5 runs flat bed 1 run 0.25-cm ripples
DK	0.7-2.2	2.6-4.1	1.1-1.5	0.26-0.53	0.092	0.27-0.54	flat bed
MB	1.3-1.9	4.7-6.0	1.7-2.2	0.063-0.125	0.046	0.018-0.036	1.2-1.7

and predicted bedforms demonstrate the need for independent measurement of the bedforms in field experiments.

As described earlier, each measurement of the mean concentration can be used to obtain an estimate of γ_0. The values of γ_0 obtained from the two runs of the set VG, named VG2046 and VG2047, respectively, are plotted in Figure 22. The figure shows the values of γ_0 on the horizontal axis while the vertical axis indicates the level of the measured mean concentration from which the estimate was made. The estimates of γ_0 cluster around the value 1×10^{-3} in the region near the bottom and then increase with increased elevation of the measuring point.

If all the estimated values of γ_0 had been the same it would have meant that the predicted mean concentration profile has exactly the same shape as the measured profile. The increase in γ_0 with height indicates that the predicted profile decreases with height more rapidly than the measurements. This difference in the profiles can be seen in Figures 25 and 26 of Chapter 5.1 where the profiles are discussed in detail. The most probable cause of this difference is the presence of many different grain sizes in the bed.

The reference concentration model of Equation 135 assumes that γ_0 is a constant and therefore it is necessary to select a single value of this parameter. As discussed earlier, the uncertainties in the estimates of γ_0 increase with the elevation of the measuring point. Thus it appears that γ_0 should be estimated from the lowest measuring points. However, Vincent and Green (1990) point out that due to the uncertainty in the bed level the real elevation of the measuring points is not precisely known. The effect of this uncertainty will be the greatest for the lowest points.

Therefore it is decided to select γ_0 by taking an average of the estimates from the lowest set of measurements. The upper limit of this set will be taken as twice the boundary layer length scale, δ. From the values in Table 8 it is seen that the upper limit is about 5.1 cm for the set VG, so that the lowest five points will be included for the two runs shown in Figure 22. This upper limit was chosen to include as many points as possible while excluding the region over which γ_0 shows a rapid increase with height. The boundary layer length scale is the appropriate choice because it is this length that controls the decrease of the predicted concentration. For the runs VG2046 and VG2047 the estimates of γ_0 in this subset are in the ranges $0.83–2.4\times10^{-3}$ and $1.1–5.6\times10^{-3}$, respectively, with means of 1.3×10^{-3} and 2.2×10^{-3}.

Figure 23 shows the estimates of γ_0 for the single run of data set CW. As the predicted ripple height was too low by a factor of two, another calculation was done using a fixed bed roughness of 14 cm—a value that is based on the observed mean ripple height of 3.5 cm. Both sets of estimates increase with the height of the measurement and the estimates made using the predicted roughness (6.4 cm) increase more rapidly than those made using the observed roughness.

As in the case of the VG data set the increase in the γ_0 estimates with height is due to the predicted mean concentration profile decreasing more rapidly than the measured profile, as shown in Figure 27 of Chapter 5. When the predicted roughness, which is too low, is used the shear velocity and therefore the eddy viscosity will be smaller than if the observed roughness is used. The lower eddy viscosity leads to a more rapid decrease of the mean concentration and a correspondingly more rapid increase in the predicted values of γ_0.

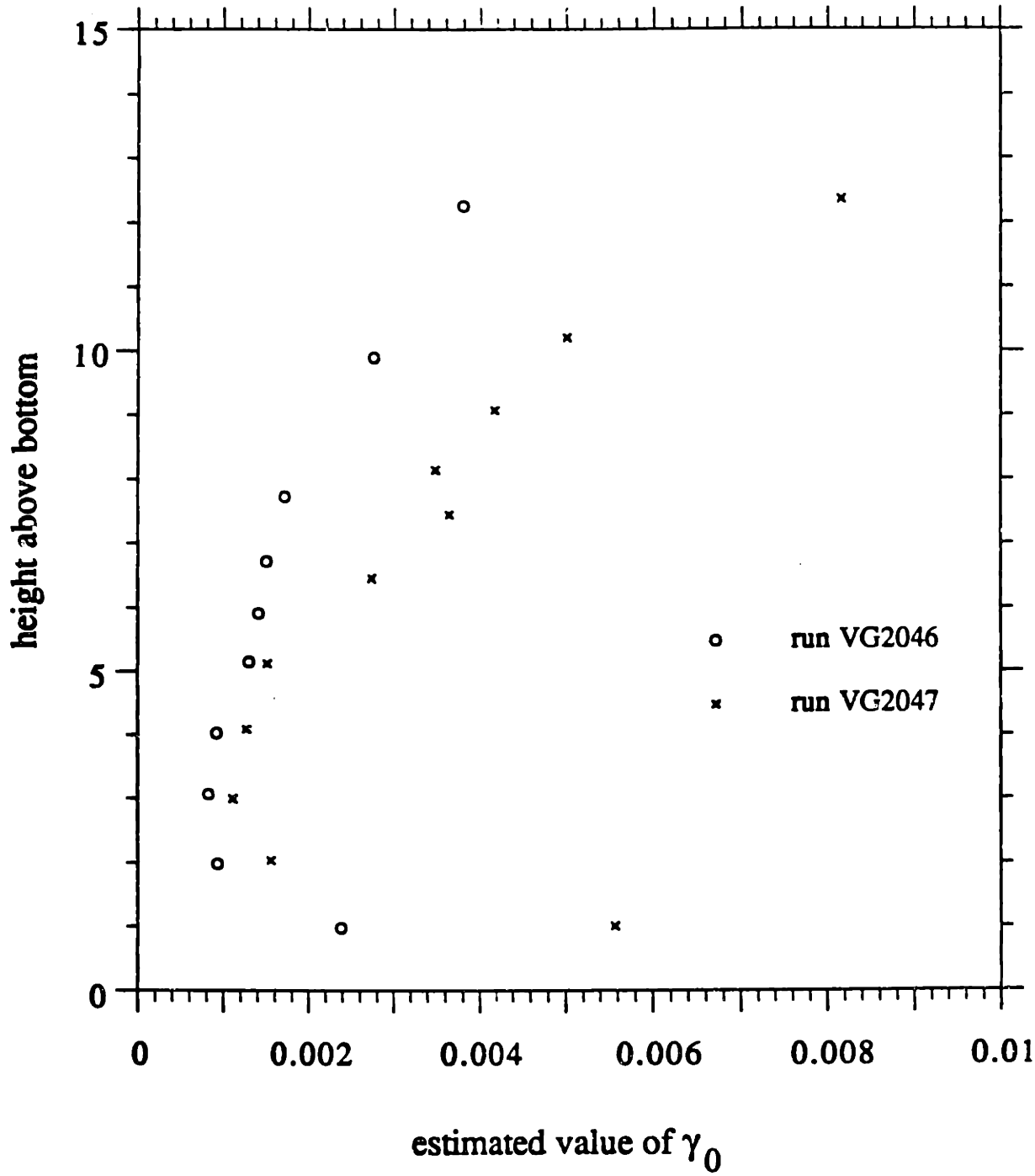

Figure 22. Variation of the estimated values of γ_0 with the height of the measurement for runs 2046 and 2047 of data set VG

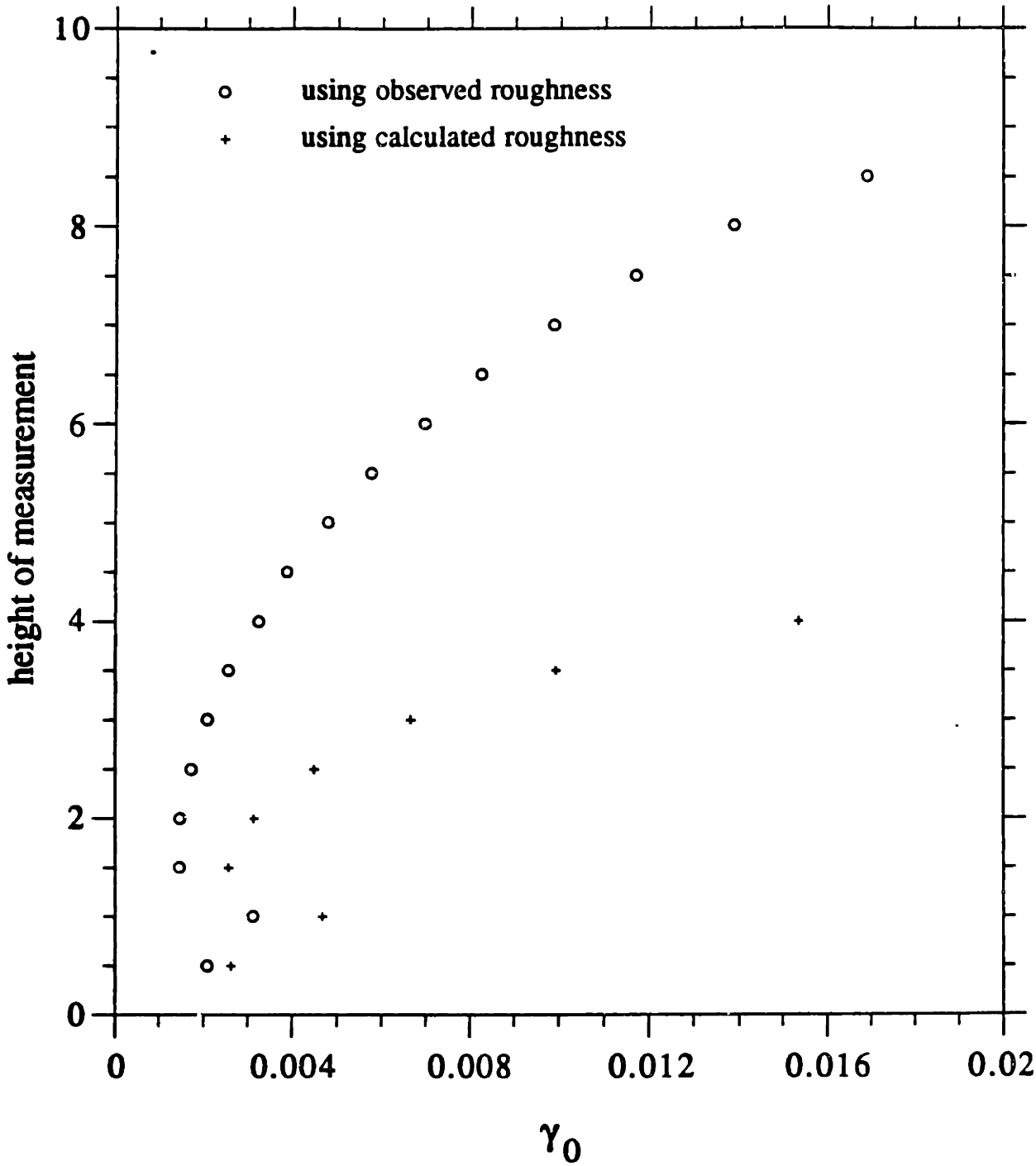

Figure 23. Variation of the estimated values of γ_0 with the height of the measurement for the data set CW using both the calculated and observed roughness

The boundary layer length scale, δ, for the CW set is 2.4 cm using the predicted roughness and 2.3 cm using the observed roughness. Using the same region, up to 2δ, as for the VG data set to obtain an average value of γ_0 results in mean values of 8.0×10^{-3} and 2.9×10^{-3}, from ranges of $2.6–22.5\times10^{-3}$ and $1.5–5.8\times10^{-3}$, for the runs using the predicted and observed roughnesses, respectively. If only the values at heights less than δ are used the estimates of γ_0 reduce to 3.3×10^{-3} and 2.0×10^{-3} for the two roughnesses.

The sediment fall velocity for the VG data set was measured by Vincent and Green (1990) while that for the CW data set was obtained from the relationship between the grain diameter and the fall velocity. The fall velocity, through the parameter a defined in Equation 93, is one of the most important factors controlling the vertical variations of the concentration profile. Therefore the estimates of γ_0 from the VG set are probably more reliable, particularly when estimating γ_0 from the higher measurement points. For this reason the estimate of γ_0 for the CW set will be made from the points lower than δ and not 2δ as in the case of the VG set. As the measurements are made every 0.5 cm there will still be four points in this region while the points that show a rapid increase will be neglected.

It should be remembered that the model calculations outlined in Chapter 4.5 and Figure 21 did not require the sediment fall velocity and the equivalent roughness of the bottom as input values. The bottom roughness can be estimated using Equations 79 and 80 derived in Chapter 3 while the fall velocity can be estimated from the grain diameter. Thus it could be argued that using the measured fall velocity of for the data set VG and the observed ripple height for the set CW is inconsistent with the intended use of the model in the predictive mode.

However, the object of the calculations in this section is to calibrate the suspended sediment model through the determination of the only undetermined parameter, the resuspension coefficient γ_0. Use of the model in the fully predictive mode would introduce the errors involved in the estimation of the ripple geometry and the fall velocity into the calculation for the sets VG and CW, respectively, into this calibration.. Therefore, in order to derive as accurate a value of γ_0 as possible, all the available additional information ,i.e., the fall velocity for the set VG, and the observed ripple height for the set CW, will be used in these calculations.

Thus the three estimates of γ_0 from the two runs of the set VG and the single run of set CW are 1.3×10^{-3}, 2.2×10^{-3}, and 2.0×10^{-3}, respectively. The mean of these three values is 1.8×10^{-3} which is proposed as a value of γ_0 that is appropriate for rippled beds. The other data set that was predicted to have a rippled bed, in addition to those considered here, was the MB data set. However, as discussed below, it was found that the calibration of the ABS instrument in this experiment was done in such a manner that the observed near-bottom concentrations, which are critical in determining γ_0, may have been incorrect. Therefore the results from this data set were not used.

The estimated γ_0 values from the six runs of data set CC are plotted in Figure 24, with ψ_w', the Shields parameter due to the wave skin friction shear stress, on the horizontal axis. It should be recalled here that only one estimate is possible for each run because only an average concentration between 0.5 cm and 4.5 cm was available. The single + symbol shows the value of γ_0 that would have been obtained from run CC4 if the ripple roughness predicted by Equation 72 had been used. However, as the bed had been observed by Hanes (1991) to be flat for all the runs, it will be the estimates shown by the o symbols, obtained using a flat bed roughness of $k_n = 10$ d, that will be used in this study. It should be noted that

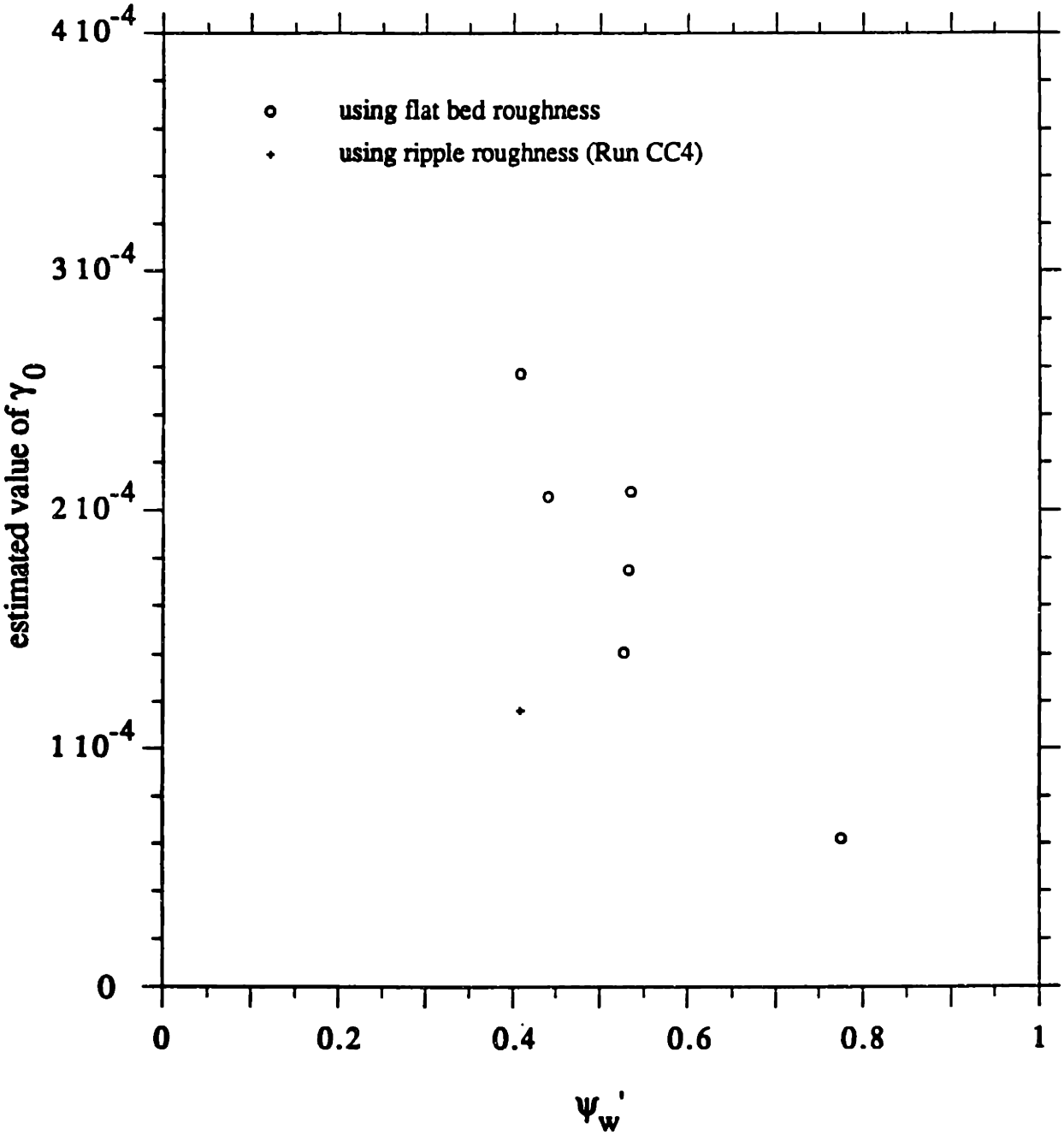

Figure 24. Variation of the estimated values of γ_0 with ψ_w', the Shields parameter based on the wave skin friction shear stress, for the six runs of data set CC

Table 8 shows the range of δ in these runs to be 1.3 cm to 2.3 cm so that the estimates are made using measurements in the region below 2δ to 3.5δ. This region is similar to the region considered for the VG data set.

Figure 24 shows that the estimated γ_0 values decrease with increasing ψ_w'. Such a decrease in γ_0 was also observed by Drake and Cacchione (1989) from the results of their field experiment and attributed by them to bed armoring. However, bearing in mind the small number of runs considered here and the many uncertainties in these estimates, it seems reasonable to adopt the mean value as an estimate of γ_0 for flat bed conditions. Therefore it is proposed that 1.8×10^{-4} is an suitable value for flat bed conditions.

The 11 runs of data set DK yielded estimates for γ_0 in the range 1.8×10^{-2} to 4.2×10^{2}. However, it is seen from Table 4 that the lowest measurement point for this set is 15 cm while Table 8 shows that boundary layer length scale, δ, ranges from 1.1 cm to 1.5 cm. In other words the estimates are made from at least 10δ for the lowest point and as much as 100δ for the highest measuring point at 105 cm. At these large heights it is very probable that the mean grain diameter of the bottom (given as 0.01 cm) is no longer representative of the sediment that is in suspension. Therefore estimates of γ_0 made using the given mean diameter are likely to be very unreliable.

This point is illustrated by the comparison of the predicted and calculated mean concentration profile for run VG2046 given in Figure 25 of Chapter 5. The figure shows that the predicted value at 15δ (which is about 37.5 cm for this run) is less than the measured value by more than an order of magnitude. Thus if the estimation of γ_0 had been done using the value measured at this height the estimated value would be greater than the value obtained from the near bottom

points by the same amount. For this reason it appears that the DK data will not give estimates of γ_0 as reliable as the near bed measurements of the VG, CC, and CW sets, and the results will not be used in this part.

The data set MB had measurements of the mean concentration at every 1.16 cm over the first 101 cm above the bottom. Table 8 shows that the length scale δ ranged from 1.7 cm to 2.2 cm for the 12 runs in this set. Therefore the first three points would be inside the range 2δ above the bottom. The 36 γ_0 values obtained from these points range from 8×10^{-3} to 5.9. However, these values of γ_0 will not be considered in this study because of the methodology that appears to have been used by Bedford et al. (1989) to calibrate their ABS instrument.

The calibration of the instrument seems to have been done using the grain size distribution obtained from samples taken in the beam of the instrument at a height of 100 cm above the bottom. The dominant grain size in these samples was 0.004 cm to 0.006 cm. In contrast grab samples taken from the bottom near the measurement site indicate that the mean grain diameter of the bottom was 0.023 cm with only about 1–3% of the sediment being in the size classes sampled 100 cm above the bottom. Thus it seems likely that the concentration very near the bottom would be dominated by the larger grains. As the instrument was calibrated using the smaller grain size it is likely that the measurements made very near the bottom would be in error. Since it is these measurements that provide the most reliable estimates of γ_0 it was decided not to use this data set in the determination of γ_0.

4.6.4 Discussion of the Results

The calculations performed in this part have led to the conclusion that the parameter γ_0 takes on a different value depending on whether the bed is rippled or

flat. In the movable bed roughness development of Chapter 3 it is the parameter Z, defined in Equation 70, that determines the nature of the bed. Therefore, for the model presented in this report γ_0 can be defined as

$$\gamma_0 = \begin{cases} 1.8\times10^{-3} & Z < 0.18 \\ 1.8\times10^{-4} & Z \geq 0.18 \end{cases} \tag{153}$$

It should be remembered that γ_0 in Equation 153 is based on just nine runs from three different field experiments. Furthermore, the definition of the onset of the flat bed by Z = 0.18 is itself based on a limited number of field ripple geometry measurements. Nevertheless Equation 153 is the first step towards quantifying the reference concentration so that the suspended sediment model can be applied in the field. Comparison with more high quality data sets will serve to make the model applicable to a wider range of grain diameters, bed forms and wave and current conditions.

The existence of two different values of γ_0 for rippled and flat beds can be justified physically by considering the vortex shedding mechanism that was described in detail in Chapter 1. The increased flow velocity over the ripple crest combined with the ejection of sediment into the flow during velocity reversal would mobilize more sediment than the action of the shear stress on a flat bed. It is likely that γ_0 decreases smoothly from the higher value to the lower value as the ripples respond to increasing flow intensity by growing smaller and finally vanishing. Data sets in the ripple disappearance region that include actual ripple measurements should help determine this variation of γ_0.

The apparent decrease of γ_0 with increasing flow intensity has been observed by Vincent et al. (1991). They considered a succession of mean concentration profiles, taken with an ABS instrument over a 0.015-cm sand bed, through the course of a

mild storm event. The model of Glenn and Grant (1987), with ripple geometry predicted by the laboratory relations of Grant and Madsen (1982), was used to estimate a value of γ_0 from the mean concentration measured 2 cm above the bottom.

The calculations showed that γ_0 was about 1×10^{-2} before the storm and then decreased to a value of about 2×10^{-4} over a period of nine hours. The value of γ_0 then increased and stabilized at a value of about 3×10^{-3} four hours later. The lowest value of γ_0 corresponded to the highest wave intensity. Whereas the ripple geometry relations used by Vincent et al. (1991) predicted the bed conditions to be rippled for the duration of the experiment, use of Equation 72 indicates that the bed would have been flat when the lowest values of γ_0 were obtained. The values of γ_0 calculated by Vincent et al. (1991) are not directly comparable to the values obtained in this part because of the different eddy viscosity model and reference level used. However, they do indicate that γ_0 could be expected to decrease smoothly between the two limits established in Equation 153. The values of Vincent et al. (1991) are also of the same order of magnitude as those derived here.

In the process of determining γ_0 the data sets used were subject to a critical analysis and only the most reliable data sets were used. Even these sets were observed to have some shortcomings such as the lack of ripple geometry measurements in the set VG. Possible improvement to field experiments will be discussed in Chapter 6.

CHAPTER 5

COMPARISON OF THE MODEL RESULTS WITH FIELD DATA

Once the value of the resuspension coefficient, γ_0, is established, the model developed in the preceding chapters will be able to predict the velocity and concentration fields and therefore the net flux fields. The predicted mean concentration profiles will be compared with the measured profiles for the data sets VG and CW. While the measured mean concentration was also available for the data sets DK and MB these sets were not used as the analysis in Chapter 4.6 showed that they were not reliable. The predicted net flux profiles and the total transport for the data sets VG and CW are compared to estimates made using the method of Vincent and Green (1990).

The effect of non-uniform grain size on the mean concentration profiles is investigated using the grain size distribution measured by Vincent and Green (1990) for the data set VG. Finally, the model will be used to calculate the time series of the near-bottom concentration corresponding to portions of the sets CC and CW. The predicted time series will be compared to the measurements and the variation of the predicted net transport with the wave frequency will be discussed.

5.1 Mean Concentration

The predicted and measured mean concentration profiles for runs VG2046 and VG2047 are plotted in Figures 25 and 26, respectively. The comparison for the set CW is shown in Figure 27 in which the predictions using both the observed and calculated bottom roughness are plotted. These figures show that the predicted values match the measured values near the bottom, with the predictions using the observed roughness showing better agreement for set CW than those made with the

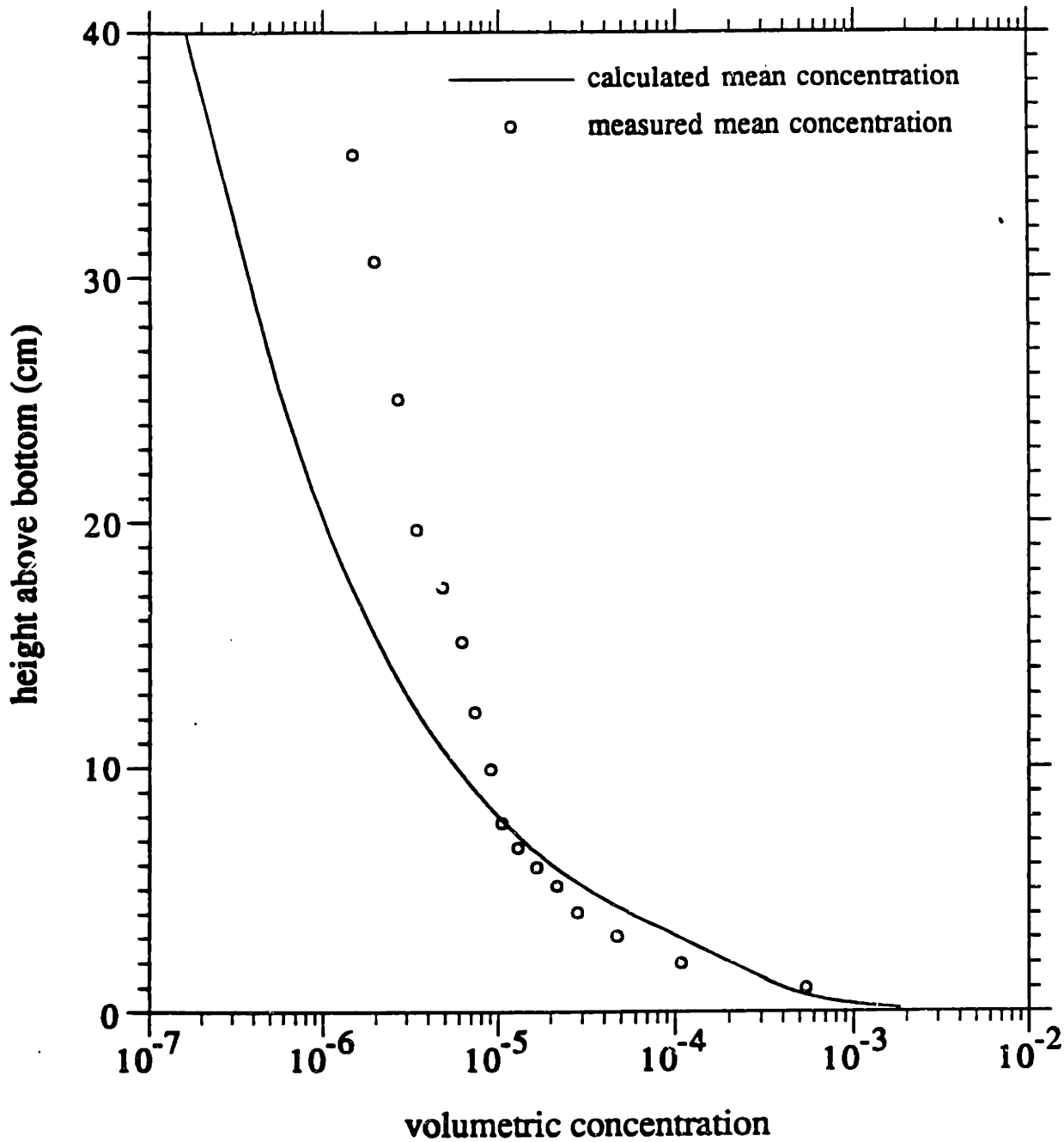

Figure 25. Comparison of predicted and measured mean concentration profiles for run VG2046 of data set VG

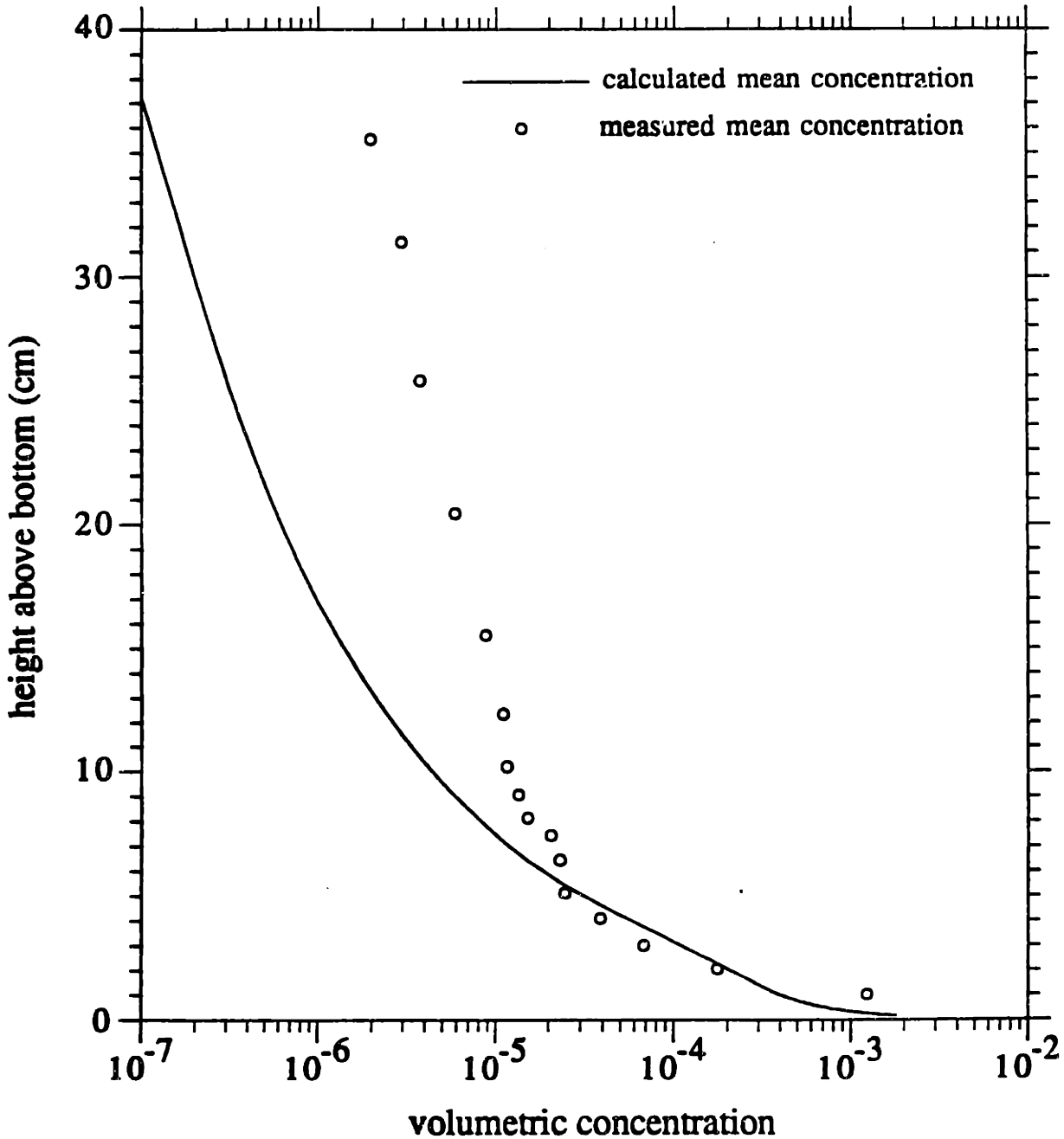

Figure 26. Comparison of predicted and measured mean concentration profiles for run VG2047 of data set VG

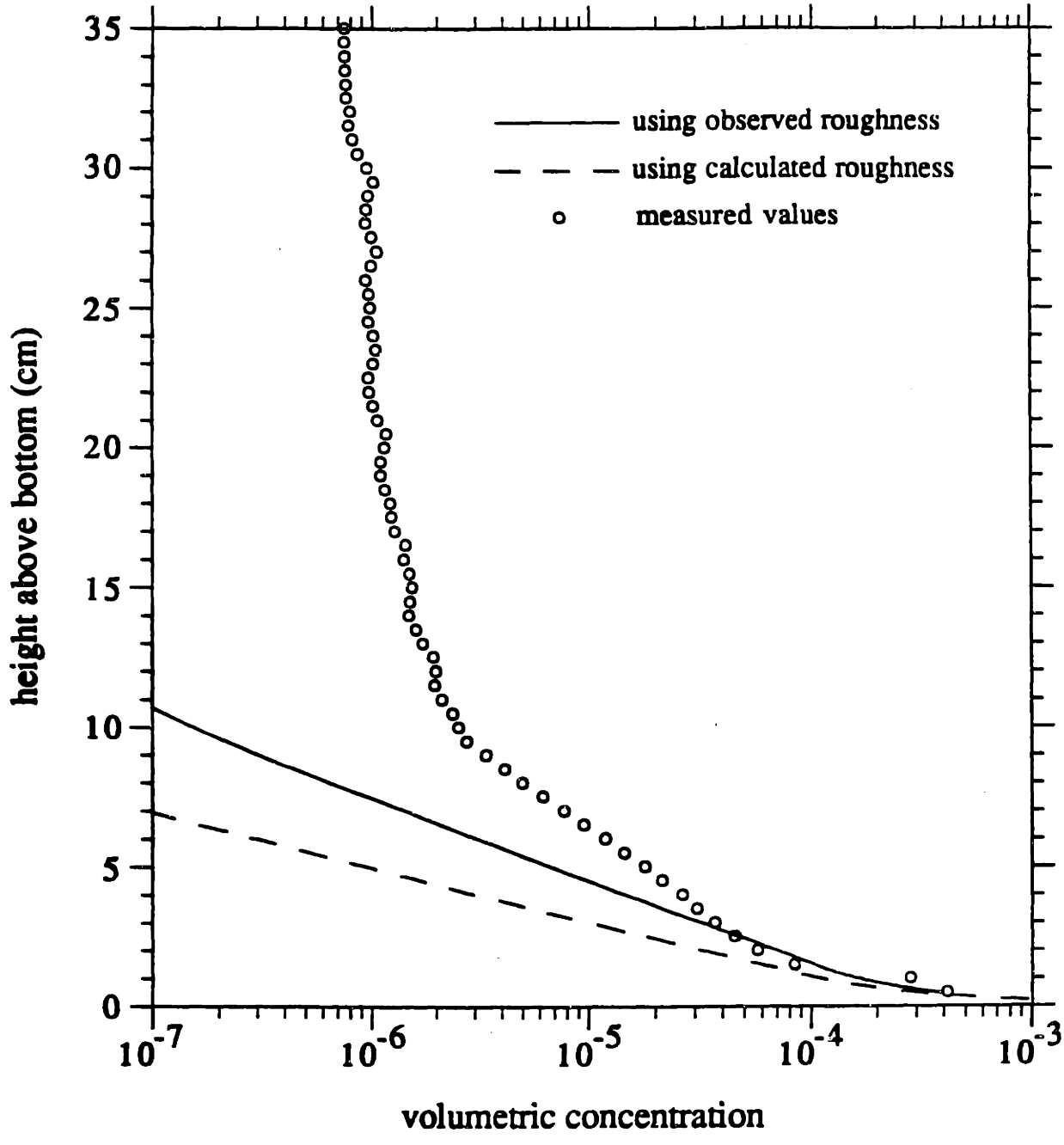

Figure 27. Comparison of the mean concentration profiles predicted using the observed and calculated roughness with the measured values for data set CW

calculated roughness. This good agreement is hardly surprising in view of the fact that the value of γ_0 used for a rippled bed, which was the case for all three runs, was obtained using the same data sets.

Figures 25, 26, and 27 show that the predicted mean concentration drops off quicker than the observed values for all three sets, resulting in an increasingly large underprediction of the concentration as the height increases. It is this behaviour that causes the estimated value of γ_0 in Figures 22 and 23 to increase with increasing height. As pointed out in Chapter 4.6, the value of γ_0 that is predicted from the higher points would be much larger than those predicted from the lower points.

The differences at large elevations above the bed is probably due to a combination of the non-uniformity of the grain size and errors in the prediction of the shear velocities. Additional measurements that would reduce these uncertainities will be discussed in Chapter 6. The effect of considering a mixture of grain sizes will be considered in Chapter 5.4.

Figure 27 shows that whereas using the observed roughness improves the agreement with the measurement for the set CW, the predictions are still much less than the measured value at heights greater than a few centimeters. The underprediction for this set is much larger than that for the comparisons with set VG in Figures 25 and 26. This difference may be due to the effects of non-uniform grain size being more important when the mean grain size is greater, as is the case for the CW data set.

Furthermore the fall velocity for the VG set was measured while it was estimated from the empirical relationship of Madsen and Grant (1976) for the CW data set. This relationship gives a fall velocity of 2.8 cm/s for the VG set while the

measured value was 2.25 cm/s. If the fall velocity for the CW data set is in reality less than the value predicted by the empirical relation, as is the case for the set VG, the agreement between the predicted and measured concentrations in Figure 27 would improve.

An interesting feature of the observed mean concentration profiles is that they show different curvatures at different heights. This feature is particularly pronounced in the profile for the CW data set in Figure 27. The figure, which plots the logarithm of the concentration against the height, shows that the profile has a steeply decreasing bottom portion followed by a linear section of smaller slope that leads into another curved section that decreases more slowly with height. The observed profiles for runs VG2046 and VG2047, in Figures 25 and 26, respectively, do not show such a well defined shape but a similar trend can be observed in Figure 26.

Comparing Figure 27 with Figure 19a shows that the observed mean concentration profile has a shape that agrees with the shape expected from the solution for the mean concentration given in Equations 95, 97, and 99. However, while the shape of the observed profile is in agreement with the theory, the parameters a, δ, and ϵ that appear in Equations 95, 97, and 99 are different for the observed and predicted profiles. For example, the equations show that the levels at which the curvature changes are $z = \alpha\delta$ and $z = \alpha\delta/\epsilon$ for the lower and upper levels respectively. The slope of the linear section is given by $a/\alpha\delta$.

These relations can be applied to the observed profile for the set CW to obtain approximate values of 4 cm, 0.22, and 0.84 for the parameters δ, ϵ, and a, respectively. The model predicts values of 2.9 cm, 0.18, and 1.13 for these parameters when the observed roughness is used. The boundary layer length scale,

δ, which is defined by Equation 52, will increase with an increase in the combined shear velocity, u_{*cw}, and a decrease in the representative frequency, ω_r. The parameter a, defined in Equation 93, will decrease with a decrease in the fall velocity and an increase in u_{*cw}.

Therefore, if it is assumed that the eddy viscosity model of Equation 8 applies to the suspended sediment problem, the observed profile indicates some combination of a larger shear velocity, a smaller fall velocity, and a smaller representative frequency. For example, the shear velocity could be increased by using the significant wave velocity instead of the root mean square value used to derive the values u_{b1} and u_{b2} in Equations 35 and 36. However, it is not possible to determine which of these parameters should be adjusted. If additional measurements, such as the fall velocity and the grain size distribution with height, had been made such an analysis may have resolved this issue.

5.2 Flux Profiles

The data sets VG and CW, described in Chapter 4.6, were obtained using an ABS instrument. This instrument measured the instantaneous suspended sediment concentration at several equally spaced points in the near-bottom region. The instantaneous sediment flux is defined here as the product of the instantaneous concentration and velocity. However, the velocity in these experiments was measured at only a single point in the flow. Therefore, in order to obtain the flux profile, the velocity at each of the points at which the concentration was measured must be estimated.

Vincent and Green (1990) estimated the flux in several ways. The mean flux, i.e., due to the product of the mean velocity and concentration, was estimated using

the predicted mean velocity from the wave-current model of Grant and Madsen (1979). The problem of estimating the instantaneous velocity over the whole depth was handled by Vincent and Green (1990) as follows. The measured velocity was split into a mean component and a wave-induced component. The wave-induced component above the wave boundary layer (as defined in the Grant and Madsen (1979) model) was assumed constant and equal to the measured irregular wave-induced velocity at 20 cm. The wave-induced component within the wave boundary layer was taken as the measured wave-induced value multiplied by an attenuation factor based on the solution for the wave velocity profile in the wave-current model. Finally, a temporal correction, based on the group speed of shallow water waves, was made to the velocity record to account for the fact that the EMCM and the ABS were 2 m apart.

Vincent and Green (1990) presented the mean and wave flux profiles estimated by this method. For the data set CW the time series of both velocity and concentration were available so that the fluxes could be estimated using the method described above with the mean velocity and attenuation factor based on the hydrodynamic solution of the present model. The variation of the mean velocity and the attenuation factor with height is similar to the profiles shown in Figures 4a and 4b.

The calculated and estimated flux profiles for runs VG2046 and VG2047 are shown in Figures 28 and 29. The figures are restricted to the first 10 cm above the bottom as the fluxes are quite small above this height. The wave flux was calculated as the sum of the fluxes due to the principal and secondary components. The figure shows that while the calculated flux profiles resemble the estimated profiles in shape, the magnitude of the fluxes do not agree very well near the bed.

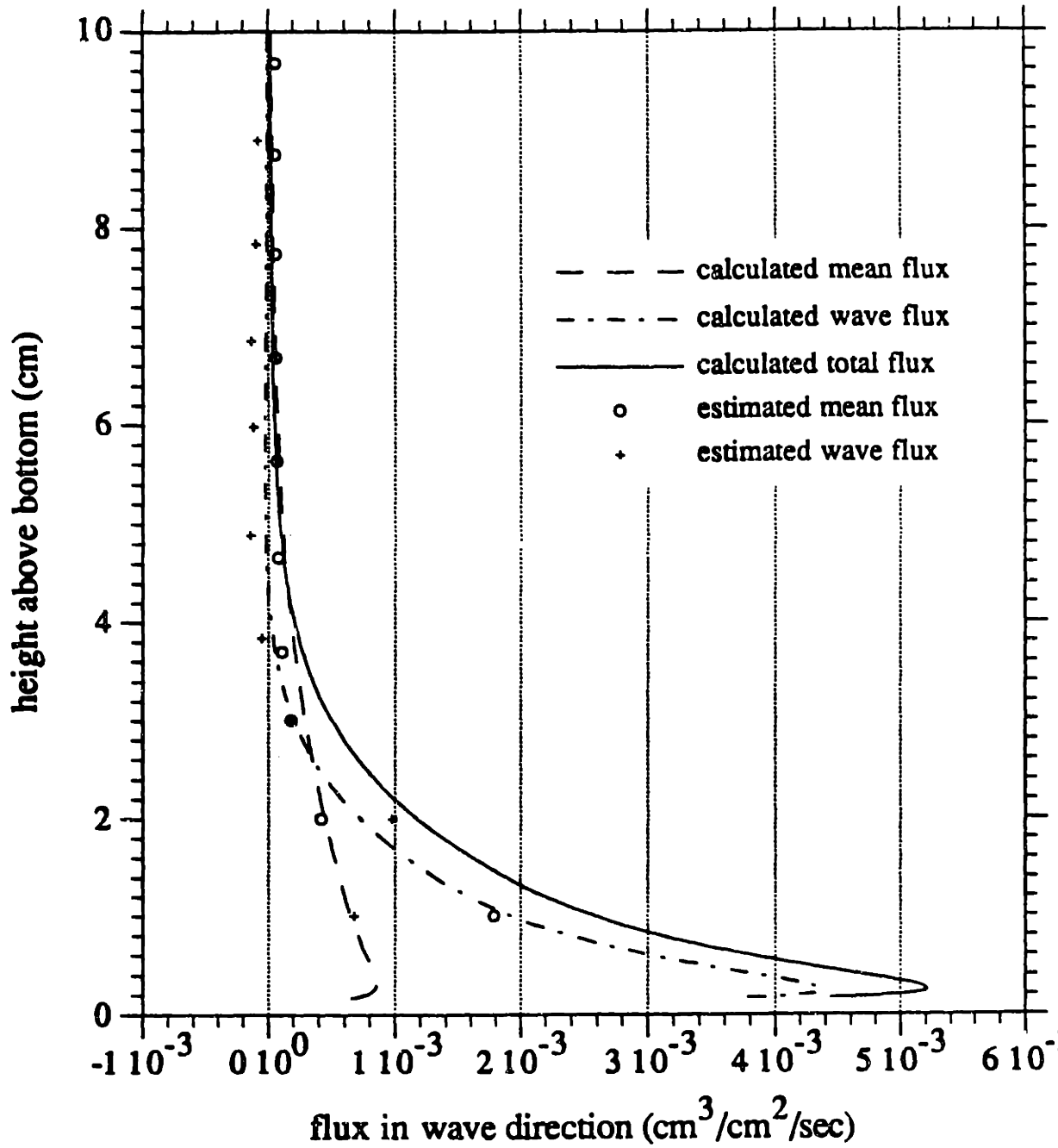

Figure 28. Predicted mean, wave, and total flux profiles for run VG2046 of set VG compared to the estimated mean and wave flux profiles

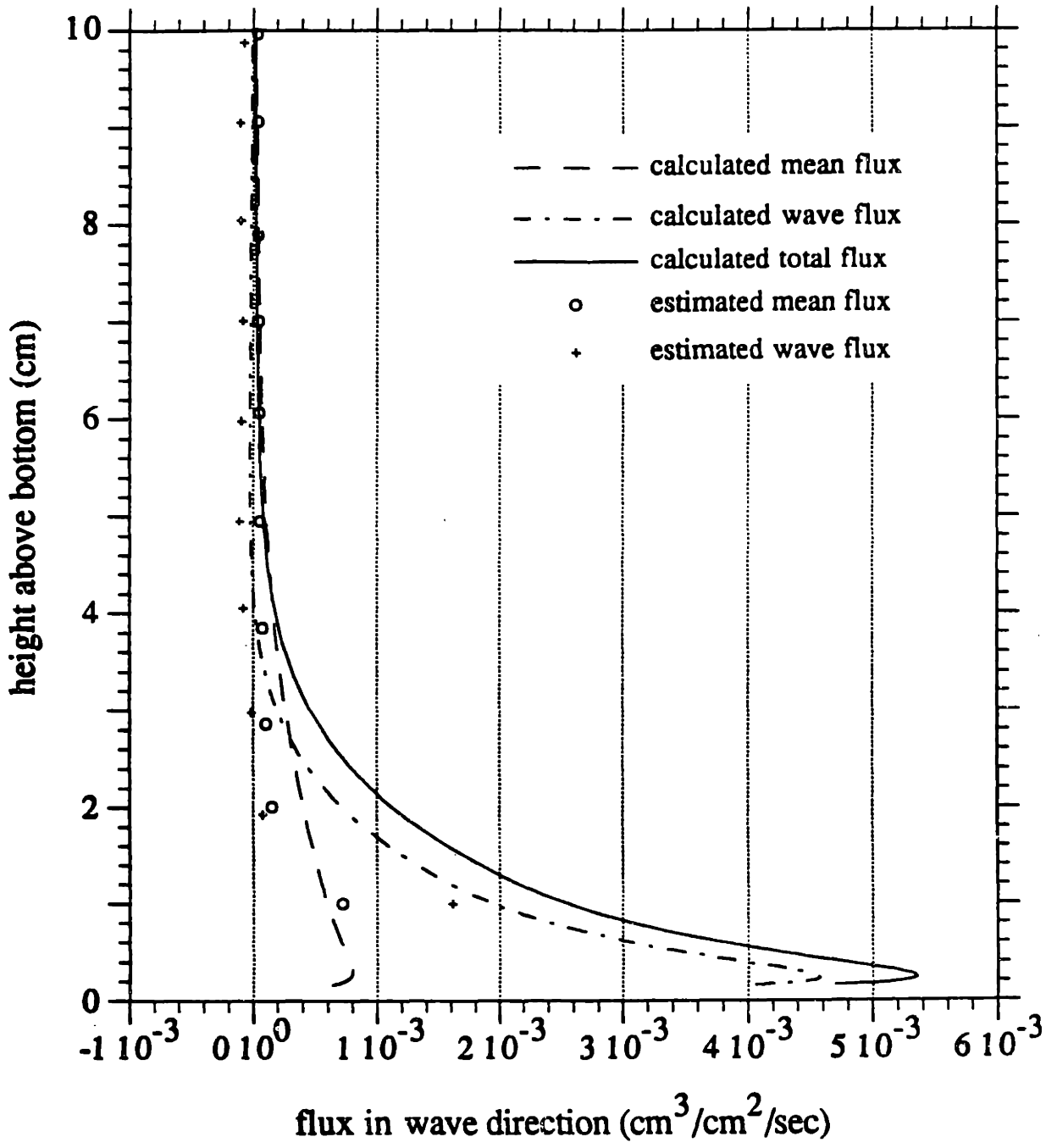

Figure 29. Predicted mean, wave, and total flux profiles for run VG2047 of set VG compared to the estimated mean and wave flux profiles

The calculated mean and wave fluxes are the greatest at levels of 0.3 cm and 0.2 cm, respectively, while the lowest level of measurement is 1 cm.

As the height above the bed increases, both the estimated and calculated wave fluxes change sign and indicate a flux in the offshore direction, i.e., against the wave direction. However, the largest calculated values of the offshore wave fluxes are $2.6\times10^{-5}cm^3/cm^2/sec$ and $2.5x10^{-5}cm^3/cm^2/sec$ for runs VG2046 and VG2047, respectively, while the corresponding estimated values are $1.1\times10^{-4}cm^3/cm^2/sec$ and $1.4\times10^{-4}cm^3/cm^2/sec$, respectively. Figures 28 and 29 also show that the maximum offshore flux occurs at a slightly lower level for the estimated flux. The estimated offshore flux is sufficiently large to cause a net offshore flux between the levels $z = 3$ cm and $z = 8$ cm and the levels $z = 3$ cm and $z = 7$ cm for the runs VG2046 and VG2047, while the calculated total flux is always onshore.

The calculated mean flux is greater than the estimated values in the region 2–7 cm above the bottom and less than the estimates above 7 cm. As the wave-current model used by Vincent and Green (1990) was quite similar to the model used here, and because the same current specification was used, these differences should be chiefly the result of under- or overprediction of the mean concentration. Inspection of the mean concentration profiles in Figures 25 and 26 shows that this explanation is correct.

The calculated and estimated flux profiles for the CW data set are shown in Figure 30. The calculated values were obtained using the observed bottom roughness. The mean fluxes are offshore because the observed mean velocity in the wave direction was offshore. The calculated wave flux has a onshore maximum at about 0.8 cm and becomes offshore at about 5.4 cm. The estimated wave flux has a similar variation but the onshore peak is at about 1.5 cm and the flux becomes

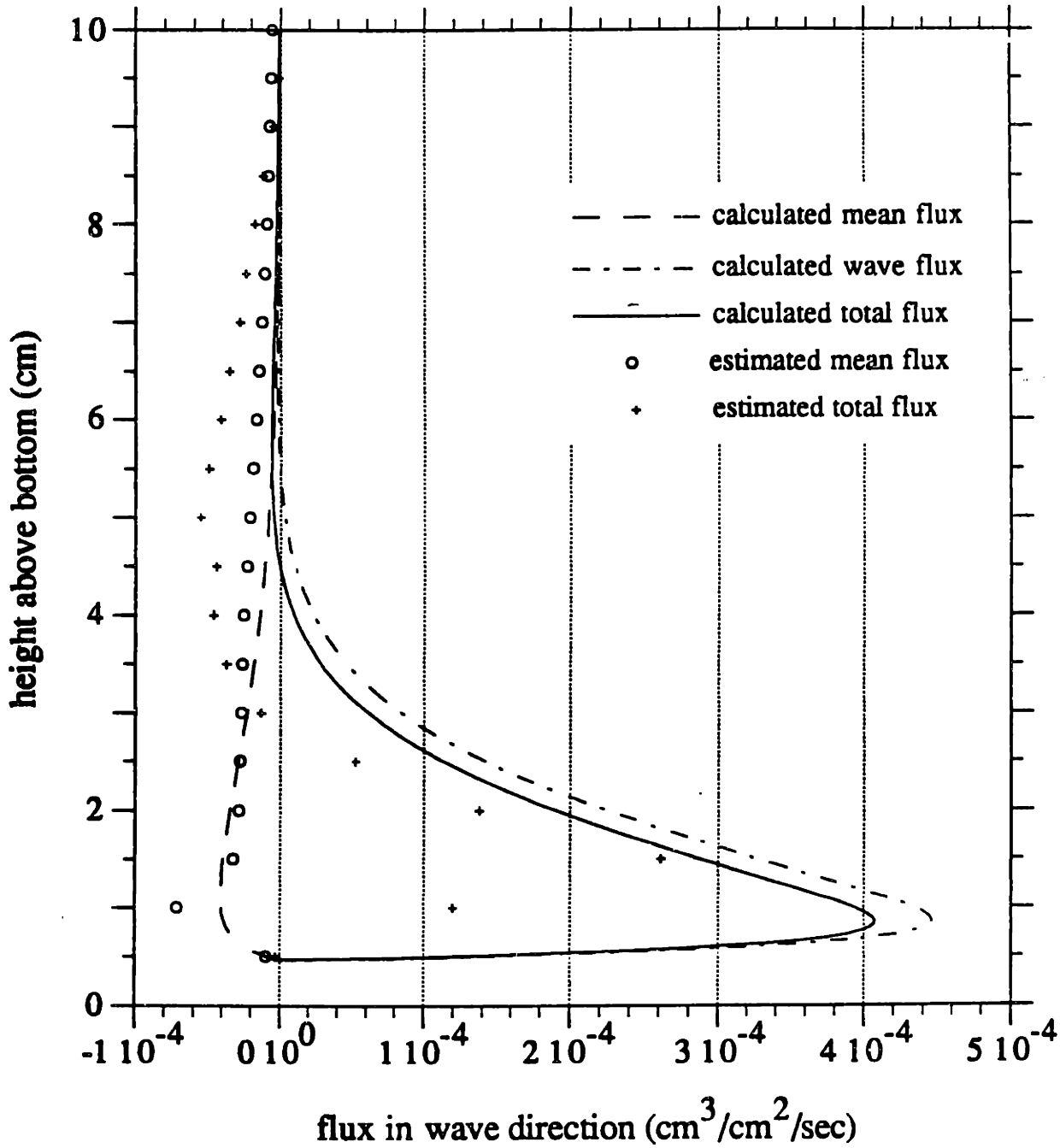

Figure 30. Mean, wave, and total flux profiles (predicted using the observed roughness) for set CW compared to the estimated mean and wave flux profiles

offshore at about 3 cm. The estimated values show quite a large offshore value of $6\times10^{-5}cm^3/cm^2/sec$ while the calculated offshore value is only about $2\times10^{-6}cm^3/cm^2/sec$.

Both the calculated mean and wave fluxes decrease with height more rapidly than the estimated values. This is because the predicted mean concentration, as shown in Figure 27, drops off much quicker than the observed values. The differences between the profiles in Figure 30 also show that the estimated profiles indicate a larger value of the boundary layer length scale, δ, than is calculated by the model.

The comparisons show that one of the most important differences between the calculated and estimated profiles is the relative magnitude of the mean and wave fluxes in the region $z = 3$ cm to $z = 8$ cm. The estimated wave flux in this region has a significant offshore value that is not shown in the calculated wave flux profile. A possible reason for this difference is that the calculated value of the periodic components decreases faster than the observed values. This decrease is probably important in the data set CW, where the predicted mean concentration also decreases faster than the observed value. However, another factor that enters the calculation of the wave flux is the phase difference between the velocity and the concentration components of the same frequency.

This phase difference is controlled by the type of boundary condition used for the periodic components. The calculations shown above were carried out using the boundary condition of Equation 135, which relates the reference concentration to the skin friction shear stress. This model was derived from models proposed for steady flow over flat beds. However, the beds over which the measurements for the data sets VG and CW were made were observed to be rippled. Vincent and Green

(1990) present a short portion of the instantaneous concentration record obtained from the first 40 cm above the bed.

The record shows a pattern of suspension that is consistent with the entrainment from rippled beds by vortex shedding that was discussed in Chapter 1. The reference concentration model of Equation 135 may not be the appropriate model under these conditions. A model that does reflect the entrainment by vortex shedding would give different values for the ratios r_1 and r_2 of Equation 147 and lead to a difference in the relative magnitude of the mean and the wave fluxes.

5.3 Total Transport

The estimated flux profiles can be integrated over the depth to obtain estimates of the mean and wave suspended sediment transports. These values are presented in Table 9 along with the calculated bed-load and suspended load transports for runs VG2046, VG2047, and CW. The transport computations for the set CW were carried out using the observed roughness of 14.0 cm. The wave components with magnitudes u_{b1} and u_{b2} will be referred to here as the principal and secondary components, respectively. The calculated values of the transports due to the principal and secondary components are calculated separately and then summed to obtain the wave transport.

Comparing the calculated and estimated transport rates for the data set VG shows that the mean transport rates for the run VG2046 are in good agreement while the agreement is not so good for run VG2047. The reason for this difference is that the mean concentration prediction for VG2046, shown in Figure 25, was greater than the observed value near the bottom and less at higher elevations. When the transport is computed these differences would tend to cancel each other out and

Table 9

Transport Calculations for Runs VG2046, VG2047, and CW

	Data Set		
	VG2046	VG2047	CW
	$10^{-4}cm^3/cm/s$	$10^{-4}cm^3/cm/s$	$10^{-4}cm^3/cm/s$
Calculated transports			
Suspended sediment transports			
Mean in wave direction	22.6	23.6	-1.3
Mean in wave-normal direction	-64.1	-43.9	-2.3
Principal wave	31.8	31.7	5.2
Secondary wave	12.0	11.5	2.0
Wave	43.8	43.2	7.2
Total in wave direction	66.4	66.8	5.9
Bed load transport			
Wave direction	86.7	86.1	44.1
Wave-normal direction	-36.5	-25.3	-3.2
Estimated transport			
Mean in wave direction	19	40	-3.0
Wave	6	3	1.4
Total in wave direction	25	43	1.6
Suspended sediment transports calculated using the lowest measuring point as the lower level of integration			
Mean in wave direction	16.6	17.2	-1.3
Principal wave	13.6	13.9	5.2
Secondary wave	2.9	2.8	2.0
Wave	16.5	16.7	7.2
Total in wave direction	33.1	33.9	5.9

result in a value close to the estimate. On the other hand, Figure 26 shows that the calculated concentration is almost always less than the observed value for run VG2047 resulting in the calculated mean transport also being less. Similarly, the calculated mean transport for the run CW was less than the estimated value because the calculated mean concentration decreased much more rapidly than the observed values.

The two runs VG2046 and VG2047 were taken within a period of 40 minutes and the hydrodynamic conditions are nearly identical. However, examination of the mean concentration profiles in Figures 25 and 26 and the transport estimates in Table 9 show that the mean concentration observed during run VG2047 is greater than that for run VG2047 by about a factor of 2. The only possible explanation for this result within the framework of the present model is that the ripple height was significantly different for the two runs despite the wave and current motions being very similar. If this was not the case the observations indicate that mechanisms not accounted for here, such as advection, play a significant role in the observed concentrations. An examination of the detailed velocity and concentration time series may shed some more light on this issue.

The calculations show that while the transport due to the secondary components are less than the transport due to the principal components they are still of the same order of magnitude. The calculated wave transport is significantly larger than the estimated values for all three runs. This difference is due to the larger negative values seen in the estimated wave fluxes of Figures 28, 29, and 30 which tend to cancel out the positive values near the bottom. Another possible reason is that the calculated transport is obtained by integrating the flux from the lower of the levels $z_0 = k_n/30$ and $z_r = 7d$, while the estimated values are integrated from the lowest measuring value.

Table 9 also includes calculations of fluxes where the lower limit was set to the level of the lowest measurement. The wave fluxes computed in this way for the runs VG2046 and VG2047 are reduced significantly, though they are still larger than the estimated values. The use of the lowest level, $z = 0.5$ cm, does not cause much change in the values for the set CW because the level z_0 is $0.4l$ cm, a value that is very close to the lowest measurement level.

The table also shows that the calculated bed-load transport is greater than the total suspended load transport for all three runs. This result is contrary to the results of Goud (1988) who used the model of Glenn and Grant (1987) and found that the bed-load transport was generally negligible. However, Goud (1988) carried out calculations for sand sizes ranging from 0.002 cm to 0.02 cm while the sand sizes for the data sets considered here were 0.023 cm and 0.03 cm. When the grain size decreases there will be much more sediment in suspension leading to an increase in the suspended sediment transport relative to the bed load transport. Another reason for the increased importance of the bed-load is that the model presented here includes the effect of wave asymmetry, a factor which will increase the net bed-load transport.

5.4 The Effect of Non-Uniform Grain Size

The comparisons of the calculated and observed mean concentration profiles in the preceding section showed that while the values agreed quite well in the near-bottom region, the predicted profiles decreased more rapidly than the observed values in the upper region of the flow. The most probable cause of this discrepancy is the existence of a mixture of grain sizes in the bed. The smaller grain sizes would be suspended to higher elevations and the result would be an increase in the

computed concentration at these elevations compared to the value that would be obtained using the mean grain size as the representative diameter.

Vincent and Green (1990) measured the fall velocity of 100 grains from a bottom sample and found the fall velocity to be normally distributed with a mean of 2.25 cm/s and a standard deviation of 0.36 cm/s. These values indicate that the non-uniformity of the grain size may be a significant factor in the modeling of this experiment. Therefore the model of this report, which was based on a single grain size, will be extended in a relatively simple fashion to account for the effect of non-uniform grain size in this section.

The different grain sizes will be considered only for the calculation of the suspended sediment profiles. The model calculations up to this point, i.e., up to the calculation of the reference concentration, will be done using the mean grain diameter. The reference level will be taken as $7d_m$ where d_m is the mean diameter.

This method implies that if p_i is the volume fraction of the size class d_i in the bed, the mean reference concentration for that class, $\bar{c}_{ri}$, would be given by

$$\bar{c}_{ri} = p_i \overline{c_r} \tag{154}$$

where $\overline{c_r}$ is the mean reference concentration calculated using the mean grain diameter. Equation 154 shows that according to this formulation the proportion of the different size classes available for suspension at the reference level $7d_m$ is the same as the proportion of the size classes in the bed. Though this method of calculating the reference values may be oversimplified, the objective here is to investigate the effect of non-uniform grain size on the mean concentration profile while keeping the other factors the same.

As an example, the calculations will be carried out for run VG2046 of set VG. The grain size distribution will be represented by five size classes. The selected diameters and fall velocities for these classes are given in Table 10. These values have been selected so that the fall velocity is approximately normally distributed with the measured standard deviation.

The calculated mean reference concentration will be exactly the same as the value obtained using a single grain size. The reference concentration for each size class is found from Equation 154. The mean concentration profiles for each class are calculated using Equations 95, 97, and 97. The only parameter in this equation that has a different value for each size class is the non-dimensional fall velocity, a, defined by Equation 93. The values of a for each size class are given in Table 10. Once the mean concentration profiles for each class are calculated they can be summed to obtain the total concentration.

The calculated mean concentration profile is shown in Figure 31, along with the observed profile and the profile calculated using the mean grain size. The figure shows that the use of many grain size classes increases the concentration in the region more than 10 cm above the bottom. The use of five grain sizes for the run VG2047 results in a similar improvement in the agreement with the measured profile. While the profile with many grain sizes is still not in full agreement with the observed profile, it accounts for about half the difference (in logarithmic terms) between the observed profile and the profile computed with a single grain size.

The concentrations of the different size classes at any level can be used to calculate a mean grain size for that level. The variation of the mean grain size with height above the bottom is shown in Figure 32. The figure shows that the mean grain size decreases linearly above the level $z = 7$ cm. This result agrees with the

Table 10

Parameters of the Different Grain Size Classes Used to Simulate the Grain Size Distribution for Run VG2046

Size class i	Grain diameter d_i (cm)	Fall velocity w_{fi} (cm/s)	Proportion of bed p_i	Non-dimensional fall velocity a_i
1	0.0273	2.97	0.09	1.136
2	0.0252	2.61	0.24	0.998
3	0.023	2.25	0.34	0.860
4	0.0208	1.89	0.24	0.723
5	0.0185	1.53	0.09	0.585

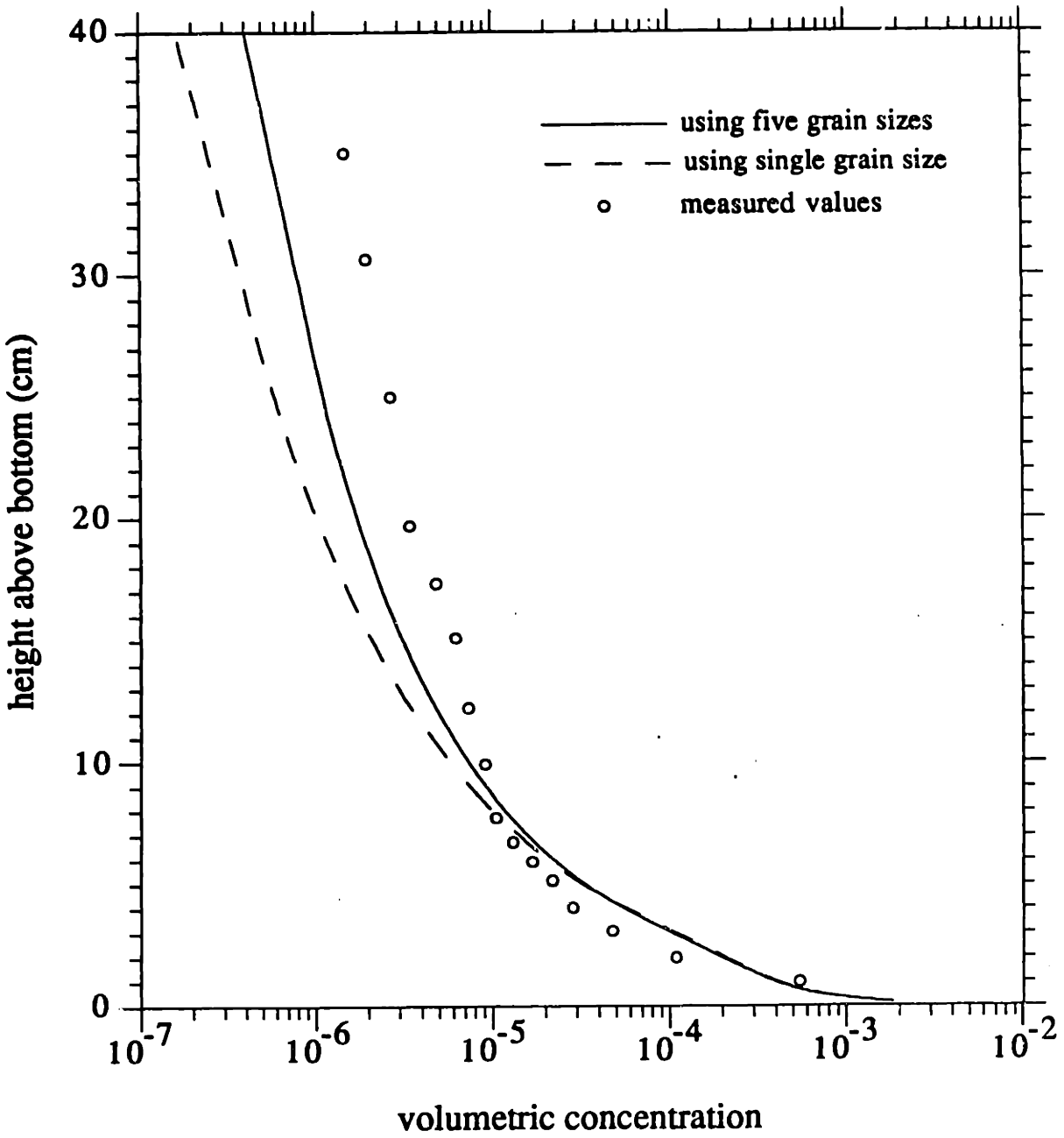

Figure 31. Mean concentration profile calculated using the grain size classes in Table 10 compared to the observed profile and the profile obtained with a single grain size, for run VG2046 of data set VG

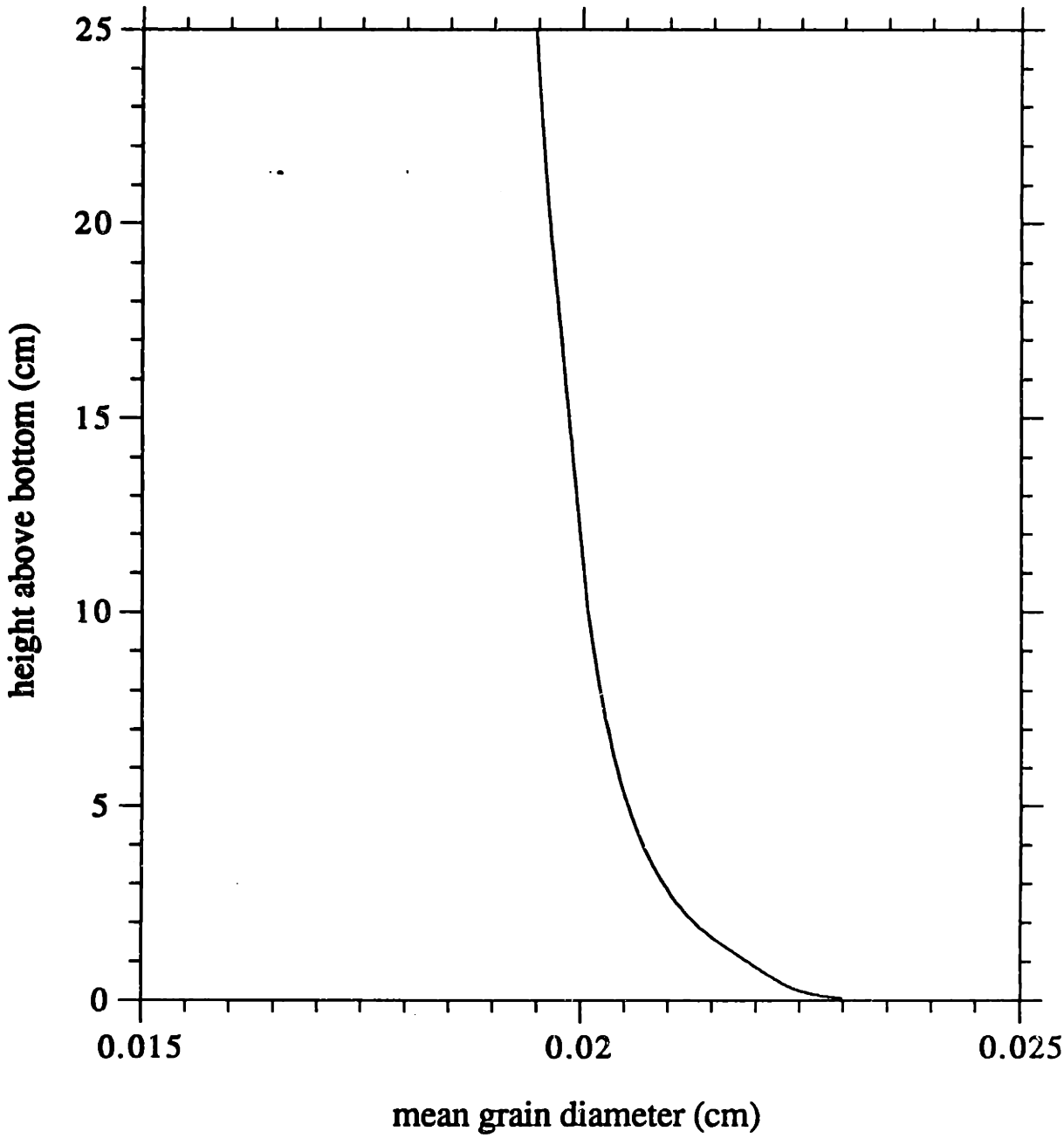

Figure 32. Variation of mean grain diameter with height for the calculation using the grain size classes of Table 10 for run VG2046 of data set VG

measurements of Hay and Sheng (1992), who used a multi-frequency ABS instrument to obtain the variation of the grain size distribution with the height above the bottom. They found that the mean grain size decreased linearly above the wave boundary layer, with a change of about 25% over 50 cm.

The decrease in grain size with height will have an effect on the interpretation of the measured backscattered acoustic signal in terms of the concentration. Vincent and Green (1990) calibrated their ABS instrument using a sample of sand from the bottom. As the calibration is sensitive to the grain size distribution there is some uncertainity associated with the measurements at the higher levels because, as shown in Figure 32, the mean grain size at these elevations has decreased appreciably from the value at the bottom.

The simple calculation presented in this section shows that non-uniformity of the bottom sediment could be the reason for the disparity between the computed and observed mean concentration profiles in the preceding section. There are also other factors, such as an errors in the calculated current shear stress and uncertainity in the calibration, that are significant. The relative effect of these factors can only be analyzed if the additional measurements discussed in Chapter 6 are available.

5.5 Comparison with the Measured Time Series of the Concentration

The comparisons so far have been with the mean concentration and the mean and wave net fluxes. These quantities are obtained by averaging over a wave period. However the model is also capable of predicting the instantaneous concentration. Comparison with a measured time series of concentration would provide a good test of the time-varying reference concentration formulation adopted for the model.

The concentration time series is available for the CC and CW data sets. Two segments of data, one from run 4 of data set CC, and the other from the single run of set CW, are selected for the comparison in this section. According to observations made during these experiments the set CC was obtained from a flat bed while the set CW was obtained from a rippled bed.

As described in Chapter 4.5.1 and Tables 5 and 6 the available data for the data set CC are the instantaneous velocity 15 cm above the bottom and the instantaneous near-bed concentration, defined as the average between 0.5 cm and 4.5 cm above the bottom. For the set CW the instantaneous velocity 10 cm above the bed is available along with measurements of the instantaneous concentration every 0.5 cm above the bed. The rate of sampling was 4 Hz for the set CC and 4.22 Hz for the set CW.

The selected times series from run 4 of set CC, of duration 62 seconds, of the velocity in the wave direction and the near-bed concentration (NBC) are shown in Figure 33. The figures shows that the velocity is highly irregular and also shows the effect of wave groupiness that results in the amplitude of the principal wave, with a period of about 8 seconds, being modulated over a long period that is comparable to the length of the record. The concentration time series also shows the effect of the wave groupiness with most of the suspension occurring during the passage of the largest wave in the group. The time series of velocity in the wave direction and the concentration 2 cm above the bottom, of duration 47.4 seconds, for the selected segment of data set CW is shown in Figure 34. Here too the velocity is quite irregular and the concentration record shows that the largest waves account for most of the suspended sediment.

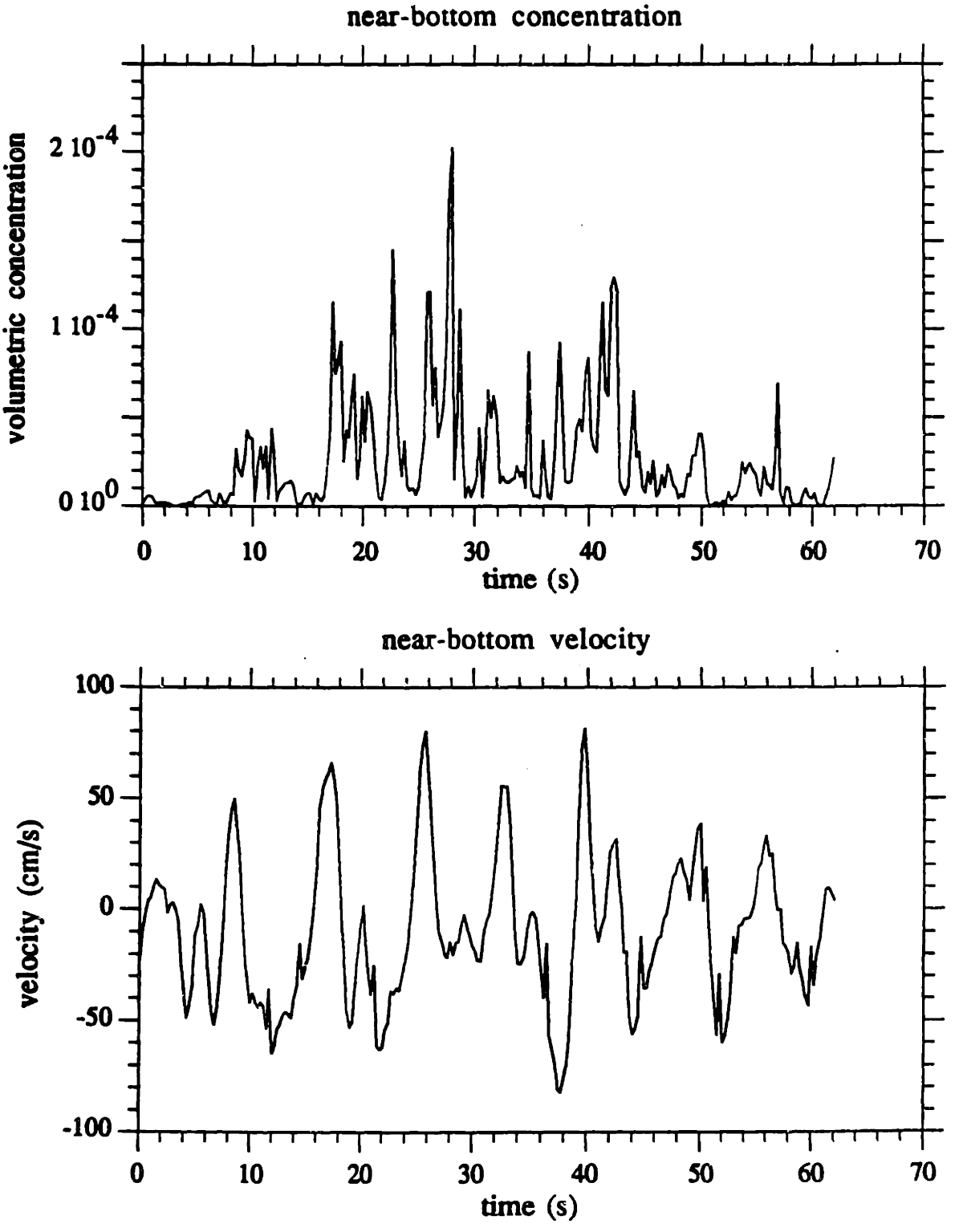

Figure 33. Selected segment of the time series of near-bottom velocity and concentration from run 4 of data set CC

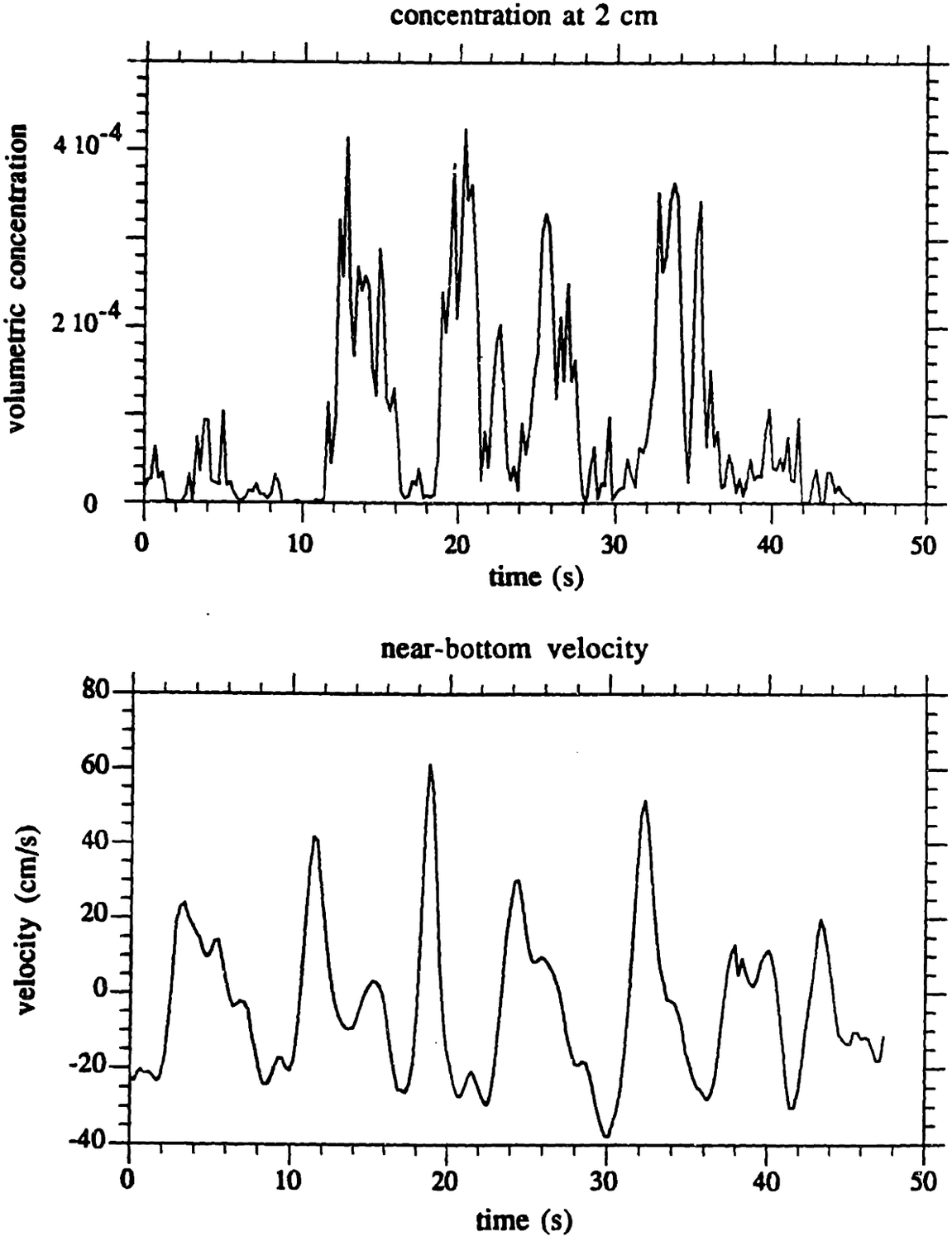

Figure 34. Selected segment of the time series of near-bottom velocity and concentration 2 cm above the bottom from data set CW

The spectral coherence between the two time series for all six runs of the data set CC was examined by Hanes (1991) who found significant coherence at both the frequency of the principal wave and the frequency of the wave groups. The effect of wave groups and the resultant variation of net transport with frequency was examined by Osborne and Greenwood (1992) and described in Chapter 1. It would be encouraging if the results of the model reproduced these features.

5.5.1 Method of Calculation

The sediment transport model developed in Chapters 2, 3, and 4 considers a fluid motion specified by a mean velocity and several sinusoidal components. Therefore the first step is to represent the velocity time series of Figures 33 and 34 in this form. This can be done conveniently by decomposing the velocity time series into Fourier components with a principal period equal to the duration of the record, 62 seconds and 47.4 seconds in these two cases. The decomposition shows that using 32 wave components results in an adequate fit for time series of Figure 33 considered here. The measured and fit velocity time series are shown in Figure 35.

The mean velocity and wave components obtained above are then used as inputs to the hydrodynamic model of Chapter 2. As described there the combined shear velocity u_{*cw} is obtained using the equivalent wave defined by Equations 50 and 51. This value is then used to solve the individual wave velocity equation and to obtain the individual wave shear strcsses and their phases by equations similar to Equation 46. Summing the individual components of the shear stress at each time will results in a time series of the shear stress.

When the equivalent roughness is set equal to the grain diameter the time series obtained in this manner will be the skin friction shear stress. These values can be

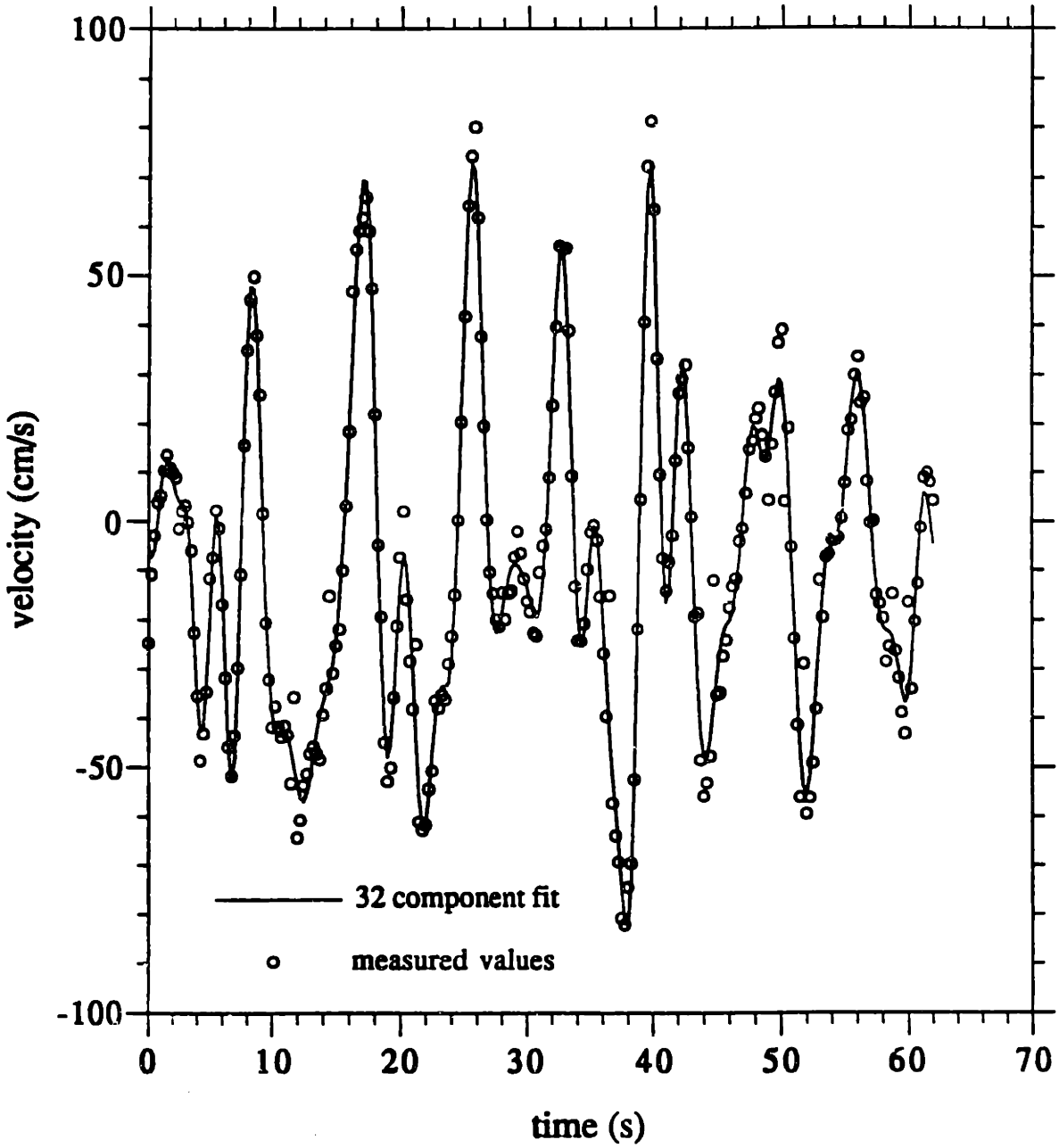

Figure 35. Comparison of the observed velocity time series for the segment from run 4 of set CC and the representation by 32 sinusoidal components

used in Equations 135, 136, and 137 to obtain the time series of the reference concentration. The calculated instantaneous reference concentration, for the segment of data set CC $c_r(t)$, using the value $\gamma_0 = 1.8\times10^{-4}$ obtained for flat beds in Chapter 4.6, is shown in Figure 36. The figure shows that the reference concentration is extremely irregular with variation at both short and long periods.

As in Chapter 4.4.4 this time series must be represented by sinusoidal components in order to use the solution derived in Chapter 4.3.3. Once again this is done by decomposing the record of $c_r(t)$ into Fourier components with a principal period equal to the duration of the record. It was found that 72 and 80 wave components were sufficient to represent the time series of the reference concentration for the segments from sets CC and CW respectively. The resulting components can be used as boundary conditions for the solution of Chapter 4.3.3 so that the magnitude and phase of the component with that particular frequency can be found as a function of z, the height above the bottom. The total instantaneous concentration at a particular height can be written as

$$c(z,t) = \bar{c}(z) + \sum_{i=1}^{n_c} c_i(z) \cos(\omega_i t + \phi_{ci}(z) + \phi_{bi}) \qquad (155)$$

where $c_i(z)$ and $\phi_{ci}(z)$ are the magnitude and phase of the component frequency ω_i at the level z, $\bar{c}(z)$ is the mean concentration, and ϕ_{bi} is the phase of the ith component of the reference concentration. n_c is the number of concentration components considered.

Similarly, the velocity at any level can be written as

$$u(z,t) = \bar{u}(z) + \sum_{i=1}^{n_u} u_i(z) \cos(\omega_i t + \phi_{ui}(z) + \phi_{ubi}) \qquad (156)$$

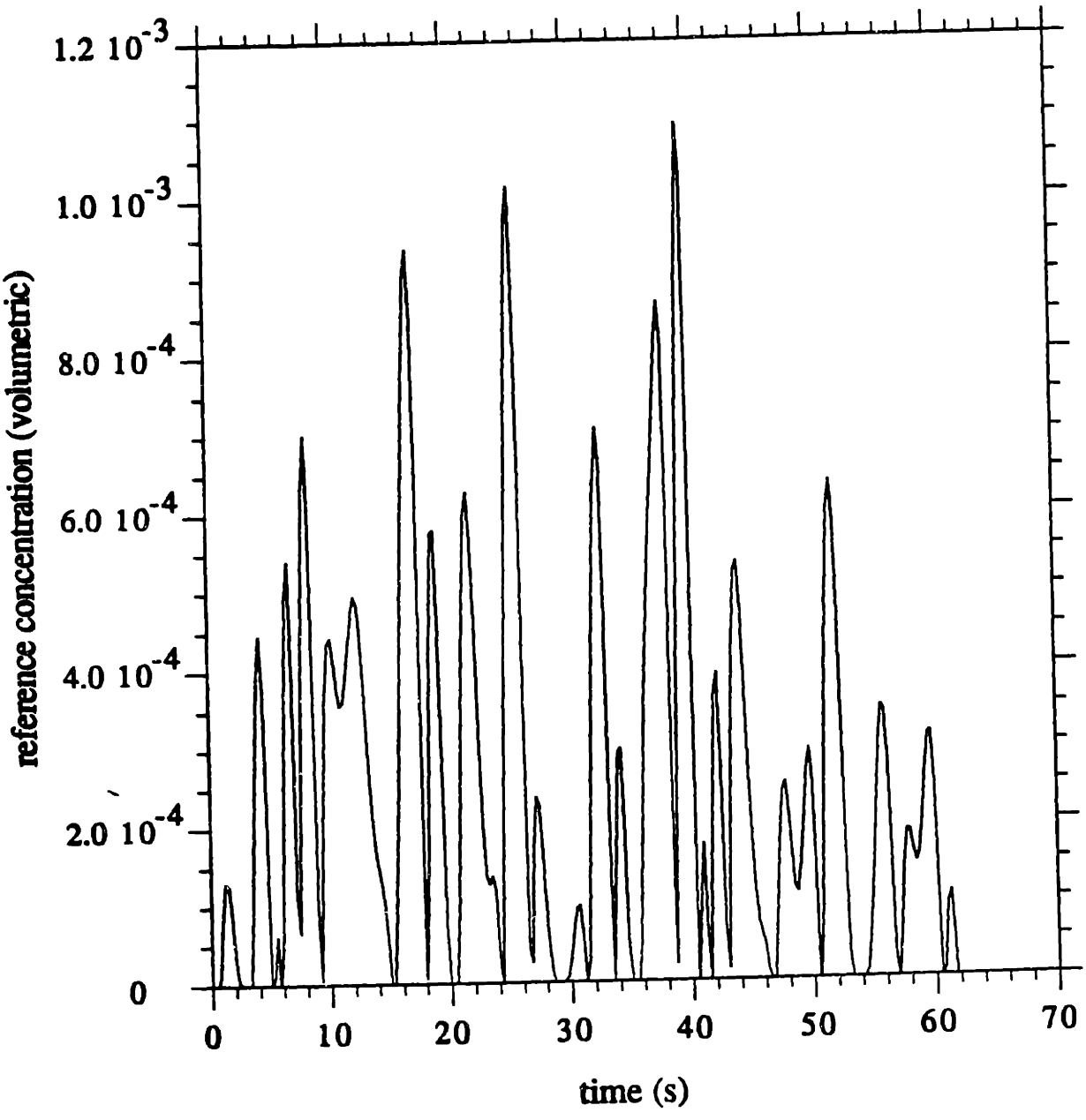

Figure 36. Time series of the instantaneous reference concentration for the segment from run 4 of set CC

where $u_i(z)$ and $\phi_{ui}(z)$ are the magnitude and phase of the velocity component with frequency ω_i, $\bar{u}(z)$ is the mean velocity, and ϕ_{ubi} is the phase of the ith component of the decomposed near-bottom velocity record. n_u is the number of velocity components considered.

Therefore the net flux at any level, T(z), can be obtained as

$$T(z) = \bar{u}(z)\bar{c}(z) + \frac{1}{2}\sum_{i=1}^{n_u} c_i(z)\, u_i(z) \cos(\phi_{ubi} + \phi_{ui}(z) - \phi_{bi} - \phi_{ci}(z)) \qquad (157)$$

while the flux for the ith periodic component will be

$$T_i(z) = \tfrac{1}{2} c_i(z)\, u_i(z) \cos(\phi_{ubi} + \phi_{ui}(z) - \phi_{bi} - \phi_{ci}(z)) \qquad (158)$$

Thus the total net transport or the net transport due to any pair of components, i.e., the net transport at a particular frequency, can be obtained by integrating Equation 157 or Equation 158 over the depth, respectively.

5.5.2 Results for the Segment of Data Set CC

For this data set the measured value is given as an average of the concentration between 0.5 cm and 4.5 cm. The corresponding value can be calculated by averaging the instantaneous concentration, c(z,t), given by Equation 155, between these levels. The predicted and measured near-bed concentrations are compared in Figure 37.

The figure shows that the time variation of the predicted time series shows some agreement with the observed time variation. Nearly all the large spikes in the measured data are represented by corresponding spikes in the prediction though the peaks do not always coincide. However, the magnitude of the predicted

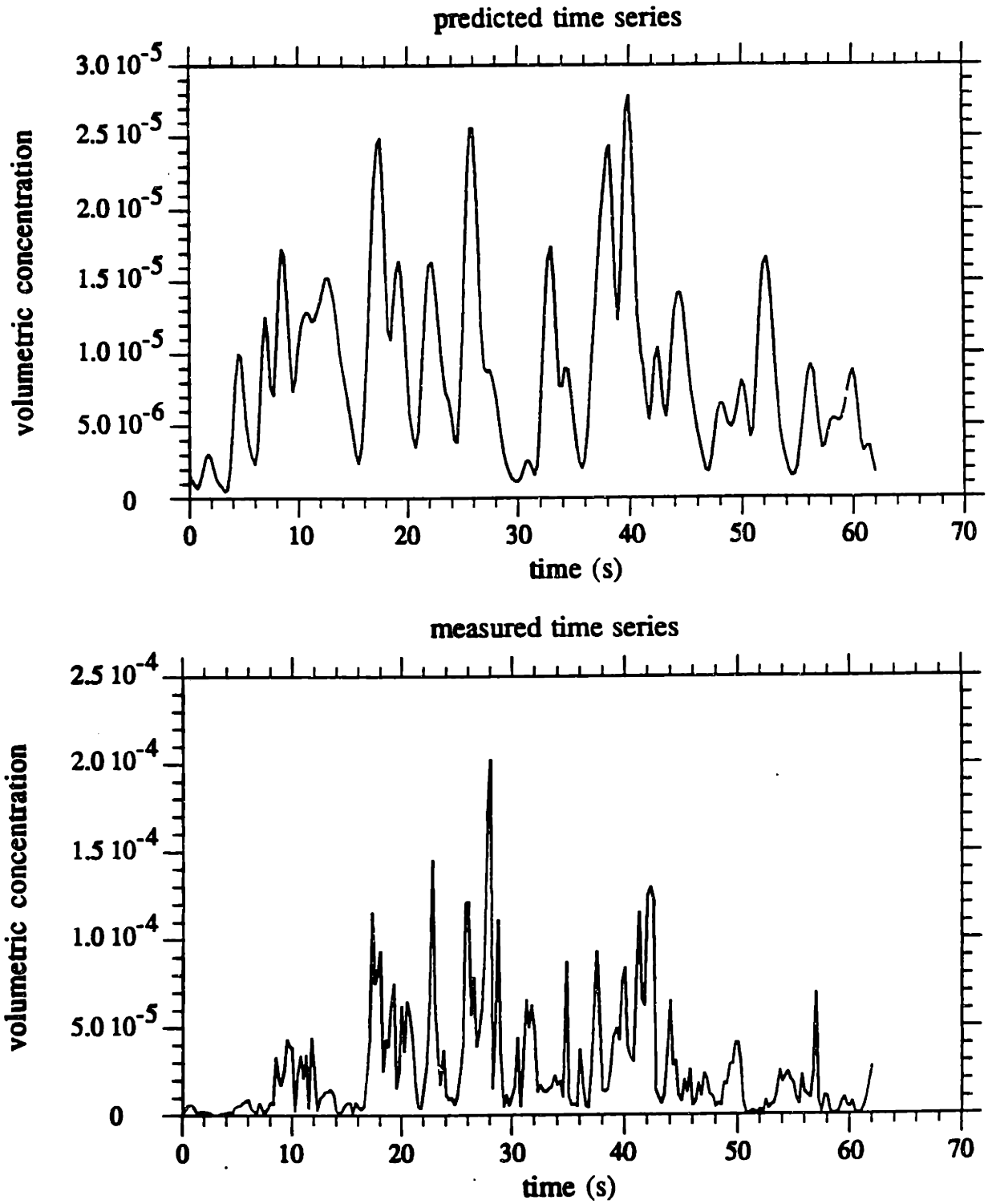

Figure 37. Comparison of the predicted time series of the near-bottom concentration with the measured time series for the segment from run 4 of set CC

concentration is less than the measured value by approximately a factor of 3. The mean of the measured time series is 2.6×10^{-5} while the mean of the predicted segment is 8.8×10^{-6}.

The difference in the magnitudes of the concentrations is due to the method used to obtain the resuspension coefficient, γ_0, in Chapter 4.6. The observed wave record was represented by just two wave components. Furthermore, the entire concentration record, of length 512 seconds, was used to obtain the mean concentration for each of the six runs in the data set CC. These mean values were used, along with the shear velocities obtained using the two-wave representation of the wave motion, to estimate the value of γ_0 shown in Figure 24. The value obtained for run 4 of this set, of which the data shown in Figure 33 is a segment, was 1.2×10^{-4} while the value of 1.8×10^{-4} given in Equation 153, and used here, is the mean of the six estimates.

Examination of the full concentration time series for the six runs of data set CC shows that the groupy nature of the waves results in the variability of the concentration record being quite high. Segments with high peaks in the concentration, such as is shown in Figure 33, are interspersed with segments of lower wave activity, with very little sediment in suspension. Therefore the mean concentration obtained by averaging the entire 512-second record will be lower than the average over a segment such as the one in Figure 33 where there is high concentration. The value of γ_0 necessary to match the means of the two time series shown in Figure 37 is 5.3×10^{-4}.

The fact that the two methods used, i.e., the two wave representations and the mean concentration over the entire record, and the duplication of the wave record, give different results for γ_0 indicates that the use of one or two wave components is

not able to capture all the details of the suspension process revealed by the time series of the concentration. However, when considering the practical application of the model to predict transport, the available information on the wave motion is likely to be limited, so that only one or two components can be used. This was the reason for basing the transport model on a wave motion represented by just two components, one with twice the frequency of the other. This representation will include the effect of wave asymmetry but will not account for the features of the wave motion, such as the processes of wave groups. The use of the model in this section is an example of the use of the solution for the periodic components of the concentration to investigate features of the detailed data that have been obtained in the last few years.

Since the resuspension coefficient, γ_0, scales both the mean and time-varying components of the concentration, the time-variation of the measured and predicted time series in Figure 37 can be compared even though their means are different. The standard deviations are 3.2×10^{-5} and 6.1×10^{-6} for the measured and predicted time series, respectively, so that the coefficients of variation are 1.23 and 0.69, respectively.

A more detailed examination of the correspondence, or lack thereof, between the two time series can be done by calculating the cross-covariance function between the two sequences. The unbiased estimate of the cross-covariance function, normalized by the product of the standard deviations of the two series, is shown in Figure 38. The high values of the cross-covariance at lags of greater than about 35 seconds are due to the large variance in the estimate of the cross-covariance function at large lags.

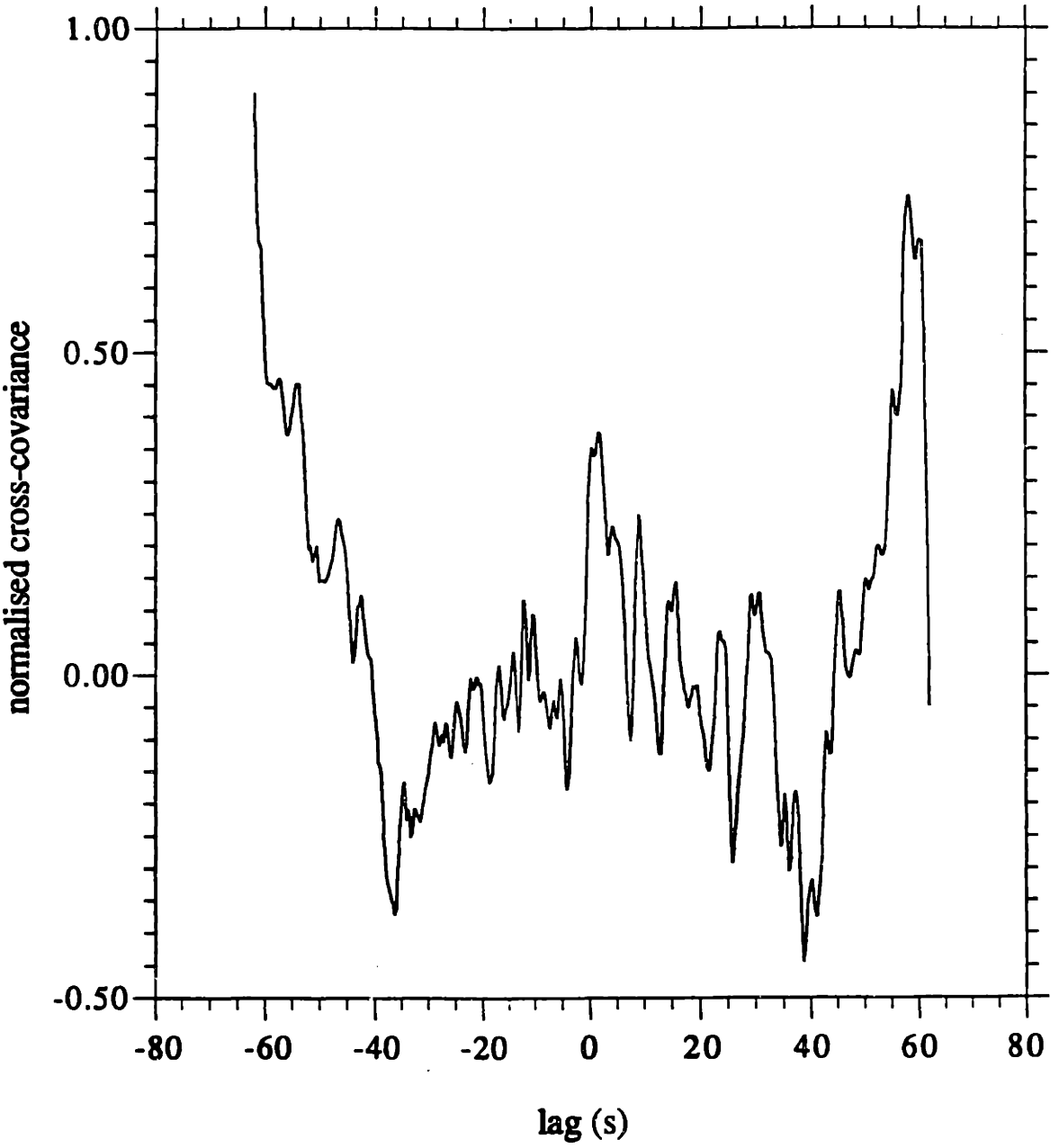

Figure 38. Normalized cross-covariance function between the measured and predicted time series for the selected segment of data set CC

The figure shows that the cross-covariance function has a peak near a lag of zero, indicating some degree of correlation between the two series. The peak occurs at a positive lag of 1.5 seconds and the covariance coefficient at this point is 0.38. The covariance coefficient at zero lag is 0.33. While these coefficients are not very high they are significant relative to the 95% confidence level for two uncorrelated series, which is about 0.13 in this case. The other peaks in the cross-covariance function are spaced about 7.5 seconds apart. Figure 33 shows that this spacing corresponds to the dominant wave period, so that both the measured and the predicted time series can be expected to vary with this period, leading to the observed behavior of the cross-covariance function.

The estimated coherence function between the two series is shown in Figure 39. This estimate was obtained by dividing the 248-point time series into sets of 124 points and using a 50% overlap. The figure shows the coherence function to vary rapidly with frequency. This spikiness, which is probably due to the small number of samples used, makes it difficult to draw any conclusions about the relation between the two time series from the coherence function. The 95% level of confidence for two uncorrelated series is about 0.25 so that the figure does imply some degree of correlation.

It should be recalled that during the calculations outlined in the preceding section, the reference concentration variation shown in Figure 36 was fit by 72 wave components. As the length of the record is 62 seconds the use of 72 components means that the smallest period present in the solution is about 0.86 seconds. This value is larger than the sampling interval of 0.25 used to obtain the measured time series, and therefore the model results shown here will not be able to represent the high-frequency variation of the data.

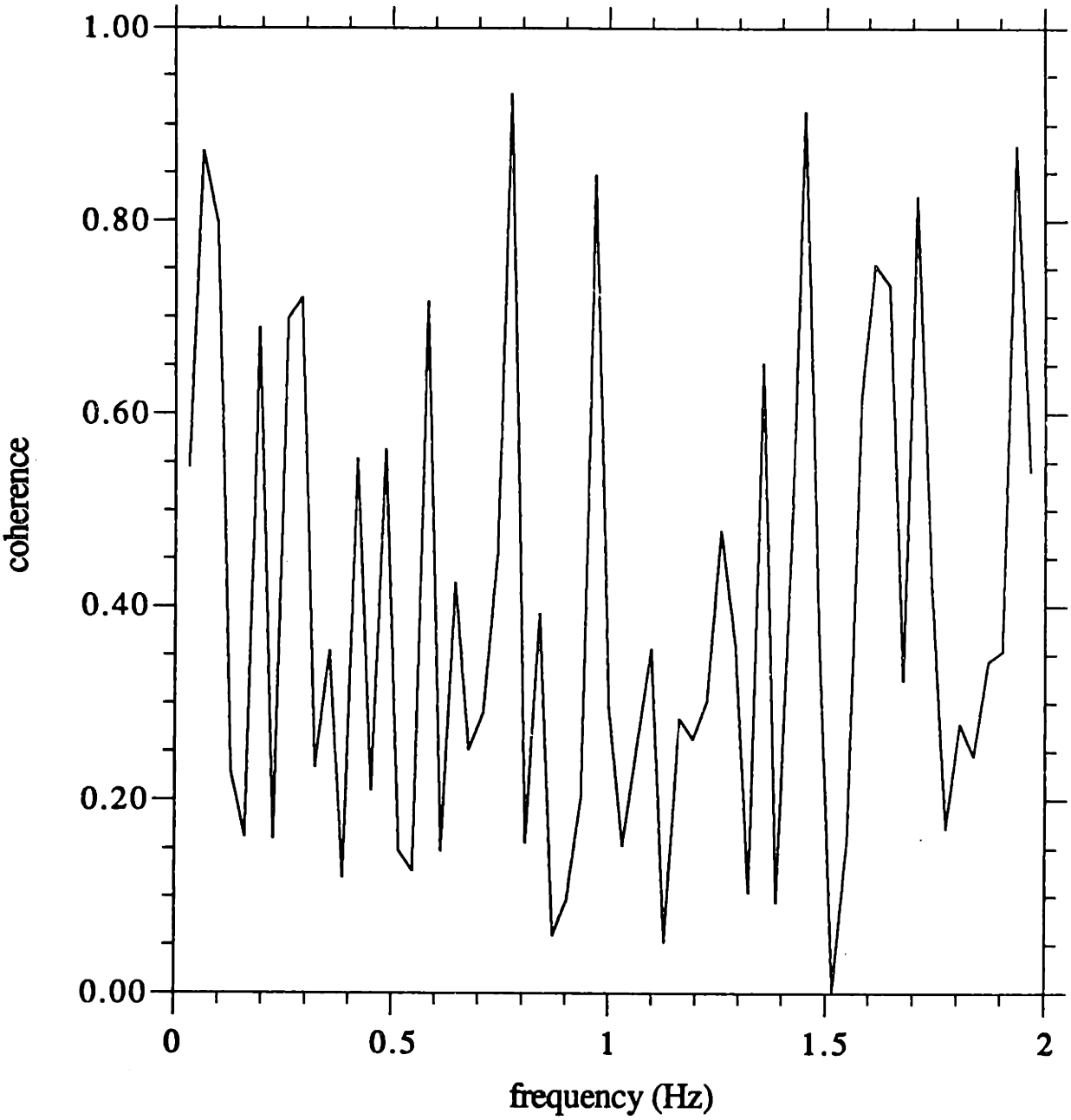

Figure 39. Spectral coherence between the measured and predicted time series for the selected segment of data set CC

Figure 40 shows the predicted time series compared to the moving average of the measured data using a 1-second averaging window. This comparison enables the similarities and differences between the two time series to be observed more clearly. The most important qualitative difference in the time variation is the fact that the response shown by the model to the larger waves in the group, relative to the response to the smaller waves, is less than the measured response. This difference can be deduced by the underprediction of the peaks near the middle of the record, where the waves are large, as shown in Figure 33, and by the overprediction of the peaks at the two ends of the record, when the waves are smaller. In other words, the variability of the predicted concentration is less than the observed variability, even though the model uses practically the same velocity record observed in the field as the input. This difference in variability is also apparent from the coefficient of variation of the measured time series being larger than that of the predicted time series.

A possible reason for the lower variability in the predicted time series of Figures 37 and 40 is the use of a combined shear velocity u_{*cw}, based on the equivalent wave defined by Equations 50 and 51. The shear velocity, through its use in the eddy viscosity distribution of Equation 8, determines the intensity of the turbulent mixing. It is likely that the mixing acting during the passage of the largest waves of the group is larger than what is indicated by the value of u_{*cw} based on the equivalent wave. Use of a larger shear velocity would reduce the relative decrease of the higher frequency components, compared to the lower frequency components, with increase in height, as shown in Figure 19. The result would be increased variability of the predicted near-bottom concentration.

Despite the difference in variability and the rather low correlation between the predicted and measured time series in Figure 37, the figure shows that the model is

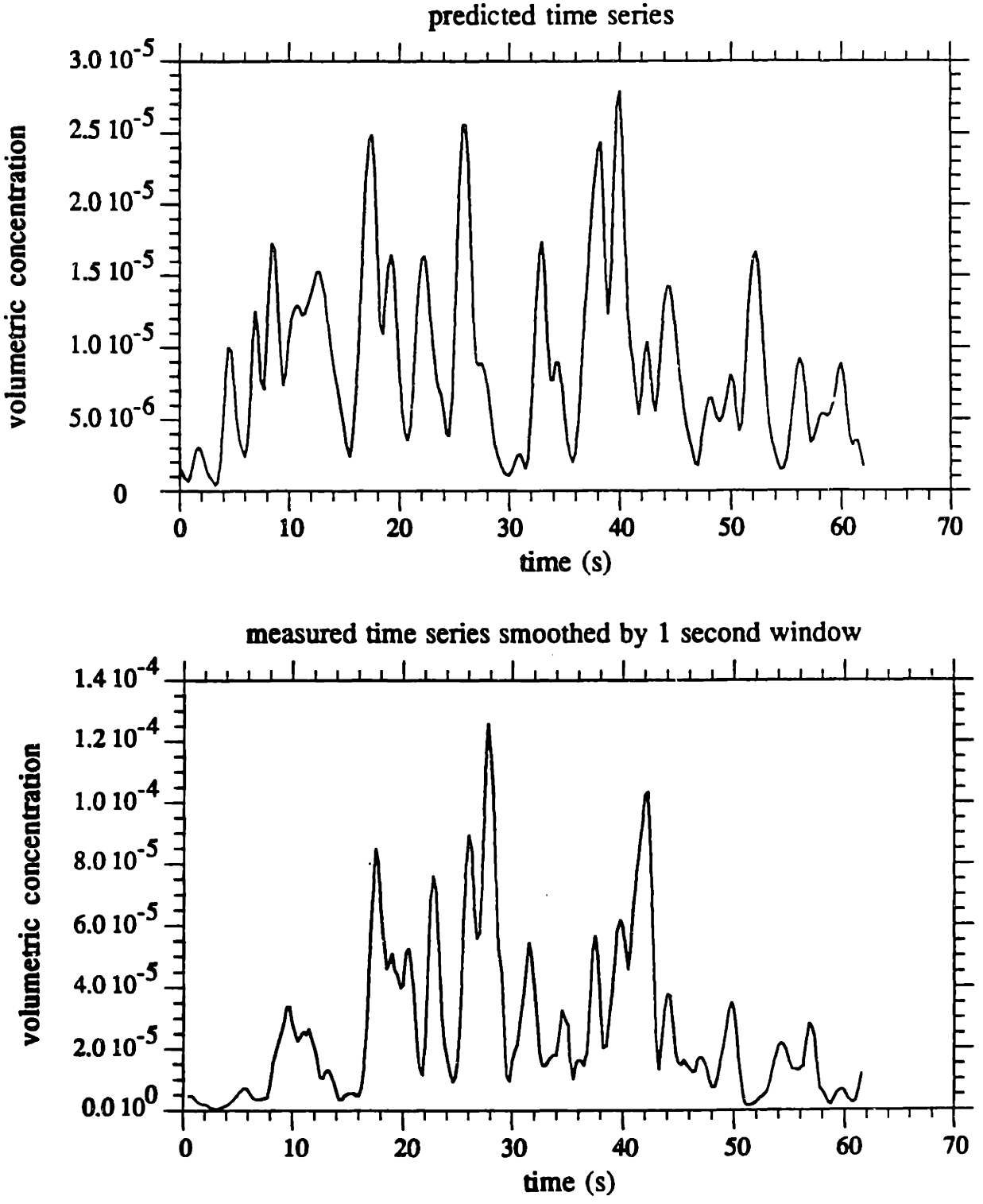

Figure 40. Comparison of the predicted time series of the near-bottom concentration with the time series obtained by smoothing the measured values using a 1-second window for the segment from run 4 of set CC

quite successful in reproducing the principal features of the observed time series. In view of the highly irregular nature of the flow this agreement is very encouraging and is evidence that the important physical processes of sediment suspension are well described by the formulation of the time-varying reference concentration used in the calculation. The calculation presented here is one of the first to attempt to model an observed time series of concentration using a single consistent model for both the velocity and concentration.

As described in Chapter 5.5.1, the transport due to each pair of velocity and concentration components, i.e., the net transport at each frequency, can be calculated by integrating Equation 158 over the depth. Since the velocity was represented by 32 components for this calculation there will be a corresponding number of components of the transform. These components along with the transport due to the mean components, is shown as a function of the frequency in Figure 41. Onshore transport is shown by a positive value in this figure.

The mean transport is offshore as the current velocity is offshore for this experiment. The transport due to the periodic components is found to be both onshore and offshore. The figure shows onshore (positive) transport at about 0.8 rad/sec and 1.4 rad/s (about 8-second and 4.5-second periods) and smaller offshore (negative) values centered around 0.2–0.4, 0.92, and 1.7 rad/sec (32-16–, 7-, and 3.7-second periods). While the wave velocity record of Figure 33 does show the effect of wave groupiness, it is difficult to estimate the associated group frequency from the short segment selected. Therefore while the transport at low frequencies is offshore the results shown here do not clearly associate this offshore transport with the wave groups.

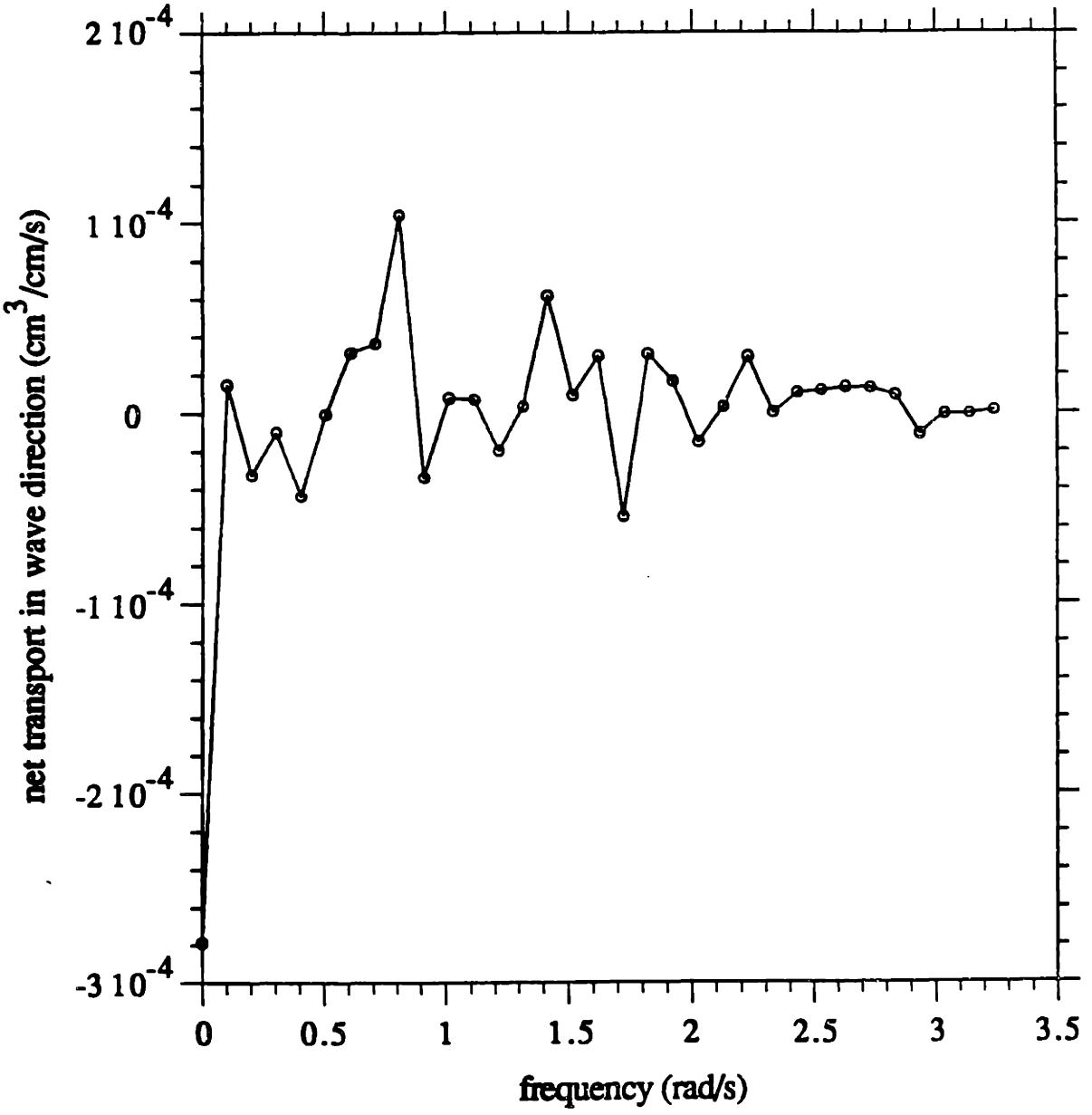

Figure 41. Variation of the calculated net suspended sediment transport with the frequency of the components for the segment from run 4 of set CC

The phenomenon of offshore transport at frequencies comparable to the group frequencies has been described by Greenwood (1992). These researchers analyzed field data and showed that the increased concentration under the large waves in a group coincided with the offshore phase of the long wave at group frequencies, resulting in a net offshore transport at these frequencies. The use of a much larger segment of data would resolve the issue of whether the model does actually reproduce this phenomenon. This is an example of the use of the model to investigate the processes that couple the fluid velocity and the resulting sediment transport.

The magnitude of the mean transport is $-2.8\times10^{-4}cm^3/cm/sec$. The mean transport calculated using the two-wave representation of the entire 512-second run, and a value of 1.8×10^{-4} for γ_0, is $-6.5\times10^{-4}cm^3/cm/sec$. The net wave transport for the 62-second segment was $2.1\times10^{-4}cm^3/cm/sec$ while it was $1.1\times10^{-4}cm^3/cm/sec$ for the whole segment. The time series of skin friction shear stress used to calculate the reference concentration can also be used to evaluate the time series of bed load flux for the time interval considered here. The average bed load transport was found to be $49\times10^{-4}cm^3/cm/sec$, i.e., onshore bed load transport. In contrast the value obtained for the entire 512-second run was -89×10^{-4}, i.e., offshore bed load transport. This difference, and also the reduced mean transport seen for the small segment relative to that for the full record, is probably due to the large asymmetric waves observed in the 62-second segment that cause sufficient onshore transport to overcome the tendency towards offshore transport caused by the offshore mean flow. In the full 512-second time series, which includes periods of lower wave strength, the effect of the current dominates to cause net offshore bed load transport.

5.5.3 Results for the Segment of Data Set CW

The predicted time series of the concentration 2 cm above the bottom is compared to the measured time series in Figure 42. The model is able to predict all the large spikes in the concentration time series. However, as with the preceding case, the magnitude of the predicted concentration is less than the measured values. The mean values for the segments shown are 8.7×10^{-5} and 1.5×10^{-5} for the measured and predicted series, respectively. As before, this difference is due to the use of the two-wave representation of the wave motion and the use of the entire 249-second record to obtain the value of $\gamma_0 = 1.8\times10^{-3}$ that was used here.

Considering the time-variation of the two sequences, the coefficient of variation is calculated as 1.2 and 1.3 for the measured and predicted time series, respectively, indicating that the variability of the two records is similar. It should be noted that 80 sinusoidal components were used to simulate the 47-second record so that the highest frequency in the predicted time series is about 1.7 Hz, while the measurements were obtained at 4.22 Hz.

The normalized, unbiased estimate of the cross-covariance function between the two sequences is given in Figure 43. As in Figure 38, the high values of the cross-covariance at lags greater than about 30 seconds are the result of the small number of estimates available to calculate the cross-covariance at these large lags. The figures show a sharp peak near zero lag. This peak is located at a positive lag of 1.2 seconds and the value of the peak covariance coefficient is 0.61, while the value at zero lag is 0.27. This value of the peak coefficient is significantly higher than 0.14 which is the 95% confidence interval for the uncorrelated series, and shows that the agreement between the two time series is much better than in the preceding calculation. In Figure 43, the subsidiary peaks in the cross-covariance function,

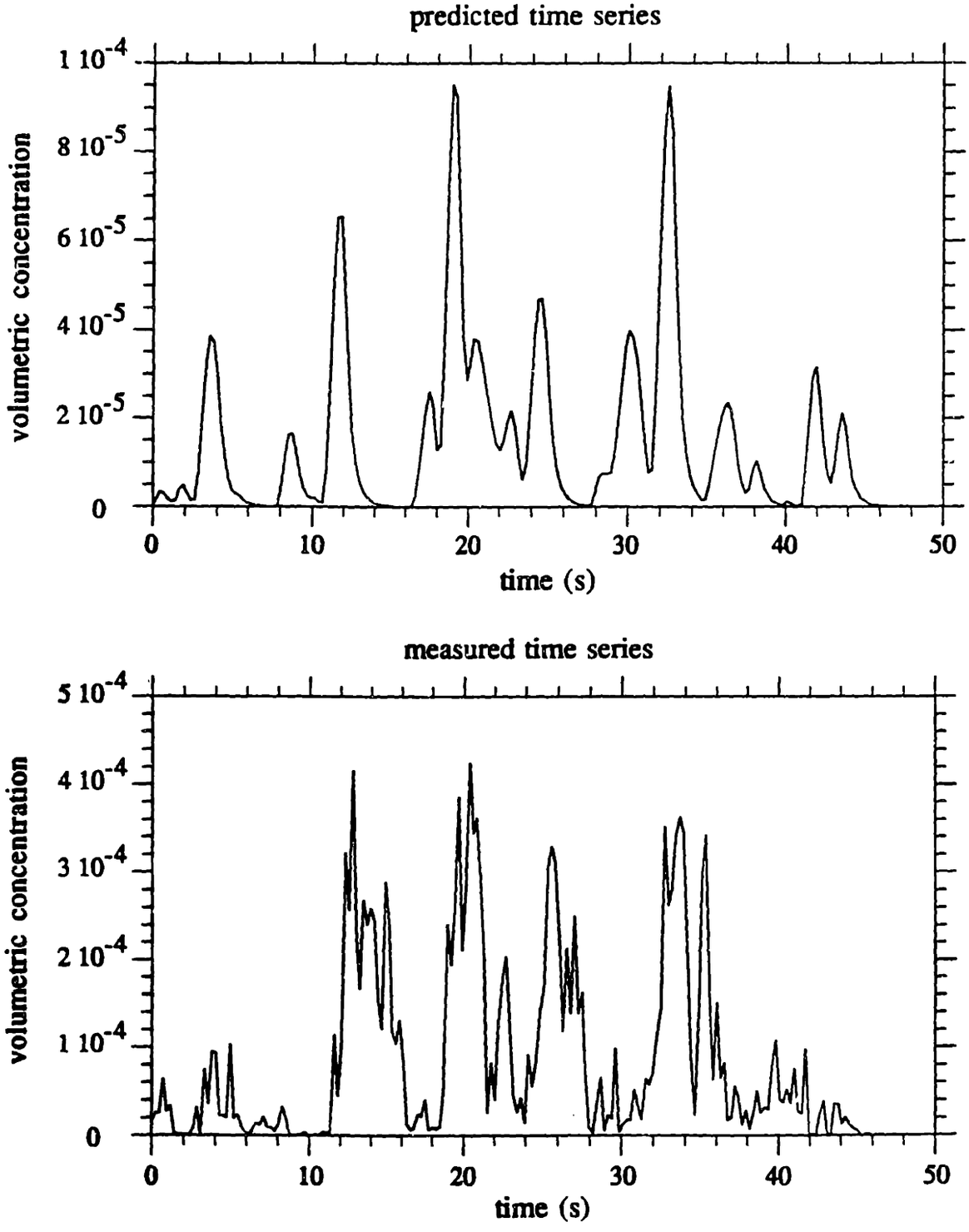

Figure 42. Measured and predicted time series for the concentration 2 cm from the bottom for the selected segment of data set CW

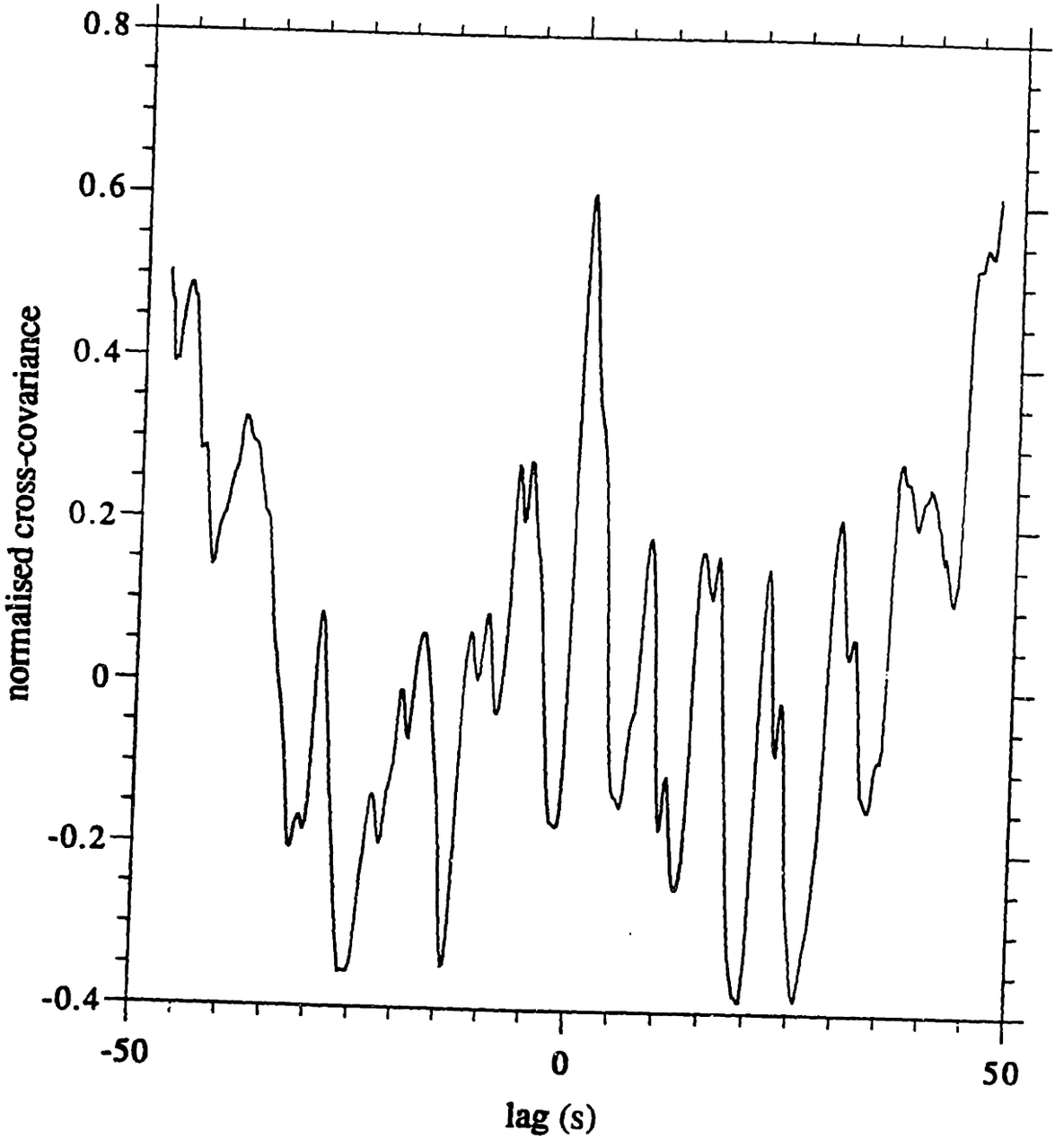

Figure 43. Normalized cross-covariance function between the measured and predicted time series for the selected segment of data set CW

spaced about 7 seconds apart, are due to both the measured and predicted time series being related to the dominant wave motion, which has a period of around 7 seconds.

The estimated coherence between the two time series is shown in Figure 44. This function was obtained by dividing the 200-point time series into sets of 100 and using a 50% overlap. The 95% confidence interval for two uncorrelated series is about 0.28. This figure indicates significant coherence at frequencies below approximately 0.4 Hz (periods above 2.5 seconds). Since it is these lower-frequency components that make important contribution to the suspended sediment flux, this result indicates that the model will be able to make a good estimate of the transport even though it is not able to represent the higher frequencies in the concentration.

The cross-covariance and coherence functions in Figures 43 and 44 show that the predicted time series is in quite good agreement with the data. In fact the agreement is significantly better for this case than for the segment of Run 4 of data set CC analyzed previously. This better agreement for the segment of set CW runs counter to the expectation that the simple reference concentration model used here would perform better for flat bed conditions, as seen for data set CC, than for rippled bed conditions, as seen for set CW.

A possible reason for the relatively poor performance of the model for the flat bed time series is that the waves were considerably stronger and more irregular than the waves for the rippled bed time series, as can be seen by comparing Figures 33 and 34. The stronger wave motion would lead to a more variable concentration. Furthermore the difference in the mean grain diameter, 0.18 mm for the flat bed run and 0.3 mm for the rippled bed, would contribute to the increased variability, particularly at high frequencies, of set CC relative to set CW.

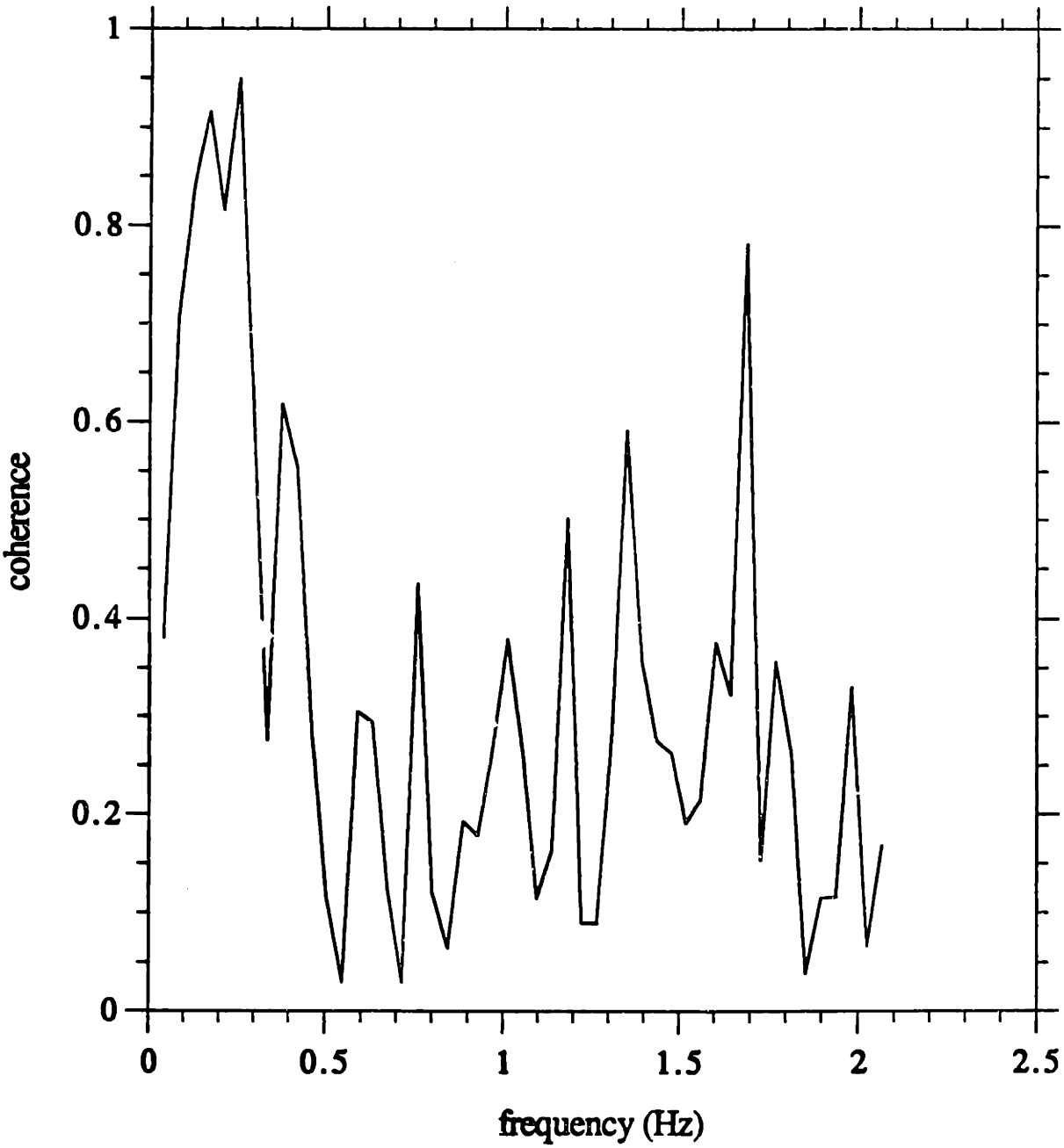

Figure 44. Spectral coherence between the measured and predicted time series for the selected segment of data set CW

The variation of net transport with frequency for the segment of data set CW is shown in Figure 45. The mean (zero) frequency transport is offshore due to the mean current being directed offshore. The mean transport for this segment is -3.9×10^{-5} cm^2/cm/s compared to the value of -1.3×10^{-4} given in Table 9 for the entire 248-second run. The wave flux shows a large peak corresponding to a wave period of about 7 seconds, which is approximately the dominant wave frequency, and subsidiary peaks at higher frequencies. Negative (offshore) transport is only shown at a few points. The net wave transport is 4.2×10^{-4} cm^3/cm/s compared with the value of 7.2×10^{-4} cm^3/cm/s for the two-wave representation given in Table 9. The bed load transport is found to be 31×10^{-4} cm^3/cm/s compared to the value of 44×10^{-4} cm^3/cm/s in Table 9.

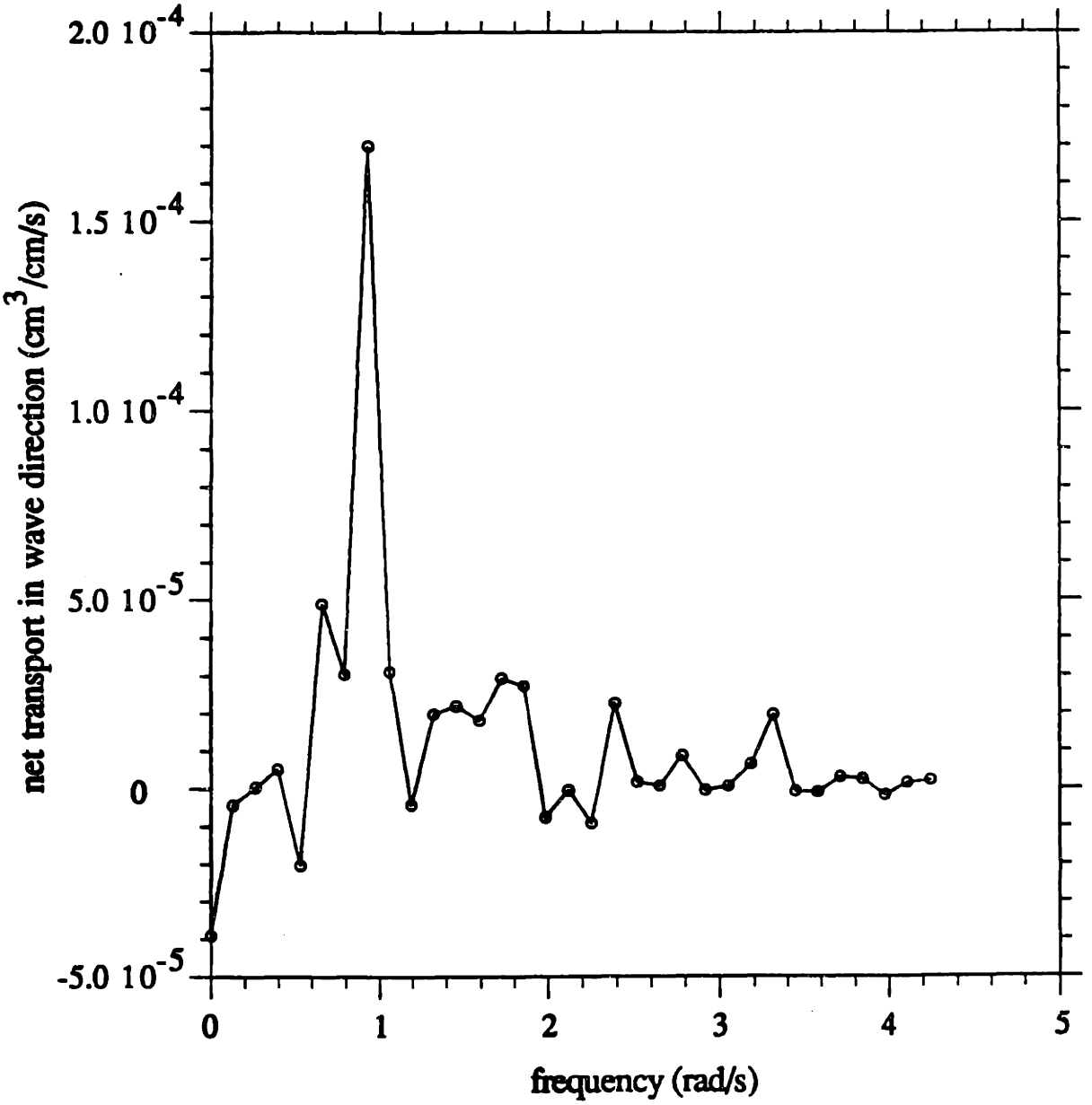

Figure 45. Variation of net transport with frequency for the selected segment of data set CW

CHAPTER 6

SUMMARY AND CONCLUSIONS

6.1 Review of Model Developments and Results

The objective of this study was to apply the simple eddy viscosity models, developed for wave-current interaction, to the problem of sediment suspension and transport in order to develop a consistent model for sediment transport in wave-current flows. The motivation for this study was first, that while the model of Glenn and Grant (1987) has been proposed and used widely for the calculation of suspended sediment transport in wave-current flows, the hydrodynamic aspect of this model was improved upon by the model Wikramanayake (1989).

Second, recent developments in instrumentation have allowed measurements of the suspended sediment concentration to be made very near the bottom under field conditions. Thus it is now possible to calibrate models of sediment suspension more accurately than before. Third, and most importantly, all proposed models calculate the suspended sediment transport by integrating the product of mean concentration and mean velocity. However, recent field experiments indicate that the flux due to the time-varying quantities is as important and sometimes dominates the flux due to the mean components. Therefore, the model developed in this report calculates the transport using both the mean and time-varying components of the concentration.

The solution of the hydrodynamic aspect of the wave-current problem using the time-invariant eddy viscosity model of Wikramanayake (1989) was described. Wikramanayake (1989) showed that the inability of this model to reproduce some effects of wave-current interaction predicted by higher order numerical models was

due to the assumption of a time-invariant eddy viscosity model. A model that included a time-varying eddy viscosity was derived in Appendix A. While this time-varying model does show the features of the more complicated models, a comparison of the results of the two eddy viscosity models showed that the velocities and shear stresses predicted were quite similar. Considering the uncertainties involved in other aspects of the model, as well as the less complicated solution involved, it was decided to use the time-invariant model of Wikramanayake (1989) for the suspended sediment model.

Since the model is meant to be used with field data, the representation of the irregular wave motion seen in the field by one or more periodic components was discussed. As some of the features of the field waves were brought out by more than one wave component, the wave-current model was extended to include a wave motion specified by an arbitrary number of wave components. Predictive relations for the equivalent roughness of a movable bed under field conditions were developed by analyzing both laboratory and field data.

Following the conceptual bed load model of Madsen (1991), Equation 81, which is a generalization of the steady flow bed load equation derived by Meyer-Peter and Muller, was selected to calculate the bed load transport under wave-current flow. A consistent method of calculating the skin friction shear stress was described. The equation governing the distribution of suspended sediment was given and solutions obtained for both the mean and the periodic components. A boundary condition of the reference concentration type was selected for the suspended sediment model.

A review of the various formulations proposed for the mean reference concentration showed that while the most commonly used model was that of Smith (1977), comparison with field and experimental data cast doubts on its general

validity. However, the consistent analysis of steady flow data by Zettler (1991) did suggest that the reference concentration was proportional to the non-dimensional excess shear stress, S', for a particular grain size for fine-grained sands. As this conclusion was also supported by the saltation model of Madsen (1991), the simple relation of Equation 133 was selected for the mean reference concentration. The reference level was specified as seven times the grain diameter based on the results of the saltation model.

Considering the time-varying components of the reference concentration the review did not find any model that had been compared to experimental data. However, bearing in mind the demonstration by Madsen (1991) that the near-bed sediment grains can be assumed to respond instantaneously to changes in the external flow, it was decided to use Equation 135, which extended Equation 133 to relate the time-varying reference concentration to the instantaneous value of S'. The derivation of the reference values for the periodic components from the instantaneous reference concentration was described.

The only undetermined parameter in the model was the resuspension coefficient, γ_0, which is the constant of proportionality in Equation 135. It was decided to use concentration measurements from recent field experiments, some of which were made very close to the bed, to determine this coefficient. After a thorough analysis it was concluded that the data sets VG, CW, and CC, obtained by Vincent and Green (1990), Vincent and Osborne (personal communication), and Hanes (1991), were the most reliable of the data sets considered.

The calculation resulted in an estimate of γ_0 from each measurement of the mean concentration. Since the concentration was measured at several points in the vertical for the data sets VG and CW, there were many estimates of γ_0 for these

runs. However only the estimates from the near-bottom region were used as these were the most reliable. The data set CC yielded only a single estimate of γ_0 for each run as only one measurement of the mean concentration was available. The selected values of γ_0 are given in Equation 153. This equation indicates different values of γ_0 depending on whether the bed is rippled or flat. Some recent measurements by Vincent et al. (1991) support this conclusion, while also indicating that there may be a smooth transition between the two values of Equation 153 as the ripples on the bed are washed away.

The calculated mean concentration and mean and wave flux profiles were compared to the observed values for the data sets VG and CW. The computed values were in good agreement with the measurements close to the bed. This agreement was to be expected because the selected value of γ_0 was chosen to fit these near-bed values. However, the predicted and observed mean concentration profiles diverged as the height increased. The effect of non-uniform grain size was investigated using a simple extension of the model. The calculations for the data set VG, where the grain size distribution at the bottom was measured by Vincent and Green (1990), showed that the non-uniformity of the grain size could explain about half the divergence between the measured and predicted mean concentration profiles.

Observation of the shape of the observed mean concentration profiles showed that while their shape corresponded to the theoretical solution of Equations 95, 97 and 99, these shapes indicated values of the parameters α, ϵ, and a that were different from the calculated values. This difference could be caused by errors in the fall velocity or the shear velocity, which were parameters calculated by the model. However, it is not possible to distinguish among these possibilities because of the lack of information about the experimental conditions. The calculated flux profiles

were found to reproduce the shape of the estimated flux profiles quite well. However, the calculated wave flux did not show as large an offshore component as the estimated value. A possible reason for this difference is the use of Equation 135 for the reference concentration. The time variation of the reference concentration specified by this equation may not be appropriate for the rippled bed conditions expected for the data sets VG and CW. The calculations of the net suspended sediment transport showed that the contribution of the time-varying components was comparable to the contribution of the mean components. The calculated net bed load transport was found to be larger than, though of the same order as, the total suspended load.

The model developed so far represents the observed wave motion by one or two periodic components. The time-varying concentration predicted by the model will therefore be only a representative periodic concentration that can not be compared directly to the observed irregular variation of the concentration. However, the extended hydrodynamic model of Chapter 2.4 can be used together with the solution for the component of the concentration and the generalized reference concentration relation of Equation 138 to calculate the time-varying concentration that corresponds to a segment of the observed velocity record.

This calculation was described and carried out in Chapter 5.5 for a segment of the data set CC and one from the data set CW, with flat bed and rippled bed conditions respectively. The time-variation of the predicted time series was quite similar to that of the measured time series. However, the predicted mean concentration over each segment was less than the measured value by a factor of about three for the segment from the set CC and about five for the segment from set CW. This difference in the mean value was a consequence of using the value of the

resuspension coefficient, γ_0, that was obtained using the entire length of the run and a different representation of the wave motion.

The correspondence between the time-variation of the measured and predicted concentration time series was examined using the cross-covariance function and the spectral coherence function. Significant correlation between the measured and predicted time series was found for both segments considered. The correlation for the rippled bed case was found to be better than for the flat bed case. The good agreement obtained for the rippled bed case indicates that the reference concentration model of Equation 138 performs adequately under these conditions. The variation of net transport with frequency was also calculated.

6.2 Effect of the Uncertainties in the Model Parameters

While the parameter γ_0 was the only undetermined coefficient of the model developed in Chapter 4, it should be recalled that the calculations involved in the calibration of this coefficient involved the estimation of several other quantities. These include the sediment fall velocity, the equivalent bottom roughness, the equivalent wave components and the critical shear stress for the initiation of motion. Therefore all the uncertainties present in these estimations, along with any measurement errors, will be reflected in a scatter of the resulting values of γ_0.

The influence of the uncertainties should be kept in mind when considering the scatter of the values of γ_0 as evidence of the validation or refutation of the adopted reference concentration model. The comparison of the model results with the field data also showed that some of the disagreement between the results and the data could be due to errors in such model parameters as the sediment fall velocity and the shear velocity. Therefore independent measurements of these quantities would

be very useful in obtaining more reliable estimates of γ_0 as well as in suggesting improvements to the model.

The model presented here calculates the equivalent bottom roughness, k_n, by first estimating the bed condition and the ripple height from Equation 72 and then calculating k_n from Equation 79, which uses the ripple height or the grain diameter to scale the roughness, depending on whether the bed was rippled or flat. The estimation of ripple height using Equation 72 involves a considerable error. Therefore it is desirable to have independent estimates of the ripple geometry by making on site measurements during the experiments. This task is usually carried out by divers. However, measurements made by divers, particularly of the ripple height, are not very accurate. A more sophisticated method is to use a high resolution tracking sonar as described by Greenwood et al. (1990).

For rippled beds the equivalent roughness can be calculated using the first part of Equation 79, which was obtained after analysis of laboratory measurements of energy dissipation under waves. The second part of this equation however, which is assumed to give the equivalent roughness for the case of sheet flow, has limited experimental backing. An alternative method of estimating the bottom roughness is by measuring the mean velocity at more than one point in the vertical.

If the measurement is done at two points, independent estimates of both the current shear velocity, u_{*c}, and the equivalent roughness, k_n, can be made once the wave conditions are known. Measuring the current at more than two points will increase the confidence in these estimates. While the roughnesses calculated in this way will be specific to the wave-current model used, the method has the advantage of avoiding the uncertainty in the prediction of the ripple geometry. If the ripple

height and bed condition are observed independently this method will also serve to check the validity of Equation 79 for wave-current interaction in the field.

Another advantage in using several current meters at different elevations to measure the horizontal velocity is that checking the internal consistency between the readings at the different levels will indicate the "quality" of the data. For example, if the mean velocity is measured at four elevations, the values would be expected to show that the mean velocity is proportional to the logarithm of the height. However, the four two-axis current meters should also show that the direction of the mean velocity was the same at the four elevations. If the directions at the four elevations are very different it would be an indication of some problem with the instruments. This type of check is particularly important in the case of field experiments because the instruments are usually left on the bottom for long periods between calibrations and other adjustments.

Another contribution to the uncertainty in the estimates of γ_0 is the fact that sediment beds in the field consist of many different grain sizes. The distribution of grain sizes in suspension will vary with height above the bottom as shown by the calculations of Chapter 5.4. This variation will affect the calibration of the concentration measuring device. Furthermore, as the model uses a single grain size, it can be expected that the predicted concentrations will decrease with height faster than the observed concentration. This difference is caused by the finer grain sizes being suspended to greater heights than predicted by the model. Estimates of γ_0 made from heights where this difference is significant will result in values of γ_0 that are too large. As discussed in Chapter 4.6, this was the situation for the DK data set.

The effect of the non-uniform grain size distribution can be assessed by taking suction samples of the sediment laden water at several levels during the experiment. These samples would verify the calibration of the instruments and at the same time indicate whether the representation of the sediment by a single diameter was valid. Another method of obtaining the grain size distribution as a function of the height is to use an ABS instrument that operates at several frequencies as described by Hay and Sheng (1992). In the absence of such measurements of the change in the size distribution with height, it should be concluded that the reliability of the estimates of γ_0 decreases with the height of measurement.

The fall velocity of the sediment is another quantity that is often neglected in field measurements. If the sediment is specified solely by the grain diameter the fall velocity can be computed using the empirical relation given by Madsen and Grant (1976). However, this relation is based on a certain shape of grain and would also require an assumption regarding the specific density of the grains. The inaccuracy that may be caused by the use of this relation can be seen in the values for the fall velocity for the sets VG and MB in Table 7. Both sets have the same mean grain diameter. Vincent and Green (1990) measured the fall velocity of 100 grains and obtained a mean fall velocity of 2.25 cm/s. The empirical relation, used for data set MB, assuming s = 2.65, resulted in a value of 2.78 cm/s. The two values differ by about 20% so that the corresponding values of the parameter a, defined by Equation 93, will also differ by 20%. This change in a could result in quite different estimates of γ_0.

The critical Shields parameter for the initiation of motion, ψ_{cr}, is calculated in the model using the modified Shields curve proposed by Madsen and Grant (1976). This curve is based on experimental data that show considerable scatter. Uncertainty in ψ_{cr} would result in uncertainty in the mean value of S' that appears

on the right-hand side of Equation 152, thus affecting the estimates of γ_0. Equation 136 shows that this uncertainty will decrease as the ratio of the wave skin friction shear stress, ψ_w', to ψ_{cr}, increases. Therefore the reliability of the estimates of γ_0 increases as the excess skin friction shear stress increases. Based on this criterion the values in Table 8 show that the data sets CC and VG would be considered more reliable while some of the estimates of γ_0 from the sets DK and MB would be subject to large uncertainties because the excess skin friction shear stress is small. Unlike the fall velocity, it is difficult to measure ψ_{cr} directly. A possible method would be to observe the near-bottom sediment motion using a video camera. These observations could be used, together with measurements of the velocity and the hydrodynamic model, to obtain a better estimate of the parameter ψ_{cr}.

6.3 Possible Improvements to the Model

The model described in Chapter 4, together with the values of γ_0 in Equation 153, is a fully predictive model for the calculation of the sediment transport due to waves and currents. The most crucial model parameter is the resuspension coefficient, γ_0, which was determined using just three field experiments for rippled bed conditions and six experiments for flat bed conditions. Therefore the most important area of possible improvement is to obtain more estimates of γ_0 using data from a wide variety of wave, current and sediment conditions. These data could be obtained in the field or in large scale laboratory experiments, i.e., using wave periods and water depths comparable to the values in the field. For example, the data obtained in the large scale laboratory experimental project SUPERTANK, described by Kraus (1991), would be ideal for this purpose.

Another area that could be improved is in the calculation of the equivalent roughness. Equation 72, which calculates the ripple height in the field was based

upon a limited number of data, some of which were obtained with considerable uncertainty as to the wave conditions. More good quality measurements of ripple geometry in the field should be done to increase the reliability of the predictive relations. The equivalent roughness for sheet flow conditions is another aspect of the model that should be improved by carrying out more laboratory and field experiments.

The comparison of the calculated and estimated wave flux profiles, i.e., the flux due to the periodic components, showed that the calculated wave flux did not show as large a region of offshore flux as the flux estimated from the measurements. A possible reason for this difference is the use of Equation 135 to represent the time variation of the reference concentration. The wave conditions and the observations of the suspended sediment concentration suggest a rippled bed for this experiment. The variation of the instantaneous concentration in Equation 135 was derived from the physical idea of entrainment from a thin bed load layer in a steady flow. While this idea may also apply in the case of a wave motion over a flat bed, i.e., condition of sheet flow, the situation is very different when ripples are present on the bed.

As described in Chapter 1.2, entrainment from a rippled bed has been observed to be caused by the periodic shedding of sand-filled vortices from the ripple crests. It is obvious that any reference concentration proposed to account for this process would vary strongly with time. Furthermore as the entrainment process is controlled by the reversal of the near-bottom flow, and not by the bottom shear stress as implied by Equation 138, such a formulation may not be suitable.

However, the calculation of the instantaneous concentration over a ripped bed, for the segment from data set CW, in Chapter 5.5 showed that Equation 135 gives good results even for a rippled bed. Therefore, the development of a more

physically realistic reference concentration model for a rippled bed would not be a very important improvement to the model when considering the other uncertainties.

The bed load transport calculation showed that the bed load transport was larger than the suspended load transport, though the two values are of the same order of magnitude. This result is contrary to some previous calculations, which, however, were carried out for finer sediments than those observed in these experiments. The bed load transport equation, Equation 81, has had only limited experimental verification under wave-current conditions. Such verification could be carried out using the recent experimental measurements made by Ribberink and Al-Salem (1992) in a large wave tunnel.

6.4 Conclusions

The model developed and calibrated in this thesis can be used to calculate the sediment transport under a combined wave and current flow. A FORTRAN program that carries out these calculations is given in Wikramanayake and Madsen (1992) along with a detailed description and instructions for its use. While it has some significant uncertainties, it is a "state of the art" model in that it is the best that can be done given the accuracy of the available experimental measurements. Further refinement of the model can be done only when more precise and detailed data become available. One of the most important assumptions of the model is the representation of the instantaneous reference concentration by Equation 135. The comparison of the predicted and measured concentration time series in Chapter 5.5 shows that this assumption is quite adequate for both rippled and flat beds.

The primary use of the model is to predict a point value of the sediment transport when given the wave, current and sediment properties at that point. This

model could be incorporated in a larger model that allows for the variation of the waves and the currents to calculate erosional and depositional patterns in the coastal environment. An example of such an application would be to calculate the equilibrium beach profile, outside the surf zone, for a given wave condition.

There are also some other important applications of the model. One of these is in the design of field experiments. The discussion of the uncertainties in the model parameters used in the calculations of Chapter 4.6 brought out some important measurements that can be used to minimize the uncertainty and provide checks of the internal consistency of the data. These measurements include

a) Measurement of the concentration as close to the bed as possible, preferably within a few multiples of the boundary layer length scale, δ, defined in Equation 49.

b) Measurement of the variation of the grain size distribution with height above the bottom. This can be done by actually collecting samples or by using a multi-frequency ABS instrument as done by Hay and Sheng (1992).

c) Measurement of the mean velocity at more than one point in the vertical. Such measurements would provide a check on the current shear velocity, u_{*c}, and the bed roughness, k_n, which are calculated by the model.

d) Measurement of the bed forms during the experiment.

e) Measurement of the fall velocity.

f) Observation of the entrainment process using a video camera.

Though this list may seem difficult to fulfill there are some experimental programs, for example that outlined by Greenwood et al. (1990), that include all the features mentioned above.

Another important application would be in the interpretation of field data. For example, the most versatile instrument for field experiments is the acoustic backscatter sensor (ABS). The calibration of this instrument depends on the mean grain size and the grain size distribution. The calculations of Chapter 5.4 show that both these quantities vary with height above the bottom. Therefore the data from an ABS calibrated using sediment from the bottom could be expected to be accurate only near the bottom. The variation of the grain size calculated by the model could be used to correct the data from higher elevations.

Finally, the model can be used to explore the processes involved in coastal sediment transport. An example of this use is the calculation of the frequency-dependent transport in Chapter 5.5. The offshore transport at wave group frequencies reported by Osborne and Greenwood (1992) is one of the processes that could be investigated by this method.

REFERENCES

Abramowitz, M., I. A. Stegun (eds.). 1971. *Handbook of Mathematical Functions.* Dover, New York.

Amos, C. L., A. J. Bowen, D. A. Huntley, C. F. M. Lewis. 1988. "Ripple generation under the combined action of waves and currents on the Canadian continental shelf." *Continental Shelf Research* 8(10):1129–1153.

Bagnold, R. A. 1946. Motion of waves in shallow water, Interaction between waves and sand bottoms. *Proceedings of the Royal Society of London*, Ser. A, 187:1–18.

Bakker, W. T. 1974. Sand concentration in an oscillatory flow. *Coastal Engineering, Proceedings of the 14th International Conference*, 1129–1148.

Bakker, W. T., and T. van Doorn. 1978. Near-bottom velocities in waves with a current. *Proc. 16th Int. Conf. Coast. Eng.*, 1394–1413.

Bedford, K. W., O. Wai, R. Van Evra, P. Velissariou, J. Lee, C. Libicki. 1990. The local near-bottom response of a dredged material placement site to wind and tide effects. Report prepared for the U.S. Army Corps of Engineers, Waterways Experiment Station, Coastal Engineering Research Center.

Boyd, R., D. L. Forbes, D. E. Heffler. 1988. Time-sequence observations of wave-formed sand ripples on an ocean shore face. *Sedimentology* 35:449–464.

Brevik, I. 1981. Oscillatory rough turbulent boundary layers. *J. Waterways, Harbors and Coastal Eng. Div., ASCE* 107(WW3):175–188.

Carstens, M. R., F. M. Neilson, H. D. Altinbilek. 1969. Bed forms generated in the laboratory under an oscillatory flow: Analytical and experimental study. TM-28, U.S. Army Corps of Engineers, Coastal Engineering Research Center.

Davies, A. G., R. L. Soulsby, H. L. King. 1988. A numerical model of the combined wave and current bottom boundary layer. *Journal of Geophysical Research* 93(C1):491–508.

Dingler, J. R. 1975. Wave formed ripples in nearshore sands. Ph.D. thesis, University of California, San Diego.

Dingler, J. R., D. L. Inman. 1976. Wave formed ripples in nearshore sands. *Proceedings of the 15th Coastal Engineering Conference*, 2109–2126.

Doering, J. C., A. J. Bowen. 1988. Wave-induced flow and nearshore suspended sediment. *Coastal Engineering, Proceedings of the 21st International Conference*, 1452–1463.

van Doorn, T. 1981. Experimental investigations of near-bottom velocities in water waves with and without a current. Report No. M1423, Delft Hydraulics Laboratory, Delft, Netherlands.

Drake, D. E., D. A. Cacchione. 1989. Estimates of the suspended sediment reference concentration and the resuspension coefficient from near-bottom observations on the California shelf. *Continental Shelf Research* 9:51–64.

Einstein, H. A. 1950. The bedload function for sediment transportation in open channels. Tech. Rep. 1026, U.S. Dept. of Agriculture, Soil Conservation Service.

Engelund, F., J. A. Fredsoe. 1976. Sediment transport model for straight alluvial channels. *Nordic Hydrology* 7:293–306.

Fredsoe, J., O. H. Anderson, S. Silberg. 1985. Distribution of suspended sediment in large waves. *Journal of Waterway, Port, Coastal and Ocean Engineering (ASCE)* 111(6):1041–1059.

Glenn, S. M., W. D. Grant. 1987. A suspended sediment correction for combined wave and current flows. *Journal of Geophysical Research* 92(C8):8244–8264.

Goud, M. R. 1987. Prediction of continental shelf sediment transport using a theoretical model of the wave-current boundary layer. Ph.D. Thesis, Woods Hole Oceanographic Institution/Massachusetts Institute of Technology, Cambridge, Massachusetts.

Grant, W. D., O. S. Madsen. 1979. Combined wave and current interaction with a rough bottom. *Journal of Geophysical Research* 85(C4):1797–1808.

Grant, W. D., O. S. Madsen. 1982. Movable bed roughness in unsteady oscillatory flow. *Journal of Geophysical Research* 87(C1):469–481.

Greenwood, B., P. D. Osborne, A. J. Bowen, D. G. Hazen, A. E. Hay. 1990. Nearshore sediment flux and bottom boundary dynamics: The Canadian coastal sediment transport programme (C-COAST). *Proc. 22nd Coastal Engineering Conference (ASCE)*, 2227–2240.

Greenwood, B., P. D. Osborne, A. J. Bowen. 1991. Measurements of suspended sediment transport: Prototype shorefaces. *Coastal Sediments '91, Proceedings of the ASCE Specialty Conference*, 284–299.

Hagatun, K., K. J. Eidsvik. 1986. Oscillating turbulent boundary layer with suspended sediments. *Journal of Geophysical Research* 91(C11):13045–13055.

Hanes, D. M. 1991. Suspension of sand due to wave groups. *Journal of Geophysical Research* 96(C5):8911–8915.

Hanes, D. M., D. A. Huntley. 1986. Continuous measurements of suspended sand concentration in a wave dominated nearshore environment. *Continental Shelf Research* 6(4):585–596.

Hay, A. E., J. Sheng. 1992. Vertical profiles of suspended sand concentration and size from multifrequency acoustic measurements. *J. of Geophys. Res. (Oceans)* 97(C10):15661–15677.

Hayakawa, N., G. Tsujimoto, H. Hashimoto. 1983. Velocity distribution and suspended sediment concentration over large scale ripples. *Coastal Engineering in Japan* 26:91–100.

Hildebrand, F. B. 1976. *Advanced calculus for applications*, Prentice-Hall, Englewood Cliffs, New Jersey, 2nd Ed.

Hill, P. S., A. R. M. Nowell, P. A. Jumars. 1988. Flume evaluation of the relationship between suspended sediment concentration and excess boundary shear stress. *J. Geophys. Res.* 93:12,499–12,509.

Hom-ma, M., K. Horikawa, R. A. Kajima. 1965. Study on suspended sediment due to wave action. *Coastal Engineering in Japan* 8:85–103.

Horikawa, K., A. Watanabe, S. Katori. 1982. Sediment transport under sheet flow conditions. *Coastal Engineering, Proceedings of the 18th International Conference*, 1335–1352.

Huntley, D. A., D. M. Hanes. 1987. Direct measurement of suspended sediment transport. *Coastal Sediments '87, Proceedings of the ASCE Specialty Conference*, 723–737.

Inman, D. L. 1957. Wave generated ripples in nearshore sands. TM-100, U.S. Army Corps of Engineers, Beach Erosion Board.

Inman, D. L., A. J. Bowen. 1963. Flume experiments on sand transport by waves and currents. *Coastal Engineering Proc. of the 8th Int. Conf.*, 137–150.

Jonsson, I. G. 1966. Wave boundary layers and friction factors. *Proceedings of the 10th Coastal Engineering Conference, Tokyo*, 127–148.

Jonsson, I. G., N. A. Carlsen. 1976. Experimental and theoretical investigations in an oscillatory turbulent boundary layer. *Journal of Hydraulic Research* 14(1):45–60.

Kajiura, K. 1968. A model of the bottom boundary layer in water waves. *Bulletin of the Earthquake Research Institute* 46:75–123.

Kennedy, J. F., M. Falcon. 1965. Wave generated sediment ripples. Report No. 86, Hydrodynamics Laboratory, Dept. of Civil Engineering, Massachusetts Institute of Technology.

Kennedy, J. F., F. A. Locher. 1972. Sediment suspension by water waves. *Waves on beaches.* R. E. Meyer (ed.). Academic Press, pp 249–295.

van Kesteren, W. G. M., W. T. Bakker. 1984. Near bottom velocities in waves with a current: Analytical and numerical computations. *Proc. 19th Int. Conf. Coast. Eng.*, 1161–1177.

Kim, S. C. 1990. Inner continental shelf benthic boundary layer dynamics and suspended sediment transport. Ph.D. Thesis, School of Marine Science, College of William and Mary in Virginia.

Kraus, N. C., J. M. Smith, C. K. Sollitt. 1991. Overview of SUPERTANK data collection project. *Transactions of the American Geophysical Union*, Fall meeting.

Lambie, J. M. 1984. An experimental study of the stability of oscillatory flow bed configurations. M.S. thesis, Massachusetts Institute of Technology.

Lofquist, K. E. B. 1978. Sand ripple growth in an oscillatory flow water tunnel. TP-78-5, U.S. Army Corps of Engineers, Coastal Engineering Research Center.

Lofquist, K. E. B. 1980. Measurements of oscillatory drag on sand ripples. *Proceedings of the 17th Coastal Engineering Conference*, 3087–3106.

Lofquist, K. E. B. 1986. Drag on naturally rippled beds under oscillatory flows. MP-86-13, U.S. Army Corps of Engineers, Coastal Engineering Research Center.

Madsen, O. S. 1991. Mechanics of cohesionless sediment transport in coastal waters. *Coastal Sediments '91, Proceedings of the ASCE Specialty Conference*, 15–27.

Madsen, O. S. 1992. Spectral wave-current bottom boundary layer flows. To be presented at the 23rd Int. Conf. on Coastal Engineering, Venice, Italy.

Madsen, O. S., W. Grant. 1976. Sediment transport in the coastal environment. Report No. 209, Ralph M. Parsons Laboratory, Dept. of Civil Engineering, MIT, Cambridge, Mass.

Madsen, O. S., P. P. Mathisen, M. M. Rosengaus. 1990. Movable bed friction factors for spectral waves. To appear in *Proceedings of the 22nd Coastal Engineering Conference.*

Madsen, O. S., L. D. Wright, J. D. Boon, T. A. Chisholm. (_____) Wind stress, bottom roughness and sediment suspension on the inner shelf during an extreme storm event. Submitted to *Continental Shelf Research.*

Mathisen, P. P. 1989. Experimental study on the response of fine sediments to wave agitation and associated wave attenuation. M.S. thesis, Massachusetts Institute of Technology.

Miller, M. C., P. D. Komar. 1980a. Oscillation sand ripples generated by laboratory apparatus. *Journal of Sedimentary Petrology* 50(1):173–182.

Miller, M. C., P. D. Komar. 1980b. A field investigation of the relationship between oscillation ripple spacing and the near-bottom water orbital motion. *Journal of Sedimentary Petrology* 50(1):183–191.

Mogridge, G. R., J. W. Kamphuis. 1972. Experiments on bed form generation by wave action. *Proceedings of the 13th Coastal Engineering Conference*, 1123–1134.

Nakato, T., F. A. Locher, J. R. Glover, J. F. Kennedy. 1977. Wave entrainment of sediment from rippled beds. *Journal of Waterway, Port, Coastal and Ocean Engineering (ASCE)* 103(WW1):83–99.

Nielsen, P. 1979. Some basis concepts of wave sediment transport. Series Paper No. 20, Institute of Hydrodynamics and Hydraulic Engineering, Technical University of Denmark.

Nielsen, P. 1983. Analytical determination of nearshore wave height variation due to refraction, shoaling and friction. *Coastal Engineering* 7:233–251.

Nielsen, P. 1984. Field measurements of the time-averaged suspended sediment concentration under waves. *Coastal Engineering* 8:51–72.

Nielsen, P. 1986. Suspended sediment concentrations under waves. *Coastal Engineering* 10:23–31.

Nielsen, P. 1988. Three simple models of wave sediment transport. *Coastal Engineering* 12:43–62.

Nikuradse, J. 1932. Gesetzmässigkeit der turbulenten. Stromung in glatten Rohren. *Forshg. Arb. Ing.–Wes.* 356

Osborne, P. D., B. Greenwood. 1992. Frequency dependent cross-shore suspended transport: 1, A non-barred shoreface. *Marine Geology* 106:1–24.

Ribberink, J. S., A. Al-Salem. 1992. Sediment transport, sediment concentrations and bedforms in simulated asymmetric wave conditions. Report H 840 Part V, Delft Hydraulics, Delft, The Netherlands.

Riedel, H. P., J. W. Kamphuis, A. Brebner. 1972. Measurement of bed shear stresses under waves. *Proceedings of the 17th Coastal Engineering Conference*, 587–603.

Rosengaus, M. 1987. Experimental study on wave generated bedforms and resulting wave attenuation. Ph.D. thesis, Massachusetts Institute of Technology.

Sato, S. 1992. Sand transport under wave groups. To be presented at the 23rd Int. Conf. on Coastal Engineering, Venice, Italy.

Sato, S., K. Horikawa. 1988. Sand ripple geometry and sand transport mechanism due to irregular oscillatory flows. *Proceedings of the 21st Coastal Engineering Conference*, 1748–1762.

Schlichting, H. 1968. *Boundary layer theory*, 6th ed., McGraw-Hill.

Shi, N. C., L. H. Larsen, J. P. Downing. 1985. Predicting suspended sediment concentration on continental shelves. *Marine Geology* 62:255–275.

Skafel, M. G., B. G. Krishnappan. 1984. Suspended sediment distribution in wave field. *Journal of Waterway, Port, Coastal and Ocean Engineering (ASCE)* 110(2).

Sleath, J. F. A. 1982. The suspension of sand by waves. *Journal of Hydraulic Research* 20(5):439–452.

Sleath, J. F. A. 1985. Energy dissipation in oscillatory flow over rippled beds. *Coastal Engineering* 9:159–170.

Smith, J. D. 1977. Modeling of sediment transport on continental shelves. *The sea*, Vol. 6., E. D. Goldberg, ed., Wiley Interscience, New York, pp 539–577.

Smith, J. D., S. R. Mclean. 1977. Spatially averaged flow over a wavy surface. *Journal of Geophysical Research* 82(12):1735–1745.

Soulsby, R. L. 1991. Aspects of sediment transport by combined waves and currents. *Proc. IAHR International Symposium on the Transport of Suspended Sediments and its Mathematical Modelling, Florence, Italy.*

Staub, C., I. G. Jonsson, I. A. Svendsen. 1984. Variation of suspended sediment in oscillatory flow. *Coastal Engineering, Proceedings of the 19th International Conference*, 2310–2321.

Stefanick, T. A. 1979. A realistic model of wave attenuation due to bottom friction. M.S. thesis, Massachusetts Institute of Technology.

Thorne, P. D., C. E.Vincent, P. J. Hardcastle, S. Rehman, N. Pearson. 1991. Measuring suspended sediment concentrations using acoustic backscatter devices. *Marine Geology* 98:7–16.

Trowbridge, J., O. S. Madsen. 1984a. Turbulent wave boundary layers: 1, Model formulation and first-order solution. *J. Geophys, Res.* 89(C5):7989–7997.

Trowbridge, J., O. S. Madsen. 1984b. Turbulent wave boundary layers: 2, second-order theory and mass transport. *J. Geophys, Res.* 89(C5):7999–8007.

Vincent, C. E., M. O. Green. 1990. Field measurements of the suspended sand concentration profiles and fluxes and of the resuspension coefficient over a rippled bed. *Journal of Geophysical Research* 95(C7):11591–11601.

Vincent, C. E., D. M. Hanes, A. J. Bowen. 1991. Acoustic measurements of suspended sand on the shoreface and the control of concentration by bed roughness. *Marine Geology* 96:1–18.

Vongvissesomjai, S. 1986. Profile of suspended sediment due to wave action. *Journal of Waterway, Port, Coastal and Ocean Engineering, ASCE* 112(1):35–53.

Vongvissesomjai, S. 1987. Wave friction factor on sand ripples. *Coastal Sediments '87: ASCE Specialty Conference*, 393–407.

Vongvissesomjai, S. 1988. Time dependent wave shear stress. *Proceedings of the 21st Coastal Engineering Conference*, 1084–1097.

Wiberg, P., J. D. A. Smith. 1983. Comparison of field data and theoretical models for wave-current interactions at the bed on the continental shelf. *Continental Shelf Research* 2:147–162.

Wikramanayake, P. N. 1989. Turbulent wave-current bottom boundary layer flows. M.S. thesis, Dept. of Civil Engineering, Mass. Inst. of Techn., Cambridge, Mass.

Wikramanayake, P. N., O. S. Madsen. 1990. Calculation of movable bed friction factors. Technical Progress Report, submitted to the U.S. Army Corps of Engineers, Coastal Engineering Research Center.

Wikramanayake, P. N., O. S. Madsen. 1992. Calculation of suspended sediment transport by combined wave-current flows. Final report submitted to Coastal Engineering Research Center, U.S. Army Corps of Engineers, Waterways Experiment Station.

Wilson, K. C. 1989. Friction of wave induced sheet flow. *Coastal Engineering* 12:371–379.

Wright, L. D., J. D. Boon, S. C. Kim, J. H. List. 1991. Modes of cross-shore sediment transport on the shoreface of the Middle Atlantic Bight. *Marine Geology* 96:19–51.

Yalin, M. S. 1963. An expression for bed-load transportation. *J. of the Hydraulics Div. ASCE* 89(HY3).

Zettler, D. T. 1991. The estimation of a near-bed reference concentration for use in suspended load computations. M.S. Thesis, Massachusetts Institute of Technology, Cambridge, Massachusetts.

NOTATION

a	non-dimensional fall velocity defined by Equation 48
A	complex constant
$A1$	real constant
$A2$	real constant
A_{br}	near-bottom excursion amplitude based on equivalent wave
B	complex constant
c	suspended sediment concentration
c'	turbulent fluctuation of the suspended sediment concentration
$\bar{c}$	mean suspended sediment concentration
$\tilde{c}$	periodic suspended sediment concentration
c_1	normalized periodic component of concentration with frequency ω_1
$\tilde{c}_1$	periodic suspended sediment concentration with frequency ω_1
c_{1r}	magnitude of reference concentration for component with frequency ω_1
$\tilde{c}_{1r}$	reference concentration of component with frequency ω_1
$\tilde{c}_2$	periodic suspended sediment concentration component with frequency ω_2
c_b	concentration of the sediment bed
$\bar{c}_r$	mean reference concentration
$\overline{c_{ri}}$	mean reference concentration for ith grain size class
$c_r(t)$	instantaneous reference concentration
C	complex constant
d	grain diameter
d_i	grain diameter for the ith grain size class
d_m	mean grain diameter
D	complex constant
E	complex constant
F	complex constant
F_d	diffusive sediment flux
g	acceleration due to gravity
h	flow depth
h_T	height of bed load layer
i	$\sqrt{-1}$
k_n	equivalent Nikuradse roughness
p	pressure
p_i	fraction of bottom sediment in the ith grain size class

p_w periodic pressure

p_{w1} periodic pressure with frequency ω_1

$\vec{q}_b$ bed load flux

q_B magnitude of bed load flux

$\bar{r}$ mean fourier coefficient of Equation 105

r_+ complex constant

r_- complex constant

r_1 first harmonic fourier coefficient of Equation 105

r_2 second harmonic fourier coefficient of Equation 105

s specific gravity of the sediment grains

S' non-dimensional excess shear stress defined by Equation 89

$\overline{S'}$ time-averaged value of S'

$S'(t)$ instantaneous value of S'

S_{ub} power spectrum of near-bottom velocity

t time

T wave period

$\vec{T}$ total suspended sediment transport

$\vec{T}_c$ suspended sediment transport due to mean components

$\vec{T}_w$ suspended sediment transport due to periodic components

u horizontal velocity in wave direction

$\bar{u}$ current (mean) velocity

$\tilde{u}$ periodic velocity

u_1 periodic velocity component with frequency ω_1

u_b magnitude of near-bottom wave velocity

$u_b(t)$ instantaneous near-bottom wave velocity

u_{b1} near-bottom wave velocity with frequency ω_1

u_{b2} near-bottom wave velocity with frequency ω_2

u_{bi} near-bottom wave velocity of the ith wave component

u_{bn} root-mean-square value of the offshore wave velocity obtained by a wave-by-wave analysis

u_{bp} root-mean-square value of the onshore wave velocity obtained by a wave-by-wave analysis

u_{br} representative near-bottom wave velocity

u_B velocity of sediment in bed load layer

u_d deficit wave velocity defined by Equation 27

u_{d1} deficit wave velocity of component with frequency ω_1

u_w	wave velocity
u_{w1}	periodic velocity component with frequency ω_1
u_{w2}	periodic velocity component with frequency ω_2
u_{*c}	current shear velocity
u_{*c}'	shear velocity based on current skin friction shear stress
u_{*cw}	combined wave-current shear velocity
u_{*cw}'	combined wave-current shear velocity based on the skin friction shear stress
u_{*w}	wave shear velocity
u_∞	magnitude of near-bottom wave velocity
$u_{\infty 1}$	magnitude of near-bottom wave velocity with frequency ω_1
w_f	sediment fall velocity
w_{fi}	fall velocity for the ith grain size class
w'	turbulent fluctuation in vertical velocity
x	horizontal coordinate in wave direction
z	vertical coordinate
z_r	reference level at which concentration is specified
z_0	bottom roughness parameter $z_0 = k_n/30$
z_{oc}	effective roughness due to wave-current interaction
Z_a	generalized Bessel function of order a
α	free parameter in eddy viscosity model $\alpha = 0.5$
β	parameter defined by Equation 118
$\beta(t)$	angle of bed slope in the direction of the instantaneous skin friction shear stress
β_0	angle of bed slope
γ_0	resuspension coefficient
δ	boundary layer length scale defined by Equations 8 and 33
Δ	relative error defined by Equation 67
ϵ	ratio of current shear velocity to combined shear velocity
ζ	nondimensional vertical coordinate $\zeta = z/\delta$
ζ_0	non-dimensional value of z0
ζ_r	non-dimensional reference level
η	ripple height
θ	phase of bottom shear stress
κ	Van Karman's constant $\kappa = 0.4$
μ	ratio of current shear velocity to wave shear velocity

μ'	ratio of current shear velocity to wave shear velocity based on skin friction values
ν	kinematic viscosity
ν_t	turbulent eddy viscosity
ρ	density
σ	relative frequency of periodic component defined by Equation 62
τ	bottom shear stress
$\tau'(t)$	- instantaneous skin friction shear stress
τ_b	magnitude of bottom shear stress
$\vec{\tau}_b'(t)$	instantaneous bottom skin friction shear stress
τ_c	bottom shear stress due to current
τ_{cw}	combined wave-current shear stress
τ_c'	current skin friction shear stress
τ_w	bottom shear stress due to waves
τ_w'	wave skin friction shear stress
τ_{w1}	bottom shear stress due to wave velocity with frequency ω_1
τ_{w2}	bottom shear stress due to wave velocity with frequency ω_2
τ_{wi}	bottom shear stress due to the ith wave velocity component
ϕ_1	phase near-bottom wave velocity component with frequency ω_1
ϕ_2	phase near-bottom wave velocity component with frequency ω_2
ϕ_{cw}	angle between waves and the current
$\vec{\Phi}_b$	non-dimensional bed load flux
ψ'	Shields parameter based on skin friction shear stress
$\psi'(t)$	Shields parameter based on the instantaneous skin friction shear stress
ψ_{cr}	critical Shields parameter for the initiation of motion
ϕ_m	angle of repose of bottom sediment
$\vec{\Phi}_b(t)$	instantaneous bed load transport
ψ_w'	Shields parameter based on the wave skin friction shear stress
ω	angular frequency
ω_1	frequency of wave component
ω_2	frequency of wave component
ω_i	frequency of ith wave component
ω_r	representative wave frequency
Re	real part of a complex number
$\|\ \|$	modulus of a number

Diacritics

- $\bar{}$ mean value of a quantity
- $\vec{}$ vector quantity

APPENDIX A.

DEVELOPMENT OF A TIME-VARYING EDDY VISCOSITY MODEL

While the time-invariant eddy viscosity model developed by Wikramanayake (1989) gave excellent results for a current velocity profile with waves in the same direction, it could not adequately represent the effect of a change in the angle between the waves and the current as shown in the data from Davies et al. (1988). The results of Davies et al. also show that the direction of the mean velocity when $0 < \phi_{cw} < 90^{\circ}$ is close to that of the mean shear stress only in the outer region, while the mean velocity closer to the bottom is deflected by the waves. These features are also apparent in the results of Van Kesteren and Bakker (1984).

The inability of the model to represent these features is a result of the simple formulation used. It was shown by Wikramanayake (1989) that once the eddy viscosity is assumed time-invariant the linearized boundary layer equation can be separated into a wave and a current problem. Once this separation is accomplished it can be seen that the wave velocity and the current velocity always lie along the direction of the free stream velocity and the mean shear stress, respectively, regardless of the sophistication of the eddy viscosity model used. This means that simply using a more elaborate time-invariant eddy viscosity model will not reproduce the phenomena discussed above. Instead it seems that an eddy viscosity that varies with time should be considered. This has been done in Trowbridge and Madsen (1984a, b) for a pure wave boundary layer and they obtain features such as a third harmonic velocity in the boundary layer that are present in physical experiments but not obtainable if a time-invariant eddy viscosity is assumed.

Therefore in this appendix a time-varying eddy viscosity model will be developed that has a form similar to that used in Trowbridge and Madsen (1984). The

assumption of a weak current is used to obtain tractable approximate governing equations for the waves and for the current. These are then solved and the results compared to the experimental data.

A.1 Derivation of Approximate Equations for the Waves and the Current

The governing equation is identical to the linearized boundary layer equation used in Chapter 2 and is given by

$$\frac{\partial \vec{u}}{\partial t} = -\frac{1}{\rho}\nabla p + \frac{\partial}{\partial z}\left[\nu_t \frac{\partial \vec{u}}{\partial z}\right] \tag{A1}$$

in which the shear stress (Reynolds stress) on horizontal planes has been expressed through the concept of a turbulent eddy viscosity

$$\vec{\tau}/\rho = \nu_t \frac{\partial \vec{u}}{\partial z} \tag{A2}$$

While the separation of the governing equation, Equation A1, for the combined wave and current flow into its time-varying (wave) and time-invariant (current) components was readily achieved in Chapter 2, due to ν_t being time-invariant, this separation is far more involved here since ν_t is considered a function of time.

To perform the separation the variables $\vec{u} = \{u,v\}$, p, and ν_t are expressed in terms of their time-dependent and time-independent contributions, denoted by tilde ($\tilde{}$) and overbar ($\bar{}$), respectively. Furthermore, since the wave motion is assumed simple periodic the time-dependent contribution is split up into its even and odd harmonics, denoted by subscripts e, $(\tilde{})_e$, and o, $(\tilde{})_o$, respectively.

Introducing this notation, i.e.,

$$\vec{u} = \{u,v\} = \{\bar{u},\bar{v}\} + \{\tilde{u}_e,\tilde{v}_e\} + \{\tilde{u}_o,\tilde{v}_o\}$$
$$p = \bar{p} + \tilde{p}_e + \tilde{p}_o \qquad \text{(A3)}$$
$$\nu_t = \bar{\nu} + \tilde{\nu}_e + \tilde{\nu}_o$$

in Equation A1 and assuming, without loss in generality, the periodic waves to propagate in the x-direction, i.e., invoking $\tilde{p}_e = 0$ and $\partial\tilde{p}/\partial y = 0$, the x and y components of the governing equation become

$$\frac{\partial(\tilde{u}_e+\tilde{u}_o)}{\partial t} = -\frac{1}{\rho}\frac{\partial(\bar{p}+\tilde{p}_o)}{\partial x} + \frac{\partial}{\partial z}\left[(\bar{\nu} + \tilde{\nu}_e + \tilde{\nu}_o)\frac{\partial(\bar{u}+\tilde{u}_e+\tilde{u}_o)}{\partial z}\right] \qquad \text{(A4)}$$

$$\frac{\partial(\tilde{v}_e+\tilde{v}_o)}{\partial t} = -\frac{1}{\rho}\frac{\partial\bar{p}}{\partial y} + \frac{\partial}{\partial z}\left[(\bar{\nu} + \tilde{\nu}_e + \tilde{\nu}_o)\frac{\partial(\bar{v}+\tilde{v}_e+\tilde{v}_o)}{\partial z}\right]$$

To obtain the equation governing the time-independent (current) velocity Equation A4 is time-averaged. Making use of the fact that only products of even or odd terms contribute to the time-average this results in the equations

$$\frac{\partial}{\partial z}\left[\bar{\nu}\frac{\partial\bar{u}}{\partial z}\right] = \frac{1}{\rho}\frac{\partial\bar{p}}{\partial x} - \frac{\partial}{\partial z}\left[\overline{\tilde{\nu}_e\frac{\partial\tilde{u}_e}{\partial z}} + \overline{\tilde{\nu}_o\frac{\partial\tilde{u}_o}{\partial z}}\right] \qquad \text{(A5)}$$

$$\frac{\partial}{\partial z}\left[\bar{\nu}\frac{\partial\bar{v}}{\partial z}\right] = \frac{1}{\rho}\frac{\partial\bar{p}}{\partial y} - \frac{\partial}{\partial z}\left[\overline{\tilde{\nu}_e\frac{\partial\tilde{v}_e}{\partial z}} + \overline{\tilde{\nu}_o\frac{\partial\tilde{v}_o}{\partial z}}\right]$$

which, by comparison with Equation 6 of Chapter 2, clearly bring out the wave-influence in the equations governing the current.

Subtracting Equation A5 from A4 and collecting even and odd harmonics, the equations governing the time-dependent (wave) motion are obtained for the direction of wave propagation

$$\frac{\partial\tilde{u}_o}{\partial t} = -\frac{1}{\rho}\frac{\partial\tilde{p}_o}{\partial x} + \frac{\partial}{\partial z}\left[(\bar{\nu} + \tilde{\nu}_e)\frac{\partial\tilde{u}_o}{\partial z}\right] + \frac{\partial}{\partial z}\left[\tilde{\nu}_o\frac{\partial(\bar{u} + \tilde{u}_e)}{\partial z}\right] \qquad \text{(A6)}$$

$$\frac{\partial \tilde{u}_e}{\partial t} = \frac{\partial}{\partial z}\left[\tilde{\nu}_o \frac{\partial \tilde{u}_o}{\partial z} - \overline{\tilde{\nu}_o \frac{\partial \tilde{u}_o}{\partial z}}\right] + \frac{\partial}{\partial z}\left[\bar{\nu}\frac{\partial \tilde{u}_e}{\partial z}\right] + \frac{\partial}{\partial z}\left[\tilde{\nu}_e \frac{\partial \bar{u}}{\partial z}\right]$$
$$+ \frac{\partial}{\partial z}\left[\tilde{\nu}_e \frac{\partial \tilde{u}_e}{\partial z} - \overline{\tilde{\nu}_e \frac{\partial \tilde{u}_e}{\partial z}}\right] \qquad (A7)$$

and for the direction perpendicular to the wave direction

$$\frac{\partial \tilde{v}_o}{\partial t} = \frac{\partial}{\partial z}\left[(\bar{\nu} + \bar{\nu}_e)\frac{\partial \tilde{v}_o}{\partial z}\right] + \frac{\partial}{\partial z}\left[\tilde{\nu}_o \frac{\partial(\bar{v} + \tilde{u}_e)}{\partial z}\right] \qquad (A8)$$

$$\frac{\partial \tilde{v}_e}{\partial t} = \frac{\partial}{\partial z}\left[\tilde{\nu}_o \frac{\partial \tilde{v}_o}{\partial z} - \overline{\tilde{\nu}_o \frac{\partial \tilde{v}_o}{\partial z}}\right] + \frac{\partial}{\partial z}\left[\bar{\nu}\frac{\partial \tilde{v}_e}{\partial z}\right] + \frac{\partial}{\partial z}\left[\tilde{\nu}_e \frac{\partial \bar{v}}{\partial z}\right]$$
$$+ \frac{\partial}{\partial z}\left[\tilde{\nu}_e \frac{\partial \tilde{v}_e}{\partial z} - \overline{\tilde{\nu}_e \frac{\partial \tilde{v}_e}{\partial z}}\right] \qquad (A9)$$

In passing it is noted, by comparison with Equation 2, that the time-independent current velocity appears explicitly in the equations governing the wave motion.

A.1.1 The weak current assumption

In order to further simplify the governing equations derived above the assumptions of a weak current, expressed through the smallness of the parameter

$$\mu = \frac{u_{*c}}{u_{*w}} < 1 \qquad (A10)$$

also used in Chatper 2, without restrictions on its magnitude, is introduced.

Since the flow in the immediate vicinity of the bottom scales with the ratio of the shear stresses it follows that

$$\{\bar{u},\bar{v}\}/\tilde{u}_o = O\left[\frac{\tau_c}{\tau_w}\right] = O(\mu^2) \qquad (A11)$$

where $\tilde{u}_o$, the odd harmonic wave velocity, is used to represent the wave velocity since this is expected to be the leading term for a simple harmonic wave motion.

As argued by Trowbridge and Madsen (1984a) and in Part II the time-varying eddy viscosity should, in the immediate vicinity of the bottom, be related to the shear velocity based on the instantaneous (time-varying) bottom shear stress, $\tau_b(t)$, i.e.,

$$u_* = u_*(t) = \sqrt{|\tau_b(t)|/\rho} \tag{A12}$$

For a periodic wave motion u_* given by Equation A12 will result in a shear velocity consisting of only even harmonics (including a constant time-invariant contribution). The addition of a small steady shear stress on top of the periodic wave shear stress will produce an asymmetry between the magnitude of the bottom shear stress associated with wave crest and trough. This asymmetry will, as demonstrated by Trowbridge and Madsen (1984b), result in odd harmonics appearing in the temporal variation of u_*.

Based on the preceding arguments it is therefore reasonable to assume—subject to later verification—that the terms in the eddy viscosity expansion given by Equation A3 are related according to

$$\tilde{\nu}_e/\bar{\nu} = O(\beta)$$
$$\tilde{\nu}_o/\bar{\nu} = O(\mu^2) \tag{A13}$$

where β is of the order 0.4 (Trowbridge and Madsen, 1984a).

Using the rough order-of-magnitude estimates presented above comparison of the first two terms on the right-hand side of Equation A7 suggests

$$\tilde{u}_e/\tilde{u}_o = O(\mu^2) \tag{A14}$$

A.1.2 Approximate Equation for the Wave Problem

Applying order-of-magnitude arguments based on the preceding estimates to Equation A6 reveals that the last term in Equation A6 is of the order $\mu^4/\beta \ll 1$ relative to the smallest of the remaining terms, $\tilde{\nu}_e \, \partial\tilde{u}_0/\partial z$, which is of the order β. The equation governing the odd harmonic wave motion in the direction of wave propagation may therefore be taken as

$$\frac{\partial \tilde{u}_0}{\partial t} = -\frac{1}{\rho}\frac{\partial \tilde{p}_0}{\partial x} + \frac{\partial}{\partial z}\left[(\bar{\nu} + \tilde{\nu}_e)\frac{\partial \tilde{u}_0}{\partial z}\right] \tag{A15}$$

which is identical to the equation solved by Trowbridge and Madsen (1984a) for a pure wave motion.

Similarly, the last two terms on the right-hand side of Equation A7 are seen to be of order $\beta < 1$ relative to the remaining terms, which are of order μ^2. Thus, the even harmonic wave problem in the direction of wave propagation may be approximated by

$$\frac{\partial \tilde{u}_e}{\partial t} = \frac{\partial}{\partial z}\left[\tilde{\nu}_0\frac{\partial \tilde{u}_0}{\partial z} - \overline{\tilde{\nu}_0\frac{\partial \tilde{u}_0}{\partial z}}\right] + \frac{\partial}{\partial z}\left[\tilde{\nu}\frac{\partial \tilde{u}_e}{\partial z}\right] \tag{A16}$$

As mentioned above the smallest term retained in the odd wave problem, Equation A15, is of order β relative to the leading, O(1), terms while the entire expression for the even wave problem, Equation A16, is of order μ^2, i.e., considerable smaller than the smallest term retained in Equation A15. It is therefore consistent, as a first approximation, to disregard the even wave problem.

For the wave motion perpendicular to the direction of wave propagation the forcing terms are associated with the current, i.e., $\tilde{\nu}_0 \, \partial\bar{v}/\partial z$ and $\tilde{\nu}_e \, \partial\bar{v}/\partial z$ in Equations A8 and A9, respectively. It follows from this that

$$\tilde{v}_o/\tilde{u}_o = O(\mu^4)$$

$$\tilde{v}_e/\tilde{u}_o = O(\beta\mu^2) \tag{A17}$$

It is therefore entirely consistent with previous approximations and not surprising that the wave motion within the boundary layer in the direction perpendicular to the direction of wave propagation is negligibly small.

A.1.3 Approximate Equations for the Current Problem

Applying order-of-magnitude arguments to the equations governing the time-independent (current) problem, Equation A5, shows that these may be approximated by

$$\frac{\partial}{\partial z}\left[\bar{\nu}\frac{\partial \bar{u}}{\partial z}\right] = \frac{1}{\rho}\frac{\partial \bar{p}}{\partial x} - \frac{\partial}{\partial x}\left[\overline{\tilde{\nu}_o \frac{\partial \tilde{u}_o}{\partial z}}\right] \tag{A18}$$

$$\frac{\partial}{\partial z}\left[\bar{\nu}\frac{\partial \bar{v}}{\partial z}\right] = \frac{1}{\rho}\frac{\partial \bar{p}}{\partial y} \tag{A19}$$

where terms neglected are at most of order β relative to those retained.

Integration of Equations A18 and A19 from the bottom, $z \to 0$, to the outer edge of the wave boundary layer, $z = \delta$, gives

$$\left[\bar{\nu}\frac{\partial \bar{u}}{\partial z}\right]_{z\to 0}^{\delta} = \frac{1}{\rho}\frac{\partial \bar{p}}{\partial x}\delta - \left[\overline{\tilde{\nu}_o \frac{\partial \tilde{u}_o}{\partial z}}\right]_{z\to 0}^{\delta} \tag{A20}$$

$$\left[\bar{\nu}\frac{\partial \bar{v}}{\partial z}\right]_{z\to 0}^{\delta} = \frac{1}{\rho}\frac{\partial \bar{p}}{\partial y}\delta \tag{A21}$$

At the outer edge of the wave boundary layer, $z = \delta$, the wave motion will not contribute to the shear stress since here $\partial\tilde{u}_o/\partial z = \partial u_\infty/\partial z \simeq 0$. Also, the contribution of the mean pressure gradient term is vanishingly small so long as δ is well within the current boundary layer sale, in which case the law of the wall may be applied to the current problem. At the outer edge of the wave boundary layer the following relations therefore hold

$$\bar{\nu}\left\{\frac{\partial\bar{u}}{\partial z}, \frac{\partial\bar{v}}{\partial z}\right\}_{z\to\delta} = \frac{\vec{\tau}_c}{\rho} = u_{*c}^2\{\cos\phi_{cw}, \sin\phi_{cw}\} \tag{A22}$$

where $\vec{\tau}_c$, the current bottom shear stress vector, is assumed to be at an angle ϕ_{cw} to the direction of wave propagation.

In the immediate vicinity of the bottom, $z \to 0$, Equations A20 and A21 may therefore be written as

$$\bar{\nu}\frac{\partial\bar{u}}{\partial z} = u_{*c}^2\cos\phi_{cw} - \overline{\tilde{\nu}_o\frac{\partial\tilde{u}_o}{\partial z}} \tag{A23}$$

$$\bar{\nu}\frac{\partial\bar{v}}{\partial z} = u_{*c}^2\sin\phi_{cw} \tag{A24}$$

which constitute the equations governing the current in the direction and perpendicular to the direction of wave propagation.

It is of particular interest to note that the time-varying eddy viscosity formulation, in contrast to the time-invariant eddy viscosity formulation of Chapter 2, gives rise to a difference between the equation governing the current velocity components.

A.2 Eddy Viscosity Formulation

Other than relating the scale of the eddy viscosity to that of the shear velocity, Equation A12, for the purpose of rough order-of-magnitude estimates, nothing has been said about its functional form up to now. To be more specific about the eddy viscosity formulation to be used in the solution of the wave and current problem, it is assumed that the eddy viscosity may be expressed as a product of two terms–one accounting for the temporal, the other for the spatial variability.

It is therefore assumed that

$$\nu_t = g(z) \cdot f(t) \tag{A25}$$

where f(t) is obtained from the temporal variation of the instantaneous shear velocity, $u_*(t) = \sqrt{|\hat{\tau}_b(t)/\rho}$.

Commensurate with the weak current assumption the instantaneous bottom shear stress vector is assumed given by

$$\hat{\tau}_b = \{\tilde{\tau}_1 \cos\theta + \tau_c \cos\phi_{cw},\ \tau_c \sin\phi_{cw}\} \tag{A26}$$

where τ_1 is the magnitude of the first harmonic shear stress at the bottom, θ is the phase of the wave, ωt, plus some arbitrary phase angle, and terms involving even harmonics in the shear stress have been neglected following the argument justifying that the even wave problem, given by Equation A16, need not be solved.

To obtain the magnitudes of the instantaneous shear stress from Equation A26 only terms linear in τ_c are retained since $\tau_c/\tilde{\tau}_1 = O(\mu^2)$. Therefore

$$|\vec{\tau}_b| = \tau_b = \{\tilde{\tau}_1^2\cos^2\theta + 2\tilde{\tau}_1\tau_c\cos\phi_{cw}\cos\theta\}^{\frac{1}{2}}$$

$$= \tilde{\tau}_1|\cos\theta|\left\{1 + 2\frac{\tau_c\cos\phi_{cw}}{\tilde{\tau}_1\cos\theta}\right\}^{\frac{1}{2}} \tag{A27}$$

The square root in this expression may be expanded treating the τ_c-term as small relative to unity. This assumption is clearly violated during a short time interval around $\cos\theta = 0$; however, for most of the wave period the assumption is a good one and when it is violated the resulting term is indeed small. Therefore formal expansion of Equation A27 yields

$$\tau_b/\rho = u_*^2 = u_{*1}^2|\cos\theta|\left\{1 + \frac{\tau_c\cos\phi_{cw}}{\tilde{\tau}_1\cos\theta}\right\} \tag{A28}$$

To obtain an expression for the instantaneous shear velocity in terms of a harmonic expansion, as assumed in Equation A3, use is made of the Fourier expansions

$$|\cos\theta| = \frac{2}{\pi}\left[1 + \frac{2}{3}\cos 2\theta + \cdots\right]$$

$$\frac{|\cos\theta|}{\cos\theta} = \frac{4}{\pi}(\cos\theta + \cdots) \tag{A29}$$

which introduced in Equation A28 yields

$$u_*^2 = \frac{2}{\pi}u_{*1}^2\left[1 + \frac{2}{3}\cos 2\theta + 2\frac{\tau_c\cos\phi_{cw}}{\tilde{\tau}_1}\cos\theta\right] \tag{A30}$$

and therefore approximately

$$u_* = \sqrt{\frac{2}{\pi}}u_{*1}\left[1 + \frac{1}{3}\cos 2\theta + \frac{\tau_c\cos\phi_{cw}}{\tilde{\tau}_1}\cos\theta\right] \tag{A31}$$

This equation can be written as

$$\frac{u_*}{u_{*1}} = \sqrt{\frac{2}{\pi}} + \mu^2 \cos\phi_{cw} \cdot \sqrt{\frac{2}{\pi}} \cos\theta + \frac{1}{3}\sqrt{\frac{2}{\pi}} \cos 2\theta \qquad \text{(A32)}$$

and the exact value of u_*/u_{*1} is obtained from Equation A27 as

$$\frac{u_*}{u_{*1}} = [\cos^2\theta + 2\mu^2 \cos\phi_{cw} \cos\theta + \mu^4]^{\frac{1}{4}} \qquad \text{(A33)}$$

Equation A32 gives an approximation to Equation A27 in terms of a constant and first- and second-harmonic terms. The "best fit" values of the three coefficients in this expansion can alternatively be obtained from a Fourier expansion of Equation A33.

Figure A1 shows the approximate expansion in Equation A32 compared to the exact expression from Equation A27 and to a "best fit" curve drawn using the first three coefficients of a Fourier cosine expansion of Equation A33, using two different values of μ and ϕ_{cw}.

It is seen that the approximate expansion is fairly close to the exact value even at these very large values of μ. For the case with $\phi_{cw} = 0$ the approximation does worst when the exact value is near zero. However, due to the persistence of turbulent fluctuation it is physically unrealistic to expect the eddy viscosity to vanish during the cycle, and this failure is therefore not considered a serious shortcoming of the approximation.

The use of the "best-fit" coefficient improves the approximation, particularly for the case with $\phi_{cw} = 90$. However, these coefficients must be calculated for each case numerically and therefore the expansion with the final coefficients in Equation A32 is considered sufficiently accurate for the purposes of the present study.

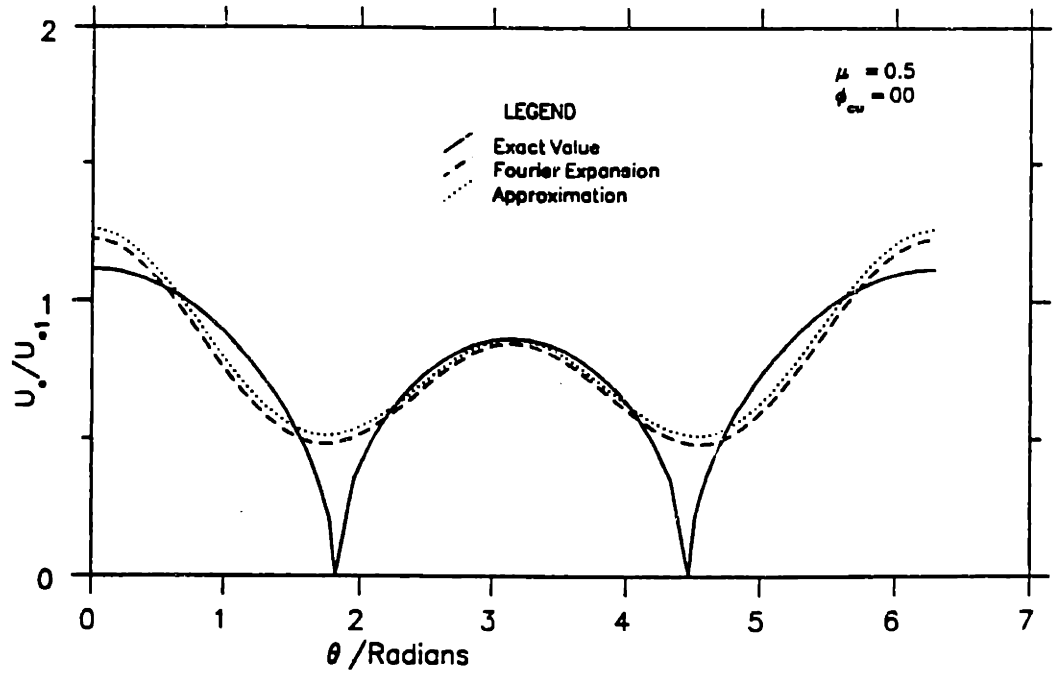

a. Comparison with $\mu = 0.5$, $\phi_{cw} = 0°$

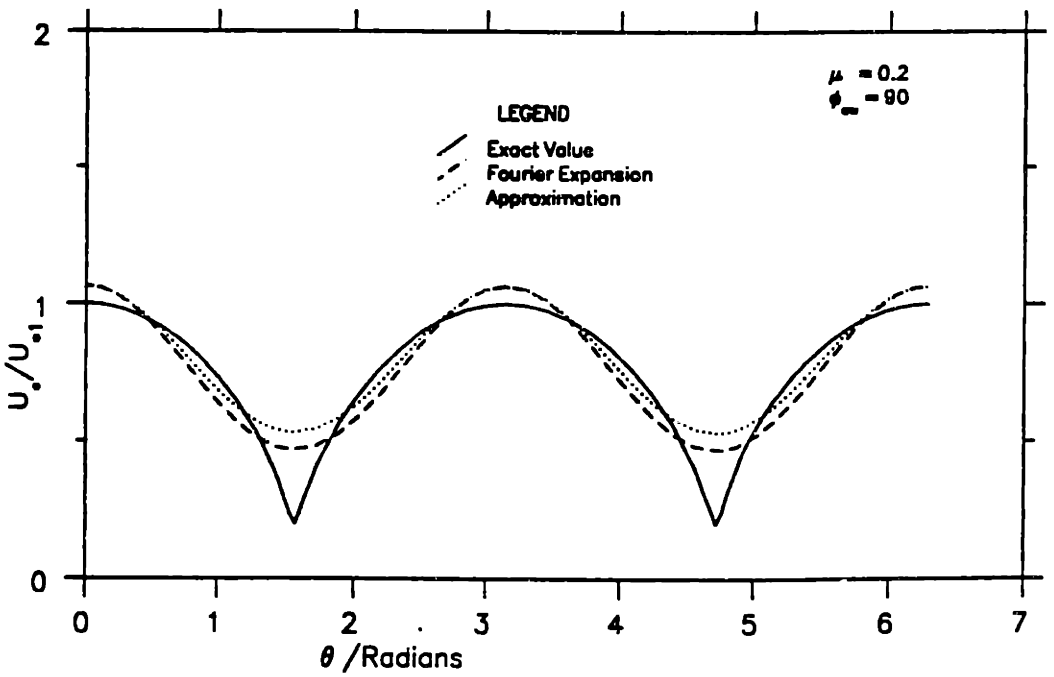

b. Comparison with $\mu = 0.2$, $\phi_{cw} = 90°$

Figure A1. Comparison of the approximate expansion of the eddy viscosity in Equation A32 with the exact value in Equation A33 and the three-term Fourier expansion

With the temporal variation of the instantaneous shear velocity given by Equation A31 and choosing the spatial variation used for the time-invariant eddy viscosity model in Chapter 2 results in the following time-varying eddy viscosity model

$$\nu_t = \begin{cases} \kappa u_* z & z \leq \alpha_1 \delta \\ \kappa u_* \alpha_1 \delta & \alpha_1 \delta \leq z \leq \sqrt{\frac{2}{\pi}} \alpha_1 \delta / \epsilon \\ \kappa u_{*c} z & z \geq \sqrt{\frac{2}{\pi}} \alpha_1 \delta / \epsilon \end{cases} \tag{A34}$$

with u_* given by Equation A31 and the definitions of δ and ϵ being the same as those introduced in Chapter 2 with the appropriate modification due to the weak current assumption. For example $u_{*cw} \simeq u_{*1}$ since the current is weak so that $\epsilon = \mu \ll 1$ and $\delta = \kappa u_{*1}/\omega$. As in the time-invariant model α_1 is a free model parameter that is determined after comparison with the experimental data.

In the time-invariant eddy viscosity model of Chapter 2 the eddy viscosity in the wave boundary layer was scaled by u_{*cw}, which was derived from the maximum shear stress. This ensures that the slope of the eddy viscosity profile in the lower region $z_0 < z < \alpha\delta$ is greater than that in the outer region.

For the time-varying model outlined above however it is seen that the slope of the mean eddy viscosity profile is greater in the wave boundary layer only if

$$\mu = \frac{u_{*c}}{u_{*1}} < \sqrt{\frac{2}{\pi}} \tag{A35}$$

which means that the use of the present model, derived for small μ, is limited by the condition given by Equation A35.

The level of the transition from an eddy viscosity scaled by the wave shear velocity to one scaled by the current shear velocity in Equation A34 is chosen so

that the mean eddy viscosity is continuous. This results in a discontinuity in the instantaneous eddy viscosity at this level because the eddy viscosity above it is considered time invariant, while that below varies with time. The time-varying eddy viscosity is due to the wave motion and therefore a more logical place to cut off the time variation would be the top of the wave boundary layer, i.e., at $z = \delta$. The wave problem could then be solved for a time-varying eddy viscosity below $z = \delta$ and a time-invariant eddy viscosity above this level with the solutions matched at this level. This procedure would, however, be cumbersome to implement. In practice it is found that the assumed form of the eddy viscosity above the level $z = \delta$ does not have much effect on the wave solution. For the solution of the wave problem it is therefore assumed that the eddy viscosity variation is as given in Equation A34 but with the time variation assumed to be present in the upper region as well. As will be seen this makes the solution far less complicated than the procedure outlined above while not being much in error so long as the level $z = \sqrt{2/\pi}\alpha_1\delta/\mu$ is greater than the level $z = \delta$, This condition will be satisfied when

$$\epsilon = \mu < \sqrt{\frac{2}{\pi}}\alpha_1 \tag{A36}$$

Before proceeding with the solution to the wave and current problem inspection of Equation A31 in conjunction with A32 shows that the assumption regarding the order of magnitude of the eddy viscosity components made in Equation A13 indeed are correct with $\beta = \frac{1}{4}$ being small—although not very small—relative to unity.

A.3 The Wave Problem

The equation governing the wave problem is given by Equation A15 and may alternatively be expressed in terms of the velocity deficit

$$\tilde{u}_d = \frac{\tilde{u}_0 - u_\infty}{u_b} \tag{A37}$$

where $u_\infty \neq u_\infty(z)$ is the near-bottom velocity predicted by linear potential wave theory, i.e., governed by

$$\frac{\partial u_\infty}{\partial t} = -\frac{1}{\rho}\frac{\partial \tilde{p}_0}{\partial x} \tag{A38}$$

Introducing these expression in Equation A15 this equation becomes

$$\frac{\partial \tilde{u}_d}{\partial t} = \frac{\partial}{\partial z}\left[\bar{\nu}\left[1 + \frac{\tilde{\nu}_e}{\bar{\nu}}\right]\frac{\partial \tilde{u}_d}{\partial z}\right] \tag{A39}$$

where

$$1 + \frac{\tilde{\nu}_e}{\bar{\nu}} = 1 + \frac{1}{3}\cos 2(\omega t + \phi_2) \tag{A40}$$

is obtained from Equations A31 and A32.

By introducing a change in the time-variable from t to $\tilde{t}$ defined by

$$\frac{\partial \tilde{t}}{\partial t} = 1 + \frac{1}{3}\cos 2(\omega t + \phi_2) \tag{A41}$$

or

$$\omega \tilde{t} = \omega t + \frac{1}{6}\sin 2(\omega t + \phi_2) \tag{A42}$$

the equation governing the wave motion becomes

$$\frac{\partial \tilde{u}_d}{\partial \tilde{t}} = \frac{\partial}{\partial z}\left[\bar{\nu}\frac{\partial \tilde{u}_d}{\partial z}\right] \tag{A43}$$

which is identical to the equation governing the time-invariant eddy viscosity formulation of the wave problem, except that the time-invariant eddy viscosity in Equation A43 is based on the average shear velocity rather than the maximum shear velocity used in Chapter 2.

To solve Equation A43 it is necessary to specify the no-slip boundary condition at the bottom

$$\tilde{u}_d = \frac{-u_\infty}{u_b} = -\cos\omega t \tag{A44}$$

in terms of the new time-variable, $\tilde{t}$.

From Equation A42, treating the factor of (1/6) in front of the cyclic term as small, the first-order relationship is that $\omega t = \omega\tilde{t}$, which may be introduced in the cyclic term to obtain

$$\omega t \simeq \omega\tilde{t} - \frac{1}{6}\sin 2(\omega\tilde{t} + \phi_2) \tag{A45}$$

Substituting Equation A45 for ωt in Equation A44 and expanding the resulting expression around $\omega\tilde{t}$, consistent with the degree of approximation adopted in Equation A45, yields the boundary condition to be satisfied for $z \to 0$

$$\begin{aligned}\tilde{u}_d &= -\cos\left[\omega\tilde{t} - \frac{1}{6}\sin 2(\omega\tilde{t} + \phi_2)\right] = -\left\{\cos\omega\tilde{t} + \sin\omega\tilde{t}\left[\frac{1}{6}\sin 2(\omega\tilde{t} + \phi_2)\right]\right\} \\ &= -\left[\cos\omega\tilde{t} + \frac{1}{12}\cos(\omega\tilde{t} + 2\phi_2) - \frac{1}{12}\cos(3\omega\tilde{t} + 2\phi_2)\right]\end{aligned} \tag{A46}$$

The approximation to $\cos(\omega t)$ is plotted in Figure A2 along with the exact value for $\phi_2 = 30°$. It is seen from the figure that Equation A46 is an excellent approximation to Equation A44 for this value of ϕ_2 which is chosen to be in the range encountered in practice.

The occurrence of third harmonics in the boundary condition indicates that the solution will contain this harmonic in addition to the fundamental harmonic motion. Since Equation 183 and its boundary condition Equation 186 are linear a solution of the form

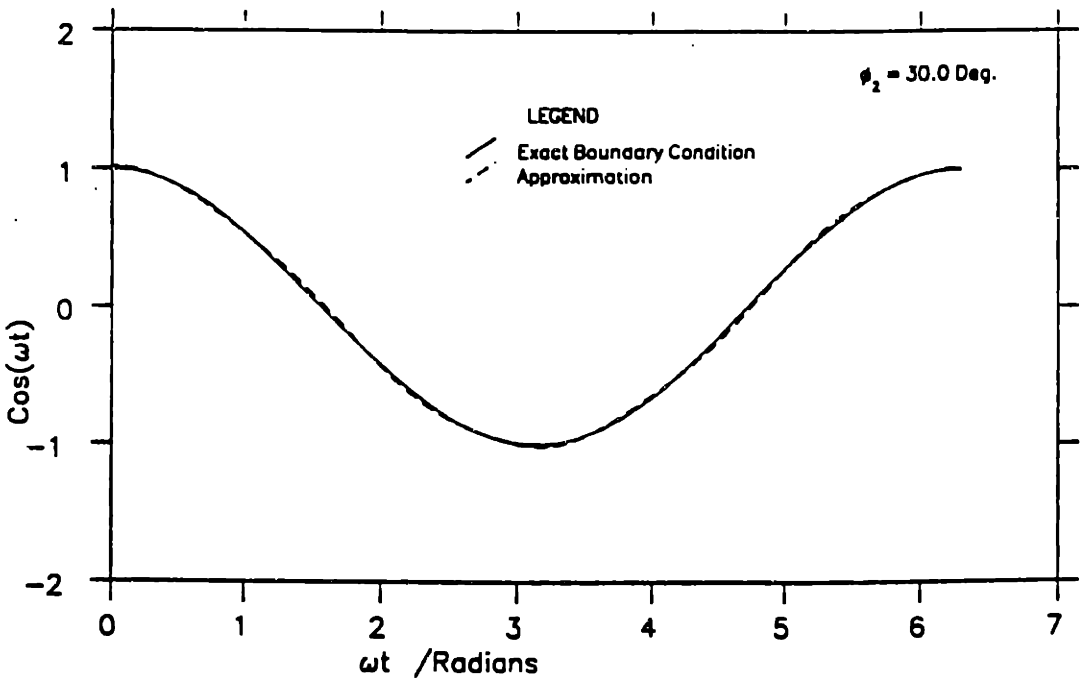

Figure A2. Comparison of the approximate boundary condition of Equation A46 with the exact value with $\phi_2 = 30°$

$$\tilde{u}_d = \mathrm{Re}\left[u_{d1}e^{i\omega\tilde{t}} + u_{d2}e^{i(\omega\tilde{t}+2\phi_2)} + u_{d3}e^{i(3\omega\tilde{t}+2\phi_2)}\right] \tag{A47}$$

is assumed. This ensures that Equation 186 is satisfied if

$$u_{d1} = -1\ ,\ u_{d2} = -\frac{1}{12}\ ,\ u_{d3} = \frac{1}{12} \quad \text{at} \quad z = z_0 \tag{A48}$$

is imposed as a boundary condition on each part of the solution. The other boundary condition is

$$u_{d1}\ ,\ u_{d2}\ ,\ u_{d3} \to 0 \quad \text{as} \quad z \to \infty \tag{A49}$$

Now the solution for each of the terms u_{d2}, u_{d2}, and u_{d3} can be found separately. Considering u_{d1} it is seen that the governing equation and boundary conditions are the same as for the wave problem of the time-invariant model in Chapter 2. The only difference is the presence of the factor $\sqrt{2/\pi}$ in the eddy viscosity distribution. Therefore the governing equation can be non-dimensionalized as in Chapter 2 with

$$\delta = \frac{\kappa u_{*1}}{\omega} \tag{A50}$$

in this case and solved to give five simultaneous equations similar to Equations 26 to 30. The only difference will be that a factor $\sqrt{2/\pi}$ appears in the denominator of the terms inside the square root sign of Equations 26, 27, and 28 and in the numerator of those terms in Equations 29 and 30.

Considering the solution for u_{d2} it is seen that the same equations are obtained as for u_{d1} with the only difference being that the first equation will have a value of -1/12 on the right-hand side instead of -1. Since the right-hand side in the other four equations is zero, cf. Equations 21 to 30, this value merely scales the five unknown coefficients in the solution. Therefore we can write

$$u_{d2} = \frac{u_{d1}}{12} \tag{A51}$$

Finally, it is seen that the solution for the third harmonic term u_{d3} will yield five equations similar to those for u_{d1} with a factor 3 (3ω replaces ω) appearing in the numerator of all the terms inside the square root and a value 1/12 on the right-hand side of the first equation instead of -1.

Therefore after solution of these two sets of simultaneous equations the solution can be written as

$$\tilde{u}_d = \mathrm{Re}\left\{u_{d1}e^{i\omega\bar{t}} + \frac{u_{d1}}{12}e^{i(\omega\bar{t}+2\phi_2)} + u_{d3}e^{i(3\omega\bar{t}+2\phi_2)}\right\} \tag{A52}$$

It should be noted that the first term in Equation A52 is of zeroth order in the small parameter assumed in the expansion of the boundary condition, Equation A46, while the other two terms are of first order.

The result obtained so far is in terms of the variable $\bar{t}$ and therefore the solution must be completed by transforming Equation A52 into the real time variable t using the relationship between the variables in Equation A42. To be consistent, this reverse transformation needs to be carried out to the same order in the small parameter of Equation A45 as was used in the expansion of the boundary condition to obtain Equation 146. This means that the term $\exp(i\omega\bar{t})$ in Equation A52 must be expanded to first order while the other two exponentials need be expanded to leading order only. These expansions result in

$$e^{i\omega\bar{t}} = e^{i\omega t} - \frac{1}{12}e^{-i(\omega t+2\phi_2)} + \frac{1}{12}e^{i(3\omega t+2\phi_2)} \tag{A53}$$

$$e^{i(\omega\bar{t}+2\phi_2)} = e^{i(\omega t+2\phi_2)} \tag{A54}$$

$$e^{i(3\omega\bar{t}+2\phi_2)} = e^{i(3\omega t+2\phi_2)} \tag{A55}$$

Substituting Equations A53 to A55 into Equation A52 yields

$$u_d = \mathrm{Re}\left\{u_{d1}\left[e^{i\omega t} + \frac{i}{6}\sin(\omega t+2\phi_2)\right] + e^{i(3\omega t+2\phi_2)}\left[\frac{u_{d1}}{12} + u_{d3}\right]\right\} \tag{A56}$$

The solution of the wave problem is closed, as in the case of the time-invariant model, by defining the bottom shear stress as in Equation 32. In this case the definition is

$$\frac{\tau_b}{\rho} = \lim_{z=z_0}\left[(\bar{\nu}+\tilde{\nu}_e)\frac{\partial \tilde{u}_0}{\partial z}\right] \tag{A57}$$

Since the deficit velocity in Equation A56 involves first and third harmonics, the shear stress in Equation A57 will also have first and third harmonics. By writing

$$\lim_{z=z_0}\left[\frac{\partial u_{d1}}{\partial z}\right] = \left|\frac{\partial u_{d1}}{\partial z}\right|_{z=z_0} e^{i\gamma} \tag{A58}$$

$$\lim_{z=z_0}\left[\frac{\partial u_{d3}}{\partial z}\right] = \left|\frac{\partial u_{d3}}{\partial z}\right|_{z=z_0} e^{i\sigma} \tag{A59}$$

it then follows from Equation A56 that

$$\begin{aligned}\frac{1}{u_b}\lim_{z=z_0}\left[\frac{\partial \tilde{u}_0}{\partial z}\right] &= \lim_{z=z_0}\left[\frac{\partial u_d}{\partial z}\right] \\ &= \left|\frac{\partial u_{d1}}{\partial z}\right|_{z=z_0}\left[\cos(\omega t+\gamma) - \frac{1}{12}(\cos(\omega t+2\phi_2-\gamma) - \cos(\omega t+2\phi_2+\gamma))\right. \\ &\quad \left. + \frac{1}{12}\cos(3\omega t+2\phi_2+\gamma)\right] + \left|\frac{\partial u_{d3}}{\partial z}\right|_{z=z_0}\cos(3\omega t+2\phi_2+\sigma)\end{aligned} \tag{A60}$$

This expression can be substituted into Equation A57 along with the expression for the eddy viscosities from Equation A40 to obtain an expression for the bottom shear stress. Let the first and third harmonic shear stresses be denoted by τ_1 and τ_3, respectively. Then, after carrying out the substitution in Equation A57 and

separating the first and third harmonics while retaining only those terms of the first order in the small parameter the shear stresses are obtained as

$$\frac{1}{u_b}\frac{\tau_1}{\rho} = \sqrt{\frac{2}{\pi}}\kappa u_{*1}\left|\zeta\frac{\partial u_{d1}}{\partial\zeta}\right|_{z=z_0} \left[\cos(\omega t+\gamma) + \frac{1}{12}(\cos(\omega t+2\phi_2+\gamma) + \cos(\omega t+2\phi_2-\gamma))\right] \tag{A61}$$

Now τ_1 and u_{*1} are related by

$$\frac{\tau_1}{\rho} = u_{*1}^2\cos(\omega t+\phi_2) \tag{A62}$$

By rearranging the term giving the time variation in Equation A61 it is seen that

$$\begin{aligned}\cos(\omega t+\gamma) + \frac{1}{12}[\cos(\omega t+2\phi_2+\gamma) + \cos(\omega t+2\phi_2-\gamma)] \\ = \cos(\omega t+\phi_2)\left[\cos(\gamma-\phi_2) + \frac{1}{6}\cos\gamma\cos\phi_2\right] \\ - \sin(\omega t+\phi_2)\left[\sin(\gamma-\phi_2) + \frac{1}{6}\sin\phi_2\cos\gamma\right]\end{aligned} \tag{A63}$$

From Equation A62 the time variation of τ_{w1} is given as proportional to $\cos(\omega t+\phi_2)$. Therefore the second term in Equation A63 must vanish for all t. This leads to

$$\phi_2 = \tan^{-1}\left[\frac{6}{5}\tan\gamma\right] \tag{A64}$$

and the closure equation, i.e., Equation A61, can be written as

$$\frac{u_{*1}}{u_b} = \sqrt{\frac{2}{\pi}}P\kappa\left|\zeta\frac{\partial u_{d1}}{\partial\zeta}\right|_{z=z_0} \tag{A65}$$

with

$$P = \cos(\gamma-\phi_2) + \frac{1}{6}\cos\gamma\cos\phi_2 \tag{A66}$$

Equation A65 is an implicit equation for u_{*1} and can be solved by iteration. For small μ it is seen that this equation differs from the closure equation of the time-invariant model only in the presence of a factor $\sqrt{2/\pi}P$ in Equation A65. From Equations A64 and A65 it is found that $P = 1.12$ for $\gamma = 30°$ which is a typical value in practice. This results in the extra factor in the closure equation having a value of 0.89.

As a result of this similarity in the closure equations it can be expected that the wave solution from the time-varying model will be close to that of the time-invariant model. This can be seen in Figure A3 which compares the wave friction factor for a pure wave motion obtained from the two models. It is apparent that the friction factors differ by only about 9%.

It should be noted that the wave friction factor for the time-varying model plotted in Figure A3 is defined using the magnitude of the first harmonic of the bottom shear stress, i.e., by

$$\tau_1 = \frac{1}{2}\rho f_w u_b^2 \tag{A67}$$

and not by the maximum bottom shear stress. In the time-invariant model the assumption of a constant eddy viscosity resulted in the bed shear stress containing only a first harmonic component which meant that the maximum bed shear stress was equal to the magnitude of that component.

Furthermore, since the near bottom eddy viscosity is scaled by u_{*1}, the only effect of a current (i.e., $\mu \neq 0$) on the wave problem will be to impose a linear variation of the eddy viscosity above the level $\zeta = \sqrt{\frac{2}{\pi}}\alpha_1/\mu$ instead of the constant value used in the pure wave problem (i.e., when $\mu = 0$). The wave friction factor in the presence of currents, f_{wc}, is plotted against A_b/k_n in Figure A4 for several values

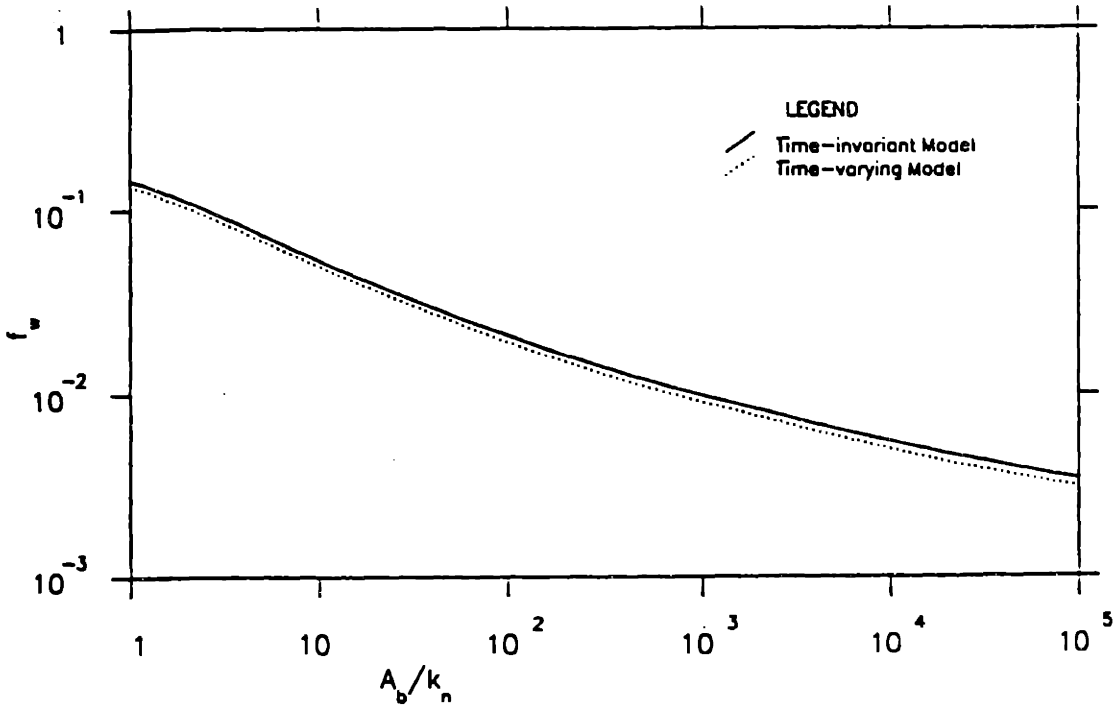

a. Wave friction factor diagram

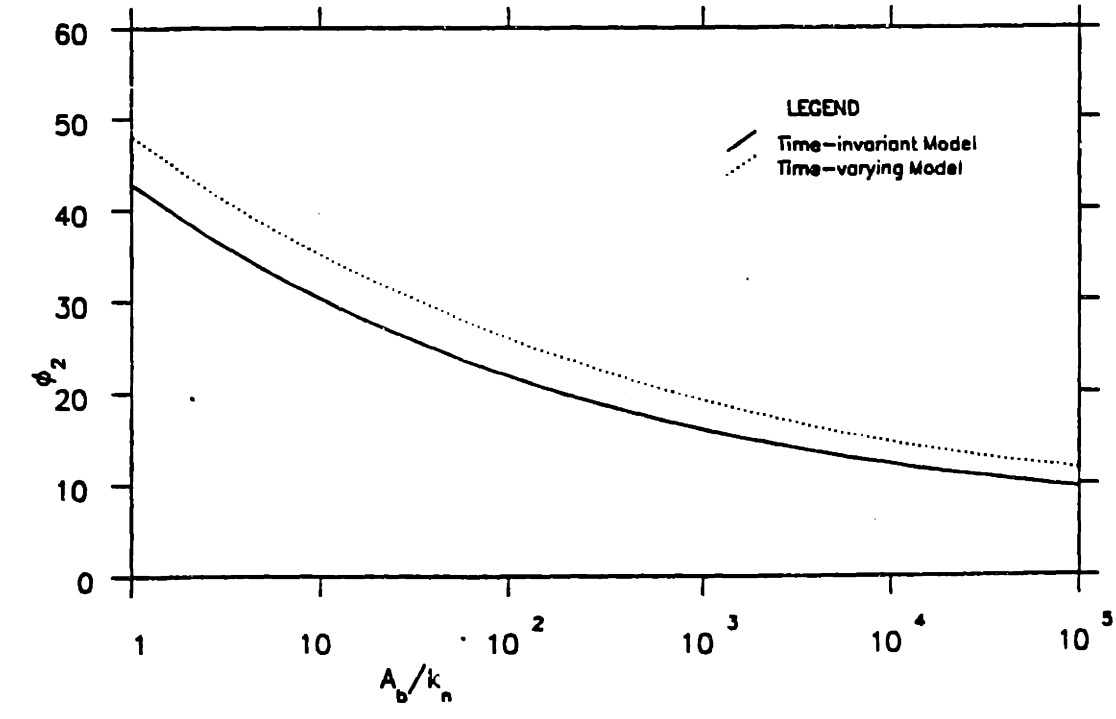

b. Phase lead of the bottom shear stress

Figure A3. Comparison of the wave friction factor and phase leads of the bottom shear stress obtained from the time-invariant and time-varying models

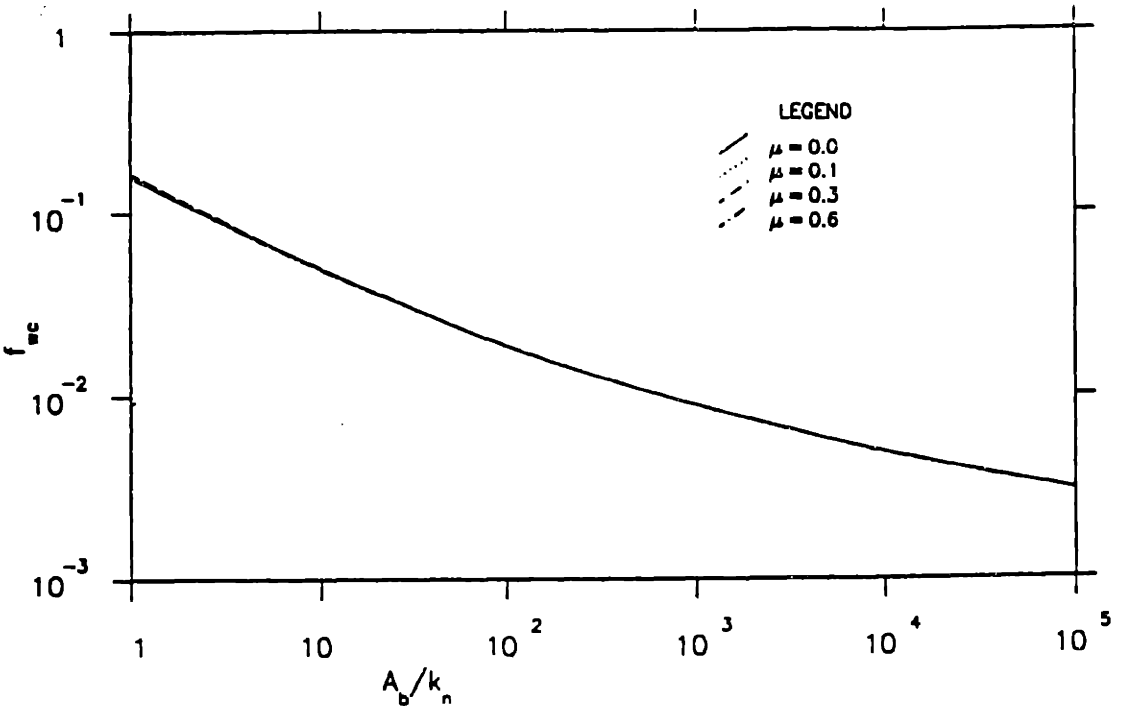

a. Wave friction factor diagram

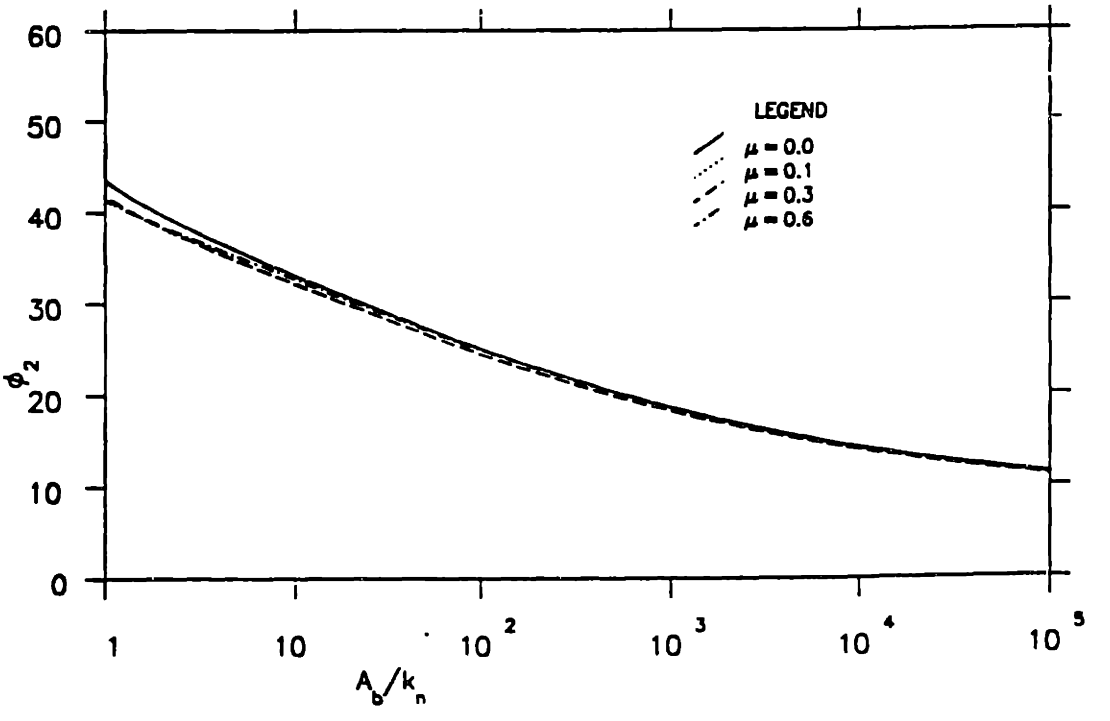

b. Phase lead of the bottom shear stress

Figure A4. Wave friction factor in the presence of a current, f_{wc}, against A_b/k_n for several values of μ from the time-varying models

of μ. It is seen that f_{wc} is only very weakly dependent on μ. However, the symbol f_{wc} will still be used to denote the presence of a current.

Similarly, after substitution into Equation A57 the third harmonic shear stress can be written as

$$\frac{1}{u_b}\frac{\tau_3}{\rho} = \sqrt{\frac{2}{\pi}}\kappa u_{*1}\left\{\left|\zeta\frac{\partial u_{d1}}{\partial\zeta}\right|_{z=z_0}\frac{1}{4}\cos(3\omega t+2\phi_2+\gamma) + \left|\zeta\frac{\partial u_{d3}}{\partial\zeta}\right|_{z=z_0}\cos(3\omega t+2\phi_2+\sigma)\right\} \tag{A68}$$

After manipulating this expression as done for Equation A61 the third harmonic shear stress can be written as

$$\frac{\tau_3}{\rho} = \sqrt{\frac{2}{\pi}}\kappa u_b u_{*1} Q\cos(3\omega t+\phi_3) \tag{A69}$$

where

$$\phi_3 = \tan^{-1}\left[\frac{\frac{1}{4}\left|\zeta\frac{\partial u_{d1}}{\partial\zeta}\right|_{z=z_0}\sin(2\phi_2+\gamma) + \left|\zeta\frac{\partial u_{d3}}{\partial\zeta}\right|_{z=z_0}\sin(2\phi_2+\sigma)}{\frac{1}{4}\left|\zeta\frac{\partial u_{d1}}{\partial\zeta}\right|_{z=z_0}\cos(2\phi_2+\gamma) + \left|\zeta\frac{\partial u_{d3}}{\partial\zeta}\right|_{z=z_0}\cos(2\phi_2+\sigma)}\right] \tag{A70}$$

and

$$Q = \frac{1}{4}\left|\zeta\frac{\partial u_{d_1}}{\partial\zeta}\right|_{z=z_0}\cos(2\phi_2+\gamma-\phi_3) + \left|\zeta\frac{\partial u_{d_3}}{\partial\zeta}\right|_{z=z_0}\cos(2\phi_2+\sigma-\phi_3) \tag{A71}$$

Therefore the magnitude of the third harmonic shear stress can be found using Equations A69–A71. It is found that the ratio τ_1/τ_3 is 0.115 for $A_b/k_n = 4$ and 0.136 for $A_b/k_n = 10^6$. Furthermore, ϕ_3 was found to have almost three times the value of ϕ_2. This means that the peak shear stress will be very close to the sum of τ_1 and τ_3. In other words the peak shear stress is about 12% greater that τ_1. Recalling that the value of τ_1 from the time-varying model was about 9% less than the maximum shear stress given by the time-invariant model it is seen that the maximum bed shear stresses predicted by both models will be nearly identical.

The first and third harmonic velocities, denoted by u_{w1} and u_{w3}, can be obtained from Equation 196 as

$$u_{w1} = u_b\left\{\cos\omega t + \mathrm{Re}\left[u_{d1}\left[e^{i\omega t} + \frac{i}{6}\sin(\omega t+2\phi_2)\right]\right]\right\} \tag{A72}$$

and

$$u_{w3} = u_b\mathrm{Re}\left[e^{i(3\omega t+2\phi_2)}\left[\frac{u_{d1}}{12} + u_{d3}\right]\right] \tag{A73}$$

A.4 The Current Problem

The governing equations are Equations A23 and A24. The second term in Equation A23 appears as a result of the eddy viscosity being allowed to be time-varying. From Equations A32 and A34 it is seen that

$$\tilde{\nu}_0 = \bar{\nu}\mu^2\cos\phi_{cw}\cos(\omega t+\phi_2) \tag{A74}$$

and from Equation A72 it is found that

$$\frac{\partial\tilde{u}_0}{\partial z} = u_b\mathrm{Re}\left\{\frac{\partial u_{d1}}{\partial z}\left[e^{i\omega t} + \frac{i}{6}\sin(\omega t+2\phi_2)\right]\right\} \tag{A75}$$

Let

$$\frac{\partial u_{d1}}{\partial z} = \frac{u_b}{\delta}U'(z)e^{i\phi_1(z)} \tag{A76}$$

where δ is defined in Equation A50 and

$$U'(z) = \left|\frac{\partial u_{d1}}{\partial\zeta}\right| \tag{A77}$$

Then

$$\frac{\partial\tilde{u}_0}{\partial z} = \frac{u_b}{\delta}U'(z)\left[\cos(\omega t+\phi_1(z)) - \frac{1}{6}\sin\phi_1(z)\sin(\omega t+2\phi_2)\right] \tag{A78}$$

and the second term on the right-hand side of Equation A23 can be evaluated as

$$\overline{\tilde{\nu}_0 \frac{\partial \tilde{u}_0}{\partial z}} = \bar{\nu}\mu^2 \cos\phi_{cw} \frac{U_b}{\delta} U'(z) \frac{1}{2}\left[\cos(\phi_1(z)-\phi_2) - \frac{1}{6}\sin\phi_1(z)\sin\phi_2\right] \quad \text{(A79)}$$

Substituting Equation A79 into Equation A23, dividing by $\bar{\nu}$, and integrating from z_0 to a level z gives

$$\bar{u} = \cos\phi_{cw}\left[\int_{z_0}^{z} \frac{u_{*c}^2}{\bar{\nu}} dz - \frac{\mu^2 u_b}{\delta}\int_{z_0}^{z} \frac{U'(z)}{2}\left[\cos(\phi_1(z)-\phi_2) - \frac{1}{6}\sin\phi_1(z)\sin\phi_2\right] dz\right] \quad \text{(A80)}$$

Introducing the non-dimensional vertical coordinate ζ, defined in Equation 9, gives

$$\bar{u} = \cos\phi_{cw}\left[\int_{\zeta_0}^{\zeta} \frac{\delta u_{*c}^2}{\bar{\nu}} d\zeta - \mu^2 u_b \int_{\zeta_0}^{\zeta} \frac{U'(\zeta)}{2}\left[\cos(\phi_1(\zeta)-\phi_2) - \frac{1}{6}\sin(\phi_1(\zeta))\sin\phi_2\right] d\zeta\right] \quad \text{(A81)}$$

This can be written as

$$\bar{u} = \cos\phi_{cw}[I_1(\zeta) - I_2(\zeta)] \quad \text{(A82)}$$

with

$$I_1(\zeta) = \int_{\zeta_0}^{\zeta} \frac{u_{*c}^2 \delta}{\bar{\nu}} d\zeta \quad \text{(A83)}$$

and

$$I_2(\zeta) = \int_{\zeta_0}^{\zeta} \frac{\mu^2 u_b U'(\zeta)}{2}\left[\cos(\phi_1(\zeta)-\phi_2) - \frac{1}{6}\sin\phi_1(\zeta)\sin\phi_2\right] d\zeta \quad \text{(A84)}$$

Integration of Equation A24 results in

$$\bar{v} = I_1(\zeta)\sin\phi_{cw} \tag{A85}$$

It is seen from Equation A82 that the equation for the component of the current velocity in the wave direction has two terms—the first due to the mean shear stress and the second due to the time-varying eddy viscosity, i.e., due to the wave motion. Equation A85 which is for the component in the direction normal to the wave motion has only the contribution from the mean shear stress.

Equation A82 can be written as

$$\bar{u} = \int_{z_0}^{z} \frac{u_{*c}^2 \cos\phi_{cw}}{\bar{\nu}}[1-R(z)]dz \tag{A86}$$

where

$$R(z) = \frac{\overline{\tilde{\nu}_0 \frac{\partial \tilde{u}_0}{\partial z}}}{\overline{u_{*c}^2 \cos\phi_{cw}}} \tag{A87}$$

Using Equation A74 for the relation between $\tilde{\nu}_0$ and $\bar{\nu}$ and Equation A59 for the definition of μ Equation A87 can be written as

$$R(z) = \frac{\bar{\nu}}{u_{*1}^2} \overline{\frac{\partial \tilde{u}_0}{\partial z}\cos(\omega t+\phi_2)} \tag{A88}$$

The function R(z) gives the importance of the second term which is related to the wave motion, to the first, which is related to the mean shear stress. In the limit as z approaches z_0 it is seen that

$$\lim_{z \to z_0}[R(z)] = \frac{1}{u_{*1}^2}\kappa\sqrt{\frac{2}{\pi}}u_{*1}\lim_{z \to z_0}\left[z\overline{\frac{\partial \tilde{u}_0}{\partial z}\cos(\omega t+\phi_2)}\right] \tag{A89}$$

where the expansion for $\bar{\nu}$ from Equation A34 has been used. From the closure of the wave problem in the time-varying model in Equation A65 this can be written as

$$\lim_{z \to z_0} [R(z)] = \frac{\left[\cos(\phi_2 - \gamma) - \frac{1}{6}\sin\phi_2 \sin\gamma\right]}{2P} \tag{A90}$$

where γ is defined in Equation A58 and P in Equation A66.

Equation A90 has been evaluated for range of values of μ and A_b/k_b. It is found that the value of R(z) at the bottom lies between 0.423 and 0.428 for $1 < A_b/k_b < 10^6$ and for any value of μ.

The above result shows that near the bottom the mean velocity component in the wave direction, $\bar{u}$, increases less rapidly than that in the direction normal to the waves, $\bar{v}$. This means that the value of the mean velocity will be sensitive to ϕ_{cw} because the partitioning of the velocity into the two components depends on ϕ_{cw}. It is hoped that this new mechanism by which the current velocity is linked to ϕ_{cw} will lead to results that are in better agreement with the data than the results of the time-invariant model, where this mechanism was not present.

The integral $I_1(\zeta)$ can be evaluated analytically using the eddy viscosity distribution given in Equation A34 to yield

$$I_1(\zeta) = \begin{cases} \frac{u_{*c}}{\kappa}\mu\sqrt{\frac{\pi}{2}}\ln\left[\frac{\zeta}{\zeta_0}\right] & \zeta_0 < \zeta < \alpha_1 \\ \frac{u_{*c}}{\kappa}\mu\sqrt{\frac{\pi}{2}}\left[\frac{\zeta}{\alpha_1} - 1 + \ln\left[\frac{\alpha_1}{\zeta_0}\right]\right] & \alpha_1 < \zeta < \frac{\alpha_1\sqrt{\frac{2}{\pi}}}{\mu} \\ \frac{u_{*c}}{\kappa}\left[\ln\left[\frac{\zeta\mu}{\alpha_1\sqrt{\frac{2}{\pi}}}\right] + 1 + \mu\sqrt{\frac{\pi}{2}}\left[\ln\left[\frac{\alpha_1}{\zeta_0}\right] - 1\right]\right] & \zeta > \frac{\sqrt{\frac{2}{\pi}}\alpha_1}{\mu} \end{cases} \tag{A91}$$

where the constants of integration have been determined by requiring continuity of the velocity at the various matching levels.

Once the wave problem is solved the values of $U'(\zeta)$ and $\phi_1(\zeta)$ can be found at any level, thus allowing the numerical integration of I_2. Finally, the angle between the current velocity vector and the direction of waves, ϕ_c, is given by

$$\phi_c = \tan^{-1}\left[\frac{\tan(\phi_{cw})I_1(\zeta)}{I_1(\zeta) - I_2(\zeta)}\right] \tag{A92}$$

Equation (A90) shows that near the bottom $I_2(\zeta)$ is positive and less than $I_1(\zeta)$. Therefore $I_1(\zeta)$ is greater than $I_1(\zeta) - I_2(\zeta)$ which results in $\phi_c > \phi_{cw}$ from Equation A92. In other words the effect of the waves is to deflect the current velocity further from the wave direction than the mean shear stress. Since the second term in Equation A23 is related to the waves it can be expected to die out near the top of the wave boundary layer. Then $I_2(\zeta)$ will reach a constant value at that level while $I_1(\zeta)$ keeps on increasing. This will result in the difference between ϕ_c and ϕ_{cw} decreasing and therefore at large heights above the bottom the direction of the current will approach that of the mean shear stress. This feature was not present in the time-invariant model and its presence here is an indication that the time variation of the eddy viscosity provides a more complete representation of the problem.

It should be noted that when $\tilde{\nu}_0$ is defined by Equation A74 it is implied that the eddy viscosity varies with time for all values of z, whereas in Equation A34 the time variation is specified only below the level $z = \sqrt{2/\pi}(\alpha_1/\mu)$. As discussed above the wave effects die out around the level $z = \delta$ and integral I_2 will reach a constant value. Therefore use of Equation A74 will not lead to significant error so long as the inequality in Equation A36 holds.

Another point to be kept in mind is that α_1 the model parameter has not been specified as yet. As in the time-invariant model this is done by comparing the

model results to the experimental data and selecting a value that gives the best agreement.

A.5 Comparison with Experimental Data

A.5.1 Description of the Data

The results of the model will be compared to the same data used by Wikramanayake (1989). These were the velocity and phase profiles obtained from the pure wave experiments of Jonsson and Carlsen (1976) and Van Doorn (1981), the mean velocity measurements in wave-current flow made by Bakker and Van Doorn (1978), and the results of the numerical turbulence model of Davies et al. (1988). The four data sets will be referred to by the codes JC, VDW, BVD, and DV, respectively. The parameters of the experimental runs available from these sets are given in Tables A1 and A2. In Table A1 the pure wave runs of the set DV are labeled as DVW. A detailed description of the data is given by Wikramanayake (1989).

A.5.2 Waves Alone

The first harmonic wave velocity and phase from Test 1 of Jonsson and Carlsen (1976) are compared in Figure A5 to the predictions from the time-varying model using three different values of the parameter α_1. As shown in Figure A5 the three values of α_1 give identical results near the bottom, which are in good agreement with the data while diverging at the top of the boundary layer where the agreement with the data is not that good. These results are very similar to those obtained by Wikramanayake (1989) using the time-invariant model. The comparison with the

Table A1

Experimental Parameters for the Data Sets
from a Pure Wave Motion

Data Set	u_b cm/s	ω s^{-1}	k_n cm	A_b/k_n
JC1	211.0	0.749	1.59	177.2
JC2	153.0	0.873	7.50	23.4
VDW	26.5	3.142	2.10	4.1
DVW05	50.0	0.785	15.0	4.2
DVW10	100.0	0.785	15.0	8.5
DVW15	150.0	0.785	15.0	12.7

Table A2

Experimental Parameters for the Data Sets
from a Combined Wave and Current Motion

Data Set	u_b cm/s	ω s^{-1}	k_n cm	A_b/k_n	ϕ_{cw} deg	Current Specification
BVD10	25.7	3.142	2.1	3.9	0	$u_c = 8.2$ cm/s at $z = 4.6$ cm
BVD20	24.3	3.142	2.1	3.7	0	$u_c = 22.4$ cm/s at $z = 5.9$ cm
DV0500	50.0	0.785	15.0	4.2	0	$\tau_c = 3.5$ Pa
DV1000	100.0	0.785	15.0	8.5	0	$\tau_c = 3.5$ Pa
DV1045	100.0	0.785	15.0	8.5	45	$\tau_c = 3.5$ Pa
DV1090	100.0	0.785	15.0	8.5	90	$\tau_c = 3.5$ Pa
DV1500	150.0	0.785	15.0	12.7	0	$\tau_c = 3.5$ Pa

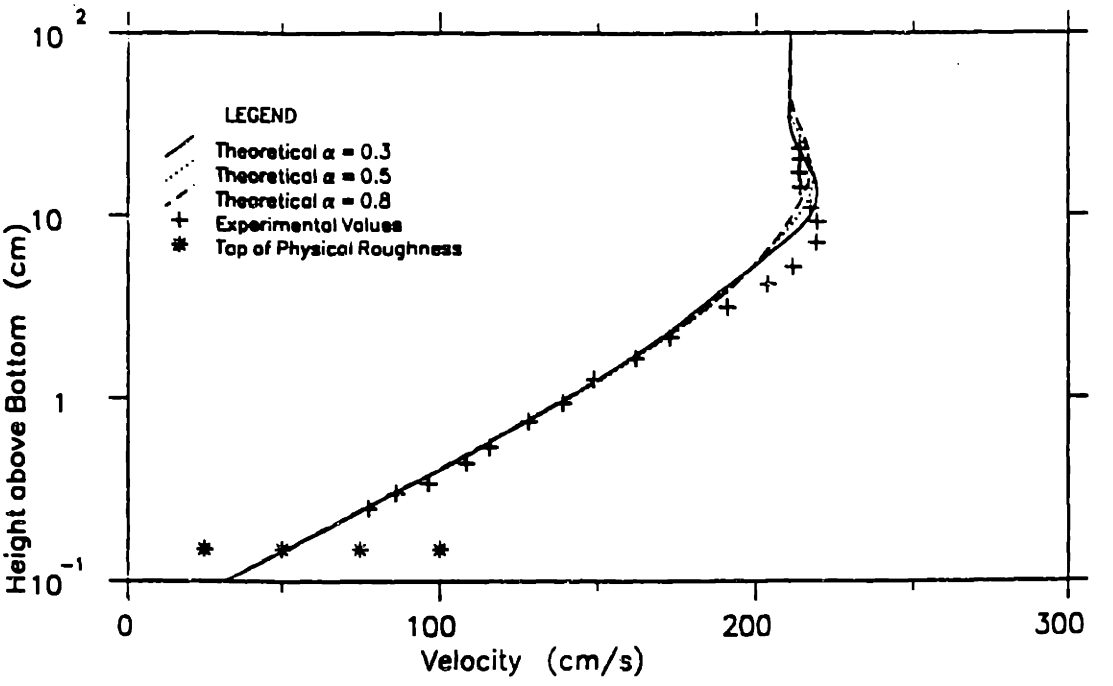

a. Wave velocity

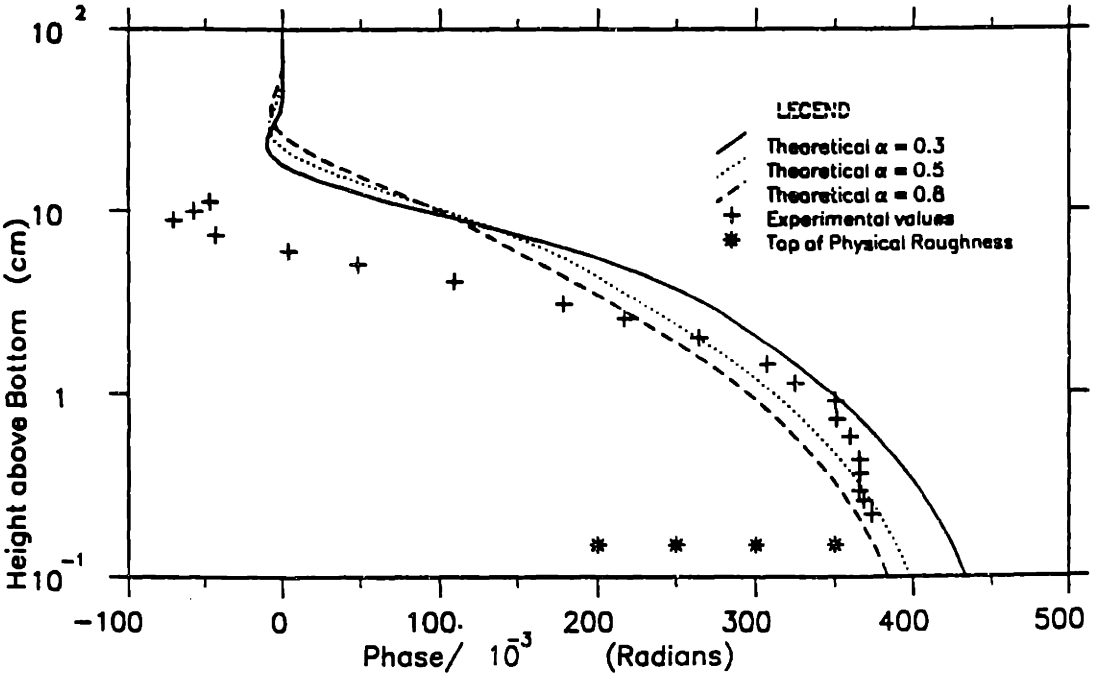

b. Phase

Figure A5. Comparison of the first harmonic wave velocity and phase profiles of Jonsson and Carlsen (1976) Test 1 with the results of the time-varying model using three different values of α_1

data sets JC2 and VDW are very similar to that shown in Figure A5, and will not be presented here.

The third harmonic wave velocity and phase for the same experiment are compared to the predictions from the model, using the same values of α_1, in Figure A6. It is seen that the predicted maximum magnitude of the results is less than the experimental value by 60% or more while the shape of the velocity profile is obtained reasonably well. The theoretical phase profile of the third harmonic is similar to the experimental values but with a shift in the vertical axis. The comparison between theory and experiment for the third harmonic of Test 2 of Jonsson and Carlsen is similar to Figure A6 and is therefore not shown. The agreement with the data shown in Figure A6 is similar to that obtained by Trowbridge and Madsen (1984). It should be noted that the data clearly show the existence of a third harmonic component thus justifying the inclusion of a time-varying eddy viscosity.

The predicted first harmonic, third harmonic, and peak shear stresses and the phase of the peak shear stress from the time-varying model are presented in Table A3 along with the peak shear stress and phase from Davies et al. (1988). It is seen that the magnitude of the third harmonic shear stress is about 11% of that of the first harmonic shear stress. It is found that these two shear stresses have nearly the same phase resulting in the peak shear stress being the sum of the two components.

It was seen in Figure A3 that the friction factor for the time-varying model was about 9% less than that for the time-invariant model. This friction factor was defined using the first harmonic shear stress only. However when the sum of the two harmonics is considered it is seen that the peak shear stress in the time-varying

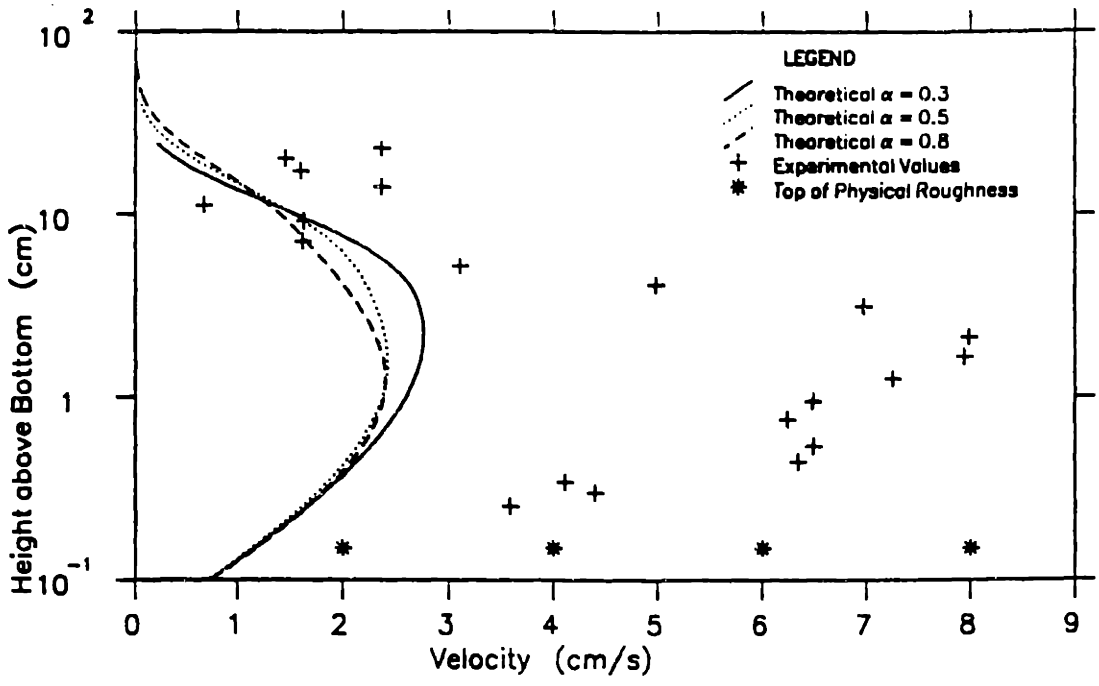

a. Wave velocity

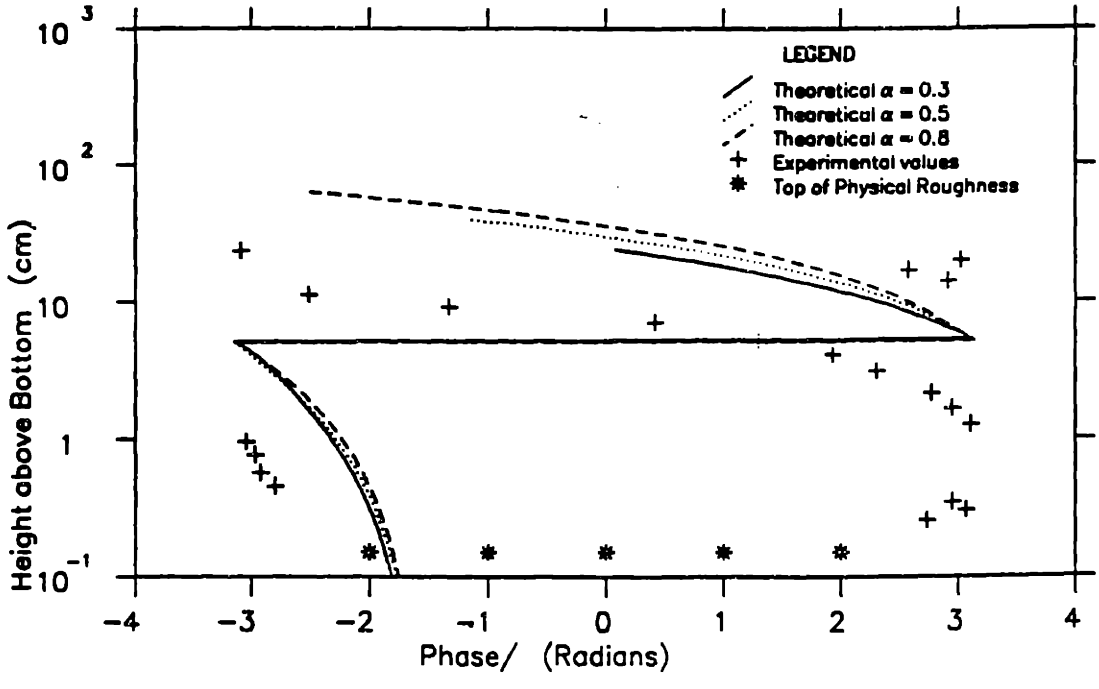

b. Phase

Figure A6. Comparison of the third harmonic wave velocity and phase profiles of Jonsson and Carlsen (1976) Test 1 with the results of the time-varying model using three different values of α_1

Table A3

Calculated First Harmonic, Third Harmonic, and Peak Shear Stresses and the Phase of the Peak Shear Stress for the Conditions of Davies, Soulsby, and King (1988) from the Time-varying Model Compared to the Results of Davies, Soulsby, and King

	Time Varying Model Results								Davies et al	
	Shear Stresses (Pa)						Phase of Peak Shear Stress deg		Peak Shear Stress Pa	Phase of Peak Shear Stress deg
	First Harmonic		Third Harmonic		Peak Shear Stress					
Data Set	α_1=0.5	α_1=0.8	α_1=0.5	α_1=0.8	α_1=0	α_1=0	α_1=0.5	α_1=0.8		
DVW05	9.3	9.4	1.1	1.1	10.3	10.5	39.4	35.1	8.1	28.2
DVW10	26.9	26.9	3.2	3.2	30.0	30.0	34.8	32.3	23.5	26.4
DVW10	50.3	50.1	6.0	5.9	56.3	56.0	32.9	30.8	44.3	25.2

Table A4

Calculated Maximum and Current Shear Stresses for the Conditions of Bakker and Van Doorn from the Time-varying Model for Three Values of α_1 and the Time-Invariant Model with $\alpha = 0.5$

	Current Shear Stress (Pa)				Maximum Shear Stress (Pa)			
	Time-Varying model			Time-Invariant Model	Time-Varying Model			Time-Invariant Model
Data Set	α_1=0.5	α_1=0.8	α_1=1.0	α=0.5	α_1=0.5	α_1=0.8	α_1=1.0	α=0.5
BVD10	0.17	0.21	0.23	0.19	3.0	3.1	3.1	3.0
BVD20	0.67	0.72	0.74	0.74	3.3	3.4	3.4	3.5

model is very close to the peak shear stress of the time-invariant model, which only allowed a first harmonic. This agrees with the results of Trowbridge and Madsen (1984).

As in the case of the time-invariant model the comparison shown in Figures A5 and A6 indicates that a value of α_1 equal to 0.3 or slightly less will result in the best agreement with the data. However, it is seen that the higher values of α_1 agree with the data near the bottom. Therefore, as in the time-invariant model, determination of a value for α_1 is deferred until the comparison with the experimental current velocity profile is made.

A.5.3 Waves and Currents

The current velocity profiles obtained from the time-varying model using three different values of α_1 are compared to the Bakker and Van Doorn data in Figure A7. The profiles obtained using $\alpha_1 = 0.8$ and $\alpha_1 = 1.0$ for the data set BVD10 are in better agreement with the data than the profile obtained with $\alpha_1 = 0.5$. Considering the set BVD20 it is seen that all three values of α_1 give good results with the two higher values doing slightly better.

However, it should be noted that in these two sets the current is specified by the velocity at a point in the upper logarithmic region, i.e., the calculated profile is required to pass through a selected data point. Since the model also uses a logarithmic profile in the outer region this means that the calculated profile will not be very sensitive to the value of α_1.

A better test for the appropriate value of α_1 is with data sets where the current is specified by the mean shear stress as in the conditions of Davies et al. (1988). The results for waves and currents in the same direction using $\alpha_1 = 0.5$ and $\alpha_1 = 0.8$

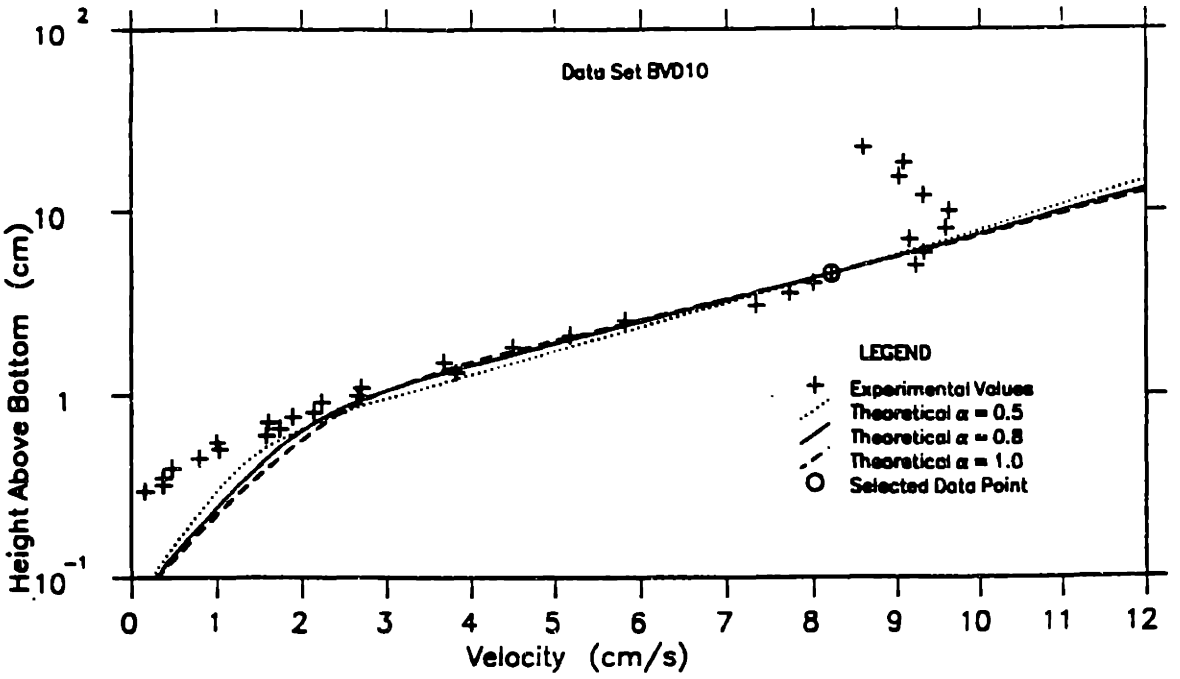

a. Data set BVD10

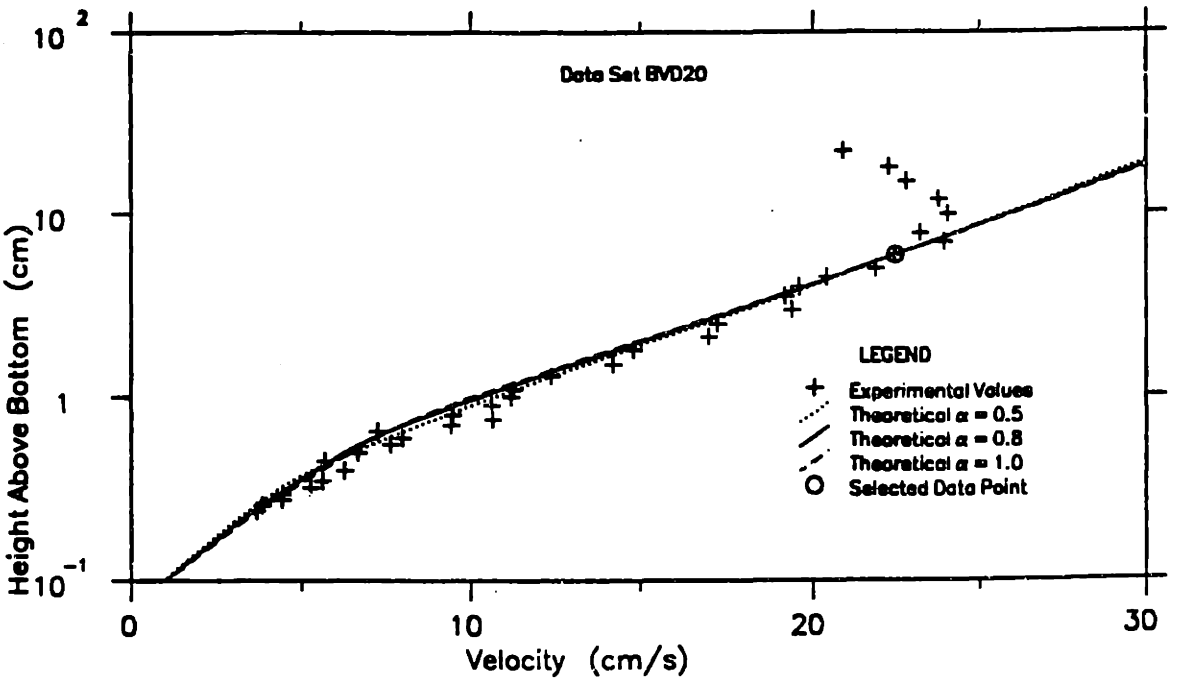

b. Data set BVD20

Figure A7. Comparison of the current velocity profiles from Bakker and Van Doorn (1978) with the results of the time-varying model with $\alpha_1 = 0.5$, $\alpha_1 = 0.8$, and $\alpha_1 = 1.0$

are compared to their results in Figure A8. It is seen that $\alpha_1 = 0.8$ gives a good fit to the data. This value of α_1 is greater than the value $\alpha = 0.5$ that was proposed for the time-invariant model.

There are two reasons for the different values of the model parameter obtained from the two models. First, the eddy viscosity used in the time-varying model is based on the mean shear velocity instead of the maximum shear velocity used in the time-invariant model. These two shear velocities differ by a factor of $\sqrt{2/\pi}$ as shown in Equation A32. Therefore, if it is required to have the same value of eddy viscosity in the intermediate region $\alpha_1\delta < z < \sqrt{2/\pi}\alpha_1\delta/\mu$ it seems that a value of α_1 around 0.625 should be used.

The second reason is that in the time-varying model the shear velocity is based on the maximum wave shear stress rather than the maximum combined shear stress. This is because the model is derived assuming a weak current relative to the waves ($\mu \ll 1$) and therefore the two shear stresses are assumed the same. However, the value of μ for the conditions simulated by Davies et al. (1988) is in the range 0.26-0.61 and is therefore not small. This means than the value of α_1 must increase further if the eddy viscosity profile used, and therefore the current velocity profiles obtained, are to be similar.

When conditions where μ is in fact small are considered it is found that a value of α_1 about 0.65 gives a current profile that matches the profile from the time-invariant model using $\alpha = 0.5$. This change in α_1 can also be seen in the values of Table A4 which gives the current shear stresses obtained for the conditions of Bakker and Van Doorn for the three values of α_1 along with the results of the time-invariant model with $\alpha = 0.5$. The data set BVD10 has a value of $\mu = 0.28$ while the set BVD20 has $\mu = 0.56$. It is seen that for the set BVD10 a value of α_1

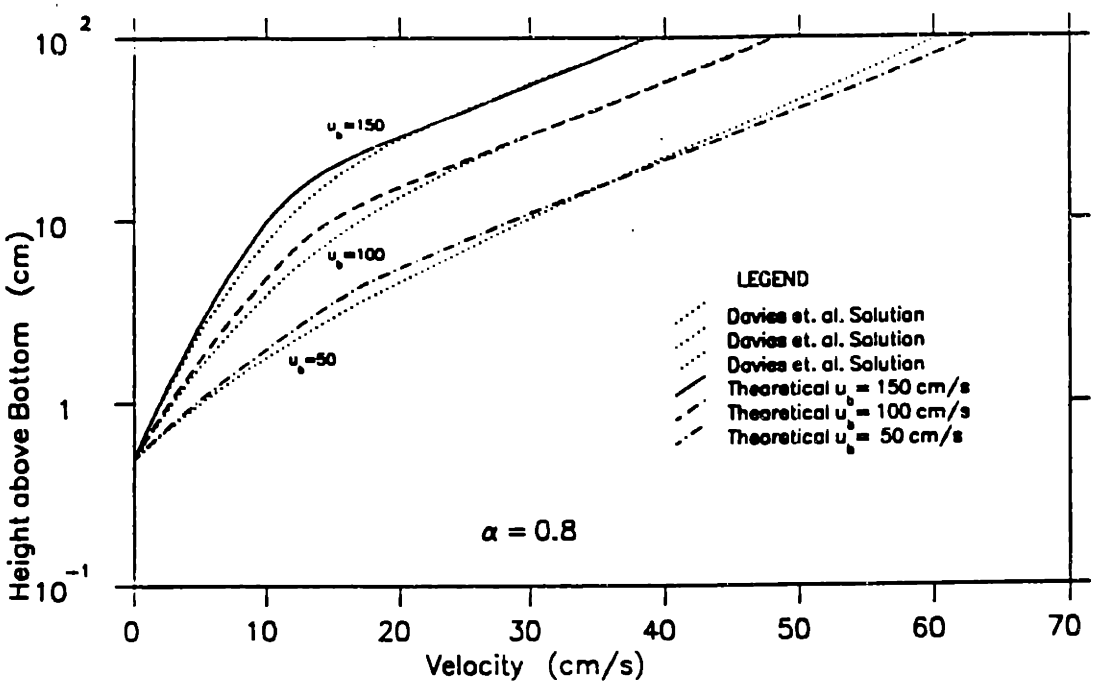

a. Comparison with $\alpha_1 = 0.8$

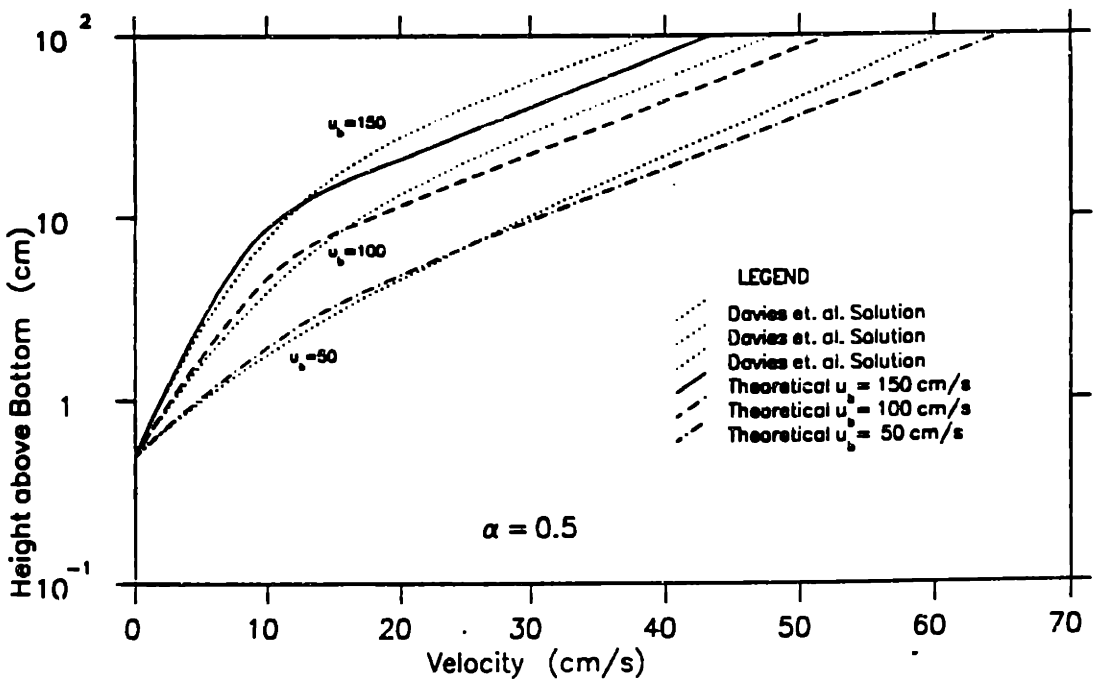

b. Comparison with $\alpha_1 = 0.5$

Figure A8. Comparison of the current velocity profiles from Davies et al. (1988) for waves and currents in the same direction with the results of the time-varying model with $\alpha_1 = 0.8$ and $\alpha_1 = 0.5$

between 0.5 and 0.8 gives the same result as the time-invariant model while $\alpha_1 = 1.0$ is required to obtain the same result for the set BVD20.

The results for waves and the current at an angle are compared with the results of Davies et al. in Figure A9 for $\alpha_1 = 0.5$ and $\alpha_1 = 0.8$. The figure shows that the time-varying model shows much greater sensitivity to the angle between the waves and the current than the time-invariant model shown in Figure A10. The velocity difference between $\phi_{cw} = 0$ and $\phi_{cw} = 90$ in the upper region is found to be 5.2 cm/s as compared to 2.5 cm/s from the time-invariant model.

This improvement is a result of the additional term in the equation for the current velocity in the wave direction, i.e., in Equation A23. It shows that there is more resistance to the mean flow in the wave direction than in the direction normal to the wave motion. In the time-invariant model the angle between the waves and the current, ϕ_{cw}, only comes in in Equation 31 which relates the combined shear stress to the wave and current shear stresses. The only effect ϕ_{cw} has on the velocity profile is to make u_{*cw} take on different values which results in only a small change in the profiles unless μ is very large.

Another result of the time-varying model using two equations from the two components of the mean velocity is that when $0 < \phi_{cw} < 90^\circ$ the direction of the mean velocity vector changes with height above the bottom as given in Equation A92. The results for the case $\phi_{cw} = 45^\circ$ are compared to those of Davies et al. in Figure A11. As expected from the form of Equation A92 the model predicts that the current velocity is at a greater angle to the wave direction than the mean shear stress. However, the predicted value of this increase is less than the data by about 4°, while the shape of the curve agrees with the data.

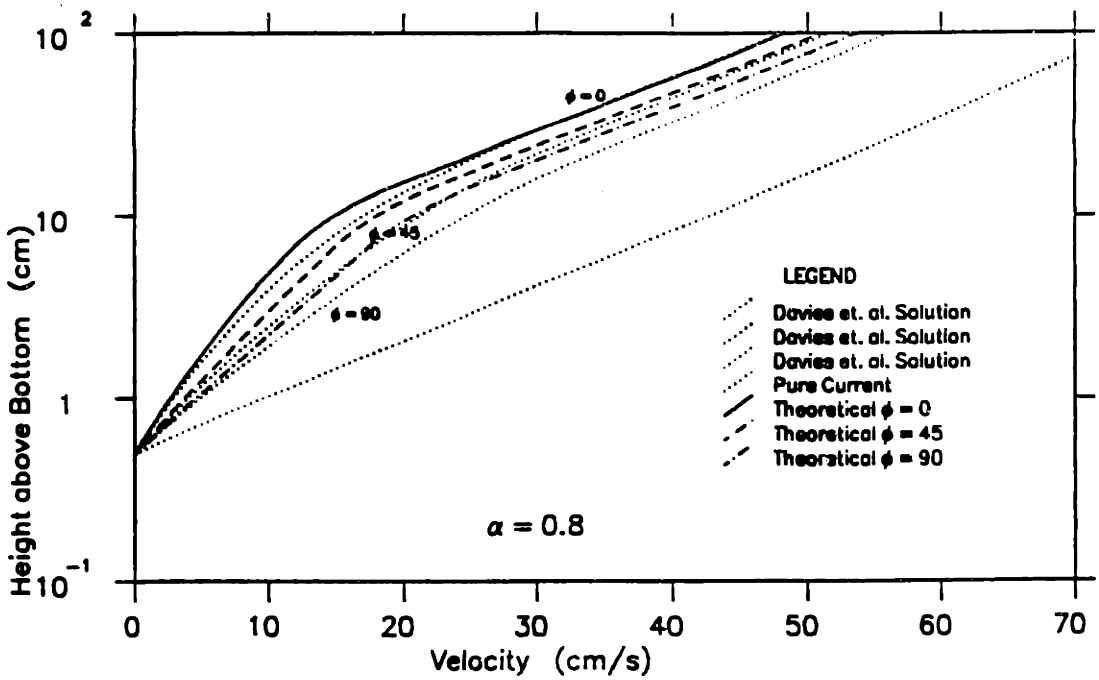

a. Comparison with $\alpha_1 = 0.8$

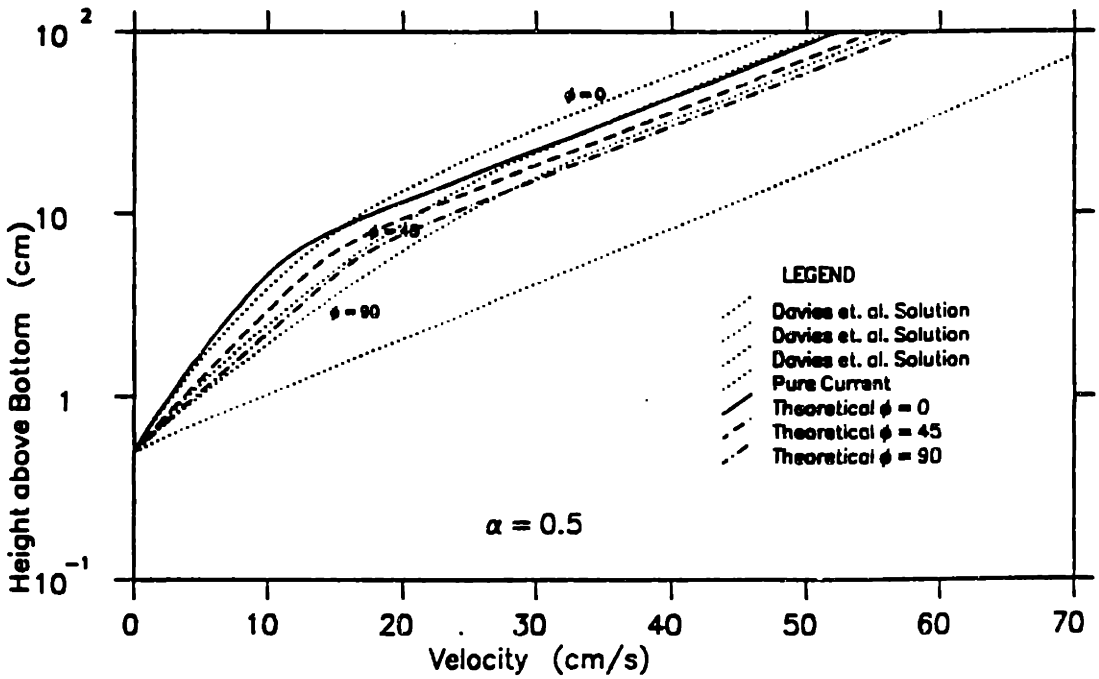

b. Comparison with $\alpha_1 = 0.5$

Figure A9. Comparison of the current velocity profiles from Davies et al. (1988) for waves and the current at an angle with the results of the time-varying model with $\alpha_1 = 0.8$ and $\alpha_1 = 0.5$

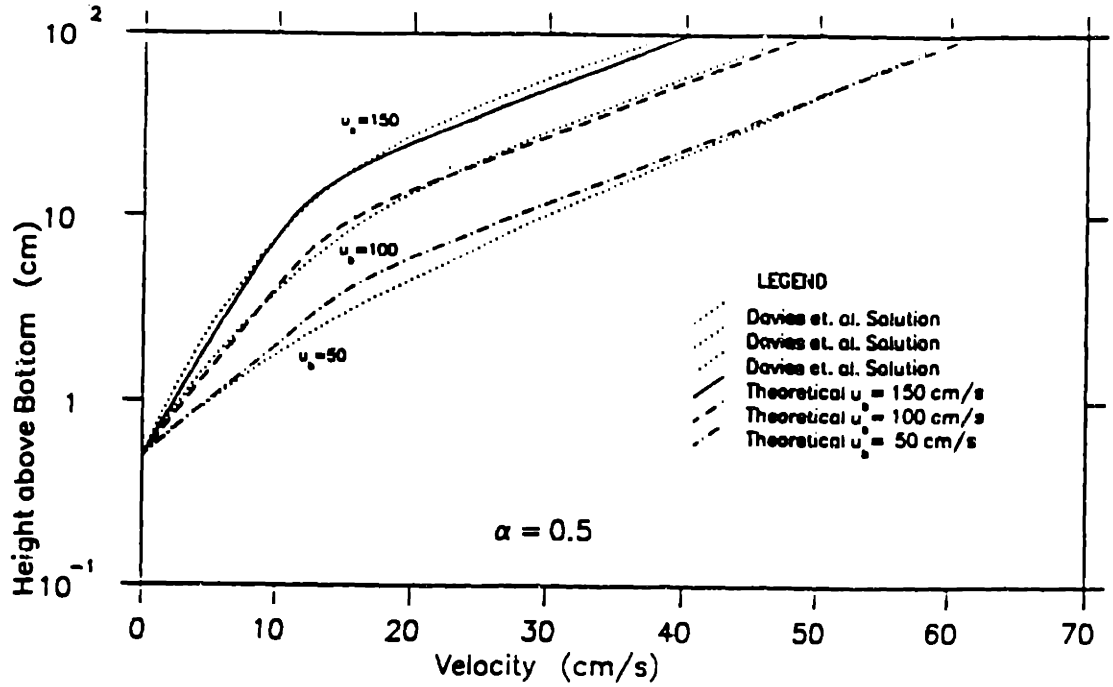

a) Waves and current in the same direction

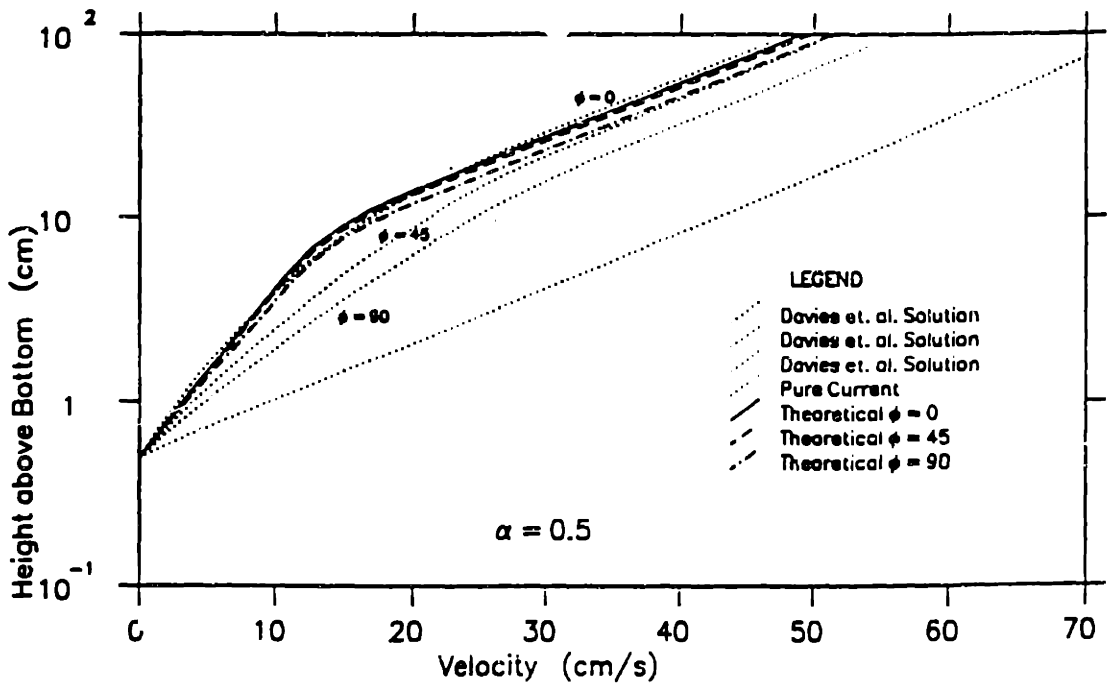

b) Waves and current at an angle

Figure A10. Comparison of the current velocity profiles from Davies et al. (1988) for waves and currents in the same direction ($\phi_{cw} = 0$), and waves and currents at an angle ($\phi_{cw} \neq 0$), with the results of the time-invariant model with $\alpha = 0.5$

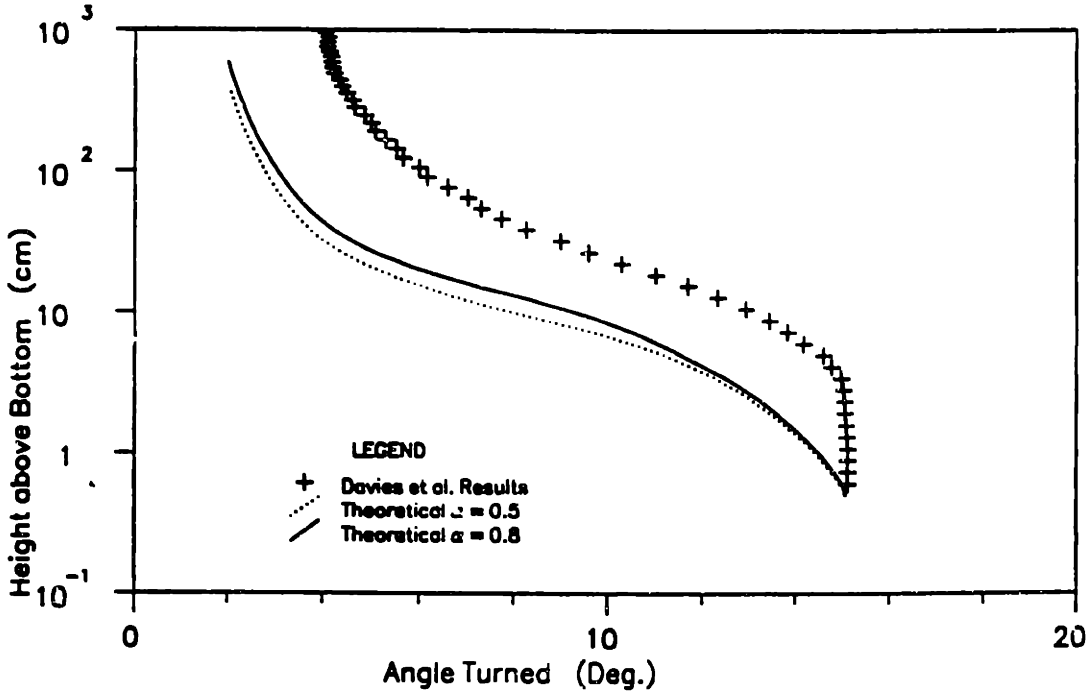

Figure A11. Comparison of the angle that the current velocity vector is deflected from the direction of the mean shear stress for the case $\phi_{cw} = 45^{\circ}$ from Davies et al. (1988) with the results of the time-varying model with $\alpha_1 = 0.5$ and $\alpha_1 = 0.8$

The comparisons of the current profiles with the experimental data strongly suggest that $\alpha_1 = 0.8$ be selected as the value of the model parameter. The comparison with the pure wave data suggests a value of $\alpha_1 = 0.3$ be used. As in the time-invariant model the model parameter will be selected so as to give the best agreement with the current profile because the resulting relatively poor agreement with the pure wave data is only at the top of the wave boundary layer, a region that is not of great importance in likely applications of the theory.

Therefore $\alpha_1 = 0.8$ is taken as the model parameter. There is however an indication that a smaller value of α_1 (around 0.65) will be more suitable in cases where μ is small. Nevertheless it is seen from Figures A7, A8, and A9 that $\alpha_1 = 0.8$ gives good agreement for conditions with μ ranging from 0.25 to 0.6. This is seen as sufficient evidence to adopt that value for the model.

A.6 Simplification of the Current Problem

The time-varying model presented in this chapter is able to represent the wave-current interaction better than the time-invariant model. This improvement was gained at the cost of requiring a numerical integration to obtain the current velocity profile. If a simple analytic form of this integral can be obtained the solution of the current problem of this model will be no more complicated than that of the time-invariant model.

As given in Equation A86 the current velocity in the wave direction can be written as

$$\bar{u} = \int_{\zeta_0}^{\zeta} \frac{u_{*c}^2 \cos\phi_{cw}}{\bar{\nu}} [1 - R(\zeta)] d\zeta \qquad (A93)$$

with $\bar{\nu}$ defined by Equation A34 and δ by Equation A50. It was seen from Equation A89 that the value of $R(\zeta)$ is between 0.423 and 0.428 at $z = z_0$. $R(\zeta)$ represents the effect of the wave motion on the current profile and can be expected to die out at a height above the bottom that is scaled by the wave boundary layer thickness.

Therefore the simplest approximation for $R(\zeta)$ will be a linear variation from a value of 0.425 at $z = z_0$ to zero at $z = \delta$ with the value being zero for $z > \delta$. In terms of the non-dimensional vertical coordinate ζ this can be written as

$$R(\zeta) = \begin{cases} A + B\zeta & z \leq \delta \\ 0 & z > \delta \end{cases} \tag{A94}$$

where

$$A = \frac{0.425}{1 - \zeta_0} \tag{A95}$$

and

$$B = -\frac{0.425}{1 - \zeta_0} \tag{A96}$$

Then $\bar{u}$ can be written as

$$\bar{u} = \cos\phi_{cw}(I_1(\zeta) - I_2(\zeta)) \tag{A97}$$

where $I_1(\zeta)$ has been evaluated and is given by Equation A91. The integral $I_2(\zeta)$ is given by

$$I_2(\zeta) = \int_{\zeta_0}^{\zeta} \frac{u_{*c}^2 \cos\phi_{cw}\delta(A+B\zeta)d\zeta}{\bar{\nu}} \tag{A98}$$

with A and B from Equations A95 and A96.

Using $\bar{\nu}$ from Equation A34 this can be evaluated analytically . The form of the solution depends on whether the level $z = \delta$ is above or below the level $z =$

$(\delta\sqrt{2/\pi}\alpha)/\mu$. As mentioned in the discussion following Equation A34, the theory developed so far can be considered justified so long as Equation A36 holds, i.e., $(\sqrt{2/\pi}\alpha_1)/\mu > 1$ holds. Since $\alpha_1 = 0.8$ has been selected for the time-varying model this reduces to $\mu < 0.64$.

When this condition is satisfied the solution for $I_2(\zeta)$ can be obtained by carrying out the integration in Equation A98 and obtaining the constants by requiring a solution to be continuous across the level $z = \alpha_1\delta$. $I_2(\zeta)$ is found to be

$$I_2(\zeta)=\begin{cases}\frac{u_{*c}}{\kappa}\sqrt{\frac{\pi}{2}}\mu\left[A\ \ln\left[\frac{\zeta}{\zeta_0}\right]+B(\zeta-\zeta_0)\right] & \zeta<\alpha_1\\ \frac{u_{*c}}{\kappa}\sqrt{\frac{\pi}{2}}\mu\left[A\left[\frac{\zeta}{\alpha_1}-1\right]+\frac{B}{2}\left[\frac{\zeta^2}{\alpha_1}-\alpha_1\right]+A\ln\left[\frac{\alpha_1}{\zeta_0}\right]+B(\alpha_1-\zeta_0)\right] & \alpha_1<\zeta<1\\ \frac{u_{*c}}{\kappa}\sqrt{\frac{\pi}{2}}\mu\left[A\left[\ln\left[\frac{\alpha_1}{\zeta_0}\right]+\frac{1}{\alpha_1}-1\right]+\frac{B}{2}\left[\alpha_1+\frac{1}{\alpha_1}-2\zeta_0\right]\right] & \zeta>1\end{cases} \quad \text{(A99)}$$

where it has been assumed that $\alpha_1 < 1$.

Therefore Equations A91 and A99 can be used to find the current velocity profile without the need of numerical integration. The solution for the conditions of Davies et al. (1988) using Equations A91 and A99 is compared to that obtained by numerical integration in Figure A12. It is seen that Equation A99 is a very good approximation to the exact value of $I_2(\zeta)$. It has been found that the approximation is good for a large range of μ and A_b/k_b and so Equation A99 can be used with confidence in the current solution.

A.7 Summary

An eddy viscosity model that included time variation was considered in this chapter. The assumption of a weak current relative to the waves was made in order to obtain simplified approximate equations for the wave and current motions. It

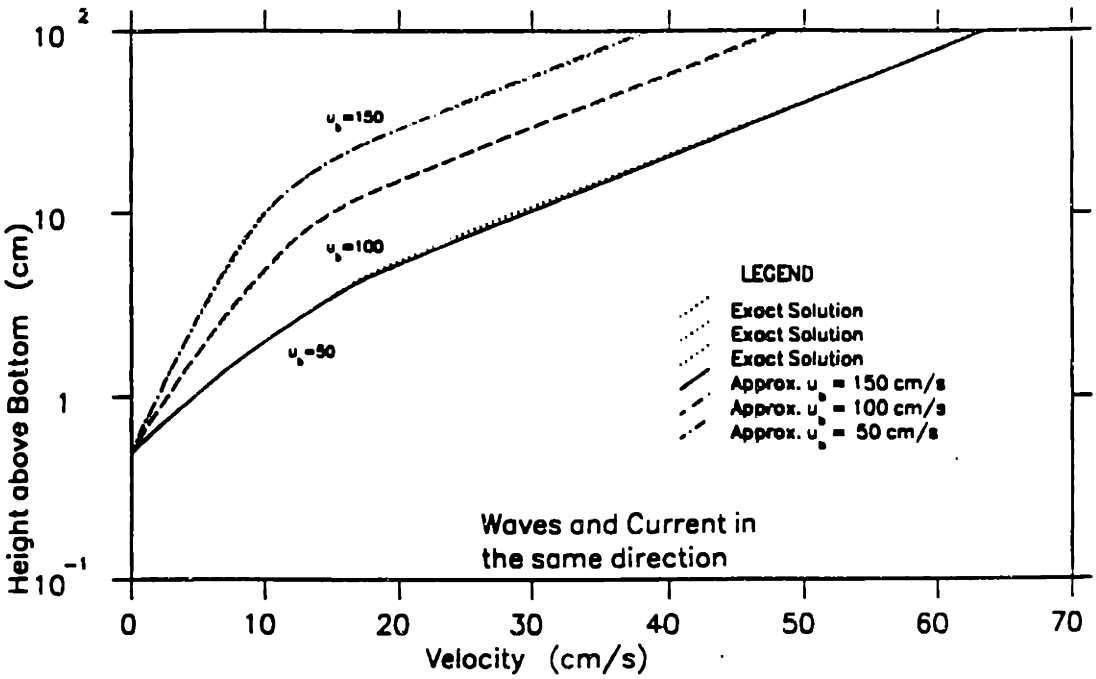

a. Comparison for waves and current in the same direction

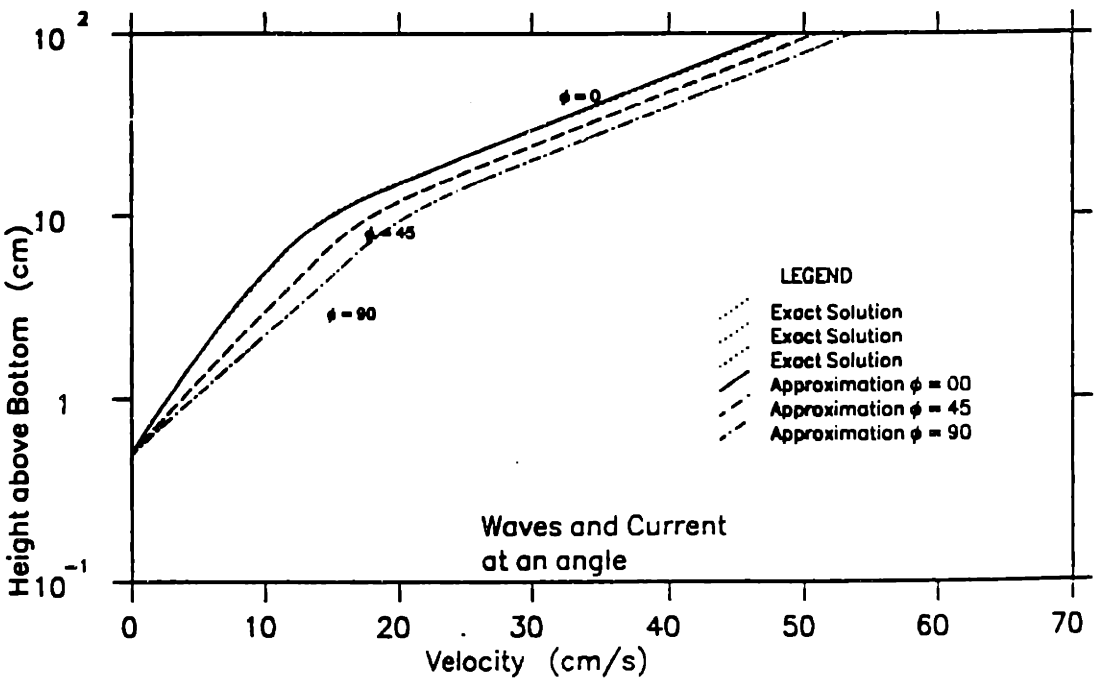

a. Comparison for waves and current at an angle

Figure A12. Current velocity profiles for the conditions of Davies et al. (1988) obtained from the numerical integration of Equation A84 and using the approximation of Equation A99

was seen that the wave problem was similar to the wave problem of the time-invariant model.

The approximate equations for the current showed that the component of the mean velocity in the wave direction is governed by a different equation from that which governs the mean velocity in a direction normal to the wave motion. This results in a significant increase in the sensitivity of the current velocity profile to ϕ_{cw}, the angle between the waves and the current, in agreement with experimental evidence. Another feature is the variation with height of the direction of the mean velocity when $0° < \phi_{cw} < 90°$—a feature that was not present in the time-invariant model but was indicated by the sophisticated numerical models.

However, the time-varying model is derived only for small values of μ and bases its eddy viscosity on the wave shear stress only. This results in the shear velocity used in the time-varying model, unlike the time-invariant model, being insensitive to the magnitude or the direction of the current. When μ is small this effect is negligible but it may be significant for stronger currents. Thus it is seen that the time-varying model includes a sensitivity to ϕ_{cw} that is not present in the time-invariant model while neglecting an effect that could be important at higher values of μ. It should also be remembered that the solutions obtained are expected to be good only for $\mu < \sqrt{2/\pi}\alpha_1$.

These objections notwithstanding, it is seen from the comparisons with the experimental data that the selection of $\alpha_1 = 0.8$ gives good agreement with all the data sets. The agreement for waves and the current in the same direction is as good as from the time-invariant model while the agreement for waves and the current at an angle is much better than that from the time-invariant model. It should be noted that there is an indication that a value of α_1 around 0.65 is more suitable for

conditions with smaller (< 0.1) values of μ. A simple approximation of the integral involved in the current solution resulted in an analytic expression for the current velocity.